# Infrared and Photocatalytic Studies of Model Bacterial Species for Water Treatment

A thesis presented to the
Queensland University of Technology

in fulfilment of the requirements for the degree of
Doctor of Philosophy

by
Sarah Ede
Bachelor of Applied Science (Hons)

Under the Supervision of:
Dr. Geoffrey Will
A. Prof. Louise Hafner
Prof. Ray Frost

*Inorganic Materials Research Program*
School of Physical and Chemical Sciences
Queensland University of Technology

November 2006

# ABSTRACT

The use of a $CO_2$ infrared (IR) laser and photocatalysis for water treatment micro-organism disinfection purposes was investigated.

During $CO_2$ infrared (IR) laser treatment *E. cloacae* inactivation was comparable to inactivation via ultraviolet (UV) treatment; however no inactivation of the more-resistant *B. subtilis* endospores occurred. Fourier Transform Infrared-Attenuated Total Reflectance (FTIR-ATR) spectroscopy of the bacterial cells displayed increased polysaccharide contents after IR treatment. FTIR and Raman spectroscopy of simple carbohydrates before and after IR laser treatment displayed no spectral changes, with the exception of N-acetyl-D-glucosamine (NAG), which was partially attributed to sampling techniques. *E. cloacae* inactivation during IR treatment was attributed to localised and overall temperature increases within the water. Due to the inability to inactivate *B. subtilis* endospores this technique is not suitable for water treatment purposes.

Photocatalytic water treatment using novel $TiO_2$ colloids prepared via a post-synthetic microwave-modification process (MW-treated) was also examined. These colloids were characterised using X-ray photoelectron spectroscopy (XPS), X-ray diffraction (XRD) and Brunauer-Emmett-Teller (BET) analyses and compared to Degussa P25 and convection hydrothermally-treated (HT-treated) $TiO_2$. Slurry suspensions displayed comparable *E. coli* inactivation rates, so the colloids were examined in immobilised form using both a model organic degradant, oxalic acid, and *E. coli*. Oxalic acid degradation studies showed that the MW-treated colloids displayed similar inactivation rates to the HT-treated $TiO_2$, due to their pure anatase composition, while Degussa P25 displayed higher inactivation rates. Investigations into the effect of shortening UV wavelength were also performed. Degussa P25 was the only catalyst which displayed higher apparent quantum yields upon shortening the UV wavelength, which was attributed to its mixed-phase anatase-rutile composition.

As *E. coli* inactivation was observed using distilled water, photocatalysis in natural river water was trailed. It was discovered that the pH had to be lowered from 7.5 to 5.0 and the initial cell concentration must be approximately 1 x $10^3$ colony forming units (CFU) per $cm^3$ or less for inactivation to be observed during a 5 hour treatment period. At a catalyst loading of 1.0 mg per $cm^2$, Degussa P25 absorbed all the applied UVA irradiation; however the MW- and HT-treated $TiO_2$ colloids did not due to their smaller particle size. Therefore sandwich experiments were devised to evaluate the effect of unabsorbed UV irradiation within the system. Small colony variants were identified after photocatalytic and UV treatment, which pose a potential threat to public health.

Further investigation of the different $TiO_2$ colloids was performed using *in situ* FTIR, both with and without an applied potential and compared to a thermally prepared $TiO_2$ catalyst. The latter displayed potential dependent photocatalysis, while the mesoporous $TiO_2$ catalysts displayed potential independent photocatalysis. All catalyst types displayed increased degradation rates upon the application of a positive bias, which was followed *in situ* via the production of $CO_2$. Sodium oxalate and NAG was examined for photocatalytic degradation, both of which were degraded to $CO_2$, with proposed break-down products identified when using NAG.

# STATEMENT OF ORIGINAL AUTHORSHIP

The work contained in this thesis has not been previously submitted to meet requirements for an award at this or any other higher education institution. To the best of my knowledge and belief, the thesis contains no material previously published or written by another person except where due reference is made.

Sarah Ede Date

# NOTE TO READER

The research within the thesis is based on work conducted by the candidate under the primary supervision of Dr Geoffrey Will, as well as A. Prof. Louise Hafner and Prof. Ray Frost. All colloidal dispersions utilised by the candidate were prepared by Aaron Matijasevich. *In situ* FTIR studies of electrochemically-assisted photocatalysis were performed by the candidate at the University of Newcastle upon Tyne (UK) under the supervision of Professor P. A. Christensen. Immobilised photocatalytic investigations using the stirred-tank reactor were performed by the candidate at the University of Ulster (UK), within the Northern Ireland Bioengineering Institute, under the supervision of Dr Tony Byrne.

# PUBLICATIONS AND CONFERENCE PRESENTATIONS

## Publications

1. Ede SM, Frost RL, Hafner LM, Will GD, Disinfection and structural changes of *E. cloacae* and *B. subtilis* endospores during infrared laser water treatment, *Water Research*, (in preparation)

2. Ede SM, Byrne JA, Dunlop PSM, Will GD, Photocatalytic water treatment of oxalic acid using Microwave-treated $TiO_2$, *Journal of Photochemistry and Photobiology: A Chemistry*, (in preparation)

3. Ede SM, Byrne, JA, Dunlop PSM, Hafner LM, Will GD, Immobilised $TiO_2$ photocatalytic water treatment of bacterial pollutants, *Journal of Photochemistry and Photobiology: A Chemistry*, (in preparation)

4. Ede SM, Will GD, Christensen PA, *In situ* FTIR studies of immobilised $TiO_2$ photocatalysis and electrochemically-assisted photocatalysis, *Journal of Applied Electrochemistry*, (in preparation)

## Conference presentations

1. Ede SM, Frost RL, Will GD, (2004) "A vibrational spectroscopic study of micro-organisms in $H_2O$ during light irradiation treatment" presented at the CPC2004 Conference on Physical Chemistry, Tasmania, Australia

# ACKNOWLEDGEMENTS

No PhD is completed without the assistance of others and a few people must be mentioned for their help throughout this project.

First and foremost, my supervisor, Dr Geoffrey Will for his guidance and patience throughout the PhD journey. Many thanks also go to A. Prof. Louise Hafner for her never-ending help regarding all things microbiological, and her willingness to learn and understand the chemistry within this project.

Many thanks must go to Prof. P. A. Christensen for letting an antipodean visit his research group at the University of Newcastle upon Tyne. His insistence for results each and every day helped push the project to completion. His work ethic was the best ever seen and yet, he retained a sense of humour. I also give my appreciation to Dr Tony Byrne at the University of Ulster, for also letting me visit his research group. NIBEC was the most professionally set up lab I have worked in, whilst remaining a friendly and rewarding place to work. If only all workplaces were the same.

Support staff never receive enough thanks, but without them most laboratories would fall apart. I would especially like to thank Dr's Llew Rintoul and Chris Carvalho and Ms Sue Gill for their assistance throughout this time. I would also like to acknowledge Dr Steven Cooper at the University of Queensland for allowing a microbiologist to play with his optics laser: you were braver than you realised.

To all the postgraduates who helped, especially Patrick Dunlop, I give thanks.

I wish to thank the Inorganic Materials Research Program, School of Physical and Chemical Sciences, Faculty of Science, Prof. Ray Frost and the former CIDC for financial support.

Finally, to my partner, Steve, and my family and friends: without your support and understanding this would have taken a much longer time to finish.

# TABLE OF CONTENTS

# LIST OF FIGURES

# LIST OF TABLES

| Abbreviation | Description |
|---|---|
| $\tilde{\upsilon}$ | Wavenumber |
| $\lambda$ | Wavelength |
| $\mu$m | Micrometer |
| Abs | Absorbance |
| AFM | Atomic Force Microscopy |
| APO | Advanced photocatalytic oxidation |
| $_{as}$ | Asymmetric vibration |
| ATP | Adenine tri-phosphate |
| ATR | Attenuated total reflectance |
| BET | Brunauer-Emmett-Teller |
| BJH | Baret-Joyner-Halenda |
| *C. parvum* | *Cryptosporidium parvum* |
| *C. perfringens* | *Clostridium perfringens* |
| ca. | Approximately |
| CB or cb | Conduction band |
| CFU | Colony Forming Unit |
| $cm^{-1}$ | Wavenumber |
| CoA | Co-enzyme A |
| CV | Cyclic voltammogram |
| DI | Distilled water |
| $D_p$ | Particle diameter |
| $e^-$ | Electron |
| *E. coli* | *Escherichia coli* |
| EAP | Electrochemically-assisted photocatalysis |
| $E_{bg}$ | Band gap |
| $E_r$ | Reference potential |
| $E_s$ | Sample potential |
| $e_t$ | Lattice trapping site for electrons |
| eV | Electron volt |
| FTIR | Fourier transform infrared |

| Abbreviation | Description |
|---|---|
| FWHM | Full width half maximum |
| $h^+$ | Hole |
| $H_2Ox$ | $(COOH)_2$ |
| $HOx^-$ | $HOOCOO^-$ |
| $h_t$ | Lattice trapping sites for holes |
| HT | Hydrothermal |
| hν | Photon of light/energy |
| ip | In-plane vibration |
| IR | Infrared |
| $L_{abs}$ | Absorbing-layer depth |
| LB | Luria Bertani |
| LUMO | Lowest unoccupied molecular orbital |
| MDA | Malondialdehyde |
| MW | Microwave |
| NA | Nutrient agar |
| NAG | N-acetyl-D-glucosamine |
| NAM | N-acetylmuramic acid |
| nm | Nanometer |
| NW | Natural river water |
| $O_2^{\cdot-}$ | Superoxide |
| $OH^{\bullet}$ | Hydroxyl radical |
| oop | Out of plane vibration |
| Ox. | Oxidation |
| PC | Personal computer |
| PCA | Principal Component Analysis |
| ppm | Parts per million |
| QUT | Queensland University of Technology |
| R or RH | Organic pollutant |
| Red. | Reduction |
| RNA | Ribonucleic acid |
| rpm | Revolutions per minute |
| s | Symmetric vibration |

| Abbreviation | Description |
|---|---|
| *S. cerevisiae* | *Saccharomyces cerevisiae* |
| SVC | Small variant colony |
| *S. sobrinus* | *Streptococcus sobrinus* |
| SCE | Saturated calomel electrode |
| $S_r$ | Reference spectrum |
| $S_s$ | Sample spectrum |
| TEM | Transmission Electron Microscopy |
| TOC | Total organic carbon |
| UV | Ultraviolet |
| UVA | Ultraviolet region A |
| UV-Vis | Ultraviolet-visible |
| V | Volt |
| VB | Valence band |
| W | Watt |
| w/v | Weight per volume |
| WHO | World Health Organisation |
| XPS | X-ray Photon spectroscopy |
| XRD | X-ray diffraction |
| $\delta$ | Bending vibration |
| $\nu$ | Stretching vibration |
| $\Phi_{app}$ | Apparent Quantum Yield |
| $\chi$ | Absorption index |

# CHAPTER 1

# INTRODUCTION

## 1.1 Background

Water is one of the most critical resources on the planet, with less than one percent of the total water on the planet available for human use.[1] Recent shortages in fresh water around the world have highlighted the need for greater re-use and recycling of water resources. However, re-using water including stormwater, treated industrial discharge, treated sewage effluent and 'grey' (household) wastewater has been neglected. Australia is one of the world's driest countries, yet 97% of city run-off and 86% of effluent water is unproductive.[2] Developing methods for recycling and re-use of stormwater and effluent water/wastewater has become an important and urgent issue. The increasing pressure on water resources means that there may be a need for lower quality source water for potable purposes. Despite this, treatment technologies are required to meet the demands of consumers, water companies and regulators, without compromising public health and safety.

## 1.2 Biological contaminants in water

The removal of biological organisms from water before it can be used is of major importance. From a public health perspective, disinfection is practised to protect water quality for subsequent use as important disease-causing microbiological contaminants can be present in untreated water and cause disease.[3] These micro-organisms come from three main groups: bacteria, parasites and viruses. The diseases caused from poorly treated water include Legionnaires' disease, Cholera, Giardia, Cryptosporidiosis, Polio, respiratory tract diseases, conjunctivitis, viral gastroenteritis and Hepatitis A. In addition to these, other micro-organisms have the potential to cause disease within immuno-suppressed or immuno-compromised people. These include bacteria and protozoa, free-living nematodes and filamentous micro-organisms such as fungi and the actinomycetes. To further illustrate this, Table 1.1 shows orally transmitted waterborne pathogens and their significance in water supplies compiled by the World Health Organisation.[4] The most commonly occurring micro-organism groups within water are bacteria and protozoa. This is due to the existence of more sophisticated survival mechanisms found within these organisms when compared to viruses.

**Table 1.1 Orally transmitted waterborne pathogens and their significance in water supplies[4]**

| Pathogen | Health Significance | Persistance in water supplies | Resistance to chlorine | Relative infective dose |
|---|---|---|---|---|
| **Bacteria** | | | | |
| *Campylobacter jejuni, C. coli* | High | Moderate | Low | Moderate |
| Pathogenic *E. coli* | High | Moderate | Low | High |
| *Salmonella typhi* | High | Moderate | Low | High |
| Other *salmonellae* | High | Long | Low | High |
| *Shigella spp.* | High | Short | Low | Moderate |
| *Vibrio cholerae* | High | Short | Low | High |
| *Yersinia enterocolitica* | High | Long | Low | High (?) |
| *Pseudomonas aeruginosa* | Moderate | May multiply | Mod | High (?) |
| *Aeromonas spp.* | Moderate | May multiply | Low | High (?) |
| **Viruses** | | | | |
| Adenoviruses | High | ? | Moderate | Low |
| Enteroviruses | High | Long | Moderate | Low |
| Hepatitis A | High | ? | Moderate | Low |
| Enterically transmitted non-A, non-B hepatitis viruses, Hepatitis E | High | ? | ? | Low |
| Norwalk virus | High | ? | ? | Low |
| Rotavirus | High | ? | ? | Moderate |
| Small round viruses | Moderate | ? | ? | Low (?) |
| **Protozoa** | | | | |
| *Entamoeba histolytica* | High | Moderate | High | Low |
| *Giardia intestinalis* | High | Moderate | High | Low |
| *Cryptosporidium parvum* | High | Long | High | Low |
| **Helminths** | | | | |
| *Dracunculus medinensis* | High | Moderate | Moderate | Low |

## *1.3 Cell structure*

Cell structures vary between the micro-organism groups as well as within each group. Figure 1.1 shows a diagrammatic representation of a bacterial cell, viral particle and a Eukaryotic cell (characterised by segregation of internal cell structures which have different functions). Bacteria are single-celled organisms defined by a

lack of internal cellular structure to separate molecules of different functions within the cell.

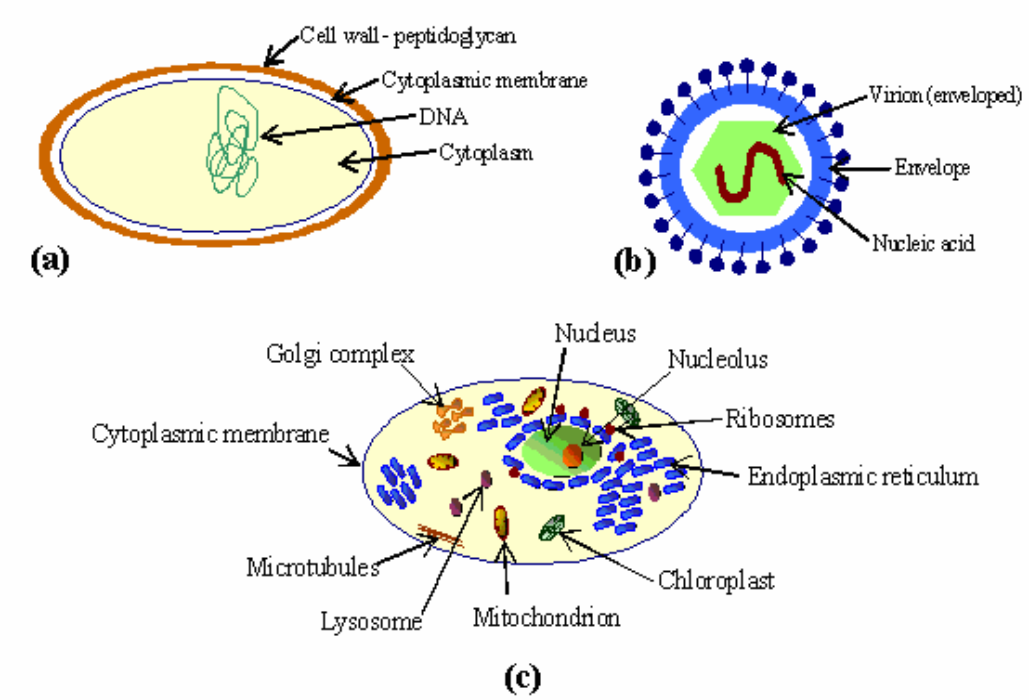


**Figure 1.1 Schematic representations of the general cell structure of (a) bacteria (gram-positive), (b) viruses and (c) Eukaryotic cells**

As this investigation is focused on bacterial cells, the different structures found within a bacterial cell will now be discussed in more detail.

The bacterial cell structure plays an important role in preventing oxidative stress. Cells consist of several layers which protect the contents from invasive attack and leakage of cellular components into the neighbouring environment. These layers are known as the cell envelope and consist of the outer capsule, cell wall and cytoplasmic membrane. Held within the envelope is the cytoplasm, containing a single deoxyribonucleic acid (DNA) chromosome as well as proteins, carbohydrates, lipids, salts and inorganic ions suspended in water.

### 1.3.1 Glycocalyx

Some species of bacteria can secrete a polysaccharide layer which acts as a buffer between the cell and the external environment. This layer has a high water content

which protects the cell from dehydration and the loss of nutrients. In animals, the presence of a glycocalyx (known as a capsule) aids in the establishment of disease. White blood cells which normally engulf and destroy bacteria (the process is known as phagocytosis) can not perform this function on encapsulated bacteria. This polysaccharide layer also aids the bacteria in colonising solid surfaces forming biofilms.[5]

### 1.3.2 Cell wall

Due to the concentration of solutes inside the bacterial cell, considerable turgor pressure develops (estimated at 2 atmospheres). To withstand these pressures, bacteria possess cell walls, which also function by giving shape and rigidity to the cell. Bacteria are divided into two major groups, called gram-positive and gram-negative. The original distinction between these groups was based on a special staining procedure, the Gram stain, but differences in cell wall structure are at the heart of the differences in the Gram-staining reaction. Gram-positive and gram-negative cells differ markedly in the appearance of their cell walls as shown in Figure 1.2. The gram-negative cell wall is a complex, multilayered structure, whereas the gram-positive cell wall primarily consists of a much thicker single layer. The gram-positive cell wall is approximately 20 – 80 nm thick with the peptidoglycan layer consisting of as much as 90% of the cell wall. The remainder consists of teichoic acids, proteins and lipopolysaccharides.[6]

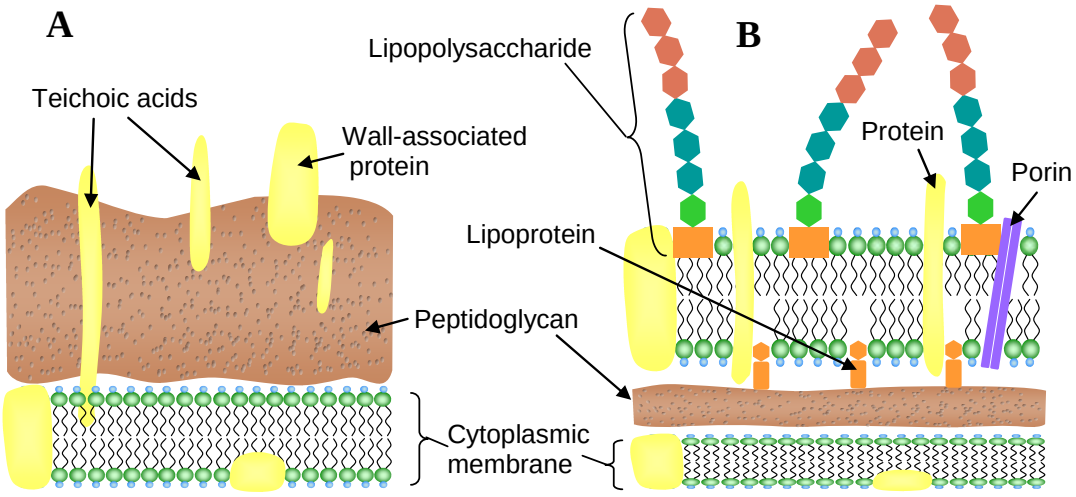


**Figure 1.2 Schematic representation of (A) gram-positive and (B) gram-negative cell walls**[7]

The gram-negative cell wall is much more complex, containing a thin 2 – 6 nm layer of peptidoglycan consisting of approximately 10% of the cell wall. The cell wall also consists of an outer membrane, consisting of 50% lipopolysaccharides, 35% phospholipids and 15% proteins.[8] The surface lipid, also referred to as lipid A, is a fatty acid connected via an ester amine linkage to a disaccharide composed of N-acetyl-glucosamine phosphate.[7] The lipid A is associated with the toxic properties of gram-negative bacteria and is also known as an endotoxin which is toxic when present in the host's bloodstream or gastrointestinal tract. The gram-negative cell wall also has channels, called porins, for the transport of low molecular weight substances.

### 1.3.3 Periplasmic space

The periplasmic space lies between the cell membrane and the cell wall and contains enzymes, proteins and electron mediators in a gel-like environment. Enzymes in the periplasmic space can break down material that has entered through the cell wall but is too large to penetrate the cell membrane.[9]

### 1.3.4 Cyptoplasmic membrane

The cytoplasmic membrane is a thin structure lying inside the cell wall and encloses the cytoplasm of the cell.[10] The membrane plays several important roles in cell function; the most critical of these is maintaining osmotic equilibrium. The membrane consists primarily of phospholipid bilayer with proteins floating throughout the structure. The proteins can be arranged on the periphery of the bilayer and may function as enzymes or mediators of membrane shape changes during movement, or they can penetrate the membrane completely and only be removed after disruption of the bilayer. The latter act as channels through which non-soluble substances (e.g. amino acids and nitrogenous bases) enter and exit the cell.

The cytoplasmic membrane also acts as a supporting framework for the main cell functions. The membrane contains the necessary enzymes for synthesis, assembly and transport of cell wall components and the machinery for electron transport and

oxidative phosphorylation reactions. The cytoplasmic membrane is also involved in DNA replication as adhesion sites within the membrane structure allow DNA anchoring prior to the initiation of replication.

If the cell membrane is compromised, or significantly damaged, the integrity of the cell structure is destroyed resulting in leakage of internal cellular contents and subsequent cell death.[10]

### 1.3.5 Cytoplasmic contents

The cytoplasm refers to the substance of the cell inside the cytoplasmic membrane and consists of approximately 80% water primarily containing proteins, carbohydrates, lipids, inorganic ions and many low-molecular weight compounds.[7] The cytoplasm also contains ribosomes and reserve deposits called inclusions, as well as the DNA chromosome. The chromosome is a single continuous strand of DNA and is localised, but not contained, within a region called the nucleoid.

### 1.3.6 Flagella, fimbriae and pili

Some bacteria have flagella which are hair-like helical protein appendages that provide cells with the ability to move. Flagella are arranged differently on different bacteria and can be attached at one or both ends, or can occur all over the cell surface. Each flagellum moves in a propeller-like motion propelling the cell towards nutrients or away from toxic substances.[11]

Fimbriae are structurally similar to flagella but are not involved in motility. Fimbriae are considerably shorter and more numerous than flagella and are used for attachment. Fimbriae are found on gram-negative bacteria and are often used for attachment to tissue to facilitate disease.[11]

Pili are structurally similar to fimbriae, but are generally longer. Only one or a few pili are present on the surface and are used to join bacterial cells in preparation for conjugation, during which two bacteria exchange fragments of plasmid DNA. Pili are also involved in attachment to human tissues by some pathogenic bacteria.[6]

### 1.3.7 Bacterial spores

Some gram-positive bacteria, under extreme environmental conditions produce specialised structures called endospores. Endospores are formed internal to the bacterial membrane, during the process of sporulation. Sporulation represents a dormant stage within the bacterial lifecycle.[12]

Endospores are highly durable dehydrated cells with thick walls and additional layers, which are much more complex than that of vegetative cells. Unique to endospores is a dipicolinic acid-calcium-peptidoglycan complex found in the spore coat. This layer represents about 10% of the endospore dry-weight and it is thought that this layer, along with the dehydrated cytoplasm, is responsible for the spore's resistant qualities.[12]

The durability of endospores allows them to survive for many years until conditions become favourable for germination, at which time the endospore converts back to a vegetative cell. Endospores can survive extreme heat, lack of water and exposure to many toxic chemicals and radiation.[13]

## *1.4 Conventional water treatment*

Ensuring the microbiological safety of drinking water is of extreme importance. Generally, after the elimination of particles in suspension by filtration and flocculation, biological contaminant treatment is performed.[14] Many techniques have been developed to remove and/or destroy micro-organisms from wastewater. These include: filtration; chlorination; bromination; sonication; ozonation; and irradiation.[15] Chlorination is by far the most widely used technique and has been used to protect public health against waterborne disease since the early 1900's.[14,16-20] While this method is inexpensive and efficient, recently issues with this process have become apparent. The chlorination of organic compounds present within source water can lead to the formation of undesirable by-products some of which have mutagenic properties.[21] Chemical disinfectants can also cause problems with odour and taste.[22] However, the emergence of waterborne pathogens which are resistant to

chemical disinfection has led to many investigations into alternative sterilisation procedures.[23-25]

The growing pressure to use lower quality source water may require the use of higher chlorination levels, which could increase by-product formation. Future demands on the chemical industry to reduce the use of chlorine-based disinfectants for environmental reasons may force a change in disinfectants or increased use of non-chemical disinfection processes. [26]

## *1.5 Alternative methods of water treatment*

A number of alternative methods are commercially available for the removal of microbiological pollutants and some chemical contaminants from water sources. Membrane filtration systems are in use, but generally on a small scale and to target specific problems. These include micro-filtration, ultra-filtration, nano-filtration and reverse osmosis. [27,28] Generally, overall costs are greater for filtration processes compared with chlorination, with the increasing costs inversely proportional to the contaminant size to be removed.[29] Difficulties in ensuring the integrity of the membrane and removal of the microbiological waste are encountered with this treatment method.[30-32]

### 1.5.1 Ultraviolet treatment

It was first demonstrated in 1877 by Downes and Blunt[33] that sunlight is capable of killing micro-organisms. By using a series of filters, it was established that the actinic rays (encompassing the ultraviolet (UV) region) were responsible for this lethal effect. Since then, the use of UV irradiation for the disinfection of waters has become accepted as an effective and economical alternative to chlorine use.[19] As a consequence, the number of treatment plants installing the process is growing.

Conventionally, the UV spectrum is divided into three discrete sections: UVA (320 – 400 nm); UVB (280 – 320 nm); and UVC < 280 nm). Radiation at UVB and UVC wavelengths has genotoxic properties and is invariably harmful to living cells. By

damaging the DNA, it can induce deleterious processes such as mutagenesis, carcinogenesis and cell death.

Exposure to UV light can result in the formation of a range of photoproducts whose distribution and relative yields depend on the wavelength and intensity of incident radiation.[33] The photo-reactivity of DNA is a function of its absorption spectrum, and it is the latter which determines the mechanisms by which radiation damages DNA. Photons in the UVC region are strongly absorbed by the purine and pyrimidine bases. This creates excited-state species that undergo intramolecular photochemical reactions, such as thymine photo-dimerisation (see Figure 1.3). In contrast, photons with wavelengths in the UVA region are not absorbed at all. However, they can indirectly damage DNA through the use of photosensitiser molecules, whereby the photosensitiser absorbs the UVA radiation and initiates damage through processes such as triplet energy transfer, photo-adduct formation and the generation of active oxygen species.[33] Photons in the UVB range are only weakly absorbed by DNA and can damage it by either or both mechanisms depending on the experimental conditions. When cells are irradiated in their natural physiological environment, DNA damage induced by the direct absorption of photons is the most important source of mutations and cytotoxic effects.

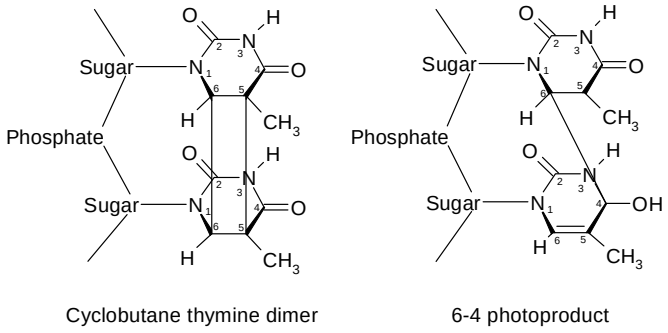


**Figure 1.3 Photoproducts of DNA after ultraviolet irradiation[33]**

Disinfection of secondary wastewater effluents compared to stream and river water by UV requires higher doses (50 – 60 mW $cm^{-2}$) due to the higher concentration of micro-organisms and increased micro-organism resistance. Uneconomically viable values exceeding 100 mW $cm^{-2}$ are required to inactivate protozoan pathogens such as *Cryptosporidium* and *Giardia*.[34]

### 1.5.2 Infrared treatment

The first evidence of infrared (IR) radiation used for micro-organism inactivation was presented in 1975, by Molin and Ostilund.[35] Their research involved the use of unfocused IR lasers to sterilise bacterial spores on metal substrates. Soon after in 1976, Pratt[36] performed similar research investigating the effects of unfocused $CO_2$ and CO lasers to deactivate bacterial spores on metal and paper substrates. In this case, sterilisation was accomplished thermally, by rapidly heating the surface to temperatures exceeding 500 °C. However, a water treatment apparatus was not developed until 2002, when Baca[37] built a near-point near-infrared laser water treatment apparatus for use in dental hand-pieces. This technique is limited, however, by the energy consumption and cost required to deactivate the micro-organisms.

## *1.6 Photocatalytic processes for water treatment*

Photocatalysis has great potential as an alternative water treatment method due to the possibility to remove by-product precursors. This process also ensures the public health safety of drinking water due to its ability to inactivate micro-organisms.

Photocatalytic processes are divided into two groups: homogeneous photocatalytic oxidation, e.g. UV/hydrogen peroxide; and heterogeneous photocatalytic oxidation, such as UV/semiconductor photocatalysis.[38] In the homogeneous system, photolysis of either hydrogen peroxide or ozone under UV illumination supplies hydroxyl radicals.[39] During this process continual consumption of oxidant occurs. Comparatively, in the heterogeneous process, hydroxyl radicals are produced from the redox reaction between photo-excited electrons and electron acceptors on the surface of the semiconductor photocatalyst. The process is catalytic and allows the semiconductor to remain active for long periods of time.[40,41] Due to these advantages, this investigation was focused on heterogeneous photocatalysis, which will now be discussed further.

### 1.6.1 Semiconductors

Electrical solids are divided into three groups depending on their ability to conduct electricity: metals; insulators; and semiconductors. Metals are good thermal and electrical conductors due to their chemical bonding structure. Insulators are poor conductors as they are covalently bonded non-metals. Lying between these two groups are semiconductors, whose band structure can, under certain circumstances, allow electrical and thermal conductivity. Semiconductors have been of interest since the 1950's due to their unique optical and electronic properties.

### 1.6.2 Energy levels

In an isolated atom, electrons occupy various discrete energy levels which are closely spaced. In a crystal, these energy levels are modified into millions of separate levels, collectively termed an energy band. A semiconductor contains two energy bands known as: the valence band (the highest occupied band (VB)); and the conduction band (the lowest unoccupied band (CB)). At normal temperatures, due to thermal promotion, a metal possesses electrons in the CB, whereas an insulator possesses no electrons in the CB. A semiconductor falls between these two categories. Figure 1.4 shows the relative positions of the conduction and valence bands, with the corresponding area between them known as the band gap, in which no electron energy levels exist.

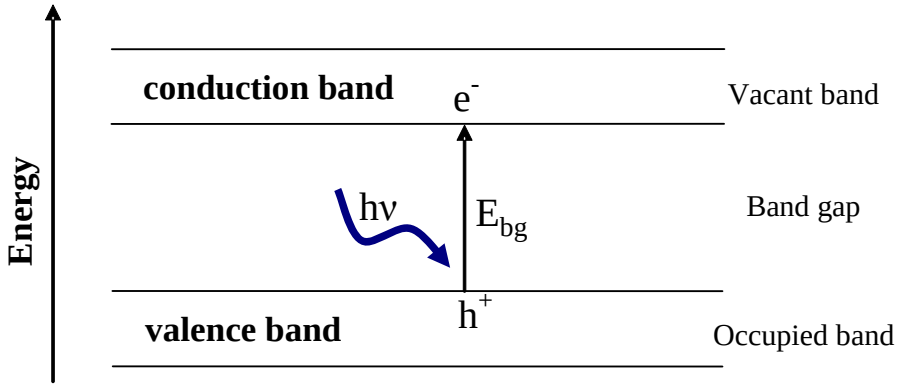


**Figure 1.4 Semiconductor valence and conduction bands**

The band gap shown in Figure 1.4 is assigned an energy value ($E_{bg}$) which corresponds to its width in energy, and is the additional energy (denoted as hν)

required for an electron ($e^-$) to move from the VB into the CB. This implies that an electron possessing the required amount of energy can separate from the parent atom and become free to move at random through the crystal structure in the CB. The promotion of an electron to the CB leaves a positive hole ($h^+$) in the VB. Thus the action of promoting an electron from the VB to the CB creates an electron-hole pair. Electrons may be promoted to the CB following absorption of a photon of energy greater than or equal to the $E_{bg}$. If an electron recombines with a hole, the conservation of energy demands that the absorbed energy be dissipated as heat or light.

### 1.6.3 Choice of semiconductors for water treatment

Most of the semiconductors which have been investigated as photocatalysts for water treatment have been metal oxides (eg $TiO_2$, ZnO, $SnO_2$, $WO_3$) and chalcogenides (CdS, ZnS, CdSe).[42] Metal chalcogenides possess narrower band gaps, which make them sensitive to visible irradiation; however they are subject to photocorrosion. The photocatalysts' effectiveness for oxidation of organics in water treatment is dependent on the oxidation potential of the VB and the reduction potential of the CB. Figure 1.5 shows the relative positions of the surface bands of the common semiconductors at pH 7.[43] It can be seen that the CB of $TiO_2$ is sufficiently negative for the reduction of $O_2$, while the VB is sufficiently positive for the oxidation of $OH^-$ making it an excellent semiconductor for the oxidation of organics in water. The reduction potentials of $SrTiO_3$, $WO_3$ and ZnS could also be used for the photocatalytic oxidation of organic pollutants; however it is often found that $TiO_2$ is the most efficient semiconductor for the treatment of water containing organic pollutants.[44-46] ZnO is a possible alternative as it has a similar band gap energy, however it has been reported to be unstable under irradiation.[45]

### 1.6.4 Titanium dioxide

$TiO_2$ is a white pigment commonly used in paint, paper, ceramics, household (toothpaste) and food products (chewing gum) and as a bulk filler in pharmaceuticals. It is thermally stable, insoluble in most conditions and effectively non-toxic. It is virtually inert, and exists in its purest form as a colourless crystalline

solid. It absorbs almost no visible light and has a large refractive index. Titanium is the ninth-most abundant element, with limonite, iron titanium oxide (45 – 60% $TiO_2$), its most abundant ore.

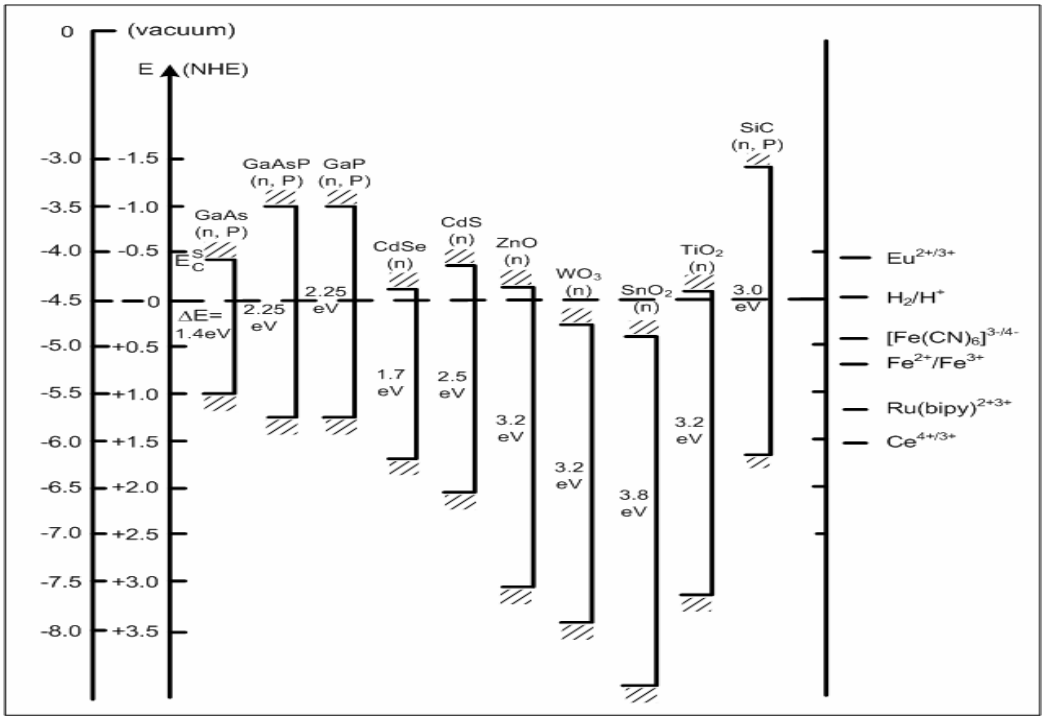


**Figure 1.5 Selected wide band-gap semiconductors[43]**

### 1.6.4.1 Physical and chemical characteristics

Three morphological forms of $TiO_2$ exist: anatase, rutile and brookite. Brookite exhibits low stability and is usually ignored for practical applications. The anatase and rutile forms are commonly available in industrial $TiO_2$ products, with anatase most often used for catalytic purposes due to its larger photoreactivity than rutile. Anatase is thermodynamically stable up to 800 °C, above which a phase transformation to rutile occurs. The backward transition is not observed on cooling due to the high activation energy required. Both anatase and rutile exist as a tetragonal crystal lattice, each Ti atom is coordinated to six O atoms and each O atom is coordinated to three Ti atoms (Figure 1.6). The number of common edges of the $TiO_6$ octahedra differs between the two forms: anatase has four while rutile has two.[47] The VB is comprised of the O 2p orbitals and the CB is comprised of the Ti 3d orbitals. Figure 1.7 shows the molecular orbital scheme for rutile ($Ti_2O_4$).

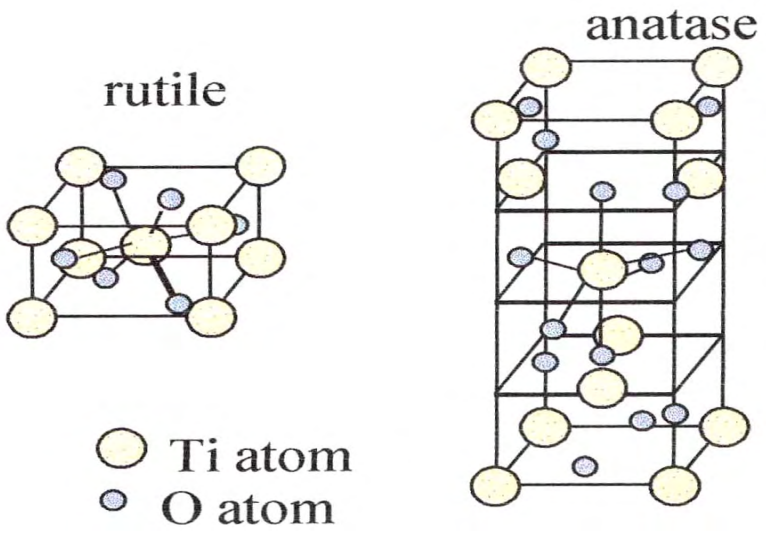


**Figure 1.6 Structure of rutile and anatase phases of titanium dioxide crystals[48]**

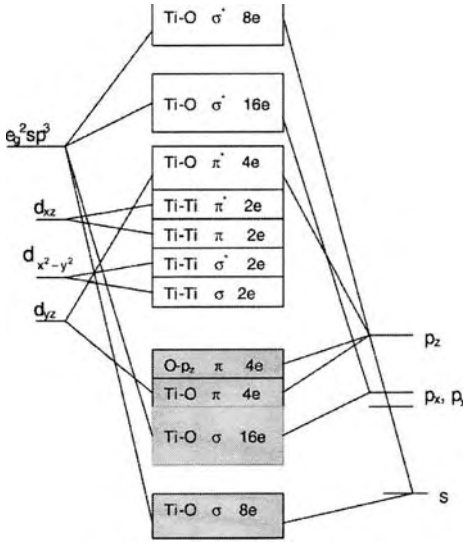


**Figure 1.7 Molecular orbital scheme for rutile ($Ti_2O_4$). The occupied energy levels are represented by gray shadings.[49]**

The two principal catalytic phases of $TiO_2$, anatase and rutile, have numerous structural and functional differences. Commercially available anatase is typically less than 50 nm in size with the particles possessing a band gap of 3.2 eV, corresponding to a UV wavelength of 387 nm. The adsorptive affinity of anatase for organic compounds is higher than that of rutile and anatase exhibits lower rates of recombination in comparison to rutile due to its 10-fold greater rate of hole trapping. In contrast, the thermodynamically stable rutile phase generally contains particles

larger than 200 nm with a smaller band-gap of 3.0 eV with excitation wavelengths that extend into the visible spectrum at 410 nm. Despite this, anatase is generally regarded as the more photochemically active phase, due to the combined effect of lower rates of recombination and higher surface adsorptive capacity.[50]

#### 1.6.4.2 $TiO_2$ preparation

Different synthesis methods produce $TiO_2$ products with different structures, crystallinities and impurities. Therefore the surface properties are dependent on the preparation method. Photocatalytic activity is influenced by crystal structure, porosity, surface area, particle size distribution and surface hydroxyl density.[51] These factors influence the production of electron-hole pairs, surface adsorption and desorption, as well as the redox process.

$TiO_2$ is prepared on an industrial scale by the sulphate method or by vapour-phase oxidation of $TiCl_4$. The sulphate method involves the dissolution of limonite, $FeTiO_3$, in sulphuric acid, after which iron is removed and the solution is hydrolysed. The hydrated titania precipitate is calcined to remove water resulting in a predominately anatase structure stabilised by sulphate ions.

Vapour phase oxidation[52] of $TiCl_4$ results in $TiO_2$ characterised by a narrow particle size distribution with the main impurity being chloride. The surface is dehydroxylated and the product purity is lower than the sulphate method. An example of $TiO_2$ produced by this method is Degussa P25 which contains up to 25% rutile.

Other routes to obtain $TiO_2$ include the hydrolysis of $TiCl_4$ or titanium alcoholates.[40,52] $TiCl_4$ is hydrolysed in water and $TiO_2$ is precipitated by addition of ammonia or hydroxide. Anatase $TiO_2$ is formed if hydrolysis is carried out at 5 – 10 °C, while rutile is produced at reaction temperatures above 80 °C. The degree of hydroxylation can be controlled by calcination temperature. Alternative methods for $TiO_2$ preparation are the thermal or electrochemical oxidation of the parent material.[53-56]

### 1.6.4.3 Degussa P25

Degussa P25 is one of the most efficient and extensively used commercial photocatalysts available due to its high surface area, high photoactivity and minimal impurities.[57-59] Degussa P25 is produced through vapour phase oxidation, specifically flame hydrolysis of gaseous $TiCl_4$ at temperatures greater then 1200 °C. This reaction is performed under the influence of water which develops during the oxyhydrogen reaction:[60]

$$TiCl_4 + 2\ H_2 + O_2 \rightarrow TiO_2 + 4\ HCl \qquad \textbf{1.1}$$

The resulting product is 99.5% pure $TiO_2$, which has a composition ratio of 75:25 anatase: rutile, and crystallites, which are non-porous and cubic with rounded edges. Degussa P25 has an average particle size of ~ 21 nm, a specific area of 50 ± 15 $m^2\ g^{-1}$ and low impurity level.

The high activity of Degussa P25 is thought to be due to a more positive CB potential in rutile compared to anatase. This allows photogenerated electrons to pass from anatase to rutile preventing recombination within the anatase. The lower activity of rutile could be a result of its lower over-potential for the reduction of oxygen.

## 1.6.5 Advantages of $TiO_2$ photocatalysis

$TiO_2$ photocatalysis has been reported to degrade many aqueous chemical pollutants, including pesticides, herbicides, crude oil, surfactants, and dyes. A comprehensive list of the organic pollutants degraded by $TiO_2$ photocatalysis can be found in recent review articles.[40,44,61] Advantages of using $TiO_2$ as a photocatalyst include its insolubility in water and its non-toxicity.[62] In addition, the photocatalytic process does not require the addition of consumable chemicals and a waste sludge is not produced. Anatase $TiO_2$ has a band gap energy of 3.2 eV equivalent to light of λ 387 nm or less. Since $TiO_2$ absorbs near-UV light, the exploitation of solar energy is a real possibility. A small but significant proportion of light between 300 – 400 nm of the solar spectrum reaches the earth's surface and could be utilised for the

photocatalytic treatment of water. Many investigators have reported the solar photocatalytic degradation of pollutants in aqueous solution.[61,63-70]

### 1.6.6 Mechanisms of $TiO_2$ photocatalysis

Irradiation of $TiO_2$ particles with photons of energy equal to or greater than the band gap energy, results in the promotion of an electron from the VB to the CB of the particle. The outcome of this process is a region of positive charge, termed a hole ($h^+$) in the VB and a free electron ($e^-$) in the CB (equation 1.2). This electron-hole pair can either recombine inside the semiconductor particle or move to the surface where they can react with adsorbed molecules.

$$TiO_2 + h\nu \rightarrow TiO_2 (e^-_{cb} + h^+_{vb}) \qquad \textbf{1.2}$$

Once diffusing to the $TiO_2$ particle surface, the positively charged hole can directly oxidise pollutants (R) (equation 1.3); or react with surface bound hydroxyl groups ($OH^-$) or adsorbed water molecules to form hydroxyl radicals ($OH^\bullet$), shown in equations 1.4 and 1.5, respectively.

$$h^+_{vb} + R \rightarrow\rightarrow CO_2 + H_2O \qquad \textbf{1.3}$$

$$OH^- + h^+_{vb} \rightarrow OH^\bullet \qquad \textbf{1.4}$$

$$H_2O + h^+_{vb} \rightarrow OH^\bullet + H^+ \qquad \textbf{1.5}$$

The presence of oxygen consumes trapped electrons by reacting to form superoxide ions, preventing recombination (equation 1.6). The final product of the reduction may also be $OH^\bullet$ radicals and the hydroperoxyl radical $HO_2^\bullet$ (equations 1.7 and 1.8).

$$O_2 + e^-_{cb} \rightarrow O_2^{\bullet -} \qquad \textbf{1.6}$$

$$2O_2^{\bullet -} + 2H^+ \rightarrow 2OH^\bullet + O_2 \qquad \textbf{1.7}$$

$$2O_2^{\bullet -} + H^+ \rightarrow HO_2^\bullet \qquad \textbf{1.8}$$

Reactions involving the electron and hole should proceed simultaneously to prevent the accumulation of electrons in CB and prevent the recombination of electrons and

holes. Therefore the efficient removal of electrons is essential to promote photocatalytic oxidation.

Hydroxyl radicals have long been known as strong, indiscriminate oxidising agents.[71] During photocatalysis they can react with organic compounds and bacterial species adsorbed onto, or very close to the semiconductor surface resulting in degradation (total oxidation of pollutant results in production of carbon dioxide and water).

There is great speculation within the literature regarding the actual mechanism of pollutant photo-oxidation. Great attention has been paid to determining whether the hole directly reacts with the pollutant or whether it first reacts with water or hydroxyl groups to produce hydroxyl radicals, which in turn react with the pollutant. Excellent reviews of both mechanisms are reported by Hoffmann *et al*[45] and Fox and Dulay.[42] Figure 1.8 illustrates a schematic representation of the generally accepted photocatalytic mechanism.

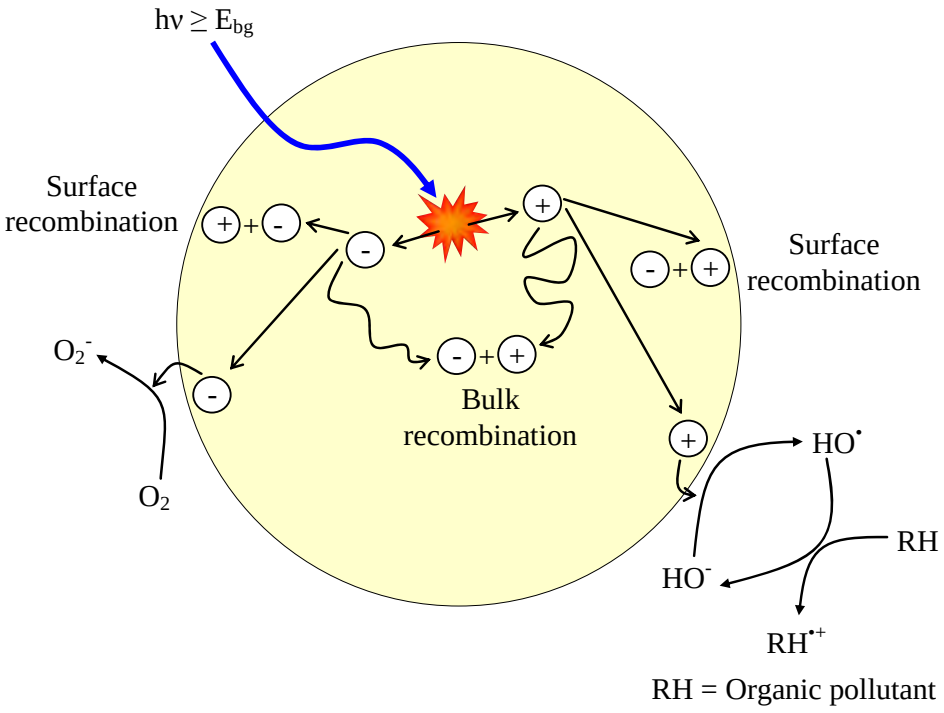


**Figure 1.8 Schematic representation of the mechanism of $TiO_2$ photocatalysis**

Given the wide range of photoefficiencies observed among the various $TiO_2$ phases and formulations, past research has been unable to comprehensively explain the high photoactivity observed in some mixed-phase $TiO_2$ preparations such as Degussa P25.

Originally proposed in the early 1990's, the current hypothesis of the enhanced activity of mixed phases relative to pure phases is due to the vectorial displacement of electrons from the anatase to rutile crystal phases. This is thought to occur through the transfer of electrons from the anatase CB to the lower energy rutile CB (see Figure 1.9). This serves to reduce the recombination rate of anatase, leading to more efficient electron-hole separation and greater catalytic reactivity.[51] While the model has gained support on the basis of the lower energy conduction bands of rutile relative to anatase, these arguments do not consider the energies of the lattice of surface trapping sites, which can be significantly lower.[50]

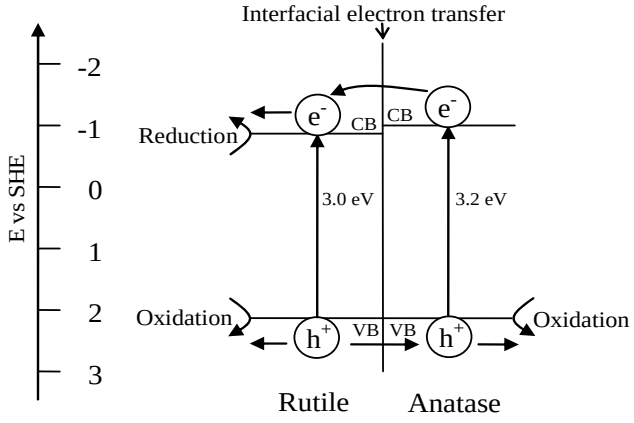


**Figure 1.9 Model of mixed-phase $TiO_2$ activity proposed by Bickley et al.[51]**

More recently, Hurum and co-workers performed a further investigation into the enhanced photocatalytic activity of Degussa P25 using Electronic Paramagnetic Resonance (EPR) Spectroscopy.[50] The critical and active role of rutile in mixed-phase formulations was detailed, whereby negative charges produced on rutile by visible light were stabilised through electron transfer to lower energy anatase lattice trapping sites ($e_t$) allowing electrons to reach the surface. Transfer of the photogenerated electron to anatase lattice trapping sites allows holes that would have

been lost to recombination to also reach the surface via lattice trapping sites ($h_t$). See Figure 1.10 for Hurum et al.'s proposed mechanism.[50]

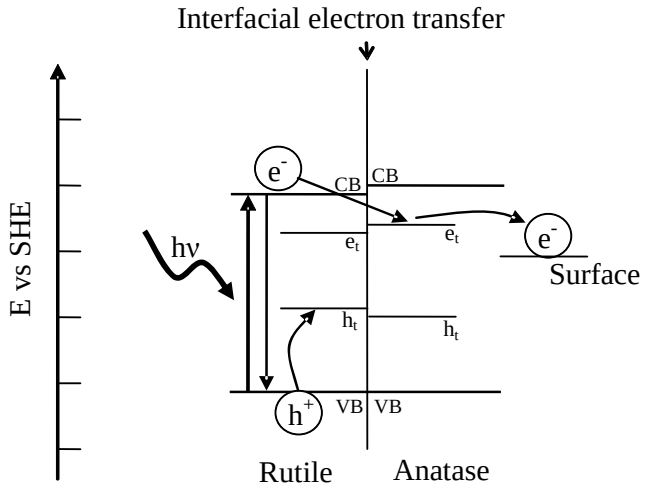


**Figure 1.10 Model of mixed-phase $TiO_2$ activity proposed by Hurum et al.[50]**

The results suggested that within Degussa P25 there are nanoclusters containing atypically small rutile crystallites interwoven with anatase crystallites, with the transition points between the two phases allowing for rapid electron transfer from rutile to anatase.

Further support of the mechanism proposed by Hurum and co-workers was provided by Sato and Taya in 2006.[72] During the photocatalytic inactivation of bacteriophages, enhanced photoactivity was noted when using mixed-phase $TiO_2$. It was proposed that the close contact between the two phases, allowed for the exchange of photo-excited electrons and holes between the particles. The photo-excited electrons were produced in rutile and transferred to a nearby anatase crystallite. Thus the quantum yield of reactive oxidative species generation was enhanced.

### 1.6.7 Increasing photocatalytic efficiency

Various methods of attempting to post-synthetically enhance the overall efficiency of the photocatalytic process have been investigated. These modifications include doping with transition metals to increase electrical conductivity,[45,73-75] loading with metal nanoclusters,[76,77] annealing the catalyst at elevated temperatures to improve

crystallinity and particle size,[78,79] using electron acceptors other than $O_2$,[76] and electrochemically-assisting the mechanism by the application of a positive bias.[80]

The most important modification to date is the reduction of the $TiO_2$ particle size to within the nanometer range which has been shown to significantly increase its catalytic activity.[63] This is due to the higher surface-to-volume ratio, and as such it is routine to use nanometer-sized particles.

Reactor performance is enhanced by dispersing the $TiO_2$ nanoparticles in water, because of higher surface contact of the nanoparticles with the target compounds. However, the difficulty in separating unsupported particles from water for reuse is limiting commercially viable industrial reactors. Therefore, a need to employ supported catalysts is realised where a thin layer of nanometer-sized $TiO_2$ particles can be formed on a supporting surface. These can be particle[81-84] or fixed supports,[74,85] with the majority of research performed in the former case. $TiO_2$, for example, has been fixed onto tubes, glass plates, fibres, membranes, or photoreactor walls.[86] However, catalytic activity approximately five to six times lower is usually seen (compared with the powdered form). This is due to: a reduced surface-to-volume ratio (from binding with the supporting surface); catalyst agglomeration (surface clumping) during fixation; and the mass transfer limit for the organic compounds.[87] Film thickness is also of great importance: if the film is too thin, not enough light will be absorbed and if too thick, the holes are generated too deep in the catalyst layer.[88] These problems can be overcome by employing a nanoporous $TiO_2$ film to ensure maximum light absorption and also by bringing the pollutant close to the $TiO_2$ surface. When $TiO_2$ was coated onto rotating disks, rotating mesh sheets and narrow light tubes, improved catalytic performance was noted, due to increased mass transfer.[89-91] As a result of the large length scales used in these structures, the catalytic performance did not approach those employing suspended nanoparticle catalysts. However, Gerischer and Heller[92] reported that the reduction of $O_2$ by CB electrons was the rate limiting step in all cases where the molecules in the solution can be quickly oxidised by hydroxyl radicals or directly by holes. Dijkstra et al.[93] compared the efficiency of a $TiO_2$ immobilised system with a suspension system, with $O_2$ as an electron acceptor in both cases, and reported that both systems were

comparable. Therefore, efficient mass transfer in a reactor can produce immobilised $TiO_2$ photocatalytic degradation rates to within those seen using suspension systems.

### 1.6.8 Electrochemically-assisted photocatalytic treatment

Photocatalysis can be further enhanced by applying a potential to the $TiO_2$ film. This induces an electric field within the particles thus increasing charge separation.[94] In a suspension, when under band-gap excitation, the semiconductor particles behave as short-circuited microelectrodes and promote oxidation and reduction on the same particle. A disadvantage of this system is the high degree of recombination between the photogenerated charge carriers. Electrochemically-assisted photocatalytic (EAP) treatment is most often performed using a semiconductor nanocrystalline film where the pollutant is in contact with the individual nanoparticles within the film. When irradiated, without an applied potential, an electron-hole pair is produced in individual particles where the holes and electrons transverse the particles within the film. The holes are eventually transferred to the pollutant and the electrons to oxygen. When using a semiconductor nanocrystalline film, the differing rates of electron and hole injection into the solution control the charge separation.[95] If one can remove the photogenerated electrons from the semiconductor particle (e.g. by application of an electric field), it is possible to increase the efficiency of oxidation at the semiconductor electrolyte interface. Figure 1.11 illustrates the difference between open circuit conditions and EAP.

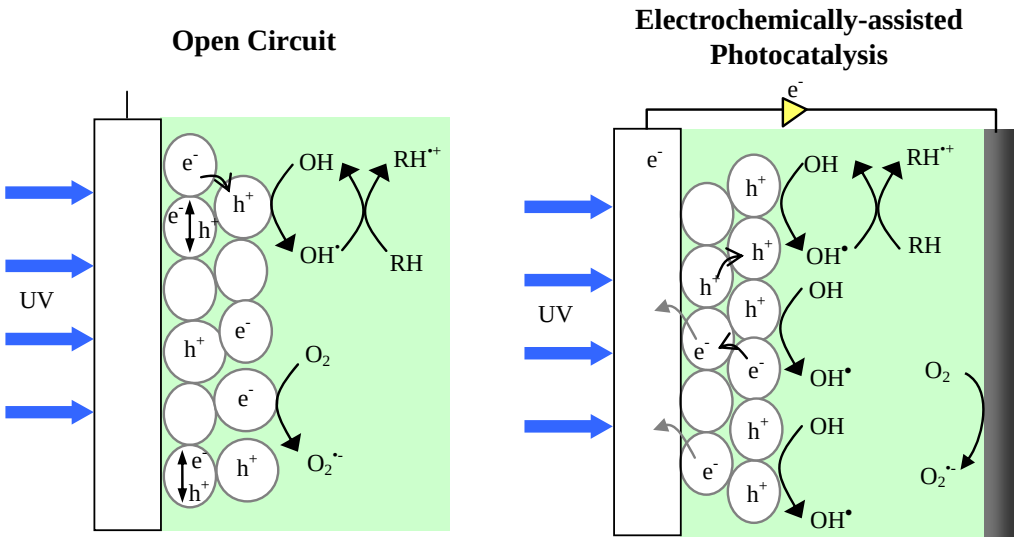


**Figure 1.11 Photo-induced charge separation in open circuit photocatalysis and EAP**

Upon application of an electrical bias to the immobilised $TiO_2$ film, CB electrons are removed to the back contact. This promotes charge separation and increases inter-particle charge transfer through the immobilised film. As electrons are removed, hydroxyl radical production is increased therefore reducing the electrostatic repulsion of negatively charged particles. This is known as the electrical double layer effect, whereby the electrode ($TiO_2$ film) becomes positively charged relative to the solution nearby, decreasing the local cation concentration within the Helmholtz layer. The potential varies with distance from the electrode surface and the electrolyte solution without a change in applied potential as shown in Figure 1.12.

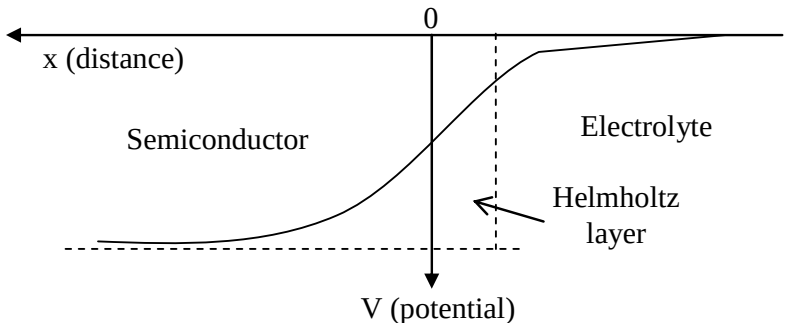


**Figure 1.12 Potential distribution for a semiconductor-electrolyte interface.**

Kim and Anderson[96] reported that the application of a +0.0 V vs. SCE potential to a $TiO_2$ electrode increased the degradation rate of formic acid. In a different study the same authors established that the formic acid degradation rate doubled when +0.3 V vs. SCE was applied.[97] Vinodgopal et al.,[95] when using a two-compartment electrochemical cell, observed a greatly increased degradation rate of 4-chlorophenol upon the application of +0.6 V vs. SCE. Candal et al.,[98] Byrne et al.[80] and McMurray et al.[99] have all reported that a potential of + 1.0 V vs. SCE increased the overall rate. Both Krysa and Jirkovsky[100] and Christensen et al.[94,101-104] investigated the effect on degradation rate over a range of potentials and demonstrated an improvement in the rate apon application of a positive bias. Dunlop et al.[105] investigated the application of + 1.0 V vs. SCE on the rate of inactivation of *E. coli* and *Clostridium perfringens* spores and found the rate increased by 30% and 72%, respectively, compared to the same system without a bias.

### 1.6.9 Applications of $TiO_2$ photocatalysis

Since Fujishima and Honda[106] used $TiO_2$ to split water in 1972, interest in $TiO_2$ photocatalysis has been extensive, covering the removal of organic and inorganic contaminants from air and water.

The inactivation of micro-organisms is a relatively new photocatalytic application. The first evidence was presented in 1985, when Matsunaga and co-workers[107] discovered that microbial cells in water could be killed via contact with a $TiO_2$-Pt catalyst irradiated with near-UV light. Since then, research on microbial photocatalytic inactivation has been intensively conducted on a wide range of organisms including viruses, bacteria, fungi, algae and cancerous cells.[108-110] Most work has been performed in the aqueous phase; however photocatalytic disinfection of humid air has been reported,[86,111] with the complete mineralisation of bacteria reported by Jacoby and co-workers.[112] Table 1.2 displays a summary of the micro-organisms subjected to photocatalytic inactivation using various reactor configurations.

#### 1.6.9.1 Bacterial organisms

A range of gram-positive and gram-negative bacterial species have been subjected to photocatalytic treatment (Table 1.2). *E. coli* has been the most extensively studied, with reports that photocatalytic treatment caused the complete mineralisation[112] of the cell and degradation of its toxin.[113] The most common source of micro-organism samples is from laboratory cultures, however disinfection of bacteria from pondwater,[114] streamwater[105] and secondary waste treatment effluents[115,116] have been reported recently. Photocatalytic enhancements have also been applied to bacteria, where the combination of light and ultrasound was found to enhance the rate of inactivation of *E. coli* in a $TiO_2$ suspension reactor.[117] $TiO_2$ doped with platinum and silver were found to be more effective for the inactivation of *E. coli* than $TiO_2$ powder alone.[107,118]

**Table 1.2 Micro-organisms and other cells inactivated using $TiO_2$ photocatalysis**

| Organism | Gram +/- | Size/Shape (μm) | Reference |
|---|---|---|---|
| **Bacteria** | | | |
| *Escherichia coli* | - | Rod 1.0 x 3.0 | 94,103,105,107,110-114,117-160 |
| *Pseudomonas stutzeri* | - | Rod 0.5 – 1.0 x 1.5 – 4 | 161 |
| *Pseudomonas fluorescens* | - | Rod 0.5 – 1.0 x 1.5 – 4 | 162 |
| *Pseudomonas aeruginosa* | - | Rod 0.5 – 0.7 x 1.5 – 3.0 | 136,141,142 |
| *Serratia marcescens* | - | Rod 0.5 – 0.8 x 0.9 – 2.0 | 63,163 |
| *Staphyloccus aureus* | + | Spherical 0.5 – 2.0 | 135,159,163 |
| *Clostridium perfringens* | + | Oval sub-terminal ~ 5.0 | 94,164,165 |
| *Salmonella typhimurium* | - | Rod 0.7 – 1.5 x 2.0 – 5.0 | 142,158 |
| *Salmonella enterica* | - | Rod 0.7 – 1.5 x 2.0 – 5.0 | 136 |
| *Streptococcus mutans* | + | Spherical 0.5 – 2.0 | 166,167 |
| *Streptococcus faecalis* | + | Spherical <2 | 168 |
| *Streptococcus aureus* | + | Spherical <2 | 135 |
| *Streptococcus cricetus* | + | Spherical <2 | 169 |
| *Streptococcus rattus* | + | Spherical <2 | 169 |
| *Streptococcus sanguinis* | + | Spherical <2 | 135 |
| *Streptococcus sobrinus* | + | Spherical >2 | 167 |
| *Actinomyces viscosus* | + | Rod 0.5 x 1.6 – 2.0 | 169 |
| *Micrococcus lutens* | + | Spherical 0.5 – 2.0 | 149 |
| *Lactobaccillus acidophilus* | + | Rod 0.6 – 0.9 x 1.5 – 6.0 | 107 |
| *Lactobacillus casei* | + | Rod 0.6 – 0.9 x 1.5 – 6.0 | 135 |
| *Bacillus pumilus* | + | Rod 0.6 x 2.0 – 3.0 | 170,171 |
| *Bacillus subtilis* | + | Rod 0.7 – 0.8 x 2.0 – 3.0 | 159,172 |
| *Bacillus cereus* | + | Rod 1.0 – 1.2 x 3.0 – 5.0 | 172,173 |
| *Bacillus megaterium* | + | Rod 1.2 – 1.5 x 2.0 – 5.0 | 128 |
| *Bacillus stearothermophilus* | + | Rod 0.6 – 1.0 x 2.0 – 3.5 | 174 |
| *Enterococcus faecalis* | + | Spherical ~ 0.4 | 127,135,168 |
| *Enterobacter cloacae* | - | Rod 0.6 – 1.0 x 1.2 – 3.0 | 142 |
| *Rhodobacter sphaeroides* | - | Ovoid 0.5 – 1.2 | 112 |
| *Aeromonas hydrophila* | - | Rod 0.3 – 1.0 x 1.0 – 3.5 | 162 |
| *Bacteroides fragilis* | - | Rod 0.8 – 1.3 x 1.6 – 8.0 | 133 |
| *Deinococcus radiophilus* | + | Spherical ~ 0.7 | 133 |
| *Granulicatella adiacens* | + | Spherical <2 | 135 |
| *Legionella pneumophila* | - | Rod 0.3 – 0.9 x 2.0 – 20 | 140 |
| **Yeast, Fungi** | | | |
| *Saccharmyces cervisiae* | | Oval 3.5 – 7.0 x 3.5 – 9.0 | 150,175 |
| *Candida albcans* | | Oval ~7 | 176 |
| *Hyphomonas polymorpha* | | Multiple shapes | 117 |
| *Penicillium expansum* | | 2 – 10 | 177 |

**Table 1.2 contd. Micro-organisms and other cells inactivated using $TiO_2$ photocatalysis**

| Organism | Gram +/- | Size/Shape (μm) | Reference |
|---|---|---|---|
| **Protozoa** | | | |
| *Cryptosporidium parvum* | | Oval ~5 | 146 |
| **Algae and Phytoplankton** | | | |
| Anabaena | | Filamentous rod | 178 |
| Bacillariophyta | | 2 – 200 | 178 |
| Melosira | | 30 – 40 | 178 |
| Microcystis | | 3 – 5 | 178 |
| Chroococcus sp | | 3.5 – 26 | 179 |
| **Viruses** | | | |
| Phage Qβ | | 0.028 | 146 |
| Phage MS2 | | 0.024 | 72,180 |
| Phage λNM1149 | | - | 122 |
| Poliovirus 1 | | 0.028 | 115 |
| Lactobacillus phage PL-1 | | 0.05 | 181 |
| Enterobacteria phage MS2 | | 0.026 | 133 |
| **Cancer Cells** | | | |
| HeLa | | 10 – 16 | 182-186 |
| T24 | | 30 | 187-190 |
| U937 | | 14 – 20 | 191 |
| Mouse lymphoma L5179Y | | 11 – 12 | 192 |
| SPC-A1 | | 15-22 | 193 |
| **Other** | | | |
| Human skin fibroblasts | | 16 – 18 | 175,194 |
| Alverolar macrophage | | 20 – 30 | 195 |
| Chinese hamster CHL/IU cells | | 14 – 16 | 192 |
| Microcystin-LR (algae toxins) | | - | 196-206 |
| *E. coli* DNA plasmid | | - | 175 |
| Estrogens | | - | 91,207 |

### 1.6.9.2 Viruses and protozoan organisms

Compared to bacteria, only a small number of viruses and protozoa have been subjected to photocatalytic treatment (Table 1.2). The polio virus 1 has been inactivated in secondary waste effluent after 30 minutes of irradiation.[115] Similar virus photocatalytic inactivation rates were observed when compared to *E. coli* indicating that this virus showed no heightened resistance mechanisms to photocatalytic treatment. When phage MS2 was inactivated in phosphate buffer with

Degussa P25,[180] an increase in the inactivation rate was seen upon addition of ferrous sulphate, suggesting Fenton chemistry might augment the photocatalytic effect.

*Cryptosporidium parvum* is the only protozoan micro-organism to undergo photocatalytic treatment to date. Otaki and co-workers[146] carried out a brief study to determine *C. parvum* viability after photocatalytic treatment where it was found that the organism could indeed be inactivated by photocatalytic treatment. This is the only study of protozoans to date, with most investigators preferring to use a surrogate micro-organism. Bacterial surrogates are often used during water treatment investigations as protozoan research has serious methodological and financial limitations.[208] While no surrogates are perfect, bacterial endospore-formers: including *C. perfringens* and several *Bacillus* species have been identified as suitable surrogates for traditional water treatment methods.[209] The endospores of both *C. perfringens*[94,165] and several *Bacillus* species,[170-174] have also been investigated using $TiO_2$ photocatalysis. Endospore inactivation was achievable, however, the inactivation rates were shown to be much lower than those obtained using bacterial cells. When using an immobilised $TiO_2$ film, Dunlop and co-workers witnessed 92% *C. perfringens* endospore inactivation after 120 minutes of photocatalytic treatment.[165] Due to the extended treatment times required to achieve inactivation, several reports showing EAP treatment of endospores suspended in water have been published.[94,165] In all cases, the application of a positive bias produced greatly improved inactivation rates.

#### 1.6.9.3 Cancer cells

Numerous types of cancerous cells have been subjected to photocatalytic treatment, the most common of which are HeLa cells (cervical carcinoma). HeLa were inactivated after incubation with ultrafine $TiO_2$ powder for 24 hours followed by a period of illumination.[183] Transmission Electron Microscopy (TEM) demonstrated that $TiO_2$ particles had been adsorbed onto the surface, as well as into the cells, which catalysed inactivation even after removal of excess $TiO_2$ from the medium.[185] Tumours caused by transplanting HeLa cells into nude mice were suppressed by irradiation with 300 – 400 nm light in the presence of $TiO_2$.[182-184,186,210] Similar results have been reported using malignant T-24 cell implantation.[189] The effects of

irradiated $TiO_2$ on T-24 cells ability to uptake calcium ions as a measure of cell viability was investigated.[190] Initially cells were incubated with $TiO_2$ particles, which were shown to be incorporated into the cell cytoplasm. Upon UV irradiation, calcium ion uptake was decreased indicating cell damage. Following these observations, the authors proposed a mechanism for T-24 inactivation with cell membrane damage identified as the main cause for cell death.[187] In a separate investigation into the photocatalytic inactivation of human U937 leukaemia cells, results led the authors to conclude that the apoptosis was caused by cell membrane damage followed by DNA fragmentation.[191] EAP inactivation of cancerous cells have also been investigated.[188] Again, upon the application of a + 1.0 V vs. SCE, increased cell inactivation rates were observed.

#### 1.6.9.4 Photocatalysis of cellular components

In order to gain an understanding into the bactericidal mechanism of photocatalytic inactivation, a number of photocatalytic investigations using bacterial cellular components have been undertaken. These molecules include carbohydrates, lipids, proteins and nucleic acids, which once damaged can no longer perform in cell metabolism and reproduction, often resulting in cell death. $TiO_2$ has shown pronounced adsorption of basic L-amino acids such as L-lysine and L-arginine in aqueous solution.[211] It has been demonstrated that the nitrogen moiety of amino acids are converted to ammonia upon exposure to $TiO_2$ illuminated with UV light.[212] The photodegradation of deoxyribonucleic acid (DNA) and ribonucleic acid (RNA) was confirmed by the formation of nitrate, $CO_2$ and ammonia produced from their breakdown.[213] Direct DNA damage, including strand breakage and the hydroxylation of guanine has also been reported.[214,215] Cellular RNA was found to be more susceptible to photocatalytic attack than DNA due to the protection provided by compartmentalisation of DNA within the cell and the availability of cellular DNA self repair mechanisms.[194] However, the first evidence that lipid peroxidation is the underlying mechanism of cell death was discovered when Maness and co-workers[124] demonstrated the photocatalytic degradation of bacterial cell membranes. Further evidence of this has been provided using X-ray diffraction (XRD),[216] Fourier transform infrared (FTIR) spectroscopy[217] and Atomic Force microscopy (AFM).[134]

### 1.6.10 Mechanisms of $TiO_2$ photocatalytic bactericidal action

In order for photocatalysis to be a viable water treatment process, the detailed mechanistic action of the bactericidal effects of $TiO_2$ photocatalysis must be understood. Compared to the number of published investigations on the bactericidal effect of $TiO_2$, relatively few studies deal with the mechanism of bactericidal action. Several possible mechanisms have been suggested for the inactivation effects witnessed.

The earliest mechanism for cell inactivation was proposed by Matsunaga and co-workers,[107] who presented evidence for the oxidation of co-enzyme A (CoA) in *S. cerevisiae*. As CoA participates in enzymatic reactions involved in cell respiration and fatty acid oxidation, its photo-oxidation could prevent cellular respiratory function and ultimately lead to cell death. Matsunaga and co-workers performed further microscopic studies, but did not find evidence of cell wall damage.[218] This was an interesting result, as the actions of highly oxidative species generated on the surface of illuminated $TiO_2$ are generally regarded as non-selective, it was reasonable to expect that the cell membrane would have to be oxidised first, losing its semipermeability before the intracellular CoA is photo-oxidised.

Other workers however, did find evidence for disruption of the cell membrane and leakage of cellular contents. Cell membrane disruption of *S. sobrinus* was reported by Saito and co-workers.[167] Following exposure to UV illuminated $TiO_2$ powder potassium ion leakage indicated cell membrane damage had occurred. After continued exposure to illuminated $TiO_2$, RNA and proteins leaking from the cell were detected. Cell viability was lost after one to three minutes of exposure to photocatalytic treatment; however, electron micrographs indicated that 30 minutes of exposure was required before visible disruption of the cell wall occurred. After 120 minutes of exposure, the cell structure was visibly ruptured. From this, it was proposed that reactive oxygen species produced under photocatalytic conditions reached and compromised the cell wall before disrupting the cell structure.

Sunada et al.[113] also provided evidence of cell wall damage from investigation using *E. coli* and its endotoxin. The endotoxin is a lipopolysaccharide cell wall constituent of many gram-negative bacteria which is only released from the bacterial cell when the structure is compromised. A release of endotoxin was witnessed, which indicated outer membrane damage of the cell wall had taken place.

Further evidence of cell membrane damage during photocatalytic inactivation was provided by Sakai and co-workers.[188,190] Upon exposure of human T-24 cancer cells to illuminated $TiO_2$, leakage of cellular calcium ions from the cells was detected, indicating cellular damage. It was concluded that the calcium leakage arose from cell membrane damage and that further release was due to oxidative damage of internal $Ca^{2+}$ stores, e.g. calcium binding proteins and cellular organelles, within the cytoplasm. Cell death was attributed to attack of the cytoplasmic membrane by reactive oxygen species, generated at the surface of the $TiO_2$ particles.

In order to investigate the effect of various reactive oxidative species responsible for the bactericidal effect, Kikuchi and co-workers[130] used a porous membrane to physically separate the *E. coli* suspension from the $TiO_2$ film. It was thought that the less mobile radical species would be unable to traverse the 50 μm distance from the $TiO_2$ surface to the bacterial suspension. However, excellent cell inactivation was achieved with and without the membrane. In both cases, the addition of catalase, an enzyme which acts to neutralise hydrogen peroxide by converting it to water and oxygen, significantly quenched the cell inactivation. This led the authors to conclude that hydrogen peroxide rather than hydroxyl radicals play a significant role in long-range bactericidal effects.

Maness and co-workers[124] investigated the oxidation of *E. coli* cytoplasmic membranes during photocatalysis. During the photo-inactivation of *E. coli* in water, malondialdehyde (MDA), a breakdown product of lipid peroxidation was detected. Correlation between an increase in production of MDA and a decrease in cell viability was observed. Loss of respiratory activity was also monitored, and correlated with cell inactivation. The authors concluded that alterations of the

membrane structure, due to lipid peroxidation, led to conformational changes in membrane-bound proteins and electron mediators, which span the cell membrane and facilitate electron-transport during respiration. It was thought that the electron transport pathway was short-circuited as the cell membrane was no longer able to maintain a sufficiently negative redox potential. Farr and Kogoma[158] have also suggested that oxidative disruption to the cytoplasmic membrane reduces the proton motive potential; the driving force for adenine tri-phosphate (ATP) synthesis.

Further evidence of cell membrane damage by photocatalysis has been reported recently by Sunada and co-workers.[119] The study measured the inactivation rate of intact *E. coli* cells and spheroplasts (viable cells with the cell wall removed). Intact cells showed two step "photo-killing" reactions: an initial slower rate, followed by a higher rate. In contrast, the spheroplasts exhibited only single step kinetics with a higher rate, which suggested that the cell wall of the *E. coli* cell acts as a barrier. Furthermore, AFM measurements of intact *E. coli* cells showed that the outer cell wall membrane decomposed first and with continued illumination, the cells completely decomposed. Figure 1.13 shows a schematic illustration of the process of *E. coli* "photo-killing" on a $TiO_2$ film proposed by the authors. The authors note that the peptidoglycan layer does not possess a barrier function, allowing the oxidative species to permeate.

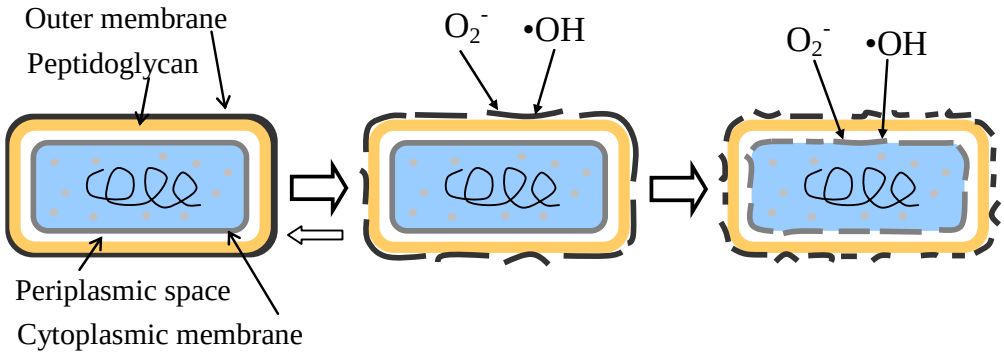


**Figure 1.13 Schematic representation of the process of *E. coli* inactivation on a $TiO_2$ film proposed by Sunada et al.[119]**

More recently, Nadtochenko and co-workers[134] performed a similar investigation into the dynamics of *E. coli* membrane cell peroxidation using AFM and FTIR-ATR

spectroscopy in relation to viable cell counts. FTIR spectroscopy of the *E. coli* cells followed the formation of peroxidation products due to photocatalysis of the cells, as well as structural changes of the cell wall membranes, while AFM spectroscopy confirmed cell lysis took place after $TiO_2$ illumination for one hour. TEM showed the positively charged Degussa P25 aggregates interacting with the negatively charged bacterial cells.

Aside from the destruction of cell structure, another possible cause of cell inactivation could be their detrimental effects on DNA and RNA. A number of investigations have been performed on supercoiled plasmid DNA with illuminated $TiO_2$ which demonstrated that the plasmid DNA was first converted to the relaxed form and later to the linear form, indicating strand breakage.[175,194,213-215,219] RNA exposed to illuminated $TiO_2$ have also shown oxidative damage leading to strand breakages.[194,213]

In summary, there is conflicting evidence in the literature as to the direct cause of cell death from $TiO_2$ photocatalysis and of the oxidative species responsible. Despite this there is substantial evidence that the bacterial cytoplasmic membrane is the primary site of attack. Oxidative attack at this site causes lipid peroxidation, leading to loss of cell membrane integrity and the termination of cellular respiration. The loss of energy production mechanisms and subsequent oxidative attack of internal cellular components ultimately results in cell death.

## *1.7 Project rationale*

With the increasing awareness of micro-organism resistance and toxic by-products produced during conventional water treatment processes, increased attention has been directed to alternative water treatment processes for the production of safe drinking water. IR radiation for water treatment has received attention in recent years, with literature reports providing evidence that it may be a possible alternative water treatment method and this warrants further research.

$TiO_2$ photocatalysis is also an emerging technology for remediation of polluted water, and has a number of environmental and economical advantages over conventional treatment processes. Photocatalysis has the potential to be used as an alternative or complementary technology to conventional chemical based disinfection processes.

While Degussa P25 is currently regarded as the most efficient photocatalyst within the industry, much research has been performed to develop novel photocatalysts equal to or greater than Degussa P25. A novel $TiO_2$ photocatalyst was developed at the Queensland University of Technology (QUT) using post-synthetic microwave treatment[220] and will be employed as a photocatalyst for the photo-oxidation of an organic pollutant and micro-organism inactivation. The immobilisation of the photocatalyst onto a solid support is desirable therefore negating the need for a catalyst recovery stage. Employing the catalyst in this form can substantially reduce the rate of pollutant degradation. In order to address this problem the efficiency of the immobilised reactor can be increased with the application of a small electrical bias to the semiconductor electrode, which will also be examined.

The photocatalytic inactivation of micro-organisms suspended in distilled water has previously been demonstrated; however, there is limited evidence that the photocatalytic process can be used to disinfect raw water.

There is also conflicting evidence within the literature regarding the effect of photocatalytic treatment on bacterial cell walls and further study into its effect must be performed before the photocatalytic bactericidal mechanism can be completely understood.

The aims of this study were to:

1. Study the effect of IR laser radiation on micro-organism inactivation.
2. Demonstrate the photocatalytic inactivation of micro-organisms using a novel, post-synthetically treated $TiO_2$ photocatalyst, and compare this to Degussa P25.
3. Immobilise $TiO_2$ photocatalysts onto solid supports and study the degradation of model organic pollutants.
4. Study the photocatalytic inactivation of micro-organisms in raw water.
5. Perform an *in situ* FTIR investigation to study the photocatalytic and electrochemically-assisted photocatalytic degradation of model organic pollutants, including a model bacterial cell wall component.

## 1.8 References


(1) Rowe, D.; Abdel-Magid, I. *Handbook of Wastewater Reclamation and Reuse*; Lewis Publishers: New York, 1995.

(2) Dillon, P. "Current Issues: Water Reclamation," CSIRO Land and Water, 2002.

(3) Gerardi, M. H. *Wastewater Biology: The Microlife*; Water Pollution Control Federation: Alexandria, 1990.

(4) WHO "Guidelines for Drinking Water Quality, 2nd edn, Vol. 1," World Health Organisation, 1993.

(5) Somasundaran, P.; Deo, N.; Deo, P.; Natarajan, K. A. *Miner. Metallurg. Process.* **2005**, *22*, 1-11.

(6) Madigan, M. T.; Martinko, J. M.; Parker, J. *Brock Biology of Microorganisms*; 9th ed.; Prentice-Hall, Inc.: New Jersey, 2000.

(7) Tortora, G. J.; Funke, B. R.; Case, C. L. *Microbiology: an introduction*; 6th ed.; Benjamin/Cummings Publishing Company: Menlo Park, 1997.

(8) Alcamo, I. E. *Fundamentals of Microbiology*; Benjamin/Cummings Publishing Company: Redwood City, 1990.

(9) Graham, L. L.; Beveridge, T.; Nanninga, N. *Trends Biochem. Sci* **1991**, *16*, 328.

(10) Volk, W. A.; Wheeler, M. F.; Brown, J. C. *Basic microbiology*; Benjamin Cummings: Menlo Park, Calif., 1997.

(11) Hogg, S. *Essential microbiology*; John Wiley and Sons: West Sussex, 2005.

(12) Austin, J. W. *Curr. Challenges. Food Microbiol.* **2003**, 77-93.

(13) Ricca, E.; Henriques, A. O.; Cutting, S. M. *Bacterial spore formers : probiotics and emerging applications*; Horizon Bioscience: Wymondham, 2004.

(14) Kolarik, L. O.; Priestley, A. J. *Modern Techniques in Water and Wastewater Treatment*; CSIRO: Melbourne, 1995.

(15) Schroeder, E. D. *Water and Wastewater Treatment*; McGraw-Hill: New York, 1977.

(16) Binnie, C.; Kimber, M.; Smethurst, G. *Basic Water Treatment*; 3rd ed.; Royal Society of Chemistry: Cambridge, 2002.

(17) Joret, J. C.; Mennecart, V.; Robert, C.; Compagnon, B.; Cervantes, P. *Water Sci. Technol.* **1997**, *35*, 81-86.

(18) Lazarova, V.; Janex, M. L.; Fiksdal, L.; Oberg, C.; Barcina, I.; Pommepuy, M. *Water Sci. Technol.* **1998**, *38*, 109-117.

(19) Longley, K. E. *Wastewater Disinfection*; Pot City Press: Viginia, USA, 1986.

(20) Lorch, W. *Handbook of Water Purification*; 2nd ed.; John Wiley & Sons: New York, 1987.

(21) Johnson, J. D.; Jolley, R. L. In *Water Chlorination. Chemistry, Envrionmental Impact and Health Effects*; Jolley, R. L., Johnson, J. D., Minear, Jacobs, Condie, Katz, Mattice, Eds.; Lewis Publishers Inc.: Chicago, 1990.

(22) Gray, N. F. *Drinking Water Quailty, Problems and Solutions*; John Wiley & Sons, 1994.

(23) Betancourt, W. Q.; Rose, J. B. *Vet. Parasit.* **2004**, *126*, 219-234.

(24) Jakubowski, W.; Boutros, S.; Fayer, R.; Ghiorse, W.; LeChevallier, M.; Rose, J. B.; Schaub, S.; Singh, A.; Stewart, M. *J. Amer. Water Works Assoc.* **1996**, *88*, 107-121.

(25) Lazarova, V.; Savoye, P.; Janex, M. L.; BlatchleyIII, E. R.; Pommepuy, M. *Water Sci. Technol.* **1999**, *40*, 203-213.

(26) Dunlop, P. S. M. D. Phil., University of Ulster, 2001.

(27) Van der Bruggen, B.; Vandecasteele, C. *Environ. Pollut.* **2003**, *122*, 435-445.

(28) del Pino, M. P.; Durham, B. *Desalination* **1999**, *124*, 271-277.

(29) Schafer, A. I.; Fane, A. G.; Waite, T. D. *Water Res.* **2001**, *35*, 1509-1517.

(30) Masson, M.; Deans, G. *Desalination* **1996**, *106*, 11-15.

(31) Mavrov, V.; Chmiel, H.; Belieres, E. *Desalination* **2001**, *138*, 65-74.

(32) Wend, C. F.; Stewart, P. S.; Jones, W.; Camper, A. K. *Water Res.* **2003**, *37*, 3367-3378.

(33) Davies, R. J. H. *Biochem. Soc. Trans.* **1995**, *23*, 407-18.

(34) Carrington, E. G.; Nettleton, K.; Haley, J.; Whitehead, A. P.; Jackson, P. "Disinfection of Potable Water by UV Irradiation - A Critical Review," Water Research Centre, 1989.

(35) Molin, G.; Ostilund, K. *Antonie van Leeuwenhoek* **1975**, *41*, 329-35.

(36) Pratt, G. W., Jr. In *U.S.*; (Massachusetts Institute of Technology, USA). USA, 1976, p 15.

(37) Baca, A. M. In *U.S. Pat. Appl. Publ.*; (USA). USA, 2002.

(38) Legrini, O.; Oliveros, E.; Braun, A. M. *Chem. Rev.* **1993**, *93*, 671-698.

(39) Yang, H.; Lin, W. Y.; Rajeshwar, K. *J. Photochem. Photobiol., A* **1999**, *123*, 137-143.

(40) Ding, Z. PhD, The University of Queensland, 2000.

(41) Schiavello, M. *Heterogeneous Photocatalysis*; John Wiley & Sons: Chichester, 1997; 3.

(42) Fox, M. A.; Dulay, M. T. *Chem. Rev.* **1993**, *93*, 341-57.

(43) Hagfeldt, A.; Grätzel, M. *Chem. Rev.* **1995**, *95*, 49-68.

(44) Mills, A.; Le Hunte, S. *J. Photochem. Photobiol., A* **1997**, *108*, 1-35.

(45) Hoffmann, M. R.; Martin, S. T.; Choi, W.; Bahnemann, D. W. *Chem. Rev.* **1995**, *95*, 69-96.

(46) Yoneyama, H. *Crit. Rev. Solid State Mater. Sci.* **1993**, *18*, 69-111.

(47) Hadjiivanov, K. I.; Klissurski, D. G. *Chem. Soc. Rev.* **1996**, *25*, 61-69.

(48) Clarke, R. J. H. "The Chemistry of Titanium and Vanadium," Elsevier, 1968.

(49) Jiang, B.; Zuo, J. M.; Jiang, N.; O'Keeffe, M.; Spence, J. C. H. *Acta Crystallogr., Sect A: Foundations* **2003**, *A59*, 341-350.

(50) Hurum, D. C.; Agrios, A. G.; Gray, K. A.; Rajh, T.; Thurnauer, M. C. *J. Phys. Chem. B* **2003**, *107*, 4545-4549.

(51) Bickley, R. I.; Gonzalez-Carreno, T.; Lees, J. S.; Palmisano, L.; Tilley, R. J. D. *J. Solid State Chem.* **1991**, *92*, 178-90.

(52) Presley, R. W. In *Sci. Technol. Alliance, Mater. Conf.* 1995, p 211-16.

(53) Yan, M.; Chen, F.; Zhang, J.; Anpo, M. *J. Phys. Chem. B* **2005**, *109*, 8673-8678.

(54) Camara, O. R.; De Pauli, C. P.; Vaschetto, M. E.; Retamal, B.; Aquirre, M. J.; Zagal, J. H.; Biaggio, S. R. *J. Appl. Bacteriol.* **1995**, *25*, 247-51.

(55) Arsov, L. D.; Kormann, C.; Plieth, W. *J. Raman Spectrosc.* **1991**, *22*, 573-5.

(56) Hwang, B. J.; Hwang, J. R. *J. Appl. Electrochem.* **1993**, *23*, 1056-62.

(57) Kontos, A. I.; Arabatzis, I. M.; Tsoukleris, D. S.; Kontos, A. G.; Bernard, M. C.; Petrakis, D. E.; Falaras, P. *Catal. Today* **2005**, *101*, 275-281.

(58) Lee, M. S.; Cheon, I. C.; Kim, Y. I. *Bull. Korean Chem. Soc.* **2003**, *24*, 1155-1162.

(59) Piscopo, A.; Robert, D.; Weber, J. V. *J. Photochem. Photobiol., A* **2001**, *139*, 253-256.

(60) "Degussa Technical Report," Revised reprint from Chem. Ing. Techn., 1980.

(61) Devipriya, S.; Yesodharan, S. *Sol. Energy Mater. Sol. Cells* **2005**, *86*, 309-348.

(62) Herrmann, J.-M. *Catal. Today* **1999**, *53*, 115-129.

(63) Goswami, D. Y. *L. Solar Ener. Eng.* **1997**, *119*, 101-107.

(64) Herrmann, J.-M.; Disdier, J.; Pichat, P.; Malato, S.; Blanco, J. *Appl. Catal., B* **1998**, *17*, 15-23.

(65) Herrmann, J.-M.; Guillard, C.; Disdier, J.; Lehaut, C.; Malato, S.; Blanco, J. *Appl. Catal., B* **2002**, *35*, 281-294.

(66) Ljubas, D. *Energy* **2005**, *30*, 1699-1710.

(67) Romero, M.; Blanco, J.; Sanchez, B.; Vidal, A.; Sixto Malato; Cardona, A. I.; Garcia, E. *Sol. Energy* **1999**, *66*, 169-182.

(68) Parent, Y.; Blake, D.; Magrini-Bair, K.; Lyons, C.; Turchi, C.; Watt, A.; Wolfrum, E.; Prairie, M. *Sol. Energy* **1996**, *56*, 429-437.

(69) Vidal, A.; Diaz, A. I.; El Hraiki, A.; Romero, M.; Muguruza, I.; Senhaji, F.; Gonzalez, J. *Catal. Today* **1999**, *54*, 283-290.

(70) Alfano, O. M.; Bahnemann, D.; Cassano, A. E.; Dillert, R.; Goslich, R. *Catal. Today* **2000**, *58*, 199-230.

(71) Dorfman, L. M.; Adams, G. E. *NSRDS-NBS* **1973**, *46*, 1-72.

(72) Sato, T.; Taya, M. *Biochem. Eng. J* **2006**, *28*, 303-308.

(73) Tseng, I. H.; Wu, J. C. S.; Chou, H.-Y. *J. Catal.* **2004**, *221*, 432-440.

(74) Peill, N. J.; Bourne, L.; Hoffmann, M. R. *J. Photochem. Photobiol., A* **1997**, *108*, 221-228.

(75) Dvoranova, D.; Brezova, V.; Mazur, M.; Malati, M. A. *Appl. Catal., B* **2002**, *37*, 91-105.

(76) Alberici, R. M.; Jardim, W. F. *Water Res.* **1994**, *28*, 1845-1849.

(77) Cozzoli, P. D.; Fanizza, E.; Comparelli, R.; Curri, M. L.; Agostiano, A.; Laub, D. *J. Phys. Chem. B* **2004**, *108*, 9623-9630.

(78) Komarneni, S.; Rajha, R. K.; Katsuki, H. *Mater. Chem. Phys.* **1999**, *61*, 50-54.

(79) Bavykin, D. V.; Parmon, V. N.; Lapkin, A. A.; Walsh, F. C. *J. Mater. Chem.* **2004**, *14*, 3370-3377.

(80) Byrne, J. A.; Davidson, A.; Dunlop, P. S. M.; Eggins, B. R. *J. Photochem. Photobiol., A* **2002**, *148*, 365-374.

(81) Xu, Y.; Langford, C. H. *J. Phys. Chem. B* **1995**, *101*, 2611-2616.

(82) Ding, Z.; Zhu, H. Y.; Lu, G. Q.; Greenfield, P. F. *J. Colloid Interface Sci.* **1999**, *209*, 193-199.

(83) Karches, M.; Morstein, M.; Rudolf von Rohr, P.; Pozzo, R. L.; Giombi, J. L.; Baltanas, M. A. *Catal. Today* **2002**, *72*, 267-279.

(84) Aguado, J.; van Grieken, R.; Lopez-Munoz, M. J.; Marugan, J. *Catal. Today* **2002**, *75*, 95-102.

(85) Feitz, A. J.; Boyden, B. H.; Waite, T. D. *Water Res.* **2000**, *34*, 3927-3932.

(86) Ollis, O. F.; Al-Ekabi, H. *Photocatalytic Purification and Treatment of Water and Air*; Elsevier-Science: Lausanne, 1993.

(87) Pozzo, R. L.; Giombi, J. L.; Baltanas, M. A.; Cassano, A. E. *Catal. Today* **2000**, *62*, 175-187.

(88) Krysa, J.; Bouzek, K.; Stollberg, C. *J. Appl. Electrochem.* **2000**, *30*, 1033-1041.

(89) Dionysiou, D. D.; Balasubramanian, G.; Suidan, M. T.; Khodadoust, A. P.; Baudin, I.; Laine, J.-M. *Water Res.* **2000**, *34*, 2927-2940.

(90) Dionysiou, D. D.; Suidan, M. T.; Baudin, I.; Laine, J.-M. *Appl. Catal., B* **2002**, *38*, 1-16.

(91) Nakashima, T.; Ohko, Y.; Kubota, Y.; Fujishima, A. *J. Photochem. Photobiol., A* **2003**, *160*, 115-120.

(92) Gerischer, H.; Heller, A. *J. Phys. Chem.* **1991**, *95*, 5261-7.

(93) Dijkstra, M. F. J.; Michorius, A.; Buwalda, H.; Panneman, H. J.; Winkelman, J. G. M.; Beenackers, A. A. C. M. *Catal. Today* **2001**, *66*, 487-494.

(94) Butterfield, I. M.; Christensen, P. A.; Curtis, T. P.; Gunlazuardi, J. *Water Res.* **1997**, *31*, 675-677.

(95) Vinodgopal, K.; Hotchandani, S.; Kamat, P. V. *J. Phys. Chem.* **1993**, *97*, 9040-4.

(96) Kim, D. H.; Anderson, M. A. *Environ. Sci. Technol.* **1994**, *28*, 479-483.

(97) Kim, D. H.; Anderson, M. A. *J. Photochem. Photobiol., A* **1996**, *94*, 221-229.

(98) Candal, R. J.; Zeltner, W. A.; Anderson, M. A. *Environ. Sci. Technol.* **2000**, *34*, 3443-3451.

(99) McMurray, T. A.; Byrne, J. A.; Dunlop, P. S. M.; McAdams, E. T. *J. Appl. Electrochem.* **2005**, *35*, 723-731.

(100) Krysa, J.; Jirkovsky, J. *J. Appl. Electrochem.* **2002**, *32*, 591-596.

(101) Christensen, P. A.; Eameaim, J.; Hamnett, A. *In situ FTIR studies of the photo-electrochemical behaviour of thermal $TiO_2$ films as a function of temperature* **1999**, *1*, 5315-5321.

(102) Christensen, P. A.; Dilks, A.; Egerton, T. A.; Temperley, J. *J. Mater. Sci.* **2000**, *35*, 5353-5358.

(103) Christensen, P. A.; Curtis, T. P.; Egerton, T. A.; Kosa, S. A. M.; Tinlin, J. R. *Appl. Catal., B* **2003**, *41*, 371-386.

(104) Shaw, K.; Christensen, P.; Hamnett, A. *Electrochim. Acta* **1996**, *41*, 719-728.

(105) Dunlop, P. S. M.; Byrne, J. A.; Manga, N.; Eggins, B. R. *J. Photochem. Photobiol., A* **2002**, *148*, 355-363.

(106) Fujishima, A.; Honda, K. *Nature* **1972**, *238*, 37.

(107) Matsunaga, T.; Tomada, R.; Nakajima, T.; Wake, H. *FEMS Microbiol. Lett.* **1985**, *29*, 211-214.

(108) Amezaga-Madrid, P.; Silveyra-Morales, R.; Cordoba-Fierro, L.; Nevarz-Moorillon, G. V.; Miki-Yoshida, M.; Orrantia-Borunda, E.; Solis, F. J. *J. Photochem. Photobiol., B* **2003**, *70*, 45-50.

(109) Blake, D. M.; Maness, P.-C.; Huang, Z.; Wolfrum, E. J.; Huang, J.; Jacoby, W. A. *Sep. Purif. Meth.* **1999**, *28*, 1-50.

(110) Tao, H.; Wei, W.; Zhang, S. *J. Photochem. Photobiol., B* **2004**, *161*, 193-199.

(111) Sato, T.; Koizumi, Y.; Taya, M. *Biochem. Eng. J* **2003**, *14*, 149-152.

(112) Jacoby, W. A.; Maness, P. C.; Wolfrum, E. J.; Blake, D. M.; Fennell, J. A. *Environ. Sci. Technol.* **1998**, *32*, 2650-2653.

(113) Sunada, K.; Kikuchi, Y.; Hashimoto, K.; Fujishima, A. *Environ. Sci. Technol.* **1998**, *32*, 726-728.

(114) Ireland, J.; Klostermann, P.; Rice, E.; Clark, R. *Appl. Environ. Microbiol.* **1993**, *59*, 1668-1670.

(115) Watts, R. J.; Kong, S.; Orr, M. P.; Miller, G. C.; Henry, B. E. *Water Res.* **1995**, *29*, 95-100.

(116) Arana, J.; Herrera Melian, J. A.; Dona Rodriguez, J. M.; Gonzalez Diaz, O.; Viera, A.; Perez Pena, J.; Marrero Sosa, P. M.; Espino Jimenez, V. *Catal. Today* **2002**, *76*, 279-289.

(117) Stevenson, M.; Bullock, K.; Lin, W. Y.; Rajeshwar, K. *Res. Chem. Intermed.* **1997**, *23*, 311-323.

(118) Thornton, H. M.; Christensen, G. L.; Suri, R. P. S. *Haz. Indust. Wastes* **1997**, *29th*, 195-204.

(119) Sunada, K.; Watanabe, T.; Hashimoto, K. *J. Photochem. Photobiol., A* **2003**, *156*, 227-233.

(120) Dillert, R.; Siemon, U.; Bahnemann, D. *Chem. Eng. Technol.* **1998**, *21*, 356-358.

(121) Wei, C.; Lin, W. Y.; Zainal, Z.; Williams, N. E.; Zhu, K.; Kruzic, A. P.; Smith, R. L.; Rajeshwar, K. *Environ. Sci. Technol.* **1994**, *28*, 934.

(122) Belhacova, L.; Krysa, J.; Geryk, J.; Jirkovsky, J. *J. Chem. Technol. Biotechnol.* **1999**, *74*, 149-154.

(123) Huang, Z.; Maness, P.-C.; Blake, D. M.; Wolfrum, E. J.; Smolinski, S. L.; Jacoby, W. A. *Bactericidal mode of titanium dioxide photocatalysis* **2000**, *130*, 163-170.

(124) Maness, P.-C.; Smolinski, S.; Blake, D. M.; Huang, Z.; Wolfrum, E. J.; Jacoby, W. A. *Appl. Environ. Microbiol.* **1999**, *65*, 4094-4098.

(125) Rincon, A. G.; Pulgarin, C. *Appl. Catal., B* **2003**, *44*, 263-284.

(126) Rincon, A. G.; Pulgarin, C.; Adler, N.; Peringer, P. *J. Photochem. Photobiol., A* **2001**, *139*, 233-241.

(127) Rincon, A.-G.; Pulgarin, C. *Appl. Catal., B* **2004**, *49*, 99-112.

(128) Fu, G.; Vary, P. S.; Lin, C.-T. *J. Phys. Chem. B* **2005**, *109*, 8889-8898.

(129) Harper, J. C.; Christensen, P. A.; Egerton, T. A.; Curtis, T. P.; Gunlazuardi, J. *J. Appl. Electrochem.* **2001**, *31*, 623-628.

(130) Kikuchi, Y.; Sunada, K.; Iyoda, T.; Hashimoto, K.; Fujishima, A. *J. Photochem. Photobiol., A* **1997**, *106*, 51-56.

(131) Kim, S. H.; Kwak, S.-Y.; Sohn, B.-H.; Park, T. H. *J. Membr. Sci.* **2003**, *211*, 157-165.

(132) Koizumi, Y.; Yamada, R.; Nishioka, M.; Matsumura, Y.; Tsuchido, T.; Taya, M. *J. Chem. Technol. Biotechnol.* **2002**, *77*, 671-677.

(133) Laot, N.; Narkis, N.; Neeman, I.; Bilanovic, D.; Armon, R. *J Adv. Ox. Technol.* **1999**, *4*, 97-102.

(134) Nadtochenko, V. A.; Rincon, A. G.; Stanca, S. E.; Kiwi, J. *J. Photochem. Photobiol., A* **2005**, *169*, 131-137.

(135) Nagame, S.; Kambara, M.; Onoe, T.; Kamada, A.; Yoshino, K. *Jpn J. Appl. Phys. 1* **2003**, *42*, 6625-6626.

(136) Robertson, J. M. C.; Robertson, P. K. J.; Lawton, L. A. *J. Photochem. Photobiol., A* **2005**, *175*, 51-56.

(137) Sun, D. D.; Tay, J. H.; Tan, K. M. *Water Res.* **2003**, *37*, 3452-3462.

(138) Wist, J.; Sanabria, J.; Dierolf, C.; Torres, W.; Pulgarin, C. *J. Photochem. Photobiol., A* **2002**, *147*, 241-246.

(139) Yu, J. C.; Tang, H. Y.; Yu, J.; Chan, H. C.; Zhang, L.; Xie, Y.; Wang, H.; Wong, S. P. *J. Photochem. Photobiol., A* **2002**, *153*, 211-219.

(140) Coronado, J. M.; Soria, J.; Conesa, J. C.; Bellod, R.; Adan, C.; Yamaoka, H.; Loddo, V.; Augugliaro, V. *Top. Catal.* **2005**, *35*, 279-286.

(141) Drees, K. P.; Abbaszadegan, M.; Maier, R. M. *Water Res.* **2003**, *37*, 2291-2300.

(142) Ibanez, J. A.; Litter, M. I.; Pizarro, R. A. *J. Photochem. Photobiol., A* **2003**, *157*, 81-85.

(143) Coleman, H. M.; Marquis, C. P.; Scott, J. A.; Chin, S. S.; Amal, R. *Chem. Eng. J.* **2005**, *113*, 55-63.

(144) Lu, Y.-g.; Ma, J.-j. *Beijing Gongshang Daxue Xuebao, Ziran Kexueban* **2005**, *23*, 4-7.

(145) Huang, N.; Xiao, Z.; Huang, D.; Yuan, C. *Supramol. Sci.* **1998**, *5*, 559-564.

(146) Otaki, M.; Hirata, T.; Ohgaki, S. *Water Sci. Technol.* **2000**, *42*, 103-108.

(147) Horie, Y.; Taya, M.; Tone, S. *Kagaku Kogaku Ronbunshu* **1996**, *22*, 1241-1245.

(148) Horie, Y.; Taya, M.; Tone, S. *J. Chem. Eng. Jpn.* **1998**, *31*, 577-584.

(149) Horie, Y.; Taya, M.; Tone, S. *J. Chem. Eng. Jpn.* **1998**, *31*, 922-929.

(150) Horie, Y.; David, D. A.; Taya, M.; Tone, S. *Ind. Eng. Chem. Res.* **1996**, *35*, 3920-3926.

(151) Zhang, P.; Scrudato, R. J.; Germano, G. *Chemosphere* **1994**, *28*, 607-11.

(152) Bekbolet, M.; Araz, C. V. *Chemosphere* **1996**, *32*, 959-65.

(153) Matsunaga, T.; Okochi, M. *Environ. Sci. Technol.* **1995**, *29*, 501-5.

(154) Kuo, W. S.; Lin, Y. T. *J. Environ. Sci. Health., Part A* **2000**, *A35*, 671-680.

(155) Kuo, W. S.; Lin, Y. T. *J. Environ. Sci. Health., Part B* **2000**, *B35*, 61-75.

(156) Chai, Y.-S.; Lee, J.-C.; Kim, B.-W. *Korean J. Chem. Eng.* **2000**, *17*, 633-637.

(157) Choi, Y.-S.; Kim, B.-W. *J. Chem. Technol. Biotechnol.* **2000**, *75*, 1145-1150.

(158) Farr, S. B.; Kogoma, T. *Microbiol. Rev.* **1991**, *55*, 561-85.

(159) Sakurada, T. *Hyomen Gijutsu* **1990**, *41*, 1008-11.

(160) Tatsuma, T.; Takeda, S.; Saitoh, S.; Ohko, Y.; Fujishima, A. *Electrochim. Commun.* **2003**, *5*, 793-796.

(161) Biguzzi, M.; Shama, G. *Lett. Appl. Microbiol.* **1994**, *19*, 458-60.

(162) Kersters, I.; De Keyser, T.; Verstraete, W. *Indian J. Eng. Mater. Sci.* **1998**, *5*, 211-216.

(163) Block, S. S.; Seng, V. P.; Goswami, D. W. *L. Solar Ener. Eng.* **1997**, *119*, 85-91.

(164) Kuo, W. S. *J. Environ. Sci. Health., Part A* **2000**, *A35*, 419-433.

(165) Dunlop, P. S. M.; Byrne, J. A.; Manga, N.; Eggins, B. R. In *International Symposium on Waterborne Pathogens, Proceedings, Milwaukee, WI, United States, Aug. 29-Sept. 1, 1999* 1999, p 79-101.

(166) Morioka, T.; Saito, T.; Nara, Y.; Onoda, K. *Caries Res.* **1988**, *22*, 230-1.

(167) Saito, T.; Iwase, T.; Horie, J.; Morioka, T. *J. Photochem. Photobiol., B* **1992**, *14*, 369-79.

(168) Melian, J. A. H.; Rodriguez, J. M. D.; Suarez, A. V.; Rendon, E. T.; Do Campo, C. V.; Arana, J.; Pena, J. P. *Chemosphere* **2000**, *41*, 323-327.

(169) Ngame, S.; Oku, T.; Kambara, M.; Konishi, K. *J. Dental Res.* **1989**, *68*.

(170) Pham, H. N.; McDowell, T.; Wilkins, E. *J. Environ. Sci. Health., Part A* **1995**, *A30*, 627-36.

(171) Pham, H. N.; Wilkins, E.; Heger, A. S.; Kauffman, D. *J. Environ. Sci. Health., Part A* **1997**, *A32*, 153-163.

(172) Armon, R.; Weltch-Cohen, G.; Bettane, P. *Water Sci. Technol.* **2004**, *4*, 7-14.

(173) Lee, S.-H.; Pumprueg, S.; Moudgil, B.; Sigmund, W. *Colloids Surf., B* **2005**, *40*, 93-98.

(174) Tone, S.; Taya, M.; Kato, S.; Horie, Y.; Ashikaga, Y. *Kagaku Kogaku Ronbunshu* **1993**, *19*, 1149-56.

(175) Serpone, N.; Salinaro, A.; Horikoshi, S.; Hidaka, H. *J. Photochem. Photobiol., A* **2006**, *179*, 200-212.

(176) Kondo, M. M.; Orlanda, J. F. F.; Ferreira, M. d. G. A. B.; Grassi, M. T. *Quim. Nova* **2003**, *26*, 133-135.

(177) Maneerat, C.; Hayata, Y. *Inter. J. Food Microbiol.* **2006**, *107*, 99-103.

(178) Kim, S.-C.; Lee, D.-K. *Microchem. J.* **2005**, *80*, 227-232.

(179) Hong, J.; Ma, H.; Otaki, M. *J. Biosci. Bioeng.* **2005**, *99*, 592-597.

(180) Sjogren, J. C.; Sierka, R. A. *Appl. Environ. Microbiol.* **1994**, *60*, 344-7.

(181) Kakita, Y.; Kashige, N.; Miake, F.; Watanabe, K. *Biosci., Biotechnol., Biochem.* **1997**, *61*, 1947-1948.

(182) Fujishima, A.; Cai, R. X.; Sakai, H.; Baba, R.; Hashimoto, K.; Kubota, Y. In *Fifth International Symposium on Redox Mechanisms and Interfacial Properties of Molecules of Biological Importance*; Electrochemical Society: 1993; Vol. 93-11, p 363-72.

(183) Cai, R.; Hashimoto, K.; Itoh, K.; Kubota, Y.; Fujishima, A. *Bull. Chem. Soc. Jpn.* **1991**, *64*, 1268-73.

(184) Cai, R.; Hashimoto, K.; Kubota, Y.; Fujishima, A. *Chem. Lett.* **1992**, 427-30.

(185) Cai, R.; Sakai, H.; Hashimoto, K.; Kubota, Y.; Fujishima, A. *Denki Kagaku oyobi Kogyo Butsuri Kagaku* **1992**, *60*, 314-21.

(186) Cai, R.; Kubota, Y.; Shuin, T.; Sakai, H.; Hashimoto, K.; Fujishima, A. *Cancer Res.* **1992**, *52*, 2346-8.

(187) Sakai, H.; Cai, R.; Kato, T.; Hashimoto, K.; Fujishima, A.; Kubota, Y.; Ito, E.; Yoshioka, T. *Photomed. Photobiol.* **1990**, *12*, 135-8.

(188) Sakai, H.; Baba, R.; Hashimoto, K.; Kubota, Y.; Fujishima, A. *Chem. Lett.* **1995**, 185-6.

(189) Kubota, Y.; Shuin, T.; Kawasaki, C.; Hosaka, M.; Kitamura, H.; Cai, R.; Sakai, H.; Hashimoto, K.; Fujishima, A. *Brit. J. Cancer* **1994**, *70*, 1107-11.

(190) Sakai, H.; Ito, E.; Cai, R.-X.; Yoshioka, T.; Kubota, Y.; Hashimoto, K.; Fujishima, A. *Biochim. Biophys. Acta* **1994**, *1201*, 259-65.

(191) Huang, N.-p.; Xu, M.-h.; Yuan, C.-w.; Yu, R.-r. *J. Photochem. Photobiol., A* **1997**, *108*, 229-233.

(192) Nakagawa, Y.; Wakuri, S.; Sakamoto, K.; Tanaka, N. *Mutation Res.* **1997**, *394*, 125-132.

(193) Xu, M.; Huang, N.; Xiao, Z.; Lu, Z. *Supramol. Sci.* **1998**, *5*, 449-451.

(194) Wamer, W. G.; Yin, J. J.; Wei, R. R. *Free Radical Biol. Med.* **1997**, *23*, 851-8.

(195) Stringer, B.; Imrich, A.; Kobzik, L. *Cytometry* **1995**, *20*, 23-32.

(196) Feng, X.; Wei, T.; Yuan, C. *Dongnan Daxue Xuebao, Ziran Kexueban* **2004**, *34*, 705-710.

(197) Srinivasan, C.; Somasundaram, N. *Curr. Sci.* **2003**, *85*, 1431-1438.

(198) Cornish, B. J. P. A.; Lawton, L. A.; Robertson, P. K. J. *Appl. Catal., B* **2000**, *25*, 59-67.

(199) Lawton, L. A.; Robertson, P. K. J.; Cornish, B. J. P. A.; Jaspars, M. *Environ. Sci. Technol.* **1999**, *33*, 771-775.

(200) Robertson, P. K. J.; Lawton, L. A.; Cornish, B. J. P. A. *J. Porphyrins Phthalocyanines* **1999**, *3*, 544-551.

(201) Robertson, P. K. J.; Lawton, L. A.; Cornish, B. J. P. A.; Jaspars, M. *J. Photochem. Photobiol., A* **1998**, *116*, 215-219.

(202) Robertson, P. K. J.; Lawton, L. A.; Munch, B.; Rouzade, J. *Chem. Commun.* **1997**, 393-394.

(203) Liu, I.; Lawton, L. A.; Bahnemann, D. W.; Robertson, P. K. J. *Appl. Catal., B* **2005**, *60*, 245-252.

(204) Lawton, L. A.; Robertson, P. K. J.; Cornish, B. J. P. A.; Marr, I. L.; Jaspars, M. *J. Catal.* **2003**, *213*, 109-113.

(205) Liu, I.; Lawton, L. A.; Cornish, B.; Robertson, P. K. J. *J. Photochem. Photobiol., A* **2002**, *148*, 349-354.

(206) Robertson, P. K. J.; Lawton, L. A.; Munch, B.; Cornish, B. *J. Adv. Ox. Technol.* **1999**, *4*, 20-26.

(207) Nakashima, T.; Ohko, Y.; Tryk, D. A.; Fujishima, A. *J. Photochem. Photobiol., A* **2002**, *151*, 207-212.

(208) Facile, N.; Barbeau, B.; Prevost, M.; Koudjonou, B. *Water Res.* **2000**, *34*, 3238-3246.

(209) Rice, E. W.; Fox, K. R.; Miltner, R. J.; Lytle, D. A.; Johnson, C. H. *J. Amer. Water Works Assoc.* **1996**, *88*, 122-130.

(210) Fujishima, A.; Nagahara, L. A.; Yoshiki, H.; Ajito, K.; Hashimoto, K. *Electrochim. Acta* **1994**, *39*, 1229-36.

(211) Wan, J.; Gordon, J.; Hickey, M. W.; Mawson, R. F.; Coventry, M. J. *J. Appl. Bacteriol.* **1996**, *81*, 167-173.

(212) Hidaka, H.; Horikoshi, S.; Ajisaka, K.; Zhao, J.; Serpone, N. *J. Photochem. Photobiol., A* **1997**, *108*, 197-205.

(213) Hidaka, H.; Horikoshi, S.; Serpone, N.; Knowland, J. *J. Photochem. Photobiol., A* **1997**, *111*, 205-214.

(214) Ashikaga, T.; Wada, M.; Kobayashi, H.; Mori, M.; Katsumura, Y.; Fukui, H.; Kato, S.; Yamaguchi, M.; Takamatsu, T. *Mutation Res.* **2000**, *466*, 1-7.

(215) Hidaka, H.; Kobayashi, H.; Kuga, M.; Koike, T. *J. Oleo Sci.* **2005**, *54*, 487-494.

(216) Suwalsky, M.; Schneider, C.; Mansilla, H. D.; Kiwi, J. *J. Photochem. Photobiol., B* **2005**, *78*, 253-258.

(217) Kiwi, J.; Nadtochenko, V. *J. Phys. Chem. B* **2004**, *108*, 17675-17684.

(218) Matthews, C. K.; van Holde, K. E. *Biochemistry*; 2nd ed.; Benjamin/Cummings Publishing Company, Inc.: Menlo Park, 1995.

(219) Dunford, R.; Salinaro, A.; Cai, L.; Serpone, N.; Horikoshi, S.; Hidaka, H.; Knowland, J. *FEBS Lett.* **1997**, *418*, 87-90.

(220) Wilson, G. J.; Will, G. D.; Frost, R. L.; Montgomery, S. A. *J. Mater. Chem.* **2002**, *12*, 1787-1791.

# Chapter 2

## INACTIVATION AND STRUCTURAL CHANGES OF *E. CLOACAE* AND *B. SUBTILIS* ENDOSPORES DURING IR LASER WATER TREATMENT

## 2.1 Introduction

Developing methods for recycling and re-use of stormwater and effluent water/wastewater have become an important and urgent issue. Due to this, new methods for disinfecting water supplies are being investigated, one of which is the use of IR radiation.

### 2.1.1 Theory of IR radiation

IR radiation is the electromagnetic radiation of a wavelength longer than that of visible but shorter than microwave radiation. Quantum mechanics shows that a molecule can take up an amount of energy, $h\nu_s$, to reach the first vibrationally excited state.[1] Light quanta in the IR region with a wavelength (λ) of 2.5 – 1000 μm possess energies of:

$$h\nu = hc\tilde{\nu} \qquad \textbf{2.1}$$

with $\tilde{\nu}$ = 4000 – 10 $cm^{-1}$. Absorption of IR radiation causes changes in the rotational and rotational-vibrational energy states, used by FTIR spectroscopists for molecular identification and investigation purposes.

### 2.1.2 Lasers

Lasers provide an almost monochromatic source of radiation with a narrow linewidth and emit coherent, parallel and polarised radiant energy. Stimulated emission, population inversion and optical resonance are required for laser emission which are discussed in detail elsewhere.[2] Laser types are varied and include solid-state, dye, semiconductor, gas, chemical, free-electron and x-ray lasers. Applications are extremely varied, ranging from scientific military, medical and consumer uses.

#### 2.1.2.1 Theory of $CO_2$ lasers

Molecular gas lasers exploit the transitions between the energy levels of a molecule. $CO_2$ lasers are categorised as vibrational-rotational lasers, which utilise transitions between vibrational levels of the same electronic state, for example the ground state.

Therefore the energy difference between the levels falls in the middle to far IR (2.5 – 300 μm). $CO_2$ lasers use a mixture of $CO_2$, $N_2$, and He as the active medium. $N_2$ and He improve efficiency, while oscillation takes place between the two vibrational levels of the $CO_2$ molecule. Figure 2.1 shows the energy level diagrams for $CO_2$ and $N_2$.

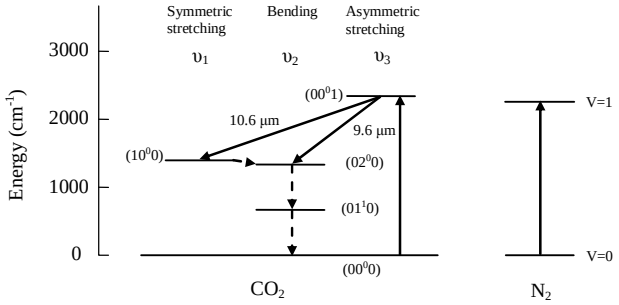


**Figure 2.1 Energy level diagrams showing lowest energy levels of the ground electronic states of a $CO_2$ and $N_2$ molecule. (Rotational levels not shown.)**

Population of the upper $00^01$ laser level is achieved through: direct electron collisions, the main one of which is considered to be:

$$e + CO_2(00^00) \rightarrow e + CO_2(00^01) \qquad \textbf{2.2}$$

and resonant energy transfer from an $N_2$ molecule, which is very efficient due to the small energy difference between the excited levels of $CO_2$ and $N_2$ ($\Delta E \approx 18$ cm$^{-1}$). A slowing of the process can occur, due to an accumulation in the $10^00$ and $02^00$ levels as these are in thermal equilibrium with $01^10$. The presence of He reduces this due to a transfer of energy to the lighter atom, according to the theory of elastic electrons. Due to its high thermal conductivity, He also aids in cooling the $CO_2$, to prevent population of the lower laser level via thermal excitation.

### 2.1.3 Bacterial disinfection using IR lasers

The first evidence of the use of IR radiation for micro-organism inactivation was presented in 1975, by Molin and Ostilund.[3] The research involved unfocused lasers to sterilise bacterial spores on metal substrates. Soon after in 1976, Pratt[4] performed similar research investigating the effects of unfocused $CO_2$ and CO lasers to

deactivate bacterial spores on metal and paper substrates. In this case, sterilisation was accomplished thermally, by rapidly heating the surface to temperatures exceeding 500 °C. However, a water treatment apparatus was not developed until 2002, when Baca[5] developed a near-point near-IR laser water treatment apparatus for use in dental hand-pieces. To date research on water sterilisation using a mid-IR laser technique is extremely limited and as such, warrants further, in-depth investigation.

### 2.1.4 Micro-organism models for water treatment

As each group, genus and species of micro-organism is different from the next, it would be ideal if a new treatment regime was tested on all the different types of micro-organisms which are potentially present within a water sample. Unfortunately, this is inefficient, time-consuming and expensive. A more economical approach uses model organisms from each group to test the treatment method.

#### 2.1.4.1 Bacterial models

Microbial indicators of water quality are commonly used within the water treatment industry.[6] According to the World Health Organisation (WHO), examinations for faecal indicator bacteria in drinking water remain the most sensitive and specific way of assessing the hygienic quality of water.[7] It is stated that the faecal indicator bacteria are universally present in high numbers in the faeces of humans and warm-blooded animals, readily detectable by simple methods, and should not grow in natural water. Furthermore, it is essential that their persistence in water and their degree of removal in water treatment are similar to those for waterborne pathogens. Bacteria which fall within this group include *E. coli*, other coliform bacteria, and to a lesser extent, faecal streptococci.[8]

The thermotolerant coliform bacteria are defined as a group of organisms able to ferment lactose at 44 – 45 °C and comprise the genus *Escherichia* as well as species of *Klebsiella*, *Enterobacter* and *Citrobacter*. Thermotolerant coliforms other than *E. coli*, may also originate from organically-enriched water such as industrial effluents or from decaying plant materials and soils. Regrowth of thermotolerant coliform

organisms within the distribution system is unlikely, unless sufficient bacterial nutrients are present, unsuitable materials are in contact with the treated water or water temperature is above 13 °C and no free residual chlorine is present.[7]

The term coliform bacteria refers to gram-negative, rod-shaped bacteria capable of growth in the presence of bile salts or other surface-active agents with similar growth-inhibiting properties which are able to ferment lactose at 35 – 37 °C with the production of acid, gas and aldehyde within the time-frame 24 – 48 hours.[9] They are also oxidase-negative and non-spore-forming and display β-galactosidase activity.

The *Enterobacter* genus, which was used in this investigation, is characterised by straight, Gram-negative rods, which are motile by peritrichous flagella (generally 4 – 6), facultatively anaerobic, and ferment glucose with the production of acid and gas.[9] Optimum growth range for these organisms is 20 – 37 °C depending on its source (20 – 30 °C for environmental isolates and 37 °C for clinical isolates). Interestingly, *E. cloacae* is less susceptible to chlorination than *E. coli*[10] and thus perhaps a more robust model organism to study.

#### 2.1.4.2 Protozoan models

Protozoan cysts, in particular organisms which cause giardiasis and cryptosporidiosis, constitute the most frequently identified cause of waterborne diseases in developed countries.[11] Due to repeated outbreaks of cryptosporidiosis in the United States of America and Europe, understanding the responses of pathogenic micro-organisms to disinfection has become an important issue. Many cyst-forming protozoa have been shown to be relatively resistant to conventional oxidative disinfection processes.[12] Several methods for direct detection[13] of protozoan cysts have been proposed; however, routine monitoring of cysts is limited because of its high cost and serious methodological limitations. This led to the investigation into the potential of surrogates to evaluate cyst removal/inactivation during drinking water sterilisation processes. In 1996, Rice et al.[14] and Coallier et al.[15] assessed the use of bacterial aerobic spores to monitor the efficiency of various water treatments and concluded that aerobic spores are a reliable and simple indicator of overall treatment performance and it is possible to correlate their removal with those of

protozoan cysts. More recently, Dow and co-workers[16] further investigated the impact of selected water quality parameters on the inactivation of *B. subtilis* endospores by monochloramine and ozone and formed similar conclusions to those previously presented.

Endospore-formers primarily consist of species within the genus *Bacillus*.[9,17] The endospores are ellipsoidal to spherical in shape and on average are approximately 0.50 × 1.0 × 2.0 µm. The structure of the endospore is much more complex than that of vegetative cells in that it has many layers. The outermost layer is the exosporium, a thin, delicate covering consisting of protein. Within this are the spore coats, composed of layers of spore-specific proteins. Below the spore coat is the cortex, which consists of loosely cross-linked peptidoglycan. Inside the cortex is the core or spore protoplast which contains the usual cell wall, cytoplasmic membrane, cytoplasm and nucleic acids etc. One compound characteristic of endospores, but not present in vegetative cells is dipicolinic acid, found in all endospores and located in the core.

Endospores are noted for their resistance to various environmental pressures, including heat, drying, radiation, chemical disinfectants and acidic conditions, and can remain dormant for extremely long periods of time.[17]

Previous studies of IR radiation effects using $CO_2$ lasers used *B. subtilis* endospores as the model organism, most likely due to the above resistance characteristics. Although disinfection was obtained, a metal substrate was used in an air medium. Therefore, due to this promising outcome, the efficacy of this technique for water disinfection will be explored here.

## 2.2 Aims and objectives

The aim of this section of work was to determine the efficiency of $CO_2$ IR laser irradiation for water disinfection purposes using *E. cloacae* and *B. subtilis* endospores as bacterial and protozoan model organisms, respectively.

Objectives:

1. To compare IR radiation disinfection of the bacterial and protozoan model organisms to UV water disinfection techniques.
2. To investigate the effect of the IR radiation on the structure and composition of the test micro-organisms using FTIR-ATR spectroscopy.
3. To apply chemometric data analysis techniques to further analyse FTIR spectra obtained in objective 2.
4. To apply the IR radiation disinfection procedure to various carbohydrates in solution.
5. To investigate structural changes which occur during objective 4, using FTIR-ATR and Raman spectroscopy.

## *2.3 Experimental*

### 2.3.1 Bacterial methodology

#### 2.3.1.1 Microbiological media and components

Microbiological media and additional high-grade chemical components were sourced from Oxoid, Difco and Sigma-Aldrich.

#### 2.3.1.2 Autoclaving

Sterilisation of bacteriological equipment and media was carried out using a bench-top autoclave (Exacta) at 121 °C for 15 minutes.

#### *2.3.1.3 Enterobacter cloacae*

##### *2.3.1.3.1 Growth of E. cloacae cells*

Fresh cells were grown for each day's experiments.

*E. cloacae* (QUT087) was grown on Nutrient Agar (NA) (Oxoid). A culture was prepared by subculturing from an existing culture held in the QUT culture collection. A pure colony grown on NA was removed using a pre-sterilised bacterial swab and

resuspended in sterile 4.5 $cm^3$ 0.9 % NaCl (saline) solution. A fresh sterile bacterial swab was then inserted into the resuspended culture solution and used to create a lawn inoculation onto sterile NA. Inoculated NA plates were incubated at 30 °C for 15 hours.

#### *2.3.1.3.2 Harvest and purification of E. cloacae cells*

A sterile bacterial swab was used to remove half of the cells from the incubated NA plates. Cells were resuspended in sterile 9.0 $cm^3$ 0.9 % NaCl solution and centrifuged (MSE Centaur 2) at 2000 rpm for 10 minutes. The supernatant was discarded and the cells resuspended in 9.0 $cm^3$ of sterile 0.9 % NaCl solution.

### 2.3.1.4 Bacillus subtilis endospores

#### *2.3.1.4.1 Growth of B. subtilis endospores*

*B. subtilis* (UQ40) was grown on R2A Agar (Oxoid) by subculturing from an existing culture held in the QUT culture collection. A pure colony grown on R2A was removed using a pre-sterilised bacterial swab and resuspended in sterile 4.5 $cm^3$ 0.9 % NaCl (saline) solution. A fresh sterile bacterial swab was then inserted into the resuspended culture solution and used to create a lawn inoculation onto sterile R2A. Inoculated R2A plates were incubated at 35 °C for 15 days.

#### *2.3.1.4.2 Harvest and purification of B. subtilis endospores*

Spores were harvested following a method comparable to one used by Facile and co-workers.[18] Spores were collected by swabbing the agar using a sterile moistened swab and suspending into sterile phosphate buffer. Centrifugation (Qualitron DW-41) at 3500 rpm for 30 minutes, removal of supernatant and resuspension in sterile phosphate buffer followed. The centrifugation and washout procedure was repeated. Suspension was placed hermetically into a waterbath at 75 °C for 15 minutes and then refrigerated at 4 °C. This suspension was kept for up to 1 year.

#### 2.3.1.5 Detection of bacterial cells

The detection of *E. cloacae* and *B. subtilis* cells/endospores before and during IR and UV experiments was performed by plating onto NA. *B. subtilis* samples were placed hermetically into a waterbath at 75 °C for 15 minutes before plating onto NA. Agar plates were poured in a sterile environment and stored at 4 °C until required. Plates were stored for a maximum of 48 hours before being discarded.

To obtain between 5 and 50 colony forming units (CFU's) per plate, a range of dilutions were prepared. Dilutions were carried out in sterile 0.9 % NaCl solution. Care was taken to ensure adequate mixing of the diluted solution before samples were removed. NA agar was incubated at 30 °C for 24 ± 2 hours before visual identification of the number of colonies present. Results are reported in CFU $cm^{-3}$.

Confirmatory tests were performed on a regular basis to ensure aseptic techniques were being used. This was to ensure that the bacterial culture examined was indeed a pure culture. Confirmatory tests for *E. cloacae* were performed using API-20E (Biomerieux) rapid testing kits. *B. subtilis* confirmatory tests included: the inability to grow anaerobically; butanediol fermentation via the Voges Proskauer test; and the reduction of nitrate to nitrite.[10]

### 2.3.2 IR laser reactor configuration

IR degradation studies were performed using a glass batch reactor (see Figure 2.2).

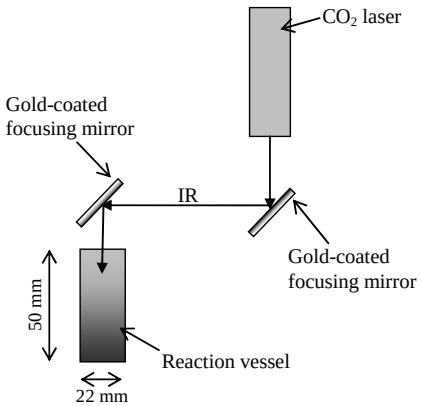


**Figure 2.2 Schematic representation of IR reactor instrumental set-up**

Reactor specifications are shown in Table 2.1. IR irradiation was provided using a Series 48 $CO_2$ laser (Synrad) emitting primarily at 10.6 µm. Maximum out-put at full power was determined to be approximately 27 W. The applied dose rate was 8.59 W $cm^{-2}$; however the IR radiation was only applied to a volume of 0.00628 $cm^3$, which constituted just $1/116^{th}$ of the total reactor volume (see section 2.3.3). Constant light intensity was obtained by switching on the laser 20 minutes prior to commencement of experiments. Two gold-coated mirrors were used to focus the IR beam from above the reaction vessel. Temperature within the reaction vessel was measured using a thermometer probe (HI 765) linked to a digital readout device (Hanna).

**Table 2.1 Specifications of IR Reactor**

| Dimensions of IR Reactor | |
|---|---|
| External diameter (mm) | 22 |
| Height (mm) | 50 |
| Reactor volume ($cm^3$) | 10.0 |

#### 2.3.2.1 IR treatment protocol for *E. cloacae* and *B. subtilis* endospores

The micro-organisms were tested using the IR laser reactor described above. 10 $cm^3$ of 18 MΩ cm Milli-Q water with ~ 1 x $10^9$ CFU $cm^{-3}$ of *E. cloacae* or 1 x $10^7$ CFU $cm^{-3}$ of *B. subtilis* endospores were added to the reaction vessel. The resulting suspension was kept in the dark at 4 °C prior to IR treatment to minimise alterations of the cellular constituents. IR treatment consisted of repeated cycles of 10 second laser pulses, followed by mixing for 5 seconds. IR irradiation was applied for a total of 0, 10, 30, 60, 120, 180 and 270 seconds. Immediately after IR exposure was completed, the cells were again kept in the dark at 4 °C until detection procedures were performed. Detection was performed as soon as practicable after completion of IR treatment (delay was no greater than 1 hour). Experiments were performed in duplicate.

### 2.3.3 Penetration depth of $CO_2$ laser beam into water

The depth of penetration of IR radiation into the test substrate is of great significance, as this determines how far into the substrate inactivation effects are expected to occur. According to Lambert-Bouguer law, the attenuation of the radiation power (K) is:[19]

$$K = \exp(-\alpha L_{abs}) \qquad \textbf{2.3}$$

where $L_{abs}$ is the absorbing-layer depth in centimetres; $\alpha = 4\pi\chi/\lambda$ is the Bouger linear absorption coefficient, and $\chi$ is the absorption index ( $\chi_{H_2O} = 0.091$ ).

From this it is calculated that the absorption depth of 10.6 μm $CO_2$ laser radiation is 64 μm, with 90% of the energy being absorbed in the layer the depth of ~ 20 μm.

### 2.3.4 UV reactor configuration

UV irradiation degradation studies were performed using a batch reactor configuration (see Figure 2.3). Reactor specifications are shown in Table 2.2.

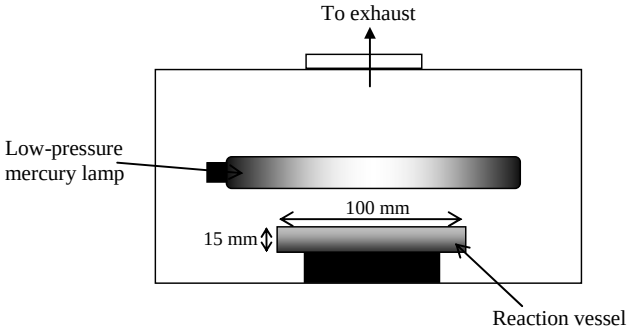


**Figure 2.3 Schematic representation cross-sectional view of UV reactor instrumental set-up**

The sample vessel was irradiated from above using a low-pressure mercury vapour lamp which primarily emits UVC radiation at 254 nm. The applied dose rate at the reaction vessel was calculated to be 5.4 mW $cm^{-2}$. The total irradiated surface area was 31.42 $cm^3$ which consisted of 1/30$^{th}$ of the total reactor volume. The lamp was encased in an opaque box, equipped with an extraction fan. Constant light intensity was obtained by switching on the lamps 20 minutes prior to experiment commencement.

**Table 2.2 Specifications of UV Reactor**

| Dimensions of UV Reactor | |
|---|---|
| Internal diameter (mm) | 100 |
| Height (mm) | 15 |
| Reactor volume ($cm^3$) | 10.0 |

#### 2.3.4.1 UVC treatment protocol for *E. cloacae* and *B. subtilis* endospores

The micro-organisms were tested using the UVC reactor described above. A volume of 10 $cm^3$ of 18 MΩ cm Milli-Q water with ~ 1 x $10^9$ CFU $cm^{-3}$ of *E. cloacae* or 1 x $10^7$ CFU $cm^{-3}$ of *B. subtilis* endospores was added to the reaction vessel. Light was excluded from the bacterial suspension at 4 °C until the start of the experiments to minimise alterations of the cellular constituents. Exposure times were 0, 10 , 30 60, and 120 seconds. Immediately after treatment was completed, the cells were again kept in the dark at 4 °C until detection procedures were performed. Detection was performed as soon as practicable after completion of UV treatment (delay was no greater than 1 hour). Experiments were performed in duplicate.

### 2.3.5 Determination of bacterial constituents using FTIR-ATR spectroscopy

IR spectra were obtained using a Nicolet 870 Nexus Fourier Transform IR spectrometer equipped with a DTGS TEC detector and an ATR objective (Nicolet Instrument Corp., Madison, WI). An Optical Path Difference (OPD) velocity of 0.6329 cm $s^{-1}$ was used. The aperture was set to 100, and a gain of 8 used. The ATR accessory was a Smart Endurance single reflection ATR accessory with a composite diamond internal reflection element (IRE) with a 0.75 mm sampling surface and a ZnSe focusing element. 0.2 $cm^3$ bacterial samples were rinsed using the harvest procedure outlined above (0.2 $cm^3$ rinse solution was added) and a 1.0 μL sample was then air-dried onto the diamond IRE for 50 minutes to remove excess water before spectral collection. Spectra were collected in the spectral range 4000 – 525 $cm^{-1}$ with 128 scans at a 4 $cm^{-1}$ resolution, and are corrected for the wavelength dependence of the ATR experiment. Sample spectra were collected in single beam mode then the IRE was cleaned immediately and a background spectrum collected.

This was to minimise $CO_2$ and water vapour effects. All spectra were normalised to the amide I band around 1650 $cm^{-1}$ In some figures spectra are offset for clarity. Chemometric analysis was performed using Grams32*AI* computer software package with the PSC-IE chemometric add-in (Galactic industries, Salem, NH).

### 2.3.6 Choice of model carbohydrates

To aid in the interpretation of the spectral differences observed within the carbohydrate region of the collected FTIR spectra, further investigation into the effect of IR radiation on model carbohydrates was undertaken. These model compounds needed to be inexpensive, water soluble, easily analysed, and present within the bacterial cell under standard conditions. The mono-saccharides: D-glucose; ribose; and NAG were chosen as they fulfil the above requirements, most importantly, they are found within *E. cloacae*.[10] A slightly more complex sugar, the di-saccharide, sucrose, was also chosen.

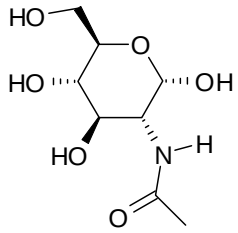


**Figure 2.4 Chemical structure of N-acetyl-D-glucosamine**

### 2.3.7 Determination of effect of laser IR treatment on chosen carbohydrates

D-glucose, NAG, D-ribose and sucrose were each suspended in 10 $cm^3$ of 18 MΩ cm Milli-Q water at a final concentration of 0.4 mol $dm^{-3}$. The resulting suspension was kept in the dark at 4 °C until experiments were commenced to minimise possible alterations. The IR laser was switched on 20 minutes prior to experiment commencement. Experiment was commenced upon exposure of the reaction vessel to the IR radiation via a series of mirrors. Treatment was performed in 10 second laser pulses, followed by mixing for 5 seconds. Total treatment times were 0, 10, 90,

and 270 seconds. Immediately after treatment was completed, the suspensions were again kept in the dark at 4 °C until detection procedures were performed.

### 2.3.8 Determination of selected carbohydrates and their break-down products by FTIR-ATR spectroscopy

IR spectra were obtained using a Nicolet 870 Nexus Fourier Transform IR spectrometer (using the same equipment parameters and spectral collection methods outlined in section 2.3.5).

A sample of 1.0 μL of carbohydrate was air-dried onto the diamond IRE for 50 minutes to remove excess water before spectral collection. Alternatively, sample solutions were dried under vacuum until a white powder was obtained. Powder samples were then transferred to the ATR crystal element and the pressure clamp engaged to ensure good sample contact with the ATR element. FTIR spectra were obtained immediately, as described above. Dried samples were stored at -15 °C as specified by manufacturer (Sigma-Aldrich).

### 2.3.9 Determination of selected carbohydrates and their breakdown products by Raman spectroscopy

Raman spectra were obtained of NAG samples which were dried under vacuum, using a Renishaw Raman Microscope System 3000 (Renishaw, Gloucestershire, UK) containing a Leica microscope equipped with a short working distance 50x objective lens and CCD detector (578 x 385 pixels). The spectra were excited by the 532 nm line of a frequency-doubled diode-pumped Nd-YAG laser. The spectral range was 4000 – 100 $cm^{-1}$ and two spectra were accumulated. Spectral information was extracted by means of spectral analysis software (GRAMS/32, Galactic Industries Corp., Salem, NH).

### 2.3.10 Statistical analysis

Where appropriate, the standard error, which shows the variation with an analytical or sampling method, was calculated and illustrated with the corresponding results.

Standard error is defined as the standard deviation of a sampling distribution with respect to size of sampling distribution. Standard error is dependant on sample size, as an increase in sample size tends to reduce the standard error. The formula for calculation of standard error of a mean[20] is ($\sigma_M$) shown Equation 2.4.

$$\sigma_M = \sigma / \sqrt{n} \qquad \textbf{2.4}$$

where σ is the standard deviation and n is the sample size.

## 2.4 Results and discussion

### 2.4.1 Model inactivation using IR and UV treatment

#### 2.4.1.1 *E. cloacae*

Figure 2.5 shows the percentage inactivation of *E. cloacae* during exposure to the IR laser and UV treatment regimes. In both experiments, a similar initial cell concentration was used (~ 1 x $10^9$ CFU $cm^{-3}$). Upon initial comparison of the two experiments, it can be immediately seen that cell inactivation occurred over a much shorter exposure time during UVC irradiation experiments compared with IR irradiation experiments. 95% inactivation of *E. cloacae* cells occurred after 10 seconds of UVC exposure, whereas 270 seconds of IR exposure was required for the same level of inactivation.

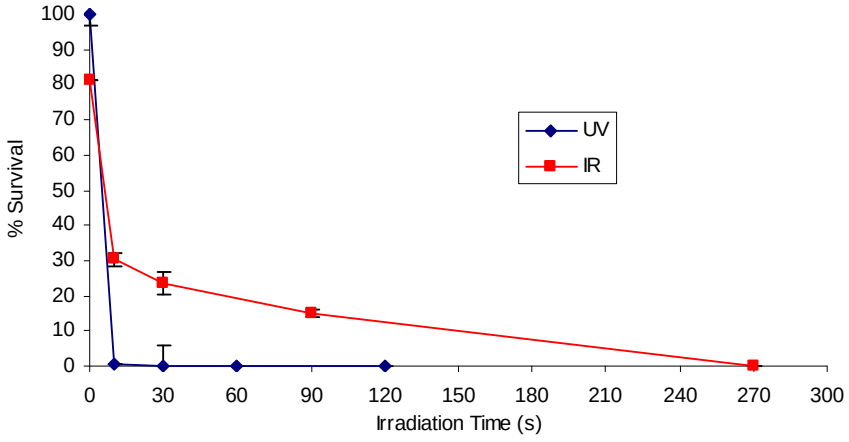


**Figure 2.5. Inactivation of *E. cloacae* as a function of time during IR laser and UVC treatment**

Both treatment methods follow pseudo-first order kinetics. Therefore, inactivation rates were calculated using Chick's law:[21]

$$\ln\left(\frac{N}{N_0}\right) = -kt \qquad \textbf{2.5}$$

where $N$ is the viable micro-organism concentration at time, $t$; $N_0$ is the initial viable micro-organism concentration; and $k$ is the inactivation rate of the micro-organism. The concentration of micro-organisms at each sampling point was ratioed against the initial concentration of micro-organisms, and the natural log of these points was plotted. The resulting slope of the line is the rate inactivation rate. Table 2.3 displays the inactivation rates for *E. cloacae* experiments during IR laser and UV treatment.

**Table 2.3 Inactivation rates for *E. cloacae* treated with IR laser and UV treatment**

| Treatment | % Inactivation after 60 s | Inactivation Rate (CFU $cm^{-3}$ $s^{-1}$ $10^{-2}$) | Inactivation Rate (CFU $cm^{-3}$ $kJ^{-1}$) | $R^2$ |
|---|---|---|---|---|
| IR (10.6 μm) | 81.83 | 2.51 | 0.0154 | 0.972 |
| UVC (254 nm) | 99.99 | 10.25 | 4.03 | 0.865 |

At first glance, the inactivation rate for UVC treatment appeared faster than that obtained using the IR laser (10.25 CFU $cm^{-3}$ $s^{-1}$ $10^{-2}$ compared to 2.51 CFU $cm^{-3}$ $s^{-1}$ $10^{-2}$, respectively). This was also true when the applied dosage was taken into account: UVC showed a rate of 4.03 CFU $cm^{-3}$ $kJ^{-1}$, compared with IR with a rate of 0.0154 CFU $cm^{-3}$ $kJ^{-1}$. Whilst the IR laser treatment system was found to be less effective than UVC irradiation, it did inactivate a significant proportion of *E. cloacae* cells within the water. To determine if the IR treatment method was suitable for water treatment purposes, it was then applied to the chosen parasite model organism.

### *2.4.1.2 B. subtilis*

Figure 2.6 shows the inactivation of *B. subtilis* endospores during exposure to the IR laser and UV treatment regimes. While the reduction profile during UV treatment was similar to that of *E. cloacae*, the cell inactivation rate was slower, due to the increased resistance of the endospores to UVC radiation. Despite this, 99.9% inactivation was attained after two minutes UV exposure. It was apparent that IR exposure did not cause any *B. subtilis* endospore inactivation and, in fact, resulted in an 270% increase in cell numbers after 60 seconds of IR exposure.

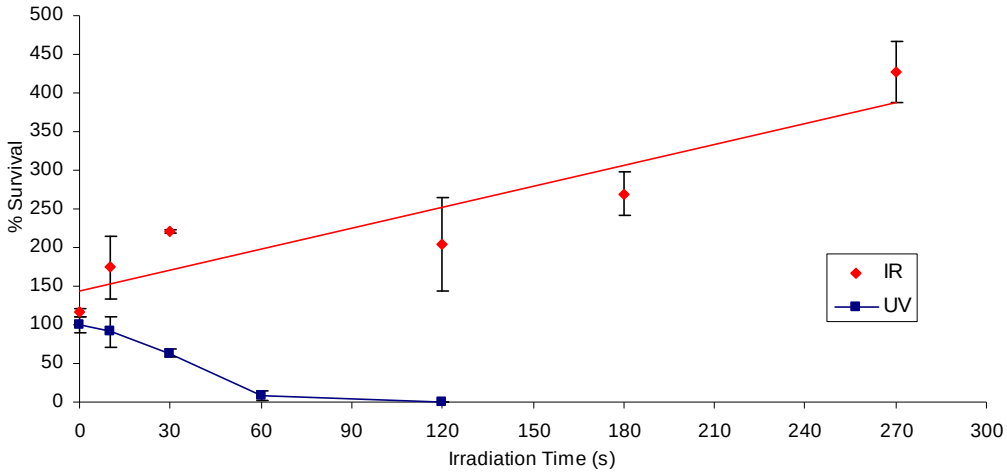


**Figure 2.6. Inactivation of *B. subtilis* endospores as a function of time during IR laser and UVC treatment**

Table 2.4 displays the inactivation rates calculated using Chick's Law. These highlight that IR treatment produced no inactivation of endospores and in fact, caused an increase in cell numbers during treatment at a rate of 2.96 x $10^{-3}$ CFU $cm^{-3}$ $kJ^{-1}$. UVC treatment produced a significant reduction in cell numbers at a rate of 2.40 CFU $cm^{-3}$ $kJ^{-1}$. In comparison to vegetative cells, the UVC treatment inactivation rate of endospores was approximately 40% lower than that obtained for vegetative cells, i.e. *E. cloacae*.

### 2.4.1.3 Control experimentation

No significant inactivation of *E. cloacae* was seen during the dark controls for UVC experiments where a similar bacterial suspension was kept in the dark; however, due

to an increased delay between experiment commencement and detection methods for IR experiments, a 32 % inactivation was observed in IR dark control. No inactivation occurred for *B. subtilis* endospore controls.

**Table 2.4 Inactivation rates for *B. subtilis* endospores treated with IR laser and UVC treatment**

| Treatment | % Inactivation after 60 s | Inactivation Rate (CFU $cm^{-3}$ $s^{-1}$ $10^{-3}$) | Inactivation Rate (CFU $cm^{-3}$ $kJ^{-1}$) | $R^2$ |
|---|---|---|---|---|
| IR (10.6 μm) | -272 | -4.8 | -0.00296 | 0.995 |
| UVC (254 nm) | 87.86 | 61.1 | 2.40 | 0.959 |

### 2.4.1.4 Effect of temperature

Effects due to temperature changes within the water medium appeared to occur during the IR laser experiments, due to localised heat transfer from the laser to the substrate. Recently, Baranov and co-workers[19] investigated modifications of biological polysaccharides and yeast cells in water droplets by $CO_2$ laser radiation. By measuring the water temperature in a heat-insulation collector it was discovered that an experimental increase in the temperature of a water droplet irradiated with 50 W of 10.6 μm radiation occurred. This was determined to be very small (2.75 K). However, the interaction time was only 8.7 ms.

Evidence for heat transfer in the present study is two-fold:

**1. Increase in *B. subtilis* endospore concentration during IR treatment.**

*B. subtilis* endospores have been shown to germinate upon heat treatment at temperatures greater than 50 °C.[22,23] Overall water sample temperatures increased to a maximum of 47.5 °C after 270 seconds of IR laser treatment, with localised boiling of the water surface layer occurring. This would result in significant germination of *B. subtilis* endospores as witnessed by a 400% increase in endospore numbers after IR laser treatment for 270 seconds. This is a result of the laser providing enough latent heat to commence germination. Conversion of endospores into vegetative cells occurs within 30 minutes of germination.[24] An unavoidable delay of one hour

occurred between IR treatment and commencement of detection techniques. Despite samples being kept at 4 °C during this time, it is probable that cellular processes were initiated, resulting in the increased viable counts.

**2. Localised heating of the *E. cloacae* samples.**

As stated above it is known that $CO_2$ lasers transfer heat to the substrate. The overall temperature of the sample solutions was recorded throughout experiments. Water sample temperatures ranged from 23 °C before treatment and increased to a maximum of 47.5 °C after 270 s of treatment. *E. cloacae*'s optimum temperature range is 30 – 37 °C.[10] Therefore, the sudden increase in temperature beyond *E. cloacae*'s optimum most likely resulted in the observed cell death. Initial reduction in cell concentration could be due to localised heating in the uppermost sample layer, thus inactivating any cells within this region. During mixing, this layer would be replenished with live cells, which would be killed in the next laser pulse. This process would continue, but as the overall temperature of the sample went beyond the optimum range, inactivation would occur more rapidly due to the higher temperature throughout the entire sample.

### 2.4.1.5 FTIR spectroscopy

Further analysis using FTIR-ATR spectroscopy was applied to understand the processes occurring during IR laser treatment. FTIR spectroscopy has proven a useful technique for investigating cellular changes within micro-organisms.[19] The *B. subtilis* endospore spectra showed only negligible changes after IR treatment. However, significant spectral changes occurred in the *E. cloacae* cells during IR treatment (see Figure 2.7 for representative spectra, normalised to Amide I band at 1640 $cm^{-1}$).

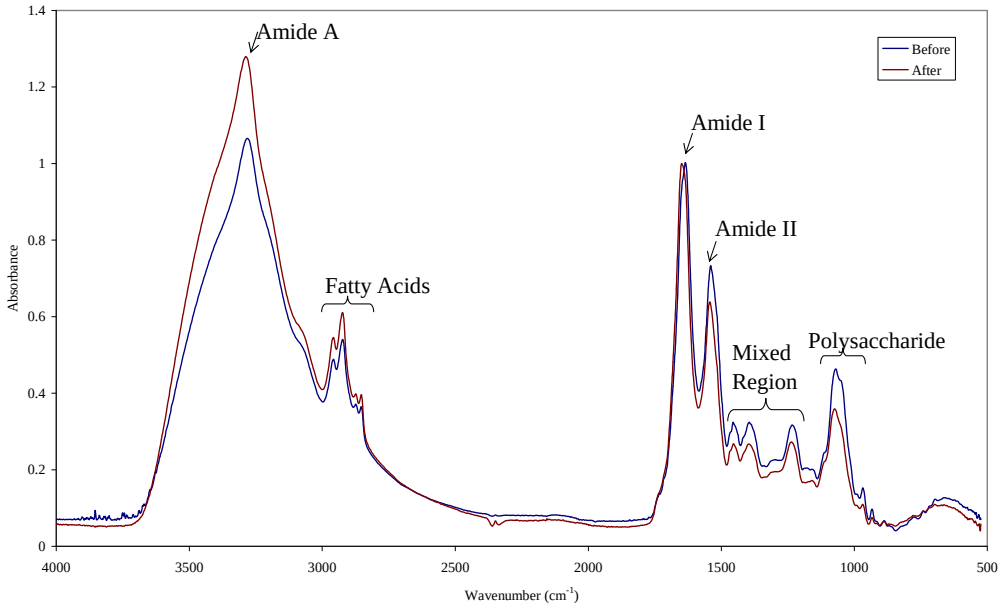


**Figure 2.7. FTIR-ATR-corrected, normalised absorbance spectra of *E. cloacae* before and after IR laser treatment for 30 s.**

The υ(NH) region (~3200 $cm^{-1}$) denoted as the amide A and the υ(CH) region (3000 – 2800 $cm^{-1}$) due to fatty acids and methane groups show increased spectral intensity after treatment.[25] Spectral variation within the region 1700 – 1500 $cm^{-1}$, dominated by amide vibrations also occurred. The bands within this region are due to υ(C=O) at ~1635 – 1700 $cm^{-1}$ denoted as amide I, and δ(NH) and υ(CN) at ~1550 – 1520 $cm^{-1}$ denoted as amide II. Assignment of these to protein confirmations revealed that proteins of the sample before treatment primarily consisted of β-turn and random coil configurations, while after treatment α-helices and random coils dominated.[26]

A reduction in spectral intensity after IR treatment occurred in the mixed region (1450 – 1220 $cm^{-1}$) and is composed of two minor groups of variations: proteins, free amino acids and polysaccharide vibrations (1450 – 1400 $cm^{-1}$); and the DNA/RNA and phospholipid vibrations (1250 – 1200 $cm^{-1}$). This region had the same peak profile after IR treatment, but again differences in intensities were seen, with smaller intensities seen after treatment which indicated changes to these compounds during treatment.

The polysaccharide region (1200 – 900 $cm^{-1}$) contains the υ(CO), υ(CH), δ(COH) and δ(COC) modes of vibration and showed the most significant differences during IR treatment. This was of interest as it is in this region that the laser emission will be directly absorbed. The increased carbohydrate content could be a consequence of the breakdown of long chain carbohydrate molecules into shorter chains, or single units, increasing the relative peak intensities within this region. Comparisons of the spectral intensity changes at 1066 $cm^{-1}$ with respect to treatment time revealed some interesting observations (see Figure 2.8). The optimum temperature range of *E. cloacae* is 30 – 37 °C,[10] and an increase in carbohydrate content was seen in those treated samples whose temperature was brought within this range. At this temperature, bacterial cells have the greatest ability to repair and renew damaged cellular components. As the IR laser used primarily emitted irradiation within the 'carbohydrate' region, it was more likely that the increased carbohydrate content seen within the bacterial samples was due the repair of damaged carbohydrates and increased production of new carbohydrate molecules.

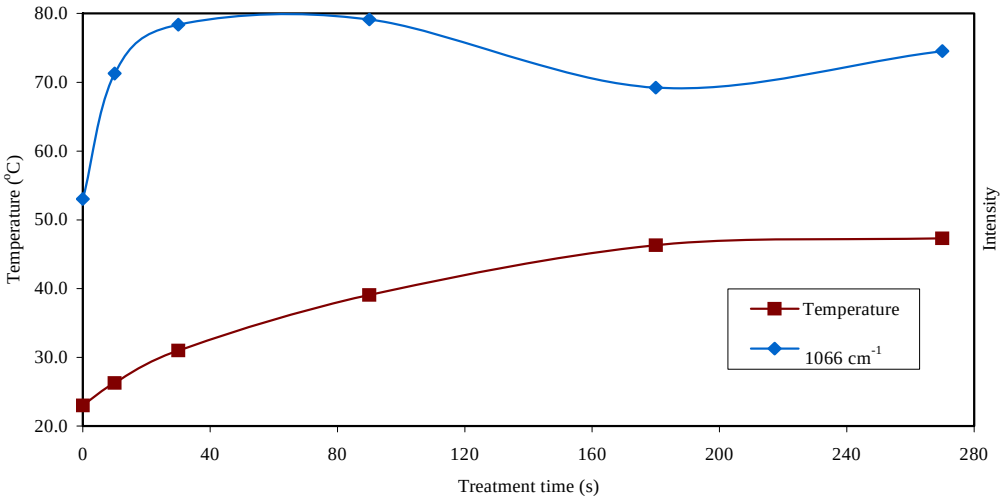


**Figure 2.8. Change in intensity of 1066 $cm^{-1}$ band (carbohydrate) of *E. cloacae* as a function of IR treatment time (-♦-); temperature change during IR treatment (-■-).**

### 2.4.1.6 Chemometric analysis

Chemometric analysis, specifically Principal Component Analysis (PCA) was applied to the FTIR-ATR spectra obtained for both *E. cloacae* and *B. subtilis* endospores using the IR laser and UV treatment regimes. The only experimental data

set which showed cluster separation was the IR laser treated *E. cloacae* samples; however, cluster overlap was still seen. The entire spectral region was investigated, but it was the region from 1760 – 850 $cm^{-1}$ that showed separation (Figure 2.9). Here, the before and after samples were separated by the PC 2 axis, predominately governed by positive factor loadings peaks (Figure 2.10) at 1625 $cm^{-1}$ (amide I), 1520 $cm^{-1}$ (amide II) and 1240 $cm^{-1}$ (phosphodiesters), and negative peaks at 1060 $cm^{-1}$ (carbohydrate) indicated that untreated samples contained more protein, due to the increased amide I and II intensities, and that treated samples possessed a higher carbohydrate content than their untreated counterparts.

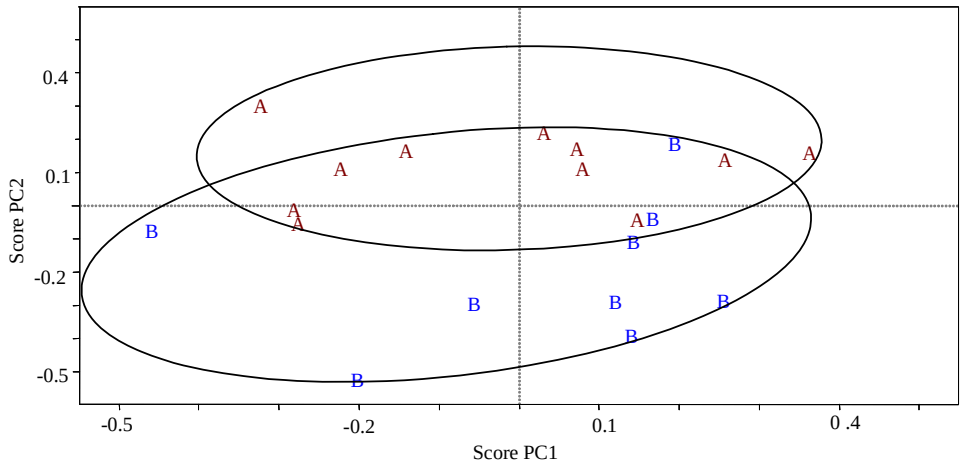


**Figure 2.9. PC1 vs PC2 Scores plot of *E. cloacae* IR treatment spectral data set from 1760 – 850 $cm^{-1}$.**

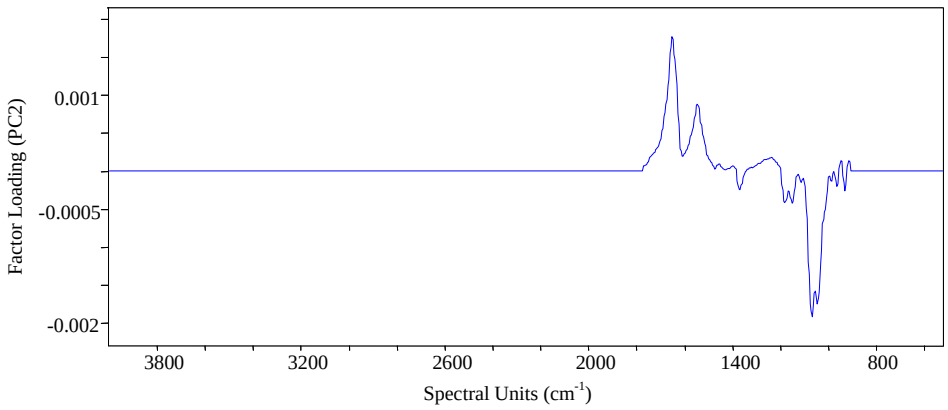


**Figure 2.10. PC2 Loadings plot of *E. cloacae* IR treatment spectral data set. NB. Only the region from 1760 – 850 $cm^{-1}$ was used for analysis shown in Figure 2.9.**

### 2.4.2 Effect of IR treatment on carbohydrates

To attempt to further understand the changes within the carbohydrate region of the *E. cloacae* FTIR spectra, the IR laser treatment system was applied to several model carbohydrates in water: D-glucose; sucrose; ribose; and NAG. *E. cloacae* contains D-glucose, ribose and NAG within its cellular constituents. FTIR spectroscopic analysis revealed no structural changes within D-glucose, sucrose and ribose after IR laser treatment; however, structural changes within NAG were apparent (Figure 2.11). See Table 2.5 for full peak assignments in the region 1650 – 750 $cm^{-1}$. The most notable differences were a general broadening of most bands, especially from 1200 – 880 $cm^{-1}$. This region is assigned to combinations of C-O and C-C stretching, as well as C-O-H and C-O-C bending vibrations of carbohydrates.[27] Determination of carbohydrate α- and β-conformers was possible using three bands: 915 $cm^{-1}$, attributed to asymmetrical ring vibrations; 840 or 890 $cm^{-1}$ to the $C_1$-H deformation mode; and the third at approximately 770 $cm^{-1}$, due to the symmetrical ring breathing vibration.[28]

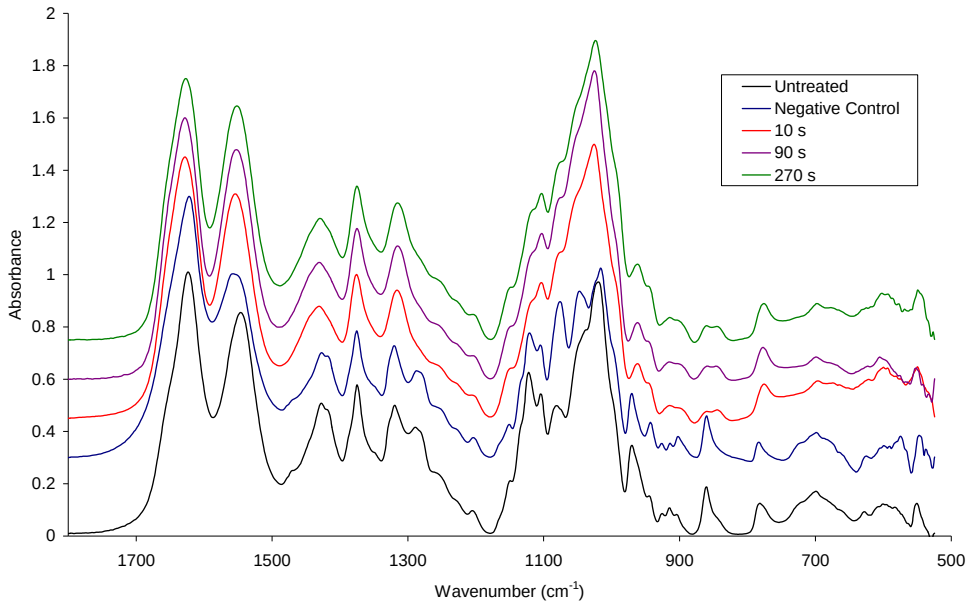


**Figure 2.11. FTIR-ATR spectra from 1800 – 500 $cm^{-1}$ collected from air-dried untreated NAG samples and after IR laser treatment for 0 (negative control), 10, 90 and 270 seconds. Spectra were normalised to the amide I band and are offset for clarity.**

The occurrence of a band at 842 $cm^{-1}$ in both treated and untreated samples was indicative of α-conformers present in both these sample types.[26] However, the relative intensity of this band was approximately half after IR laser treatment indicating some damage to the ring structure occurred. The presence of the anti-symmetrical ring vibration (untreated 912 $cm^{-1}$; treated 910 $cm^{-1}$) and the symmetrical ring breathing vibration (untreated 775 $cm^{-1}$; treated 771 $cm^{-1}$) indicated that laser irradiation did not result in permanent ring opening. The continued presence of the band at ~1623 $cm^{-1}$, predominately attributed to the υ(C=O), was indicative that the amide I group was still present after IR treatment, hence it appeared that the amine group was not cleaved during exposure to the IR laser treatment.

**Table 2.5 FTIR Peak positions and assignments of bands in the region 1800 – 500 $cm^{-1}$ for NAG**

| Band position ($cm^{-1}$) | Vibrational assignment | Reference |
|---|---|---|
| 1621 | Amide I: predominately ν(C=O) | [29] |
| 1542 | Amide II: predominately $\delta_{ip}$(N-H) | [29] |
| 1465 | δ($CH_2$) | [26] |
| 1423 | δ(C-H), δ(O-H) | [30] |
| 1415 | δ(C-H), δ(O-H) | [30] |
| 1373 | δ(C-H), δ(O-H) | [30] |
| 1360 | δ($C_6$-$H_2$) | [31] |
| 1319 | $CH_3$ | [30] |
| 1284 | $C_6$-OH, $C_1$-OH | [30] |
| 1253 | δ($C_1$-H) | [30] |
| 1224 | δ($CH_2$) | [30] |
| 1203 | - | - |
| 1145 | δ($C_1$-H) | [30] |
| 1120 | δ(C-O-H) | [30] |
| 1103 | - | - |
| 1076 | δ($C_1$-H), δ(C-O-H) | [30] |
| 1035 | ν(C-OH) | [27] |
| 1022 | δ(C-O-H) | [30] |
| 1000 | $CH_3$ | [30] |
| 968 | rocking (C-$CH_3$) | [26] |
| 943 | $_{as}$(*oop*) ring | [27] |
| 919 | $_{as}$(ring breathing) | [27] |
| 912 | δ($C_1$-H), δ(C-O-H) | [30] |
| 900 | CH | [30] |
| 860 | - | - |
| 842 | δ($C_1$-H) α conformer | [32] |
| 775 | $_{s}$(ring breathing) | [30] |

It was thought that the drying of the carbohydrate sample on the ATR crystal before FTIR sampling could have an effect on the NAG structure due to possible $O_2$ or thermal degradation. Therefore NAG samples which were untreated and those exposed to IR laser treatment were dried under vacuum and FTIR spectra collected immediately upon exposure to the ATR element. Figure 2.12 displays spectra collected from samples dried under vacuum. It was readily seen that no discernable changes were apparent after IR laser treatment. Therefore it was thought that changes observed in Figure 2.11 were due to partial $O_2$ degradation of the NAG samples due to drying in air prior to spectral collection.

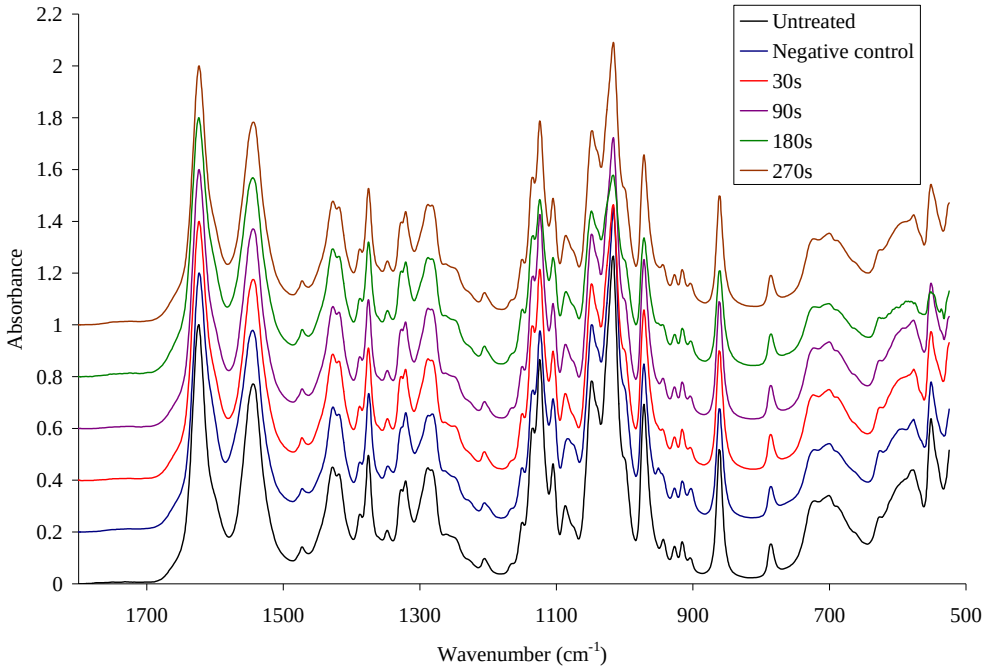


**Figure 2.12 FTIR-ATR spectra from 1800 – 500 $cm^{-1}$ collected from untreated NAG and after IR laser treatment for 0 (negative control), 30, 90, 180 and 270 seconds, dried under vacuum. Spectra were normalised to the amide I band and are offset for clarity.**

Raman spectra were also collected from NAG samples both before and after treatment, dried under vacuum. Figure 2.13 displays these spectra which were normalised to the band of maximum intensity (2940 $cm^{-1}$). Table 2.6 shows the collated vibrational peak positions and assignments for bands found within the Raman spectra. When examining the spectra in the region from 3500 – 3100 $cm^{-1}$,

notable differences were apparent after the samples were exposed to the IR laser treatment. A marked increase in the intensity of the 3460 $cm^{-1}$ band was seen. This band is assigned to anti-symmetric stretching vibrations of ($NH_2$) in primary amines.[26] Therefore, it was thought that the carbonyl group of the amide within NAG could have been cleaved during IR laser treatment. This was further supported by a notable decrease in intensity of the amide A. The spectral profile of the 3000 – 2550 $cm^{-1}$ region was similar before and after exposure, with only slight changes in intensities seen, leading to the conclusion that $CH_2$ and $CH_3$ groups were left largely unchanged during IR laser treatment.

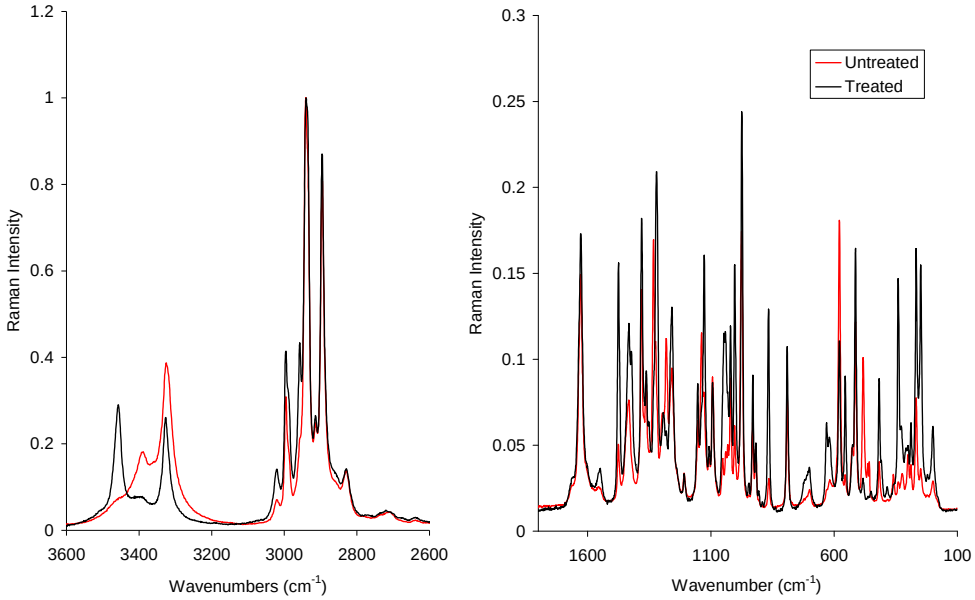


**Figure 2.13. Raman spectra of untreated NAG and NAG treated for 270 seconds. Note: Intensity scales differ.**

When examining the spectra in the region from 1800 – 200 $cm^{-1}$, in-depth analyses revealed significant differences. Firstly, the band at 1333 $cm^{-1}$ shifted to 1319 $cm^{-1}$ after IR treatment, while the peak at 1281 $cm^{-1}$ was also reduced during the IR laser treatment. The band at 1137 $cm^{-1}$ shifted to lower wavenumber at 1129 $cm^{-1}$. The bands which showed increases with IR laser treatment were 1475 $cm^{-1}$, 1431 $cm^{-1}$ (which split into two bands), 1137 $cm^{-1}$ and 866 $cm^{-1}$. These peaks were attributed to $C_6$-$H_2$, COH, CH, and OH bending vibrations, as well as ring breathing vibrations, respectively.

**Table 2.6 Raman peak positions and assignments of bands for NAG**

| Band position ($cm^{-1}$) | Vibrational assignment | Reference |
|---|---|---|
| 3460 | $\nu_{as}(NH_2)$ | [26] |
| 3400 | $\nu$(OH) | [33] |
| 3325 | Amide A | [33] |
| 3020 | $CH_3$ in acetyl amino | [33] |
| 2995 | $\nu(C_2\text{-}H)$ | [33] |
| 2940 | $\nu(C_6\text{-}H)$ | [33] |
| 2913 | $\nu(C_6\text{-}H)$ | [33] |
| 2895 | $\nu(C_6\text{-}H)$ | [33] |
| 2829 | $CH_3$ in acetyl amino | [33] |
| 1621 | Amide I: predominately $\nu$(C=O) | [33] |
| 1475 | $CH_3$, $C_6\text{-}H_2$, COH | [33] |
| 1432 | $\delta$(C-H), $\delta$(O-H) | [30] |
| 1381 | $CH_3$ | [33] |
| 1363 | $\delta$(C-H), $\delta$(O-H) | [33] |
| 1332 | $CH_3$, $C_6\text{-}H_2$, COH | [30,33] |
| 1280 | $C_6$-OH, COH | [33] |
| 1258 | $\delta(C_1\text{-}H)$ | [33] |
| 1208 | Ring Vibration | [33] |
| 1153 | CO, $\nu$(C-C), $\delta$(C-OH) | [30] |
| 1137 | Ring breathing | [33] |
| 1093 | $\nu$(C-C) | [33] |
| 1052 | $\delta(C_1\text{-}H)$ | [33] |
| 1020 | $\delta$(C-O-H) | [33] |
| 1003 | $CH_3$, $C_6\text{-}H_2$ | [33] |
| 975 | Ring breathing | [33] |
| 930 | $\nu_s$(C-O-C) | [33] |
| 917 | C1-H, $\delta(C_6\text{-}OH)$ | [30] |
| 864 | Ring breathing | [33] |
| 790 | Skeletal modes | [33] |
| 578 | Skeletal modes | [33] |
| 482 | Skeletal modes | [33] |
| 359 | Skeletal modes | [33] |
| 300 | Skeletal modes | [33] |
| 267 | Skeletal modes | [33] |

This was consistent with the hypothesis that the cleavage of the carbonyl group from the amide would produce a more stable ring system, leading to increased vibrational intensity of bands arising from the relevant functional groups. It was thought; however, that only a small portion of NAG within the sample solution was affected during the IR laser treatment process. As FTIR samples the bulk, while Raman samples were performed on single crystals, this could account for why no changes

were witnessed in the FTIR spectra, compared to Raman spectra. To further degrade NAG, increased treatment times would be necessary, however this would require further safety precautions due to the temperature increase of sample solutions experienced upon IR laser exposure. However, as the IR laser treatment method was proven to be ineffectual at inactivating the parasite model organism, this line of investigation was brought to a close.

## 2.5 Conclusions

$CO_2$ laser irradiation was tested for inactivation efficiency, and compared to that of UV irradiation, of *E. cloacae* and *B. subtilis* endospores in Milli-Q water.

In water, illumination by IR radiation produced 99.99 % inactivation of *E. cloacae* after 270 seconds exposure. In comparison, 30 seconds of UV irradiation produced the same level of inactivation. The inactivation rates for *E. cloacae*, for the IR treatment (0.01.54 CFU $cm^{-3}$ $kJ^{-1}$) was lower than that obtained using UVC irradiation (4.03 CFU $cm^{-3}$ $kJ^{-1}$).

Although 32% *E. cloacae* inactivation occurred in the IR control experiments, the rate of inactivation was significantly greater under IR experiments.

For *B. subtilis* endospores in water, UVC irradiation produced 99.9 % inactivation after 120 seconds. However, an increase in viable concentration occurred after the IR laser treatment. The inactivation rate for *B. subtilis* endospores during UV treatment (2.40 CFU $cm^{-3}$ $kJ^{-1}$), however the inactivation rate obtained during IR treatment was $-2.96 \times 10^{-3}$ CFU $cm^{-3}$ $kJ^{-1}$.

FTIR-ATR spectroscopy was used to further investigate cellular alterations occurring during IR treatment. The most dramatic change that occurred was within the polysaccharide region resulting in a marked increase in the spectral intensity. Chemometric analysis was applied to the FTIR-ATR spectra obtained for both *E. cloacae* and *B. subtilis* spores using the IR laser and UV treatment regimes. The only experimental data set which showed cluster separation was the IR laser treated *E. cloacae* samples; however, cluster overlap was still seen. It was determined that the

separation seen during IR treatment was due to a decrease in protein content and an increase in total polysaccharide. This highlighted visible changes identified during FTIR spectral analyses.

As the IR laser used emitted within the polysaccharide region it was possible that polysaccharides within the bacterial cell absorbed sufficient energy to be damaged, which in turn could cause the cell to replace the lost molecules. It is possible that excess production of these molecules occurred, or that the cells simply had not yet reached equilibrium.

The effect of IR laser irradiation on select carbohydrates found within bacterial cells was also investigated by FTIR-ATR and Raman spectroscopy. No discernable changes occurred in glucose, sucrose and ribose. FTIR spectra collected from NAG samples showed subtle changes in the amide I and II spectral regions and significant differences within the carbohydrate spectral region, but it was shown that these changes occurred due $O_2$ degradation while drying in air prior to FTIR sampling. FTIR spectra obtained after vacuum dehydration of the NAG samples showed no significant spectral differences after IR laser treatment. Raman spectra collected using the same vacuum drying method, did however show small changes within the amide group, leading to the hypothesis that the carbonyl group of the amide group may have been cleaved during IR laser treatment. These changes did not correlate with those seen within the FTIR spectra, but this may be due to comparisons of 'bulk' (FTIR) to finite (Raman) sampling methods. Increased IR laser treatment times may have resulted in noticeable changes within the FTIR spectra.

Although inactivation after exposure of *E. cloacae* to IR irradiation occurred, the IR laser treatment method failed to inactivate resistant micro-organisms, i.e. *B. subtilis* endospores, and therefore this method is not suitable for water disinfection purposes.

## 2.6 References


(1) *Infrared and Raman Spectroscopy*; Schrader, B., Ed.; VCH: New York, 1995.

(2) Svelto, O. *Principles of Lasers*; 4th ed.; Plenum Press: New York, 1998.

(3) Molin, G.; Ostilund, K. *Antonie van Leeuwenhoek* **1975**, *41*, 329-35.

(4) Pratt, G. W., Jr. In *U.S.*; (Massachusetts Institute of Technology, USA). USA, 1976, p 15.

(5) Baca, A. M. In *U.S. Pat. Appl. Publ.*; (USA). USA, 2002.

(6) Gleeson, C. *The coliform index of waterborne disease*; E & FN Spon: London, 1997.

(7) "Guidelines for Drinking Water Quality, 2nd edn, Vol. 1," World Health Organisation, 1993.

(8) Mara, D.; Horan, N. *Handbook of water and wastewater microbiology*; Academic Press: London, 2003.

(9) Madigan, M. T.; Martinko, J. M.; Parker, J. *Brock Biology of Microorganisms*; 9th ed.; Prentice-Hall, Inc.: New Jersey, 2000.

(10) *Bergey's Manual of Systematic Bacteriology*; Krieg, N.; Holt, J., Eds.; Williams and Wilkins: Baltimore, MD, 1984; 1.

(11) Craun, G. F.; Hubbs, S. A.; Frost, F.; Calderon, R. L.; Via, S. H. *J. Amer. Water Works Assoc.* **1998**, *90*, 81-91.

(12) Betancourt, W. Q.; Rose, J. B. *Vet. Parasit.* **2004**, *126*, 219-234.

(13) Jakubowski, W.; Boutros, S.; Fayer, R.; Ghiorse, W.; LeChevallier, M.; Rose, J. B.; Schaub, S.; Singh, A.; Stewart, M. *J. Amer. Water Works Assoc.* **1996**, *88*, 107-121.

(14) Rice, E. W.; Fox, K. R.; Miltner, R. J.; Lytle, D. A.; Johnson, C. H. *J. Amer. Water Works Assoc.* **1996**, *88*, 122-130.

(15) Coallier, J.; Prevost, M.; Babeau, M.; boulos, L.; Desjardins, R.; Duchesne, D. In *WQTC Proceedings*; American Water Works Association: Boston, M.A., 1996.

(16) Dow, S. M.; Barbeau, B.; von Gunten, U.; Chandrakanth, M.; Amy, G.; Hernandez, M. *Water Res.* **2006**, *40*, 373-382.

(17) Austin, J. W. *Curr. Challenges. Food Microbiol.* **2003**, 77-93.

(18) Facile, N.; Barbeau, B.; Prevost, M.; Koudjonou, B. *Water Res.* **2000**, *34*, 3238-3246.

(19) Baranov, G. A.; Belyaev, A. A.; Onikienko, S. B.; Smirnov, S. A.; Khukharev, V. V. *Quantum Electron.* **2005**, *35*, 867-872.

(20) Skoog, D. A.; West, D. M.; Holler, F. J. In *Fundamentals of analytical chemistry*; 5th ed.; Saunders College Publshing: New York, 1988.

(21) Haas, C. N.; Kaymak, B. *Water Res.* **2003**, *37*, 2980-2988.

(22) Alimova, A.; Katz, A.; Gottlieb, P.; Alfano, R. R. *Appl. Opt.* **2006**, *45*, 445-450.

(23) Daniels, J. K.; Caldwell, T. P.; Christensen, K. A.; Chumanov, G. *Anal. Chem.* **2006**, *78*, 1724-1729.

(24) *Bacterial spore formers : probiotics and emerging applications*; Ricca, E.; Henriques, A. O.; Cutting, S. M., Eds.; Horizon Bioscience: Wymondham, 2004.

(25) Ede, S. M.; Hafner, L. M.; Fredericks, P. M. *Appl. Spectrosc.* **2004**, *58*, 317-322.

(26) Parker, F. S. *Applications of Infrared, Raman, and Resonance Raman Spectroscopy in Biochemistry*, 1983.

(27) Brandenburg, K.; Seydel, U. In *Handbook of VIbrational Spectroscopy*; Chalmers, J., VSConsulting, Griffiths, P., Eds.; John Wiley & Sons Ltd: New York, 2002; 5.

(28) Tul'chinsky, V. M.; Zurabyan, S. E.; Asankozhoev, K. A.; Kogan, G. A.; Khorlin, A. Y. *Carbohydr. Res.* **1976**, *51*, 1-8.

(29) Smith, B. *Infrared spectral interpretation: a systematic approach*; CRC Press LLC: New York, 1999.

(30) Twardowski, J.; Anzenbacher, P. *Raman and IR spectroscopy in biology and biochemistry*; Ellis Horwood: New Yok, 1994.

(31) Proenca, L.; Lopes, M. I. S.; Fonseca, I.; Hahn, F.; Lamy, C. *Electrochim. Acta* **1998**, *44*, 1423-1430.

(32) Tul'chinskii, V. M.; Zurabyan, S. E.; Asankozhoev, K. A.; Kogan, G. A.; Khorlin, A. Y. *Carbohydr. Res.* **1976**, *51*, 1-8.

(33) She, C. Y.; Dinh, N. D.; Tu, A. T. *Biochim. Biophys. Acta* **1974**, *372*, 345-57.

# Chapter 3

## SUSPENSION AND IMMOBILISED PHOTOCATALYTIC STUDIES: BACTERICIDAL EFFECT OF MICROWAVE TREATED $TiO_2$ FOR DRINKING WATER TREATMENT

**Note to Reader**: The work described in this chapter was carried out by the candidate under the supervision of Dr Geoffrey Will and A. Prof. Louise Hafner. All colloidal dispersions utilised by the candidate were prepared by Aaron Matijasevich. Immobilised photocatalytic investigations using the stirred-tank reactor were performed by the candidate at the University of Ulster (NI), within the Northern Ireland Bioengineering Institute, under the supervision of Dr Tony Byrne.

## 3.1 Introduction

### 3.1.1 $TiO_2$ photocatalysis

In the search for a cost-effective solution to the removal of pollutants from water, advanced photocatalytic oxidation (APO) processes have been heavily investigated.[1] $TiO_2$ photocatalysis has been identified as a possible alternative/complementary drinking water treatment. A concerted effort to optimise $TiO_2$ properties during synthetic processing and its post-treatment is underway.[2-7] Properties of $TiO_2$ preparations, such as crystalline phase, grain size, surface area and volume can be controlled by synthetic procedures. Although the final properties of the $TiO_2$ are dependent upon its synthesis, it has been established that post-synthetic treatments such as hydrothermal processing have significant effects on crystallinity and grain size.[2,8] During hydrothermal processing, such as high-pressure convection heat treatment, Ostwald ripening occurs, where the growth of larger grains is favoured at the expense of smaller particles due to the higher solubility of the latter.[9] Recently, it has been ascertained that the same effect is generated by microwave irradiaton.[10-12]

Microwave irradiation is an effective alternative to convection hydrothermal treatment because it can accelerate reactions and may produce increased product quality and yield.[11] This technique, known as a high temperature activating method,[13] occurs via interactions between the high-frequency electromagnetic radiation and the permanent dipole moment of the liquid-phase molecules as well as intermediate metallic particles causing rapid localised-heating. This enables recrystallisation, while the bulk solution remains at a moderate temperature.

$TiO_2$ possesses high photocatalytic efficiency, non-toxicity, stability and can be obtained at a low cost.[14] Reactor performance is enhanced by dispersal of $TiO_2$ powder in the treatment solution, due to increased surface area for pollutant hydroxyl radical interaction. Photocatalytic slurry reactor configurations are simple and inexpensive to construct; however, a catalyst removal stage must be incorporated.[15-17]

### 3.1.2 Immobilisation of $TiO_2$

As a result of the inherent difficulties of post-treatment catalyst removal, immobilisation of the $TiO_2$ onto a solid support is gaining favour. Matthews[18,19] was one of the first researchers to develop a treatment system with the catalyst immobilised onto the reactor walls. Since then, numerous supporting substrates have been trialled, which include glass, stainless steel, titanium alloy, fibres and membranes.[20-22] Pozzo et al.[23] advocated that the substrate material should be chemically inert, have a high specific surface, favour strong surface chemical-physical bonding with the $TiO_2$ particles and be UV transparent. Glass is an example of such a material and has been extensively used in photocatalytic studies.[24,25]

Comparative studies between suspension and immobilised systems have been performed. Mills and Morris[26] reported that 0.102 mg $cm^{-2}$ glass-immobilised catalyst was twice as photoactive as 0.5 mg $dm^{-3}$ suspended catalyst. While Dijkstra et al.[27] reported comparable quantum yields for immobilised and suspended systems during the photodegradation of formic acid.

Adherence of the catalyst to the supporting substrate is also an important factor. Many immobilisation techniques have been investigated which include dip-coating,[28,29] electrophoretic deposition[4,30] and sol-gel related methods,[31,32] among others.

A major disadvantage of immobilised films is mass transfer limitations between the bulk of the liquid and the catalyst surface. Where mass transfer limitations exist, true comparisons between inter-laboratory experiments cannot be performed as one is only comparing the mass transfer in such reactors. Industrially, mass transfer limitations will cause lower reactor efficiencies and lower the accuracy of measured catalyst efficiencies and kinetics.[33]

### 3.1.3 Bactericidal effect of photocatalysis

$TiO_2$ with UV irradiation has been shown to exhibit strong bactericidal activity. The first evidence of this was presented in 1985, by Matsunaga *et al*[34] where they found that microbial cells in water could be killed via contact with a $TiO_2$-Pt catalyst

irradiated with near-UV light. Since then, research on $TiO_2$ photocatalytic destruction has been intensively conducted on a wide range of organisms including viruses, bacteria, fungi, algae and cancerous cells.[35-37] A number of authors have proposed mechanisms for the bactericidal action of $TiO_2$ photocatalysis which involve hydroxyl radicals.[36,38,39]

### 3.1.4 Photocatalytic disinfection of water from environmental sources

The majority of photocatalytic disinfection studies performed to date have used laboratory-cultured micro-organisms suspended in distilled water or saline solutions. However, several studies have used waters sourced from environmental origins including secondary effluents from wastewater treatment plants,[40,41] ponds[42] and streams.[43] Inactivation of a number of microbial species has been achieved including microbial indicator organisms. Investigations using environmental water samples compared to distilled water or saline solutions show slower reaction kinetics, but provide a more accurate perspective on the suitability of photocatalysis for drinking water treatment.

## *3.2 Rationale*

Following the development of colloidal $TiO_2$ via a microwave treatment method at QUT, rigorous testing of its bactericidal activity was needed to determine its efficacy as a novel photocatalyst. Comparisons of its photocatalytic efficiency would be made with the commercially available Degussa P25, previously shown to be a highly efficient and therefore popular photocatalyst, as well as $TiO_2$ manufactured using the convection hydrothermal treatment method, known to produce colloids characteristically similar to the microwave-treated $TiO_2$.

## *3.3 Aims and Objectives*

The two aims of this work were: to investigate the inactivation of bacterial indicator organisms in water using photocatalytic $TiO_2$ slurry and immobilised reactors; and to compare and contrast the efficiency of $TiO_2$ catalysts manufactured using a

microwave-treatment method to the commercially available Degussa P25 and $TiO_2$ manufactured via convectional hydrothermal treatment.

Objectives:

1. To characterise $TiO_2$ catalysts using Brunauer-Emmett-Teller (BET), X-ray diffraction (XRD) and X-ray photoelectron spectroscopy (XPS) analyses.
2. To perform preliminary investigations into the bactericidal effect of microwave-treated $TiO_2$ on a bacterial indicator micro-organism in a slurry reactor, and compare this to a commercially available catalyst and $TiO_2$ made using conventional means.
3. To immobilise the $TiO_2$ catalysts onto a suitable substrate.
4. To investigate the immobilised microwave-treated $TiO_2$ photodegradation efficiency using a model organic pollutant and to compare this to a commercially available catalyst and $TiO_2$ made using convectional means.
5. To investigate the effect of shortening the UV wavelength on photodegradation efficiencies of the chosen immobilised $TiO_2$ catalysts when tested using the model organic pollutant.
6. To investigate the bactericidal effects of immobilised microwave-treated $TiO_2$ on bacterial indicator micro-organisms suspended in river water compared to a commercially available catalyst and $TiO_2$ made using conventional means.

## *3.4 Experimental*

### 3.4.1 Chemicals

All chemicals used were of general purpose or high purity grade and unless otherwise stated were supplied by Sigma-Aldrich.

### 3.4.2 X-ray photoelectron spectroscopy

XPS spectra were obtained using a Kratos AXIS Ultra DLD spectrometer with Al (mono) X-ray source set to 5 mA 15 kV, 75 W power output and a charge neutralisation of 2.6 eV. Samples were prepared by pressing powdered $TiO_2$ into a 0.3 x 10 mm disc using a die cast. Survey scans were carried out from 1300 – 0 eV

with a step size of 0.5 eV and dwell time of 100 ms. Lens setting was on Hybrid mode with a sample area of 300 x 700 μm and a pass energy of 160 eV. Analysis was carried out using Vision Processing, version 2.25 (Kratos).

### 3.4.3 X-Ray diffraction

XRD spectra were collected using a Bruker D8 Discovery diffractometer with a CuKα 1.54 Å source with power set at 40 mA:40 kV. The tube angle was set at 0.75° with a parallel snout tube aperture with 0.8 mm tube slit used. Powdered samples were pressed into a 0.3 x 10 mm disc using a dye cast. Detector scans were collected using a speed of 60 seconds per step with a fixed increment of 0.04° over the range 10 – 80 2θ. Diffraction scans were aquired using Bruker AXS DiffracPlus XRD Commander version 2.3.1 software and analysed using Bruker AXS EVA2 version 9.0.0.2 computer software.

### 3.4.4 Brunauer-Emmett-Teller

Isothermal character, pore volume and pore size was determined by an 80 point isotherm using an Autosorb1 (Quantachrome) gas adsorption analyser. Neat powder samples were dried at 100 °C under a constant flow of UHP $N_2$ on an Autosorb flow preparation degasser for 18 hours. Data collection and analysis was performed using PC control with Quantachrome AS1 (Win Version 1.50) computer software. Pore volume and pore size were calculated by fitting the collected BET isotherm using the Baret-Joyner-Halenda (BJH) algorithm.

### 3.4.5 pH and temperature measurements

pH was measured using a pH electrode (Gelpas BDH) linked to a digital pH meter (Philips 9404). Temperature was measured using a thermometer probe (HI 765) linked to a digital readout device (Hanna).

### 3.4.6 Water sources

The river water used was obtained from the treatment plant inlet at the Dorisland water treatment works (Northern Ireland). Analysis of the typical chemical content of the river water is shown in Table 3.1. River water was sterilised by two autoclave cycles (bench-top autoclave: Exacta) at 100 °C for 30 minutes. Water was cooled between each cycle. All other water used was distilled water. Distilled water used for microbiological purposes was sterilised at 121 °C for 15 minutes. Ultraviolet-visible (UV-Vis) spectra of distilled and 0.45 μm filtered, sterilised river water used within this chapter are shown in Figure 3.1.

**Table 3.1 Chemical content of water sourced from Dorisland water treatment plant**

| pH | True colour | Aluminium (ppm) | Turbidity | Manganese (ppm) | Total organic carbon (ppm) |
|---|---|---|---|---|---|
| 8.46 | 16.85 | 0.00 | 1.21 | 0.02 | 7 |

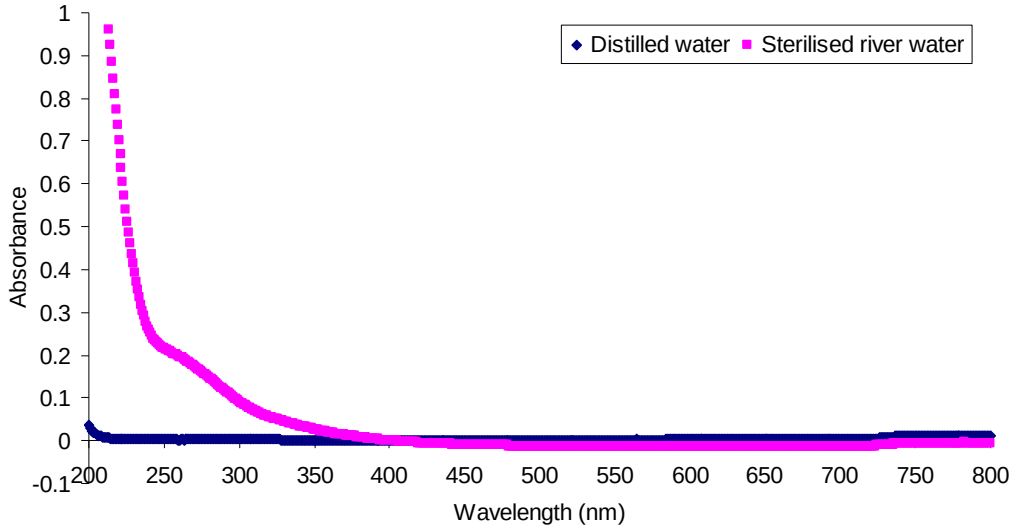


**Figure 3.1 UV-Vis spectra of distilled water and filtered, sterilised river water collected Dorisland water treatment plant**

### 3.4.7 Stabilised $TiO_2$ colloidal preparation

Degussa P25 $TiO_2$ powder (TITANDIOXID P25, D-60287, PI-52342) was purchased from Degussa AG (Frankfurt). Degussa P25 consists of 25:75 rutile:anatase crystal form, with a purity of 99.9%.

Stable colloidal $TiO_2$ solutions were prepared via the hydrolysis of titanium (IV) isopropoxide following a procedure adapted from O'Regan et al.[44] Briefly, 20.0 $cm^3$ of isopropanol and 125 $cm^3$ of titanium isopropoxide were accurately measured into a dropping funnel. The resulting solution was slowly added over 10 minutes to 750 $cm^3$ of ultra pure deionised water (18 mΩ cm) with vigorous stirring. 5.30 $cm^3$ of 69% nitric acid was then added as a peptising agent. The solution was heated to 80 °C by immersion into a waterbath and stirred continuously for 8 hours. Approximately 700 $cm^3$ of white colloidal solution remained (pH 1.2, yield 99% based on $TiO_2$ weight) and was stored in a dark glass vessel.

Convective hydrothermally treated $TiO_2$ colloids (HT-treated $TiO_2$) were prepared following a previously described procedure[45] and has been reported by Wilson et al.[46] Briefly, 100 $cm^3$ of $TiO_2$ colloid prepared as above was placed into a 200 $cm^3$ Pyrex glass-lined stainless steel autoclave Parr-bomb and treated at 145 °C for 15 hours in a convection oven (S.E.M. 1300 W), and then allowed to cool to room temperature for 2 hours. The product was allowed to stand for 24 hours.

Microwave treated colloids (MW-treated $TiO_2$) were prepared using a procedure developed by Wilson et al.[46] 30 $cm^3$ of $TiO_2$ colloid prepared as above was placed into a Teflon-lined digestion vessel. A microwave oven (MSD-2000, C.E.M. 630 ± 50 W) was set to 80% power and the pressure ramped from atmosphere to the desired pressure of 60 p.s.i., which equates to 145 °C. The samples were held at the desired pressure for 1 hour and then allowed to cool to room temperature for 2 hours. The product was allowed to stand for 24 hours.

HT- and MW-treated $TiO_2$ colloidal suspensions were then dehydrated at 80 °C for 3 hours.

## 3.4.8 $TiO_2$ immobilisation

#### *3.4.8.1.1 Substrate preparation*

Borosilicate glass (Borofloat) provided by Instrument Glasses (UK) was cut into 110 x 110 mm pieces. Before coating, the glass substrates were cleaned via ultrasonic treatment in warm water containing Decon detergent for 30 minutes, followed by multiple rinses with distilled water and further sonicated in distilled water for 15 minutes and dried at 120 °C. Substrates were accurately weighed prior to coating and stored in sealed containers.

#### *3.4.8.1.2 Dip-coating of substrates with $TiO_2$*

$TiO_2$ powders (Degussa P25, MW-treated $TiO_2$; and HT-treated $TiO_2$) were immobilised by dip-coating from a 5% w/v $TiO_2$/methanol suspension onto borosilicate glass. The withdrawal rate was maintained at 4.3 mm $s^{-1}$. The glass plates were dipped into the $TiO_2$ suspension using an 'Instron' machine (M1000) and dried after each dip using an IR lamp. This procedure was repeated approximately 20 times, until a final catalyst loading of ~ 1.0 mg $cm^{-2}$ was obtained using gravimetric methods. One side of the coated plate was cleaned to remove $TiO_2$ before accurate calculation of the final catalyst loading.

Degussa P25 coated the glass without streaking or cracking; however, it was found that dip-coating was unsuitable for the MW-treated and HT-treated $TiO_2$. The resulting films were extremely uneven and had a cracked, crystalline appearance.

#### *3.4.8.1.3 Spray-coating of substrates with $TiO_2$*

$TiO_2$ powders were also immobilised by spray-coating from a 5% w/v $TiO_2$/methanol suspension onto borosilicate glass. A thin film of $TiO_2$ was sprayed onto the substrate using a spray-coater (Paasche EZ-Starter) with air propellant. The spray-coating device was held 50 cm from the substrate and careful control of the horizontal movement of the device was maintained to ensure even coverage of the

substrate. The glass plates were alternatively sprayed with the $TiO_2$ suspension and dried after each spray-coat using an IR lamp. This procedure was repeated until a final catalyst loading of ~ 1.0 mg $cm^{-2}$ was obtained, via accurate calculation using gravimetric methods.

For each of the catalyst types used, the spray-coated films were of excellent quality, with a smooth and even appearance. Therefore for expediency, only films produced using spray-coating immobilisation were used in the photocatalytic experiments.

#### *3.4.8.1.4 Annealing of coated substrates*

The coated substrates were placed onto clean petri dishes and annealed in air in a preheated muffle furnace (Carbolite, Lenton Thermal Designs) at 400 °C for 60 minutes with a 5 °C $min^{-1}$ ramp to enable particle adhesion and cohesion. The substrates were cooled to room temperature and covered to prevent contamination. Heating and cooling was performed using controlled temperature ramping to prevent film cracking.

### 3.4.9 Diffuse-transmission measurements of immobilised $TiO_2$

Diffuse transmission measurements were recorded using a Spectra-Rad UV-Vis spectrometer (Yobin Yvon, Gemini 180) with integrating sphere attachment. The integrating sphere attachment catches all scattered light, whether direct or diffuse. The $TiO_2$-coated glass plates were placed into the path of the UV irradiation with the coated surface facing the inlet aperture of the integrating sphere. Each plate was irradiated from below with UVA or UVB irradiation. The % transmission of UV and visible irradiation through the coated glass plates was measured from 200 – 800 nm and recorded using Spectra-Rad for Windows v4.40.

### 3.4.10 Photocatalytic reactors

A slurry reactor and stirred-tank reactor were used for the photocatalytic treatment using distilled water. The latter was also used for the photocatalytic treatment of river water.

### 3.4.10.1 Slurry reactor

Photodegradation studies with a $TiO_2$ suspension were performed using a glass batch photoreactor consisting of an outer tube with ports for air supply and gas evolution, and an inner tube to house the UV light source. A cross-sectional schematic of the photoreactor layout is shown in Figure 3.2 with corresponding dimensions shown in Table 3.2.

**Table 3.2 Specifications of Slurry reactor**

| Dimensions of Slurry reactor | |
|---|---|
| Internal diameter of outer tube (cm) | 6.02 |
| External diameter of inner tube (cm) | 4.79 |
| Height (from sintered glass frit to base of gas outlet) (cm) | 46.7 |
| Reactor volume ($cm^3$) | 487.7 |
| Sample height (from reactor base) (cm) | 23.0 |

The inner tube was securely fitted into the outer tube using a ground glass joint situated above the gas evolution and sample ports. This resulted in a cross-sectional distance of 6.1 mm. The irradiation source used was a Sylvania Blacklight (F15W/350BL_T8) UV spectrum double-ended fluorescent tube. This irradiation source emits a stable output over a broad band (± 20 nm) centred at 351 nm. Constant light intensity was obtained by switching on the lamps 20 minutes prior to commencement of experiments. Air surrounding the reactor was removed using an extractor fan positioned above the reactor set-up.

The $TiO_2$ catalyst was used in the form of a sol produced from finely ground catalyst suspended in distilled water.

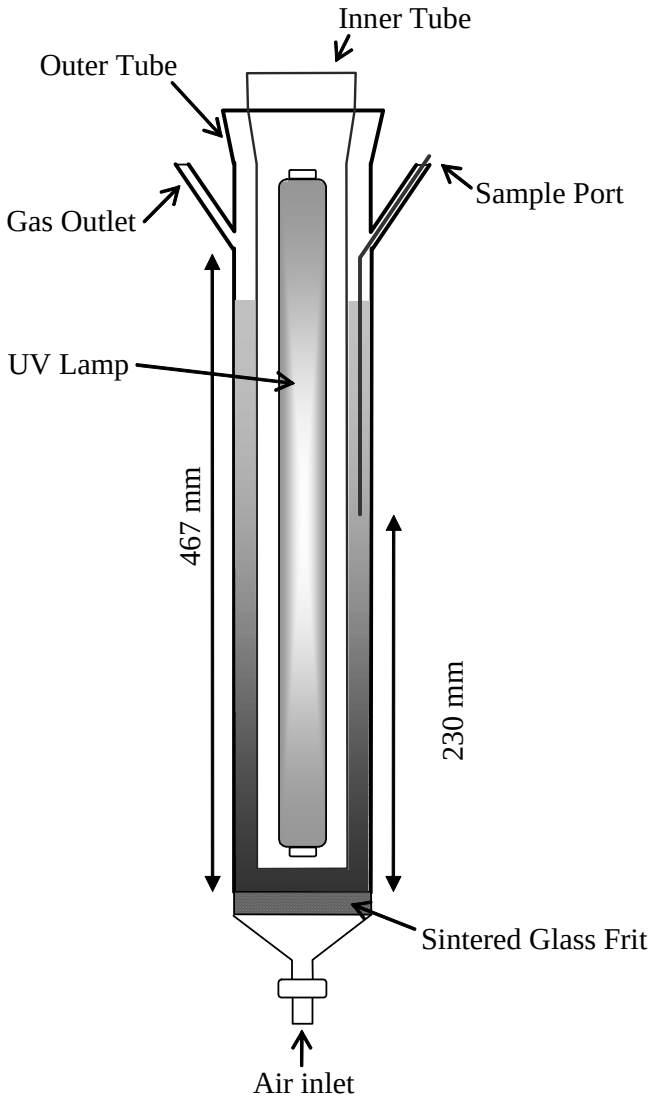


**Figure 3.2 Schematic representation of cross-sectional view of photocatalytic slurry reactor**

A sintered glass frit was inserted into the gas inlet port which operated as a semipermeable membrane that allowed a small, known amount of air to sparge into, and distribute evenly throughout, the sample chamber. The reasons for this were two-fold. First, the $TiO_2$ catalyst will settle to the bottom of the reaction vessel and air bubbling through the sample chamber from the base ensures continuous and even mixing of the reaction solution. Second, the $O_2$ acts as an electron scavenger and prevents recombination of the electron and hole in the semiconductor particle.[16]

3 mm internal diameter silicone tubing remained at a constant position within the sampling port to ensure sampling throughout the entire experiment occurred from a constant depth within the reservoir. Samples were removed for analysis via a disposable syringe.

In a typical experiment using the slurry reactor, 300 $cm^3$ of distilled water containing 0.15 g $dm^{-3}$ $TiO_2$ catalyst and an appropriate concentration of test micro-organism was placed into the slurry reactor, which then was sparged with air in the dark for 15 minutes, to allow equilibrium to occur. (Note: the UV lamp was allowed to warm up for 20 minutes prior to commencing the experiment.) The reactor was then exposed to UV irradiation and a 1.5 $cm^3$ sample was taken immediately (t=0 minutes) and subsequent samples were collected at 3 minute intervals for a total of 30 minutes, as well as after 60 and 120 minutes of exposure.

### 3.4.10.2 Stirred-tank reactor

The stirred-tank reactor used was developed by McMurray and co-workers,[47] and is shown in Figure 3.3. The $TiO_2$ catalyst was immobilised onto a 110 x 110 mm borosilicate glass plate. The $TiO_2$ catalyst plate was secured to the bottom of the water-jacketed vessel creating a 200 $cm^3$ reservoir.

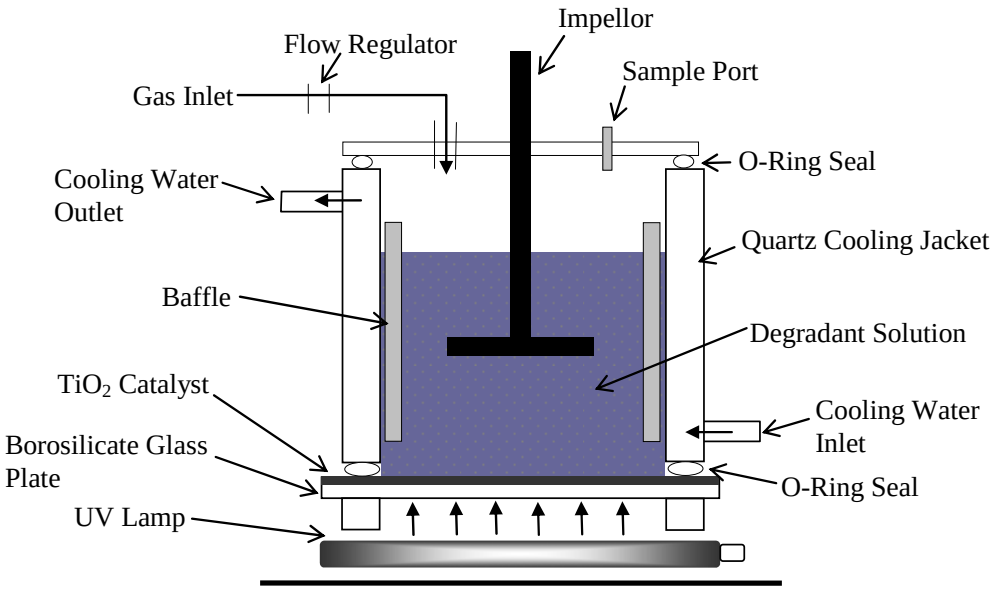


**Figure 3.3 Schematic representation of cross-sectional view of stirred-tank reactor**

**Table 3.3 Specifications of stirred-tank reactor**

| Dimensions of Stirred-tank reactor | |
|---|---|
| Outer diameter (including cooling jacket) (cm) | 10 |
| Inner diameter (excluding cooling jacket) (cm) | 8.5 |
| Height (cm) | 9.5 |
| Reactor volume ($cm^3$) | 540 |
| Irradiated catalyst Area ($cm^2$) | 56.7 |
| Distance to Impeller (from reactor base) (cm) | 4.0 |

The catalyst was irradiated from below using two Philips compact single-ended low-pressure mercury vapour fluorescent lamps (PL-S 9W/10UV-A or 12UV-B) placed at a distance of 2.5 cm away from the bottom of the catalyst-coated support. The UVA lamps exhibited a stable out-put between 350 – 400 nm with peak emission at 365 nm. The UVB lamps were used in order to compare spectral differences in the photocatalytic degradation rates; and exhibited stable output between 265 – 380 nm, with peak emission at 310 nm. See Figure 3.4 for spectral outputs of the UVA and UVB lamps. The lamps were encased in an opaque box, which contained a cooling fan. Constant light intensity was obtained by switching on the lamps 20 minutes prior to experiment commencement. The light flux irradiance entering the stirred-tank reactor was determined by McMurray and co-workers by actinometry to be 3.28 x $10^{-8}$ Einstein $cm^{-2}$ $s^{-1}$.[48]

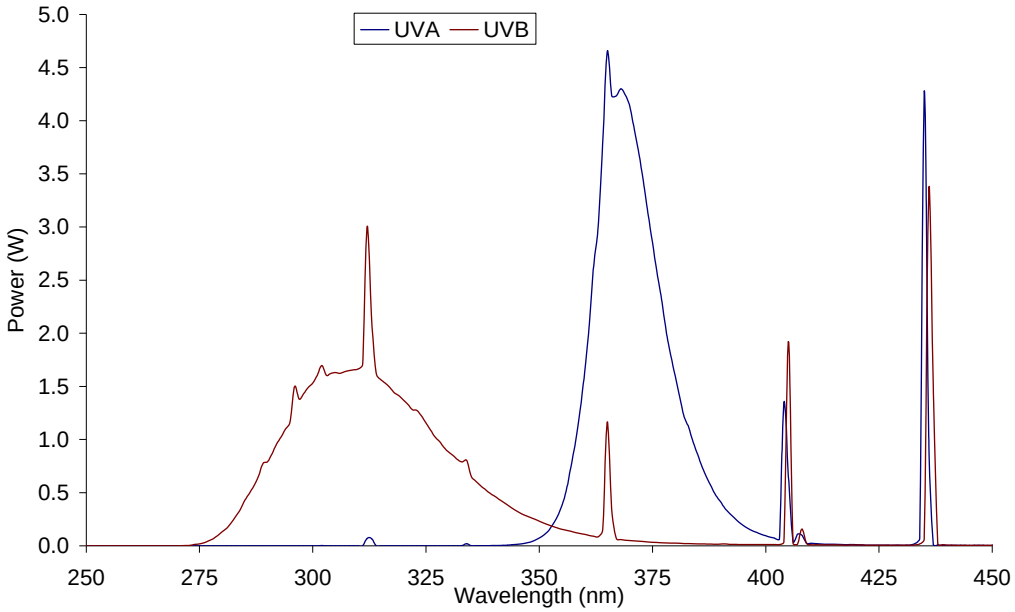


**Figure 3.4 Spectral response for PL-S9W/10UV-A (UVA); and PL-S9W/12UV-B (UVB) lamps**

Turbulent mixing to minimise mass transfer limitations was provided within the reactor via a stainless steel impellor controlled by a homogenator motor (Camlab Ltd; rotational speed 0 – 2500 rpm), and stainless steel baffle. Impellor rotational speed was calibrated using an optical tachometer (Graham & White Instruments M20). Two strips of reflective tape were placed on opposite sides of the barrel that holds the impellor shaft and by holding the tachometer parallel to the barrel, the speed of the impellor was determined.

Oxygen (99.997% purity, supplied by BOC) or air was sparged into the reactor during experiments through a flow regulator (Meterate) at rates of 900 $cm^3\ min^{-1}$ and 450 $cm^3\ min^{-1}$ respectively, to remove oxygen limitations from the system.[16]

The glass walls of the reactor consisted of a cooling jacket connected to a thermostatic circulator (Grant FH5 and FC25 cooling system) which maintained a temperature of 20 ± 2 °C throughout the experiments. Samples were removed for analysis via a sample port using a glass syringe.

In a typical experiment using the stirred-tank reactor when investigating oxalic acid degradation, 200 $cm^3$ of oxalic acid (5.0 x $10^{-3}$ mol $dm^{-3}$) was added to the reactor. The UV lamps were allowed to warm up for 20 minutes, and the reactor was sparged with $O_2$ in the dark for 15 minutes, with the impellor rotation speed set at 1700 rpm. The reactor was then exposed to the UV light with the headspace being purged with $O_2$ at a rate of 900 $cm^3$ $min^{-1}$ throughout the experiment. A 1.5 $cm^3$ sample was taken immediately (t=0 min) and every 15 minutes thereafter, usually for 180 minutes. Control experiments were performed by McMurray[47] which showed no significant reduction in the absence of $TiO_2$, UV light or both (greatest reduction over 120 minutes occurred using UV only: 6% loss).

In a typical experiment using the stirred-tank reactor and *E.coli*, a similar protocol to the oxalic acid was used except the reactor was sparged with air at a rate of 400 $cm^3$ $min^{-1}$ throughout the experiment. A 1.5 $cm^3$ sample was taken immediately (t = 0 min) and every 30 minutes thereafter, usually for 300 minutes.

Experiments to determine the effect of UV illuminating the reactor whilst still using the immobilised $TiO_2$ plates were devised. These experiments use the same reactor conditions previously described; the only difference being a clean glass plate was inserted between the immobilised $TiO_2$ plate and the O-ring seal at the base of the quartz cooling jacket. As the $TiO_2$ film is effectively sandwiched between two glass plates, experiments of this type are henceforth labelled as ‘sandwich experiments’, abbreviated to SW. The clean glass plate allows any UV not absorbed by the $TiO_2$ to pass into the reactor, whilst preventing the solution from interacting with the $TiO_2$, stopping photocatalysis. This gave a more accurate estimation of the effect of UV within the reactor.

All experiments were performed in duplicate.

### 3.4.10.3 Choice of photocatalytic reactors

The slurry reactor was used for initial testing of the bactericidal efficacy of the photocatalysts. Slurry reactors are often utilised as they afford a high surface area to volume ratio for pollutant hydroxyl radical interaction. Configurations for these reactors are generally simple and they are inexpensive to construct. However, the major disadvantage of these reactors is the necessary incorporation of a post-treatment catalyst removal step which adds to the overall capital and running costs of the treatment plant. An alternative to this method is the immobilisation of the $TiO_2$ onto a solid support which reduces the surface area to volume ratio and care must be taken to ensure the catalyst remains fixed to the support for the duration of the plant lifetime. The supporting substrate must also be UV transparent. The major advantage of immobilised reactors over suspension systems is that the post-treatment catalyst removal step is unnecessary. The immobilised reactor used in this section was, as previously mentioned, a stirred-tank reactor developed by McMurray and co-workers.[48] This reactor was chosen due to its lack of intrinsic mass transfer limitations. Extensive investigation into the effect of catalyst loading, impellor speed, pollutant concentration, light intensity, oxygen concentration and pH were performed by McMurray. It was determined that when using the operational parameters described above (section 3.4.10.2), no mass transfer limitations occur, allowing for direct comparisons between different catalyst types and also between reactor types.

## 3.4.11 Oxalic acid analysis

Oxalic acid concentration was determined via reverse phase HPLC using an Aminex HPX-87H Ion Exclusion Column (300 mm, 7.8 mm internal diameter, Bio-Rad). Isocratic elution separation was employed using a solvent delivery pump (Spectra Physics P2000) with 1 x $10^{-2}$ mol $dm^{-3}$ $H_2SO_4$ mobile phase (pH 1.5) at a flow rate of 0.8 $cm^3$ $min^{-1}$. An aliquot of 20 µL oxalic acid solution was injected onto a column with the temperature held constant at 30.0 °C. UV absorption detection at 263 nm was carried out, and under the above conditions, oxalic acid had a retention time of around 7.2 minutes. Oxalic acid solution were prepared daily from a 5.3 x $10^{-2}$ mol

$dm^{-3}$ stock solution of 0.1 mol $dm^{-3}$ oxalic acid in water. The stock solution was prepared using distilled water and stored at 4 °C.

The HPLC was calibrated for oxalic acid and the calibration checked before each experiment. HPLC calibration for oxalic acid was carried out by the injection of standards with a range of concentrations. Standards were prepared in deionised water and injected in duplicate. A plot of peak area with respect to concentration yielded linear plots, with the line of best fit being determined to be linear with a typical $R^2$ value of 0.9997. A typical calibration graph for oxalic acid is shown in Figure 3.5.

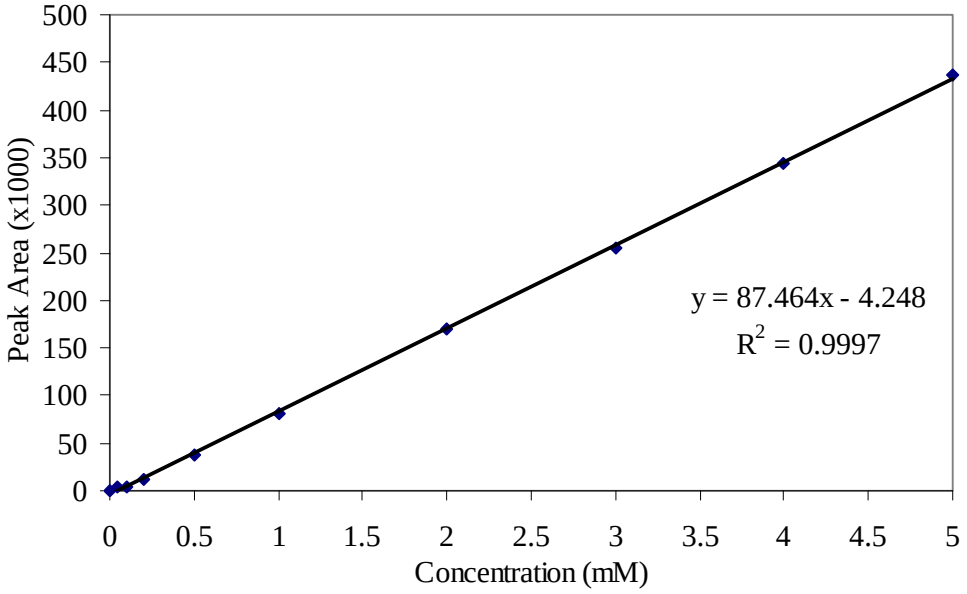


**Figure 3.5 Calibration curve for HPLC of oxalic acid**

## 3.4.12 Bacterial growth and detection

### *3.4.12.1 E. cloacae*

Procedures for the growth, harvest, purification and detection of *E. cloacae* are outlined in chapter 2 (section 2.3.1.3).

### 3.4.12.2 *Escherichia coli*

#### 3.4.12.2.1 *Growth of E. coli cells*

Fresh cells were grown for each day's experiments.

*E. coli* K12 (NCTC 10538) was grown in Luria Bertani (LB) broth. Broth components included sodium chloride 10.0 g, tryptone 10.0 g and yeast extract 5.0 g in 1 $dm^3$ distilled water, corrected to pH 7.0, dispensed into 15 $cm^3$ M$^c$Cartney bottles and autoclaved (Exacta), at 121°C for 15 minutes. A culture for use in experiments was prepared by subculturing from an existing culture held in the University of Ulster's culture collection. 50.0 μL of stock solution was transferred to 15.0 $cm^3$ of fresh sterile LB broth and incubated at 37 °C for 15 hours.

#### 3.4.12.2.2 *Harvest and purification of E. coli cells*

Cells were harvested by centrifugation (Qualitron DW-41) at 2000 rpm for 10 minutes, the supernatant discarded and the pellet resuspended in sterile 0.9 % NaCl solution. The washing and centrifuge cycle was repeated twice and the final pellet resuspended in 15 $cm^3$ of sterile 0.9 % NaCl solution. After this process, dilution by a factor of $10^3$ was required to produce a working cell suspension. 20.0 μL of the working cell suspension was transferred to 200.0 $cm^3$ of water solution immediately prior to experiment commencement to produce a working cell suspension of ~ 1 x$10^3$ *E. coli* CFU $cm^{-3}$.

#### 3.4.12.2.3 *Detection of E. coli cells*

Detection of *E. coli* cells before and during photocatalytic experiments was performed by plating a suspension onto LB agar. Agar plates were prepared in a sterile environment and stored at 4 °C until required. Plates were stored for a maximum of 48 hours before being discarded.

To obtain between 20 and 200 CFU's per plate, 50.0 μL of sample solution was directly transferred to LB agar. LB agar plates were incubated at 37 °C for 24 ± 2

hours before visual identification of the number of colonies present. Results are reported in CFU $cm^{-3}$.

Confirmatory tests were performed on a regular basis to ensure aseptic techniques were being used. This was to ensure that the bacterial culture examined was indeed a pure culture of *E. coli*. Indole production was used as a confirmatory test as *E. coli* is the only bacterial species known to produce indole in tryptone water at 44 °C.[49] Tryptone water was prepared according to the manufacturer's instructions, dispensed in 10 $cm^3$ aliquots into 10 $cm^3$ glass bottles and autoclaved at 121 °C for 15 minutes. Single colonies were picked off agar plates, inoculated into freshly prepared Tryptone water and incubated at 44 °C for 24 hours. An aliquot of 0.2 $cm^3$ of Kovack's reagent was added to each test tube. After shaking, the formation of a purple/red band in the upper layer characterised indole production and confirmed the presence of *E. coli*.[49]

### 3.4.13 Bacterial imaging

Bacterial colony photographs were obtained using a flat-bed scanner (Hewitt Packard 3670) with PC control.

### 3.4.14 Statistical analysis

Where appropriate, the standard error, which shows the variation of each sample within an analytical or sampling method, was calculated using the method outlined in section 2.4 and is illustrated with the corresponding results.

## *3.5 Results and Discussion*

### 3.5.1 $TiO_2$ catalyst characterisation

#### 3.5.1.1 XPS

Figure 3.6 shows expanded XPS spectra of the O 1s and Ti 2p regions for the Degussa P25, MW- and HT-treated $TiO_2$ films. Peaks at 456.3 and 462.5 eV correspond to $2p^{3/2}$ and $2p^{1/2}$ core-levels of Ti(IV) bound to oxygen, respectively.[50]

The atomic ratio of oxygen to titanium was measured to be 2.32 for Degussa P25, 2.31 for the HT-treated $TiO_2$ and 2.39 for the MW-treated $TiO_2$, which suggested that the deposited films were stoichiometric. The full-width at half maximum (FWHM) of Ti $2p^{3/2}$ of Degussa P25 was 0.9 eV and 1.07 and 0.94 eV for the MW- and HT-treated $TiO_2$, respectively (see Table 3.4, Table 3.5 and Table 3.6). This and the position of the Ti $2p^{3/2}$ indicated the presence of the $Ti^{4+}$ oxidation state.[51,52] The shape of the Ti 2p excluded the presence of traceable amounts of $Ti^{2+}$ and $Ti^{0}$,[53] which would be separated by approximately 3 – 4 eV from the $Ti^{4+}$ peak.[54] In the O 1s binding energy region, the peak at 528 eV corresponded to O 1s core-level of oxygen atoms bound to Ti(IV), whereas the broad shoulder at 531 eV seen in all three $TiO_2$ types was due to adsorbed hydroxyl groups (-OH). The hydroxyl groups detected on the film surface arose from chemisorbed $H_2O$.[55]

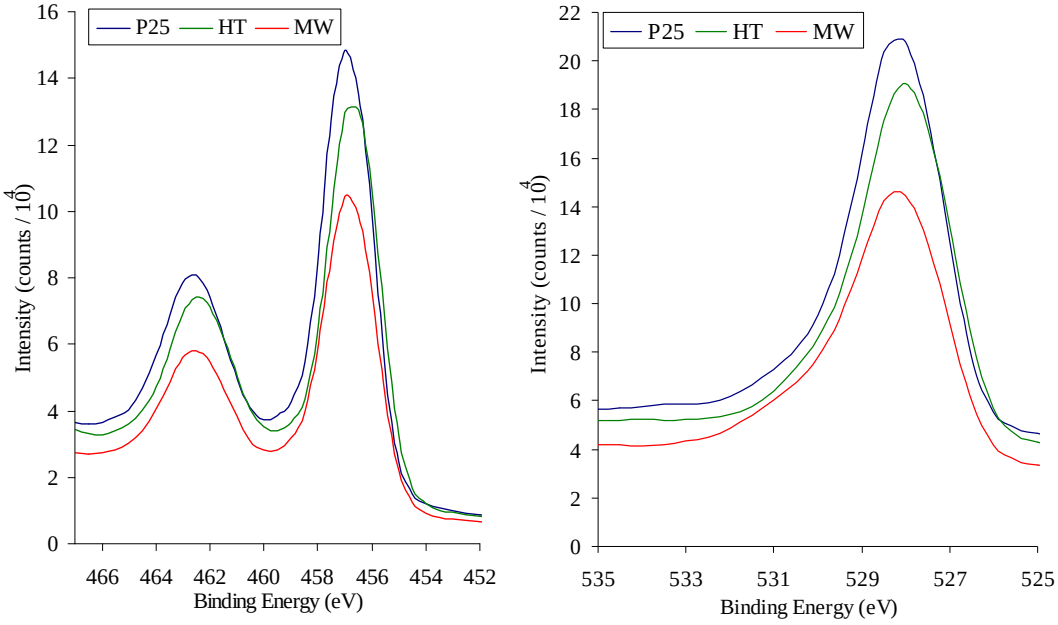


**Figure 3.6 Stacked XPS diffraction patterns for $TiO_2$ powders investigated**

**Table 3.4 Chemical composition of the Degussa P25 $TiO_2$ film surface**

| Peak | Position BE (eV) | FWHM (eV) | Atomic conc. (%) |
|---|---|---|---|
| O 1s | 527.5 | 1.09 | 58.18 |
| Ti 2p | 456.3 | 0.93 | 25.03 |
| N 1s | 397.3 | 1.29 | 0.93 |
| C 1s | 282.3 | 1.52 | 15.86 |

**Table 3.5 Chemical composition of the MW-treated $TiO_2$ film surface**

| Peak | Position BE (eV) | FWHM (eV) | Atomic conc. (%) |
|---|---|---|---|
| O 1s | 527.5 | 1.24 | 56.68 |
| Ti 2p | 456.3 | 1.08 | 23.68 |
| N 1s | 397.3 | 1.32 | 1.23 |
| C 1s | 282.3 | 1.67 | 18.41 |

**Table 3.6 Chemical composition of the HT-treated $TiO_2$ film surface**

| Peak | Position BE (eV) | FWHM (eV) | Atomic conc. (%) |
|---|---|---|---|
| O 1s | 527.2 | 1.10 | 57.24 |
| Ti 2p | 456.0 | 0.94 | 24.91 |
| N 1s | 397.3 | 1.36 | 0.85 |
| C 1s | 282.0 | 1.50 | 18.41 |

### 3.5.1.2 XRD

Wide-angle powder XRD patterns for the MW- and HT-treated $TiO_2$ and Degussa P25 $TiO_2$ powders are depicted in Figure 3.7. Peak intensities obtained from the XRD traces correlated to the quantity of crystalline material and the grain size of the particles. In comparison to traces obtained for the MW-treated $TiO_2$, the HT-treated and Degussa P25 $TiO_2$ peaks were substantially narrower (see FWHM values in Table 3.7). Despite this, there was similitude between the MW-treated and HT-treated samples.

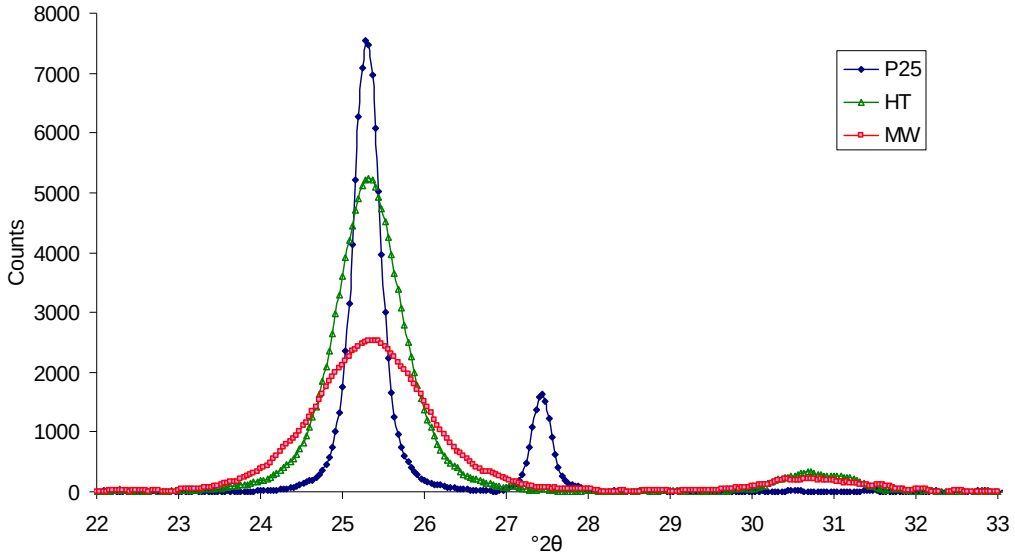


**Figure 3.7 Stacked XRD diffraction patterns for investigated $TiO_2$ powders. Traces were digitally smoothed following correction for contribution from $K\alpha_2$ radiation.**

Primary crystallite size ($P_d$) was determined by application of the Scherrer equation[56] (equation 3.1) to the FWHM measurements from the anatase (101) d-spacing peaks.

$$P_d = \frac{k\lambda}{\beta \cos\theta} \qquad \textbf{3.1}$$

where $\beta$ is the line broadening (equation 3.2)

$$\beta = \beta_s - \beta_0 \qquad \textbf{3.2}$$

where $\beta_s$ and $\beta_0$ are the half-widths of the XRD peak of the sample and of the silicon standard.

The order of primary crystallite size, in decreasing size, was found to be Degussa P25>HT-treated $TiO_2$>MW-treated $TiO_2$ (Table 3.7). Calculated crystallite sizes were in excellent agreement with reported literature values.[57-59] MW-treated $TiO_2$ samples used here were microwave-processed for 60 minutes. Previous investigations on similar samples showed extended periods of microwave processing (maximum 360 minutes) appeared to have minimal effect on the primary crystallite size.[12]

**Table 3.7 Calculated Scherrer crystallite size from Anatase (101) reflection**

| Colloid type | 2θ | FWHM | $P_d$ (nm) |
|---|---|---|---|
| Degussa P25 | 25.296 | 0.383 | 21.259 |
| MW-treated $TiO_2$ | 25.339 | 1.496 | 5.494 |
| HT-treated $TiO_2$ | 25.330 | 0.905 | 9.211 |

From comparisons to traces of known $TiO_2$ phases, it was evident that both HT and MW processing did not result in any significant phase transformation from that of anatase (Figure 3.7). From comparing Degussa P25 to synthetic rutile (PDF 00-021-1276) trace, and specifically at 27.44 2θ, small quantities of rutile within the sample were detected; consistent with literature.[57] Neither the HT- nor MW-treated $TiO_2$ samples indicated any measurable quantities of rutile over the entire region analysed (10 – 80° 2θ). However, both the HT- and MW-treated $TiO_2$ samples indicated the presence of brookite, which was easily discerned by the peak at 30.84° 2θ, indicative of brookite (121) (by comparison with synthetic brookite (PDF 00-029-1360)). The

two strongest lines for brookite (120 and 111) were obscured by the anatase (101) peak and were responsible for some of the peak broadening seen in that region.

From XRD peak fitting, it was found that Degussa P25 contained ~ 25% rutile and ~ 75% anatase. The MW-treated $TiO_2$ contained 77% anatase and 22% brookite, while the HT-treated $TiO_2$ contained 80% anatase and 20% brookite.

#### *3.5.1.2.1 Effect of annealing*

During immobilisation procedures, catalysts were annealed to the borosilicate glass support by heating to 400 °C for 60 minutes with a 5 °C $min^{-1}$ ramp to ensure the catalysts remained fixed to the support during photocatalytic experimentation. The effect of the annealing step on crystallite composition and size was investigated using XRD. No significant change in either composition or primary crystallite size was observed.

### 3.5.1.3 Isothermal nitrogen adsorption-desorption

Surface area and pore size analyses by gas sorption were performed on all catalyst types. Isothermal characterisation showed distinct separation between the different $TiO_2$ preparations. Representative $N_2$ isotherms are illustrated in Figure 3.8.

The commercially available Degussa P25 displayed typical type IV characteristics with H3 hysteresis.[60] The weakly defined step of the H3 hysteresis loop indicated negligible limiting adsorption at high $P/P_0$, often seen in aggregates of plate-like particles. Both the HT- and MW-treated $TiO_2$ samples exhibited type IV isothermal characteristics with H2 hysteresis. Analysis of this hysteresis type is complicated by the incorporation of network effects.[61] However, it is known that condensation and evaporation of the adsorbate within the mesoporous network produced the well-defined step seen between $P/P_0$ 0.55 and 0.75 within the HT- and MW-treated $TiO_2$. This has been observed to arise from hexagonal-shaped pores from the aggregation of semispherical particles.[60]

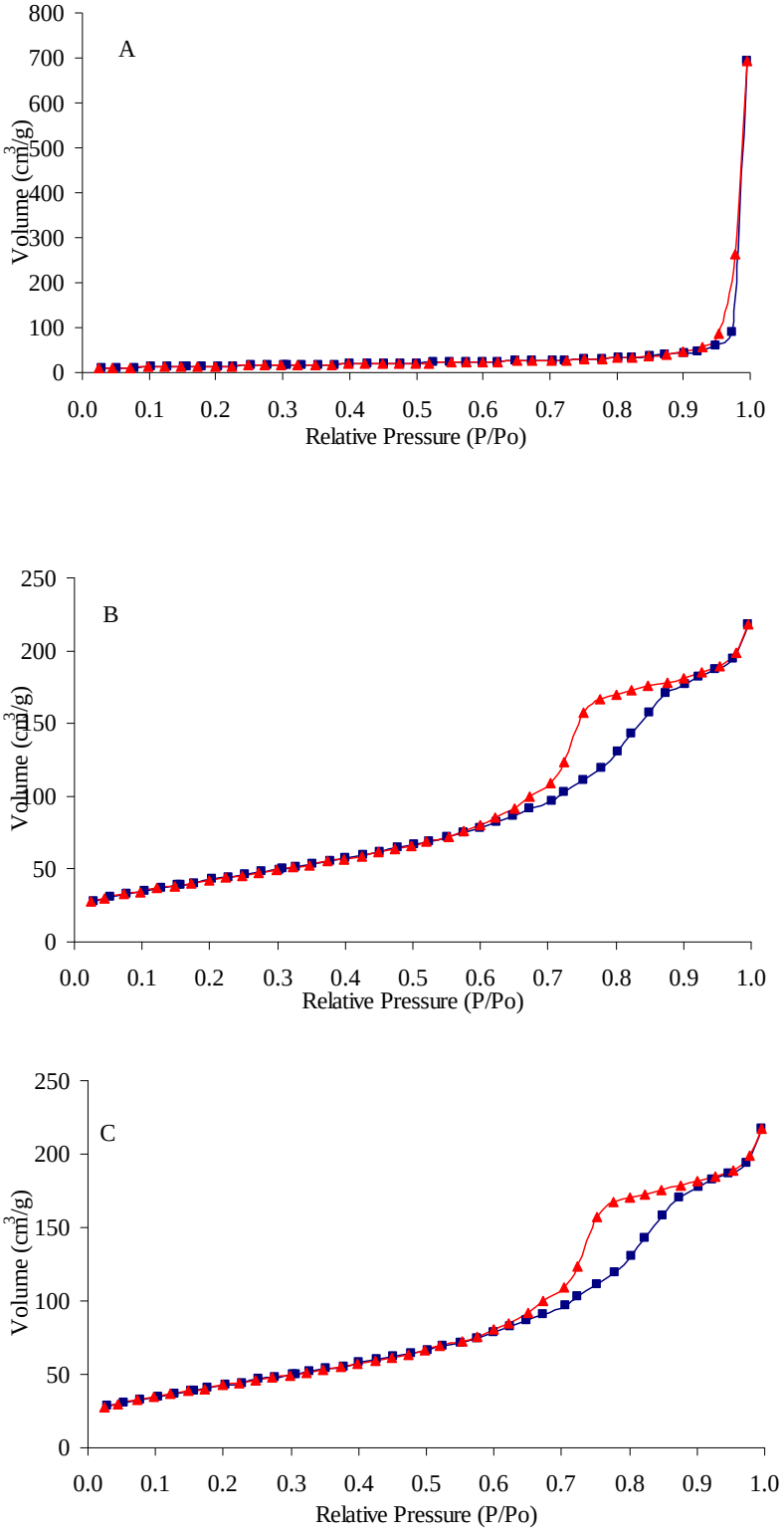


**Figure 3.8 Representative isotherms for $TiO_2$ samples: (A) Degussa P25; (B) MW-treated; and (C) HT-treated. Adsorption -■-; desorption -▲-.**

Table 3.8 presents a summary of the isothermal parameters calculated from the gas-sorption data. It can be seen that the MW- and HT-treated $TiO_2$ samples possessed a significantly higher surface area than the commercially available Degussa P25. Calculated results were consistent with those performed on similar MW- and HT-treated[12] and Degussa P25[58] $TiO_2$ samples.

**Table 3.8 Calculated isothermal parameters for $TiO_2$ catalysts**

| Colloid type | Surface area ($m^2 g^{-1}$) | Volume ($cm^3 g^{-1}$) | Pore size (nm) |
|---|---|---|---|
| Degussa P25 | 50.34 | 1.0670 | 1.829 |
| MW-treated $TiO_2$ | 235.2 | 0.2132 | 1.631 |
| HT-treated $TiO_2$ | 371.0 | 0.3414 | 1.835 |

### 3.5.2 Bacterial inactivation in slurry reactor

The bactericidal effect of $TiO_2$ photocatalysis of *E. cloacae* in sterile distilled water is illustrated in Figure 3.9. After 30 minutes of irradiation, 99.71%, 99.95% and 99.70% inactivation of *E. cloacae* occurred using Degussa P25, MW-treated $TiO_2$ and HT-treated $TiO_2$ respectively. For the three catalyst types, an initial rapid decrease in *E. cloacae* concentration occurred, followed by a slower linear decline, which follows pseudo-first order kinetics. No significant reduction of *E. cloacae* cell concentration was observed in control experiments, where an identical bacterial suspension was kept in the dark or when an *E. cloacae* suspension was exposed to only UV irradiation within the slurry reactor.

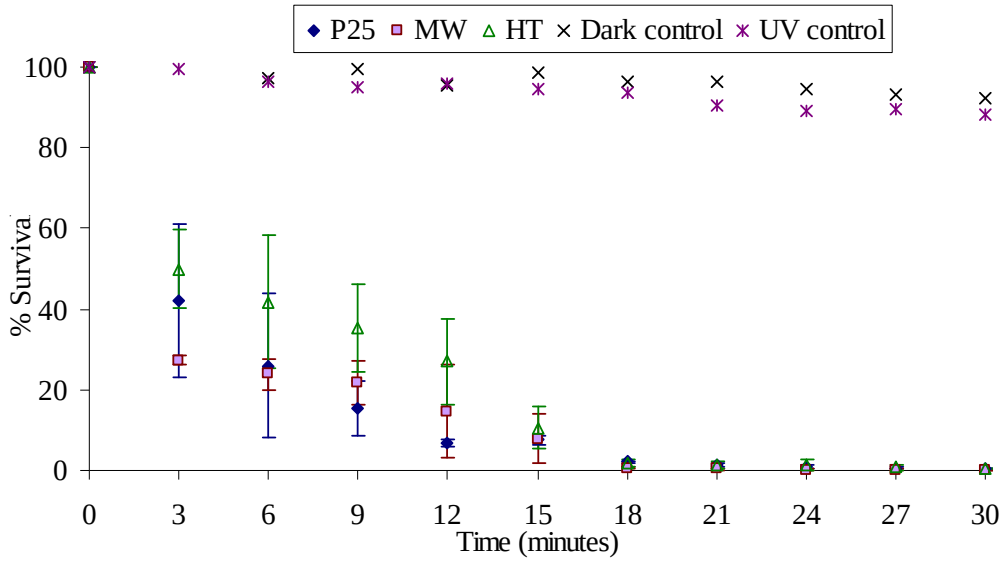


**Figure 3.9 Inactivation plots of *E. cloacae* in sterile distilled water using slurry reactor. (P25: Degussa P25; MW: MW-treated $TiO_2$; HT: HT-treated $TiO_2$.)**

Table 3.9 summarises the inactivation rates for *E. cloacae* using the 3 different catalyst types, calculated using Chick's Law. The disinfection rates were calculated based on the linear slope of the graph shown in Figure 3.9, i.e. between 3 and 18 minutes. It can be seen that the calculated inactivation rates per mg of catalyst were quite similar; the MW-treated $TiO_2$ produced the highest rate. However, when comparing inactivation rates with respect to surface area of catalyst, Degussa P25 performed the highest, with a calculated rate 28 and 14 % higher than the MW- and HT-treated $TiO_2$ samples, respectively.

**Table 3.9 Calculated photocatalytic disinfection rates of *E. cloacae* in sterile distilled water within the slurry reactor**

| Catalyst type | % Inactivation after 30 min | Rate / mg catalyst (CFU $cm^{-3}$ $s^{-1}$) / mg catalyst x $10^{-3}$ | Rate / catalyst surface area (CFU $cm^{-3}$ $s^{-1}$) / $m^2$ catalyst x $10^{-6}$ | $R^2$ |
|---|---|---|---|---|
| Degussa P25 | 99.71 | 7.11 | 1.41 | 0.988 |
| MW-treated $TiO_2$ | 99.95 | 9.43 | 0.401 | 0.945 |
| HT-treated $TiO_2$ | 99.70 | 7.33 | 0.197 | 0.949 |

While photocatalytic inactivation was achieved using the slurry suspension, the significant disadvantage of post-catalytic catalyst removal necessitated the immobilisation of the $TiO_2$ catalyst onto a supporting substrate. The chosen substrate was borosilicate glass and a spray-coating method was adopted to deposit the films.

## 3.5.3 Bacterial inactivation in stirred-tank reactor

### 3.5.3.1 Photocatalytic degradation of model organic pollutant

The photocatalytic degradation of the model organic pollutant, oxalic acid, was investigated using the immobilised $TiO_2$ catalysts within the stirred-tank reactor.

The effect of $TiO_2$ photocatalysis on 4.5 mol $dm^{-3}$ oxalic acid in distilled water is illustrated in Figure 3.10. All catalysts tested showed a linear reduction in concentration with respect to irradiation time, following pseudo-zero order kinetics, which correlate with previously reported data.[48] It can be seen that both Degussa P25 and the HT-treated $TiO_2$ catalyst produced 90% reduction after 165 and 150 minutes irradiation, respectively; however, the MW-treated $TiO_2$ required an additional 60 minutes to achieve the same level of reduction (225 minutes).

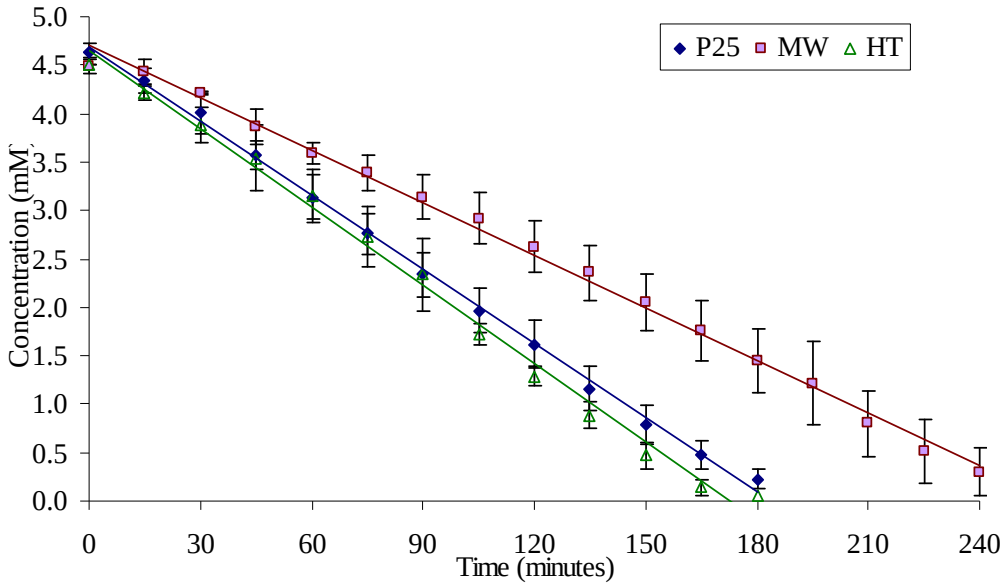


**Figure 3.10 Plot of photocatalytic degradation of 4.5 mol $dm^{-3}$ oxalic acid in distilled water using UVA irradiation in stirred-tank reactor. (P25: Degussa P25; MW: MW-treated $TiO_2$; HT: HT-treated $TiO_2$.)**

The calculated degradation rate with respect to irradiated catalyst area obtained for the MW-treated $TiO_2$ was ~ 30% lower than, but within the same order of magnitude as the Degussa P25 and the HT-treated $TiO_2$ rates (Table 3.10). However when the rates with respect catalyst surface area were calculated, both the MW- and HT-treated $TiO_2$ performed at a rate approximately 10-fold lower than Degussa P25.

**Table 3.10 Calculated degradation rates for 4.5 mol $dm^{-3}$ oxalic acid in distilled water using UVA irradiation in stirred-tank reactor**

| Catalyst type | % Degradation after 150 min | Rate / mg catalyst (mol $s^{-1}$) / mg catalyst x $10^{-9}$ | Rate / catalyst surface area (mol $s^{-1}$) / $m^2$ catalyst x $10^{-9}$ | $R^2$ |
|---|---|---|---|---|
| Degussa P25 | 83.124 | 1.59 | 30.75 | 0.993 |
| MW-treated $TiO_2$ | 54.337 | 1.04 | 4.42 | 0.996 |
| HT-treated $TiO_2$ | 89.593 | 1.53 | 4.13 | 0.998 |

### 3.5.3.2 Effect of UV irradiation wavelength on photodegradation

The effect of the wavelength of the UV irradiation source on the photocatalytic efficiencies of the $TiO_2$ catalysts was investigated. UVB rather than UVC irradiation was chosen, as borosilicate glass begins to absorb at ~ 320 nm. Therefore if UVC irradiation was used, quartz or fused silica would be required as the $TiO_2$ support, both of which are more expensive than borosilicate glass.

The photocatalytic degradation of 4.5 mol $dm^{-3}$ oxalic acid in distilled water in the stirred-tank reactor under UVB irradiation is shown in Figure 3.11. Degussa P25 required a significantly shorter treatment time to result in 90% degradation (75 minutes), than the MW- and HT-treated $TiO_2$ catalysts (240 minutes). When comparing the MW- and HT-treated $TiO_2$ catalysts, they required approximately the same treatment times to photo-oxidise 90% of the pollutant; 210 and 240 minutes respectively.

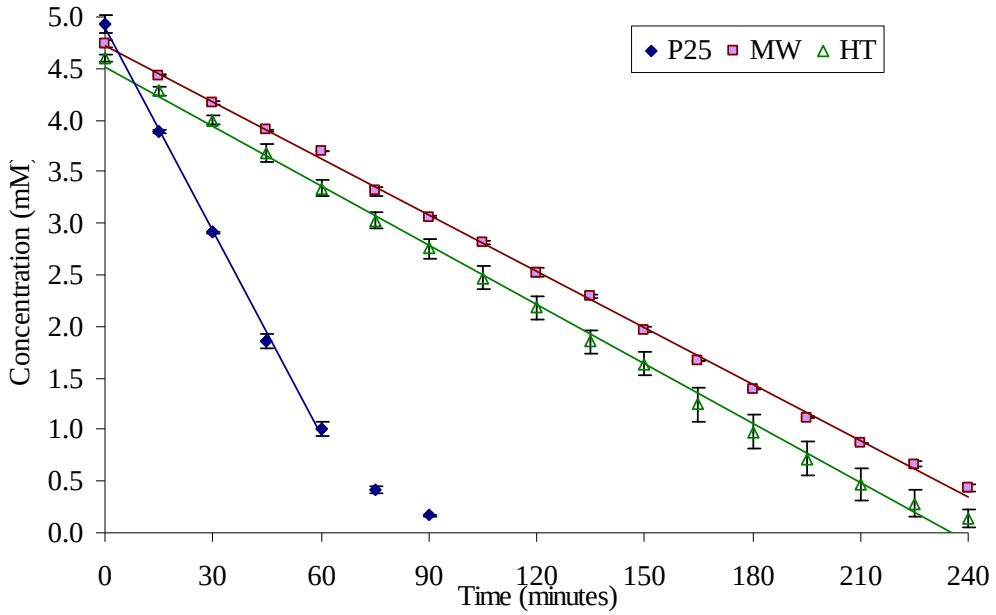


**Figure 3.11 Plot of photocatalytic degradation of 4.5 mol dm$^{-3}$ oxalic acid in distilled water using UVB irradiation in stirred-tank reactor. (P25: Degussa P25; MW: MW-treated $TiO_2$; HT: HT-treated $TiO_2$.)**

Table 3.11 summarises the calculated disinfection rates of 4.5 mol dm$^{-3}$ oxalic acid under UVB irradiation using the different catalyst types. When comparing the photocatalytic degradation rates per irradiated surface area, Degussa P25 displayed a three times greater photocatalytic degradation rate than the MW- and HT-treated $TiO_2$ catalysts. Also, when comparing the calculated degradation rates per catalyst surface area, Degussa P25 was again the most effective catalyst tested. Here, Degussa P25 produced a dramatically faster degradation rate than the other $TiO_2$ types tested, 16.93 times the MW-treated $TiO_2$ and 24.30 times the HT-treated $TiO_2$.

**Table 3.11 Calculated degradation rates for 4.5 mol dm$^{-3}$ oxalic acid in distilled water using UVB irradiation in stirred-tank reactor**

| Catalyst type | % Degradation after 90 min | Rate / mg catalyst (mol s$^{-1}$) / mg catalyst x 10$^{-9}$ | Rate / catalyst surface area (mol s$^{-1}$) / m$^2$ catalyst x 10$^{-9}$ | $R^2$ |
|---|---|---|---|---|
| Degussa P25 | 96.58 | 3.79 | 75.34 | 0.999 |
| MW-treated $TiO_2$ | 35.38 | 1.05 | 4.45 | 0.999 |
| HT-treated $TiO_2$ | 40.16 | 1.15 | 3.10 | 0.997 |

The objective of this section of work was to determine the effects of shortening the UV wavelength with respect to longer UV wavelengths on the photocatalytic degradation rate. It was discovered however, that direct comparisons between the calculated degradation rates could not be performed. The reasons for this will now be discussed.

#### *3.5.3.2.1 Diffuse-transmission UV-vis spectroscopy of immobilised $TiO_2$*

Figure 3.12 and Figure 3.13 show the diffuse-transmission UV-vis spectra collected under UVA and UVB irradiation, respectively, for Degussa P25, MW- and HT-treated $TiO_2$ catalysts. Figure 3.14 shows the reflectance UV-vis spectra of the three catalyst types examined.

Despite all immobilised $TiO_2$ plates containing a catalyst loading of ~ 1.0 mg $cm^{-2}$ the UV absorbance between the catalysts was very different. When examining the diffuse-transmission spectra, Degussa P25 absorbed the majority of UVA (99.2%) and UVB irradiation (100%) emitted from the light sources. The MW- and HT-treated $TiO_2$ catalysts absorbed the majority of the emitted UVB radiation (96.5% and 99.6% respectively), but only 75.5% and 81.2% of the emitted UVA spectrum.

By examining the reflectance UV-vis spectra (Figure 3.14) an obvious change in absorption of Degussa P25 compared to the MW- and HT-treated $TiO_2$ colloids was apparent. The Degussa P25 $TiO_2$ absorbed a higher percentage of wavelengths between 370 – 405 nm than the other catalysts.

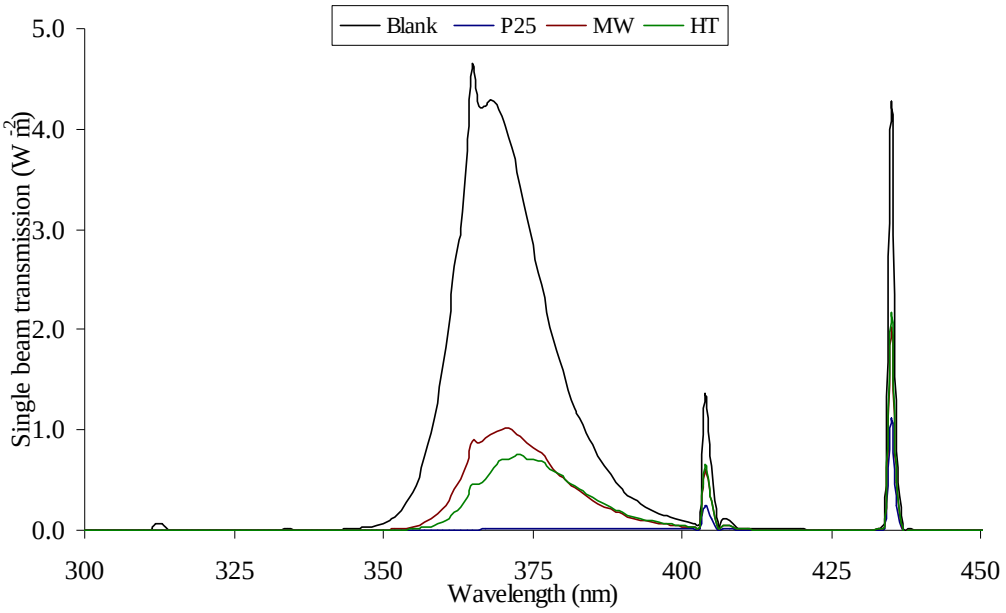


**Figure 3.12 Single beam diffuse-transmission spectra of Degussa P25, MW- and HT-treated $TiO_2$ under UVA irradiation. 'Blank' spectrum was collected through a clean borosilicate glass plate under UVA irradiation. (P25: Degussa P25; MW: MW-treated $TiO_2$; HT: HT-treated $TiO_2$.)**

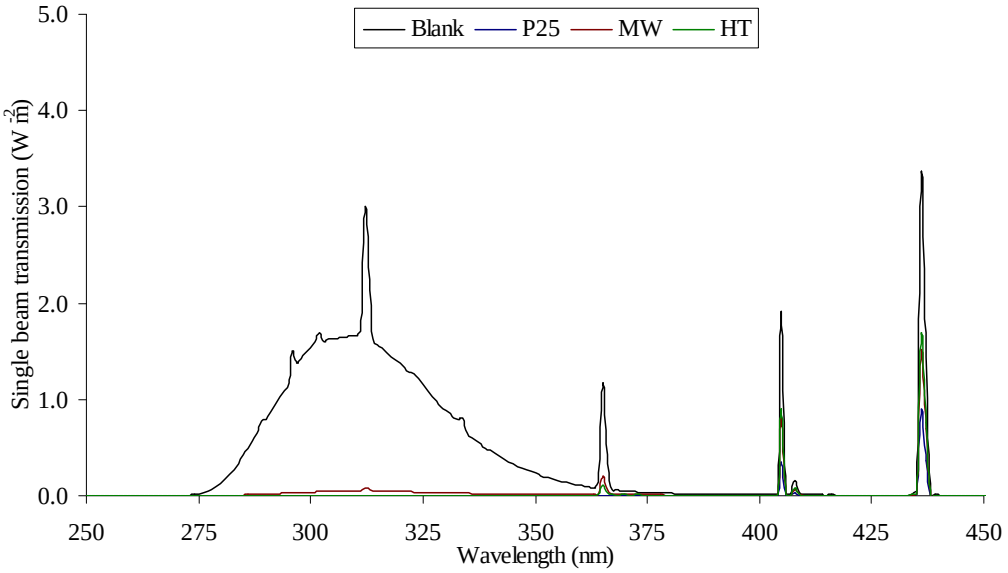


**Figure 3.13 Single beam diffuse-transmission spectra of Degussa P25, MW- and HT-treated $TiO_2$ under UVB irradiation. 'Blank' spectrum was collected through a clean borosilicate glass plate under UVB irradiation.**

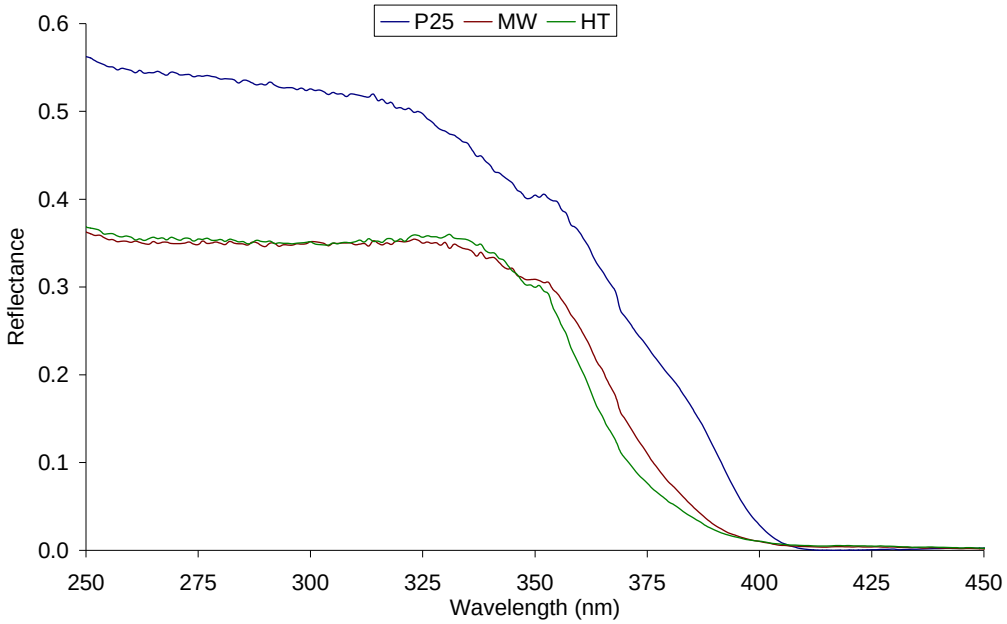


**Figure 3.14 Reflectance spectra of Degussa P25, MW- and HT-treated $TiO_2$**

This can be explained by the composition of crystallite phases within the catalyst types. From XRD analyses (section 3.5.1.2), it was found that Degussa P25 contained ~ 25% of rutile and ~ 75% anatase. The MW-treated $TiO_2$ contained 77% anatase and 22% brookite, while the HT-treated $TiO_2$ contained 80% anatase and 20% brookite. No rutile was present in either the MW- or HT-treated $TiO_2$. It is well known that the different $TiO_2$ crystallite phases possess different band-gaps and therefore absorb different wavelengths of light. Rutile absorbs irradiation $\leq$ 413 nm; anatase $\leq$ 388 nm; and brookite $\leq$ 258 nm.[62] Hence, it is expected that Degussa P25, a composite of rutile and anatase will absorb irradiation $\leq$ 413 nm, while the MW- and HT-treated $TiO_2$ should absorb irradiation of wavelengths $\leq$ 388 nm, which correlated well with the collected UV-vis reflectance data.

By comparing Figure 3.12 and Figure 3.14, it was evident that the lower maximum absorption of the MW- and HT-treated $TiO_2$ resulted in the transmission band centred around 370 nm in Figure 3.12. In contrast, the increased absorbance of Degussa P25 within this region resulted in total absorption of the emitted UV irradiation. For the MW- and HT-treated $TiO_2$, the rapid decline in reflectance at wavelengths greater than 350 nm corresponded to the shape change seen in the diffuse-transmission bands centred at 365 nm. Therefore the wavelength of maximum transmission had shifted from 365 nm to 373 nm.

By comparison of the 405 and 435 nm bands, in both the UVA and UVB diffuse transmission spectra (Figure 3.12 and Figure 3.13), it was observed that all the $TiO_2$ catalysts reflected some of the emitted radiation in these regions. Degussa P25 absorbed the greatest amount, while the MW- and HT-treated $TiO_2$ absorbed similar amounts to each other, which were approximately half the total reflected by the Degussa P25. This was partially attributed to scattering of light by the catalysts. Degussa P25 films were observed to be almost opaque, while the MW- and HT-treated $TiO_2$ films were translucent. The more opaque nature of the Degussa P25 film, and therefore significantly higher scattering of light, resulted in the lower transmission of radiation 435 nm. This reasoning, combined with the presence of rutile within Degussa P25, resulted in the lowered transmission seen at 405 nm.

The diffuse-transmission results show that the direct comparison of rates obtained for UVA and UVB irradiation were not possible. To overcome this, the apparent quantum yields ($\Phi_{app}$) of the two types of UV radiation usually are calculated and applied to the photodegradation rates as follows:

$$\Phi_{app} = (Rate_{initial} \quad (mol \quad cm^{-2} \quad s^{-1}) / photonflux \quad (Einstein \quad cm^{-2} \quad s^{-1})) \times 100 \quad \textbf{3.3}$$

However, this does not take differences in colloidal surface area into account. Therefore, the $\Phi_{app}$ was modified to include such differences as follows:

$$\Phi_{app} = (Rate_{initial} \quad (mol \quad m^{-2} \quad s^{-1}) / photonflux \quad (Einstein \quad cm^{-2} \quad s^{-1})) \times 100 \quad \textbf{3.4}$$

The light intensity entering the photoreactor (incident photon flux) was determined via potassium ferrioxalate actinometry by McMurray and co-workers.[63] For UVA and UVB irradiation, the incident photon flux was determined to be 3.28 x $10^{-8}$ Einstein $cm^{-2}$ $s^{-1}$ and 2.00 x $10^{-8}$ Einstein $cm^{-2}$ $s^{-1}$, respectively. (An Einstein is equivalent to one mol of photons.) It was necessary however, to correct the incident photon flux for the UV transmission of the individual $TiO_2$ catalyst plates examined, by ratioing the total transmission of the $TiO_2$ test plate against the total transmission of the blank, as determined using diffuse-transmission UV-vis spectroscopy. Table

3.12 gives the $\Phi_{app}$, calculated using equation 3.4, for UVA and UVB irradiation applied to the three $TiO_2$ catalysts types examined.

In the current investigation, Degussa P25 showed an increased degradation rate when moving to a shorter wavelength irradiation source, consistent with the literature.[63,64] However, the MW- and HT-treated $TiO_2$ catalysts unexpectedly showed minimal, or in the case of HT-treated $TiO_2$, no change upon irradiation with shorter UV wavelengths.

**Table 3.12 Percentage apparent quantum yields for $TiO_2$ catalysts calculated using equation 3.3.**

| Irradiation source | Degussa P25 $TiO_2$ | MW-treated $TiO_2$ | HT-treated $TiO_2$ |
|---|---|---|---|
| UVA | 94.5 | 17.9 | 15.5 |
| UVB | 377.0 | 23.1 | 15.5 |

Despite extensive use of $TiO_2$ within photocatalytic systems, there is very little understanding of the mechanistic effect of shortening the UV wavelength. It has been reported that the absorption coefficient increased with decreasing wavelength to a maximum absorption coefficient around 250 nm.[63] Therefore an increase in quantum efficiency with the use of UVB rather than UVA irradiation would be expected.

Previous investigations by Blazkova et al.[65] and Stafford et al.[66] have reported an increase in charge carrier separation when using shorter wavelength UV sources which resulted in increased efficiencies. Stafford et al.[66] stated that this effect was due to electrons absorbing more energetic photons being energised to an energy level higher than the CB minimum (or lowest unoccupied molecular orbital, known as LUMO). These higher energy electrons were less likely to recombine than electrons energised to the LUMO, resulting in the increased efficiency.

The differing recombination rates and electronic transitions of rutile and anatase, both individually and as a composite will now be discussed in more detail. Recently, Noguchi et al.[67] investigated the effect of excitation wavelength on ultra-fast electron-hole recombination within pure anatase and pure rutile $TiO_2$ crystallites. It was discovered that upon over-band-gap irradiation, a rapid rise and subsequent slow

decay in absorption occurred for both anatase and rutile crystallites compared to band-gap irradiation. The authors proved there was essentially no difference between the electron-hole recombination dynamics of anatase and rutile $TiO_2$ and shortening the wavelength actually significantly decreased the rate of recombination.

However, it has long been understood that mixed-phase materials exhibit higher photocatalytic activity than pure anatase alone. The current hypothesis was originally proposed in the early 1900's, has since been refined by Bickley et al.[68] It is thought that the enhanced activity of mixed-phases relative to pure phases is that upon UV excitation, photogenerated electrons accumulate in the CB of rutile, due to vectorial displacement from the anatase CB, whereas holes accumulate in the VBs of both anatase and rutile, as their VBs are almost at the same level. The accumulation of the photo-generated electrons within the rutile phase significantly lowers the recombining of holes within the anatase VB, leading to more efficient electron-hole separation and greater catalytic reactivity.[68] An energy level diagram for this model is shown in Figure 1.9. In 2002, Yu et al.[69] reported that the use of mixed-phase $TiO_2$ led to improved photocatalytic activity, citing the same model as shown in Figure 1.9. However, specific photoactivity within the mixed-phase $TiO_2$ only increased by 9.1% when compared to pure anatase.

In 2003, Hurum et al.[70] investigated the enhanced photoreactivity of Degussa P25 mixed-phase $TiO_2$ using Electronic Paramagnetic Resonance (EPR) spectroscopy. Whilst previous proposals considered rutile as a passive electron sink hindering recombination of anatase, the authors detailed the critical and active role of rutile within $TiO_2$ formulations. Within mixed-phase $TiO_2$, charges produced on rutile by visible illumination were stabilised through electron transfer to lower-energy, anatase lattice-trapping sites. The results suggested that Degussa P25 possessed nano-clusters containing atypically-small rutile crystallites interwoven with anatase crystallites, with the transition points between the two phases allowing rapid electron transfer from rutile to anatase. The authors proposed a model of rutile antenna and subsequent charge separation which is shown in Figure 1.10.

The conflicting evidence within the literature highlights that the mechanisms behind reported increases in photocatalytic degradation rates from both mixed-phase $TiO_2$

samples as well as shorter wavelength excitation are not well understood. It must be noted, that while more investigations into the mechanisms of electronic transitions of $TiO_2$ are being reported in the literature, often little emphasis is placed on the crystalline phase composition of the $TiO_2$ utilised. Some reports merely state $TiO_2$ crystalline composition as "mainly consisting of anatase".[71,72] Although all within the field are aware of the differing band-gap energies of rutile and anatase, a few seem to have missed the importance of reporting the ratio of anatase to rutile within $TiO_2$ samples.

In the current investigation, when comparing the calculated $\Phi_{app}$ for UVA irradiation shown in Table 3.12, it was evident that the mixed-phase Degussa P25 showed a significantly higher yield than the 'pure-phase' (see below for further explanation) MW- and HT-treated $TiO_2$ colloids. This upholds the theory that mixed-phase colloids possess greater photoreactivities than pure-phases, consisting only of anatase. These results however, can not prove which of the mechanisms for mixed-phase $TiO_2$ activity proposed by Birkley et al.[68] or Hurum et al.[70] was the most fitting.

The term 'pure-phase' was used here after taking into consideration of the presence of brookite within the MW- and HT-treated $TiO_2$ catalysts. However, as previously stated, brookite's band-gap is 4.8 eV, corresponding to 258 nm. From the diffuse-transmission measurements (Figure 3.12 and Figure 3.13) the shortest wavelength emissions of the UV lamps came from the UVB lamp at 270 nm. This was insufficient to excite electrons from the brookite VB to the CB minimum. Thus, in the current investigation the presence of brookite was thought to have no effect.

When comparing UVA to UVB irradiation, the first and most startling observation was that the MW- and HT-treated $TiO_2$, showed minimal or in the case of HT-treated $TiO_2$ no change in $\Phi_{app}$ when shorter UV wavelengths were applied (see Table 3.12). This in itself, discredited Blazkova et al.[65] and Stafford et al.'s[66] broad observations that an increase in quantum efficiency occurs upon reducing the UV wavelength. It appears likely that this was due to both Blazkova and Stafford using only mixed-phase colloids, a hypothesis up-held when examining Degussa P25's increased $\Phi_{app}$ under UVB irradiation (94.5 under UVA to 377.0 under UVB).

So, why did the MW- and HT-treated $TiO_2$ colloids display similar $\Phi_{app}$'s with either UVA or UVB irradiation? When examining the experimental data obtained during the present investigation, sufficient energy was injected into the photocatalytic system using UVA irradiation to excite electrons from the VB to CB of anatase. In fact, the maximum output of the UVA lamp was 365 nm, which was over-band-gap irradiation for anatase. Energy at this wavelength would cause rapid excitation of the electrons in the anatase phase and slow recombination rates due to excitation to an energy level higher than the CB minimum.[67] Therefore, it was likely that under UVA irradiation, the recombination rates were already slowed by over-band-gap irradiation. Moving to even greater over-band-gap irradiation in the form of UVB, did not change the $\Phi_{app}$, or in other words, did not further slow these recombination rates as the active sites were already being used to capacity.

In the case of Degussa P25, the added advantage of vectorial displacement aided in its increased efficiency. Under UVA irradiation, some electrons from the anatase CB are used to reduce the organic in solution; some are displaced to the rutile CB 'electron sink' with its ensuing reduction of the organic species; while the rest, which are not displaced or used fast enough, undergo recombination. However under UVB, more electrons are displaced to the rutile CB due to the higher over-band-gap excitation state, allowing for greater electron-hole separation, lowering recombination within anatase, and thus increasing the overall yield. See Figure 3.15 for proposed mechanism of mixed-phase $TiO_2$ activity under UVA and UVB irradiation.

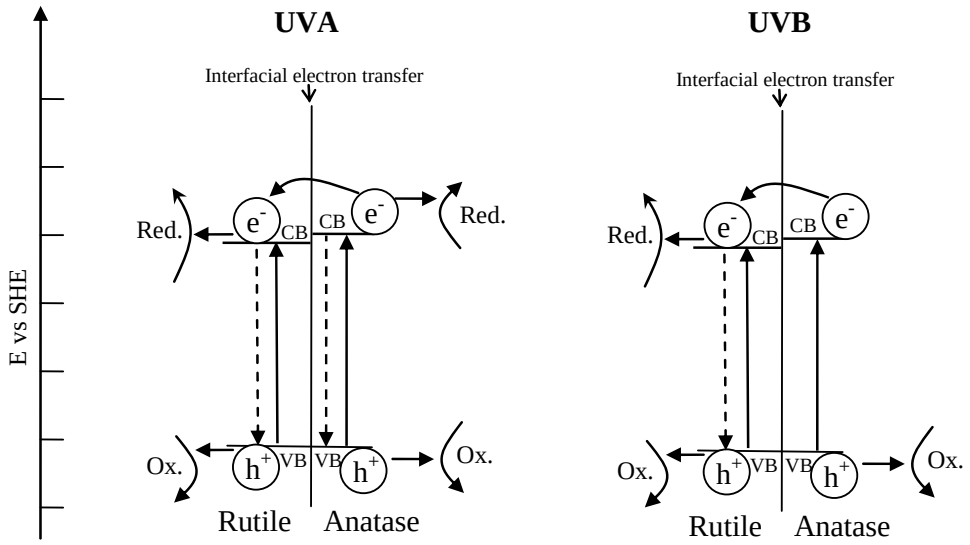


**Figure 3.15 Proposed model of mixed-phase $TiO_2$ activity under UVA and UVB irradiation**

### 3.5.3.3 Effect of natural water matrices on photocatalytic rate

A potential application of photocatalytic degradation is in the water treatment industry. Water sources for treatment include rivers, streams and secondary effluent. Before this can occur, thorough investigation of the effects of water sources must be undertaken as it has been shown that significant differences in degradation/inactivation rates occur in water from different sources.[40-43] As a step towards this goal, it was proposed that the stirred-tank reactor would be used to investigate the effect of photocatalytic degradation of natural river water obtained from the Dorisland water treatment works in Northern Ireland.

Before experiments determining the effects of *E. coli* inactivation could be performed, the effect of natural water on the immobilised $TiO_2$ was determined using oxalic acid. Figure 3.16 shows the photocatalytic degradation of 4.5 mol $dm^{-3}$ oxalic acid using immobilised Degussa P25 $TiO_2$. These experiments were performed in sequence: oxalic acid in distilled water (DI); oxalic acid in natural river water (NW); oxalic acid in DI after rinsing $TiO_2$ plate with DI (DI 2); and oxalic acid in DI after rinsing $TiO_2$ plate again with DI (DI 3). It can be seen that while performing the experiment in NW, a slight reduction in the degradation rate occurred. The most significant change occurred after rinsing the $TiO_2$ once, where a significant reduction (35.2%) in degradation rate occurred due to poisoning of the catalyst (Table 3.13).

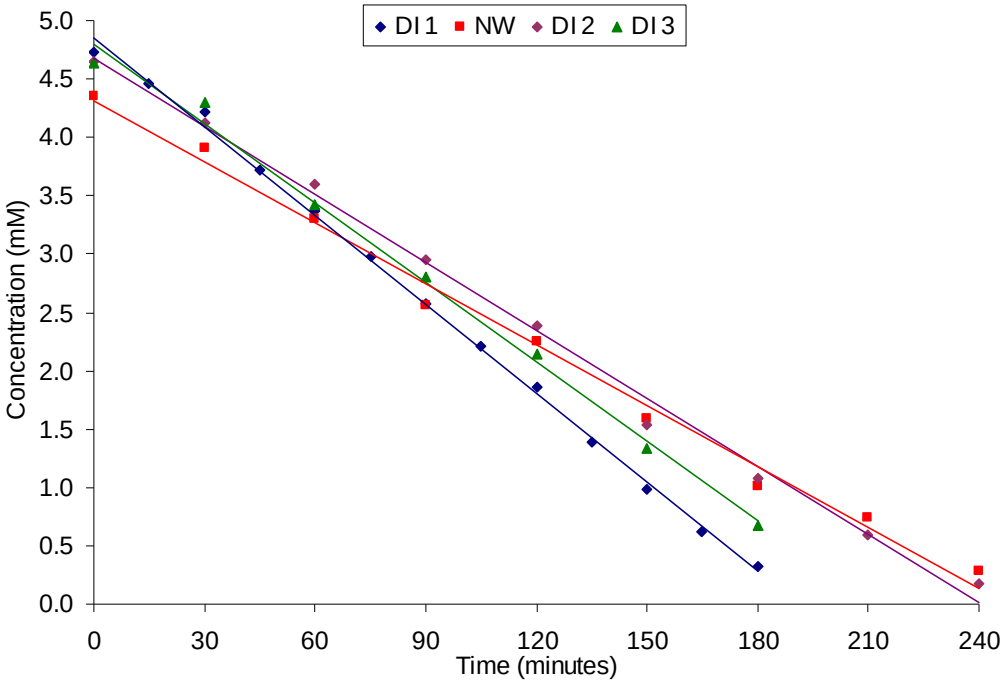


**Figure 3.16 Plot of photocatalytic degradation of 4.5 mol dm$^{-3}$ oxalic acid in distilled water (DI) then natural water (NW); after rinsing once with distilled water (DI 2) and after rinsing twice with distilled water (D1 3), using immobilised Degussa P25 $TiO_2$ and UVA irradiation in stirred-tank reactor.**

**Table 3.13 Calculated degradation rates and quantum yields for 4.5 mol dm$^{-3}$ oxalic acid using Degussa P25 $TiO_2$ and UVA irradiation in stirred-tank reactor**

| Experiment Run | % Degradation after 180 min | Rate / mg catalyst (mol $s^{-1}$) / mg catalyst x $10^{-9}$ | Rate / catalyst surface area (mol $s^{-1}$) / $m^2$ catalyst x $10^{-8}$ | % Quantum Yield mol Einstein$^{-1}$ | $R^2$ |
|---|---|---|---|---|---|
| DI | 93.12 | 1.55 | 3.07 | 94.5 | 0.993 |
| NW | 76.64 | 1.00 | 1.99 | 61.2 | 0.993 |
| Rinse 1 | 76.74 | 1.12 | 2.22 | 68.2 | 0.995 |
| Rinse 2 | 85.37 | 1.13 | 2.60 | 79.9 | 0.994 |

However, the poisoning was reversed by repeated washing, as evidenced by the increase in degradation rate after each rinsing procedure. The reduction in the calculated quantum yield was lowered to 14.6% after twice rinsing the catalyst, which is consistent with results obtained by Ibarz-Grau under similar conditions.[73]

The reasons for the lowered photocatalytic rate observed when using natural water sources will be further discussed in a later section (3.5.3.5).

### 3.5.3.4 Photocatalytic inactivation of *E. coli* in natural water

Initially the degradation rate of *E. coli* in distilled water was determined for comparative purposes. Figure 3.17 shows the inactivation rate of *E. coli* suspended in distilled water (6.70 x $10^5$ CFU $cm^{-3}$), at pH 7.1, using immobilised Degussa P25 under UVA irradiation.

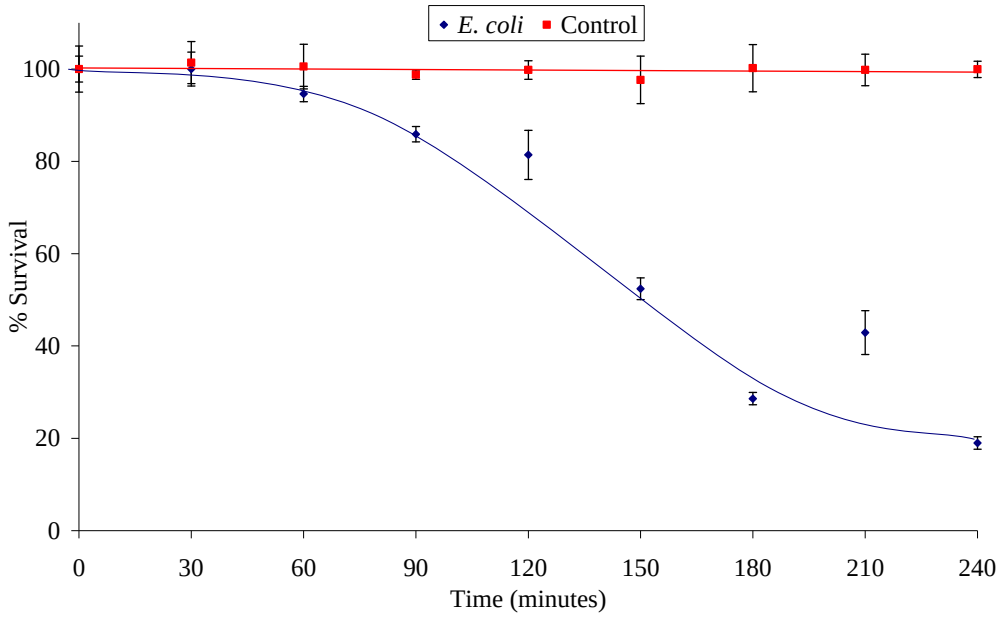


**Figure 3.17 Plot of photocatalytic inactivation of *E. coli* in distilled water using immobilised Degussa P25 $TiO_2$ under UVA irradiation in stirred-tank reactor**

81% *E. coli* inactivation was obtained after 4 hours and the inactivation rate per mg of catalyst was calculated via Chick's Law to be 2.16 x $10^{-6}$ CFU $cm^{-3}$ $s^{-1}$. Only 0.05% inactivation over the same time period was seen in the control experiments where a portion of the working *E. coli* suspension was held under similar experimental conditions; however, without UV irradiation.

When the same system was tested with natural river water instead of distilled water, no inactivation occurred after 5 hours of treatment (data not shown). It was discovered that the pH of the natural water was 7.5, which is not optimum for $TiO_2$ photocatalysis.[74] Thus, the pH of the natural water was adjusted to 5.0 and the

experiment repeated. Again, no inactivation was witnessed despite 5 hours of treatment. Competitive processes between the bacterial cells and the organic acids naturally occurring within the river water could also be occurring, significantly slowing the inactivation rate (as witnessed when degrading oxalic acid, above). Therefore, the initial bacterial cell loading was lowered to ~ 1.0 x $10^3$ CFU $cm^{-3}$ which was a more realistic estimate of the natural bacterial concentration within rivers and stream systems.[75] At this bacterial loading with the pH of the river water adjusted to 5.0, inactivation occurred. A plot of the inactivation of 2.4 x $10^3$ CFU $cm^{-3}$ *E. coli* in natural river water (pH 5.0), with immobilised Degussa P25 under UVA irradiation is shown in Figure 3.18. Under these conditions 98.0% inactivation was accomplished after 4 hours of treatment (see Table 3.14).

It must be noted that a lag period in inactivation was also observed in the photocatalytic experiments, in both distilled and river water, between 0 and 60 minutes, where the inactivation rates were slower than those observed for the remainder of the experiment. Possible reasons for this phenomenon will be discussed later.

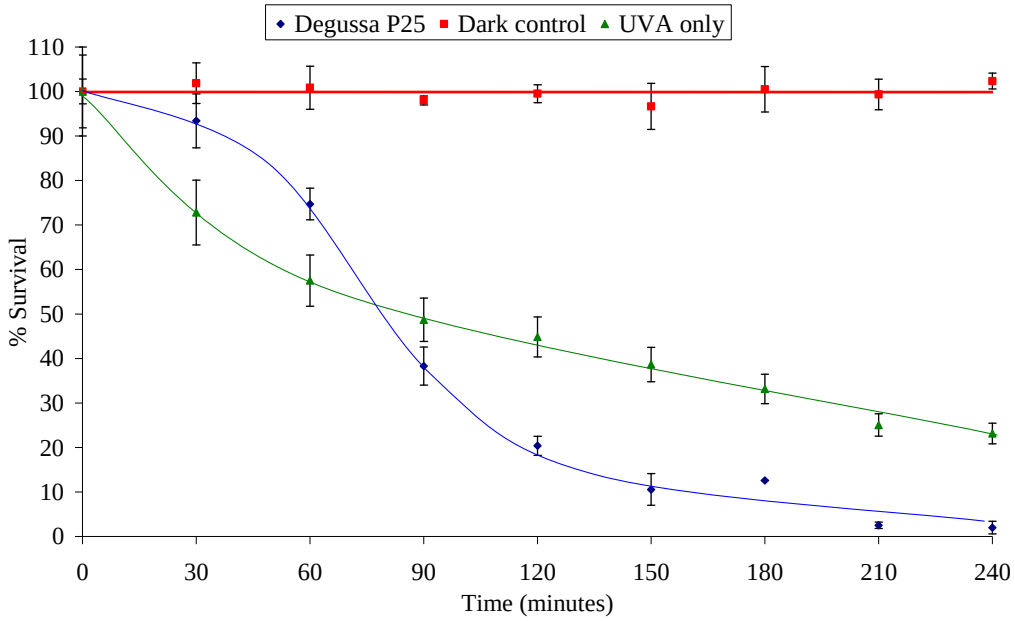


**Figure 3.18 Plot of photocatalytic inactivation in the stirred-tank reactor of 2.4 x $10^3$ CFU $cm^{-3}$ *E. coli* in natural river water using immobilised Degussa P25 $TiO_2$ under UVA irradiation (Degussa P25); without $TiO_2$ catalyst under UVA irradiation (UVA only); and in the dark (Dark control).**

Also shown in Figure 3.18 are the results obtained from similar suspensions kept in the dark as well as those where the catalyst was removed and the reactor irradiated with UVA. The dark control showed no inactivation, while UVA only experiments showed rapid *E. coli* inactivation: 76.85% within 4 hours (see Table 3.14 for calculated rates).

**Table 3.14 Calculated degradation rates and quantum yields for 2.4 x $10^3$ CFU $cm^{-3}$ *E. coli* in distilled water and natural river water (pH 5.0) using Degussa P25 $TiO_2$ (P25 DI and P25 NW, respectively) and UVA irradiation (UVA) in stirred-tank reactor**

| | % Degradation after 180 min | Rate / mg catalyst (CFU $cm^{-3}$ $s^{-1}$) / mg catalyst x $10^{-4}$ | Rate / catalyst surface area (CFU $cm^{-3}$ $s^{-1}$) / $m^2$ catalyst x $10^{-3}$ | % Quantum Yield mol Einstein$^{-1}$ x $10^6$ | $R^2$ |
|---|---|---|---|---|---|
| P25 DI | 87.41 | 0.579 | 1.15 | 1.81 | 0.824 |
| P25 NW | 56.6 | 1.49 | 2.80 | 4.42 | 0.949 |
| UVA | 66.83 | n/a | n/a | 8.79 | 0.979 |
| Dark | -0.20 | n/a | n/a | n/a | 0.978 |

It should be noted that the UVA-only control experiment was not a true representation of the effect of unabsorbed UVA irradiation during photocatalytic experiments, evidenced by the extremely high quantum yield (8.79 x $10^6$). For the UVA only experiments, the immobilised $TiO_2$ glass plate was removed and replaced with a clean glass plate, which is common practice within the field. This however allowed *all* emitted irradiation (minus minimal absorption by the glass) to enter the reactor. To show a true representation of the effect of UVA within the photocatalytic reactor a 'sandwich' experiment was developed whereby a clean glass plate was placed over the immobilised $TiO_2$ plate. This prevented any effects due to the photo-excitation of the $TiO_2$ interacting with the test solution, while simultaneously allowing unabsorbed UV irradiation to pass through the $TiO_2$ and into the reactor. To date no evidence of this type of experiment has been found in the literature.

3% *E. coli* inactivation in natural water (pH 5.0) was seen when performing the sandwich experiment with Degussa P25 $TiO_2$ under UVA irradiation; consistent with

results obtained in the dark control experiments. This was expected as diffuse-transmission experiments showed that Degussa P25 absorbed all the emitted UVA irradiation (see Figure 3.12 and relevant text for diffuse-transmission experimental results). Thus, all effects seen with Degussa P25 under UV photocatalytic treatment were due to the catalytic effect.

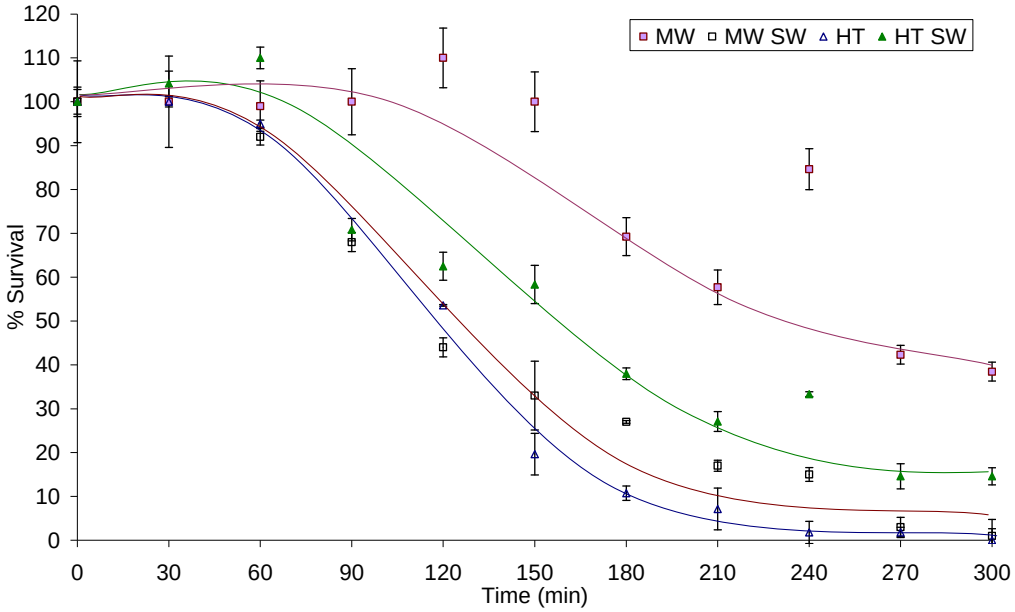


**Figure 3.19 Plots of photocatalytic inactivation in the stirred-tank reactor of ~ 1.15 x $10^3$ CFU $cm^{-3}$ *E. coli* in natural river water under UVA irradiation using immobilised MW-treated $TiO_2$ (MW); MW-treated $TiO_2$ sandwich (MW SW); HT-treated $TiO_2$ (HT); and HT-treated $TiO_2$ sandwich (HT SW).**

The photocatalytic degradation of *E. coli* with MW- and HT-treated $TiO_2$ in natural river water is shown in Figure 3.19. Interestingly these results showed an initial lag period, after which inactivation followed pseudo-first order kinetics. The disinfection rates were calculated based on the slope of the linear part of the graph between 60 and 180 minutes. Table 3.15 summarises the results of the disinfection experiments carried out in natural river water with MW- and HT-treated $TiO_2$.

The diffuse-transmission measurements (Figure 3.12) showed that for the same catalyst loadings, both the MW- and HT-treated $TiO_2$ only absorbed 75 and 81% of the emitted UVA irradiation, respectively. Therefore any disinfection seen during photocatalytic experiments was due to a combination of photocatalysis and UV effects. To determine the extent of UV inactivation, 'sandwich' experiments were

performed and are also shown Figure 3.19. The results showed both the MW- and HT-treated $TiO_2$ SW arrangements produced significant *E. coli* inactivation. Surprisingly, the rate was greater during the SW experiments than the photocatalytic experiments.

**Table 3.15 Calculated degradation rates and quantum yields for ~ 2.4 x $10^3$ CFU $cm^{-3}$ *E. coli* in natural river water (pH 5.0) using MW- and HT-treated $TiO_2$ and the aforementioned in a sandwich arrangement (denoted SW), under UVA irradiation in stirred-tank reactor**

| | % Degradation after 180 min | Rate / mg catalyst (CFU $cm^{-3}$ $s^{-1}$) / mg catalyst x $10^{-6}$ | Rate / catalyst surface area (CFU $cm^{-3}$ $s^{-1}$) / $m^2$ catalyst x $10^{-5}$ | % Quantum Yield mol $Einstein^{-1}$ $10^4$ | $R^2$ |
|---|---|---|---|---|---|
| MW | 30.77 | 1.76 | 0.746 | 0.702 | 0.953 |
| MW SW | 73.00 | 4.20 | n/a | 9.63 | 0.846 |
| HT | 89.29 | 7.65 | 2.06 | 2.94 | 0.980 |
| HT SW | 61.69 | 2.36 | n/a | 7.65 | 0.940 |

The transmission loss due to the additional glass plate was determined using UV-vis diffuse-transmission and calculated to be 6.2% and 5.6% for the MW- and HT-treated immobilised $TiO_2$, respectively. The calculated quantum yields for these experiments were corrected for this loss.

### 3.5.3.5 Photocatalytic disinfection rate in natural river water

Table 3.15 displays the calculated quantum yields obtained for *E. coli* inactivation using MW- and HT-treated $TiO_2$ catalysts in natural water from photocatalysis and SW experiments. The HT-treated $TiO_2$ produced a far greater quantum yield (2.94 x $10^2$ Einstein $cm^{-2}$ $s^{-1}$) than the MW-treated $TiO_2$ (7.02 Einstein $cm^{-2}$ $s^{-1}$); however, the most surprising discovery was even greater quantum yield obtained from the SW experiments (HT-treated $TiO_2$ SW $\Phi_{app}$ 7.65 x $10^2$ Einstein $cm^{-2}$ $s^{-1}$ and MW-treated $TiO_2$ SW $\Phi_{app}$ 9.63 x $10^2$ Einstein $cm^{-2}$ $s^{-1}$). This leads to the hypothesis that there was an inhibitory effect occurring during photocatalysis in natural water. Three possible reasons for inhibition include:

**1. pH.**

It is well documented that the pH of the degradant solution has a significant effect on the photocatalytic reaction rate.[76] Trillas et al.[77] observed that the photodegradation of 2,4-dichlorophenoxyacetic acid was greatest at a slurry pH of 3. On the other hand, the optimum pH for phenol oxidation is 7. Gimenez et al.[78] showed that the highest rate of Cr(IV) photoreduction was attained at pH 1; and catalyst deactivation occurred at pH>4. Alternatively, Vidal et al.[79] observed no discernible effect of pH during the photodegradation of ethylbenzene. Bangun and Adesina[74] showed the rate of photocatalytic degradation of sodium oxalate increased with decreasing pH up to an optimum at pH 2. Alternatively, UV is not affected by pH and would not show changes in inactivation rates at differing pH values.

The pH in the present study of 4.5 mol $dm^{-3}$ oxalic acid in distilled water was determined to be 2.5. Whilst photodegradation of oxalic acid in the natural river water proceeded, the slower oxalic acid degradation rate could not be attributed to pH effects as the solution pH was 2.6. From this, it was thought that pH alone is not the sole cause of the lowered *E. coli* deactivation rates seen.

During *E. coli* experiments the pH of the sterilised natural water was adjusted to 5.0 before photocatalytic treatment. While this was not optimum for photocatalysis, further lowering the pH may in itself contribute to the bacterial inactivation. Reasoning for this was that the optimum pH range for *E. coli* is 6.5 – 7.5.[49] Once the pH shifts away from the optimum bacterial pH, destruction of acid- or alakali-labile macromolecules, primarily within the cell wall, occurs eventually leading to the inactivation of treated bacterial cells.[80,81]

**2. The effect of inorganic ions.**

There have been several studies investigating the effect of inorganic ions on the photocatalytic degradation of organic and bacterial pollutants. Abdullah et al.[82] studied the effect of inorganic ions on the photocatalytic degradation of selected organic compounds and reported that the presence of chlorides and phosphates could decrease the degradation rate by up to 70%. Belhacova et al.[83] studied the influence of salts on the photocatalytic disinfection rate of *E. coli* and the degradation of oxalic acid in Dulbecco phosphate buffer and perchlorate solutions. Whilst the initial

bacterial count remained almost constant after four hours of photocatalytic treatment in Dulbecco phosphate buffer, significant disinfection was observed in experiments performed in distilled water. The photocatalytic degradation rate of oxalic acid was also significantly slowed in phosphate buffer. Further studies, using Ringers solution which contains a range of inorganic ions including NaCl, KCl, $CaCl_2$ and $NaHCO_3$, have been performed by Dunlop[75]. It was shown that Ringers solution prolonged bacterial stability by ensuring the bacterial cells remain in a slightly 'strengthened' state by the reducing the osmotic potential via the presence calcium ions within solution. Magnesium ions are also thought to play a vital role in prolonging bacterial viability.

In the current study, the $\Phi_{app}$ of oxalic acid in natural river water was 33% lower than similar experiments in distilled water. The $\Phi_{app}$ of *E. coli* was also lowered by 32% when performing experiments using pH-adjusted natural river water, compared to similar *E. coli* distilled water suspensions. Due to the similar levels of reduction, it was thought that the reduction in the observed disinfection rates were more likely due to the competitive action of anions with the target compounds (i.e. oxalic acid and bacterial cells) for hydroxyl radicals, rather than through reducing the osmotic potential of the bacterial cells.

**3. The effect of humic substances.**

Humic substances in aquatic systems impart a brown/yellow colour to the water, can complex with metals/organic pollutants such as pesticides and most significantly are precursors of mutagenic halogenated compounds formed after water chlorination.[84] It has been shown that $TiO_2$ photocatalysis degrades humic acid and complete mineralisation can be achieved.[85] Several investigations into the application of $TiO_2$ photocatalysis to natural water sources have been performed in recent years.[41,86-89] It has been shown that natural waters are a complex matrix and significant differences in disinfection rates in natural waters occur compared with distilled water.[40] While it has been shown that simultaneous bacterial inactivation and degradation of humic substances can be achieved by photocatalytic treatment,[90] the addition of naturally occurring organic compounds directly slow the bacterial inactivation rate. The bacteridical effect is influenced by these compounds in several ways. Humic substances can protect the bacterial cells from direct attack by physically screening

UV irradiation and hydroxyl radical attack. This occurs by adsorption onto the $TiO_2$. Alternatively, the humic acids compete for the hydroxyl radicals, reducing the number of inactivation of the target compounds. It is plausible that both of the above effects occurred, resulting in the lower rates seen during photocatalysis compared with the sandwich experiments.

In summary, it was thought that the contributing factors for the lowered inactivation rates seen when using natural river water were the competitive action of inorganic ions and humic compounds for hydroxyl radicals, as well as the adsorption of humic compounds onto the $TiO_2$, which physically screened the target compounds/cells from UV irradiation and hydroxyl radical attack.

### 3.5.3.6 Lag period in bacterial inactivation

A significant lag period was witnessed when performing the photocatalytic and UV inactivation *E. coli* experiments, both in distilled and natural river water. The lag period is defined as a period where no or minimal inactivation occurred, and was found to occur for approximately 30 minutes in distilled water (Figure 3.17) and 60 minutes in natural water (Figure 3.18 and Figure 3.19). Similar findings have been reported by other investigators.[39,42,43,91,92] These characteristics can be explained in a number of ways:

**1. The possible isotonic nature of natural water could prolong bacterial stability.**

Distilled water causes the leakage of calcium and magnesium ions from the cell surface, increasing the osmotic potential. Therefore the cells are in a weakened state and are more prone to oxidative damage. The presence of these ions in natural water decreases the osmotic stress on the cells thereby larger number of oxidative species is required to achieve cell inactivation.

**2. The presence of anions could reduce the number of hydroxyl radicals available for disinfection.**

See section 3.5.3.5, point 2. This could occur due to the competitive action of anions and bacterial cells for hydroxyl radicals.

**3. The possible recovery of bacteria from oxidative damage.**

Huang et al.[39] studied the process of bactericidal action of *E. coli* cells in a $TiO_2$ slurry reactor. The disinfection kinetics displayed a lag phase of approximately 15 minutes before inactivation was observed. Cell membrane damage was monitored, and was not found during the initial stages of photocatalytic treatment, but occurred approximately 15 – 20 minutes after its commencement. Concurrent cell viability measurements followed a similar trend: an initial 15 – 20 minute lag period followed by linear decline in viable cell concentration. Cell membrane damage is known to result in cell death; however, mechanisms to repair cell wall damage exist. Therefore cell wall damage alone will not cause bacterial inactivation. Sunada and co-workers[93] have shown this in similar experiments, and a diagrammatic representation of the proposed mechanism for the photocatalytic bactericidal effect has been shown in Figure 1.12.

As the lag phase was also observed using distilled water, which is neither isotonic in nature, nor contains inorganic ions, it is believed that the bacterial recovery phenomenon is largely responsible for the observed kinetics. In the present study, the number of hydroxyl radicals produced during the initial stages of treatment may only be sufficient to cause cell wall damage and samples removed during this stage could undergo cell wall repair and re-grow resulting in colony formation. However, the increased lag time noted during experiments using natural river water was due to the isotonic stability and the presence of inorganic ions afforded by this type of water, which 'strengthened' the bacterial cells.

### 3.5.4 Small colony variants

All photocatalytic experiments involving *E. cloacae* and *E. coli*, whether performed with suspended or immobilised $TiO_2$, or in natural or distilled water, produced small colonies upon extended treatment times. Figure 3.20 shows representative photographs obtained of *E. coli* colonies on LB agar incubated for 18 hours at 37 °C. Each plate represents *E. coli* cells within a 100 μL water suspension removed from the stirred-tank reactor during photocatalytic treatment with immobilised Degussa P25, after no treatment and treatment for 120, 240 and 360 minutes. The arrows on

each image highlight a typical colony from each treatment time. It can be seen that as treatment progresses the diameter of a typical colony was significantly reduced from 1.5 mm, until at 360 minutes, colonies were so small that it was difficult to distinguish them with the naked eye (0.3 mm). During experiments with UV irradiation (i.e. no $TiO_2$) using the stirred-tank reactor similar, smaller than average colonies were also observed.

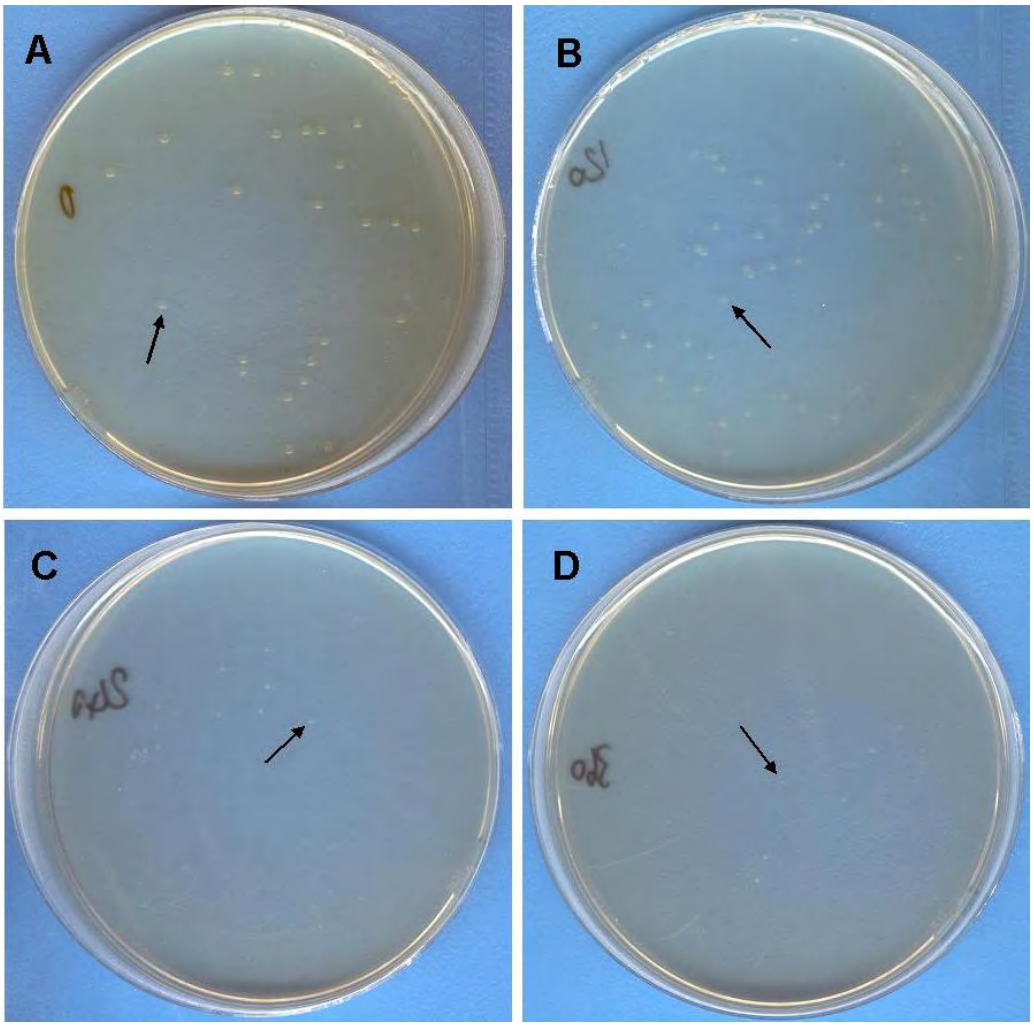


**Figure 3.20 Photographs of *E. coli* colonies on LB agar incubated for 18 hr at 37 °C. Each plate represents *E. coli* cells within a 100 µL distilled water suspension removed from the stirred-tank reactor during photocatalytic treatment with immobilised Degussa P25 and UVA irradiation at the following treatment times: A 0 min; B 120 min; C 240 min; and D 360 min.**

These smaller than average colony phenotypes among surviving bacterial population were first discovered over 80 years ago and are referred to as small colony variants (SCV's). SCV's have been previously reported in several bacterial species including *Staphylococcus aureus*, *Pseudomonas aeruginosa*, *E. coli* and *Salmonella*

*typhimurium*.[94-98] SCV's have phenotypically been characterised as hyperpilated, slow growing, non-pigmented strains which generate less toxin than the parent strain and demonstrate a different pattern of carbohydrate utilisation.[98] The appearance of SCV's is due to deficiencies in electron transport, specifically mutations in the genes responsible for menaquinone or heme biosynthesis.[95]

Recently, *E. coli* SCV's have been observed after exposure to UVA irradiation.[97] The mechanism behind this was the excitation of photosensitive molecules within the cell resulting in the production of active species such as $O_2^{\bullet-}$, $H_2O_2$ and $^{\bullet}OH$. The mechanism of photocatalytic bacterial inactivation has been proposed to occur via $O_2^{\bullet-}$ and $^{\bullet}OH$ attack.[34] It is therefore likely that the presence of SCV's after photocatalytic treatment is due to sub-lethal radical attack.

SCV's are highly invasive in animal models, but due to lower toxin production these variants may persist within host cells for extended periods without causing damage.[99] However, a typical feature of SCV's is they revert to the parent phenotype when sub-cultured onto nutrient agar. Due to this, numerous studies have demonstrated an association between SCV's and persistent, recurrent and antibiotic-resistant infections.[98] The probability of infection and its severity is dependent on a number of host and pathogen factors. Thus there is no tolerable lower limit for SCV pathogens, even very small numbers present a serious risk to immuno-compromised individuals.[98] It is due to these reasons that their presence after photocatalytic treatment is cause for concern, due to possible health hazards.

## 3.6 Conclusions

The suspended MW-treated $TiO_2$ colloids were examined for bactericidal ability. These colloids were found to inactivate 99.9% of a $10^7$ CFU $cm^{-3}$ *E. cloacae* suspension within the first 30 minutes of treatment. This was compared to similar catalyst loadings of Degussa P25 and HT-treated $TiO_2$. While all three catalyst types produced similar % inactivation after 30 minutes of treatment, when the inactivation rates were compared with the catalyst surface area, the MW-treated and HT-treated $TiO_2$ were approximately 28 and 14%, respectively, that of the Degussa P25.

Degussa P25, MW-treated $TiO_2$ and HT-treated $TiO_2$ colloids were immobilised onto borosilicate glass. It was discovered for the first time that dip-coating is unsuitable for immobilisation of both the MW-treated and HT-treated $TiO_2$ colloids. A spray-coating method was attempted and produced films of a very good quality for all three catalysts types. The immobilised colloids were then examined for photocatalytic degradation of oxalic acid.

During oxalic acid photodegradation when using UVA irradiation, the immobilised Degussa P25 $TiO_2$ produced a degradation rate of $3.08 \times 10^{-8}$ mol $s^{-1}$ per $m^2$ catalyst. The MW-treated and HT-treated $TiO_2$ immobilised colloids resulted in degradation rates of $4.42 \times 10^{-9}$ mol $s^{-1}$ per $m^2$ catalyst and $4.13 \times 10^{-9}$ mol $s^{-1}$ per $m^2$ catalyst, respectively.

When using UVB irradiation, the Degussa P25 $TiO_2$ produced a photodegradation rate of $7.53 \times 10^{-8}$ mol $s^{-1}$ per $m^2$ catalyst, while the MW-treated and HT-treated $TiO_2$ catalysts resulted in photodegradation rates of $4.45 \times 10^{-9}$ mol $s^{-1}$ per $m^2$ catalyst and $3.10 \times 10^{-9}$ mol $s^{-1}$ per $m^2$ catalyst, respectively.

The incident photon flux and diffuse-transmission spectroscopy was used to calculate the apparent quantum yield for each of the immobilised catalysts for both UVA and UVB irradiation. The quantum yields obtained for the three catalyst types using UVA irradiation were between 15.5 and 94.5%. When using UVB irradiation, the only quantum yield to significantly increase was that of Degussa P25 $TiO_2$, while

the MW-treated and HT-treated $TiO_2$ catalyst quantum yields remained unchanged. It was discovered that a mechanism change had occurred in the Degussa P25 compared to the MW- and HT-treated $TiO_2$. This was due to Degussa P25 consisting of a mixed-phase anatase and rutile composition, while the MW-treated and HT-treated $TiO_2$ colloids possess a majority of anatase crystallites and no rutile. The increased quantum yield of Degussa P25 was due to electrons in the anatase CB vectorially displacing into the conduction band of the rutile, which resulted in greater charge separation and lower recombination.

The three catalyst types were also examined for photocatalytic inactivation of *E. coli* in natural river water under UVA irradiation. It was discovered that for photocatalytic inactivation using UVA irradiation to be observed, the pH of the river water had to be lowered to 5.0 and a bacterial cell loading of approximately $1 \times 10^3$ CFU $cm^{-3}$ had to be used. The inactivation rates were calculated to be $2.80 \times 10^{-3}$ CFU $cm^{-3}$ per $m^2$ catalyst for the Degussa P25 $TiO_2$. The MW-treated and HT-treated $TiO_2$ produced inactivation rates of $7.46 \times 10^{-4}$ CFU $cm^{-4}$ per $m^2$ catalyst and $2.06 \times 10^{-4}$ CFU $cm^{-5}$ per $m^2$ catalyst, respectively.

When comparing the calculated quantum yields it was found that the HT-treated $TiO_2$ produced the best yield of the three catalyst types examined approximately 10-fold higher than the Degussa P25 and MW-treated $TiO_2$. However, it was discovered through the development of a sandwich arrangement that a significant amount of the inactivation seen using the MW-treated and HT-treated $TiO_2$ catalysts was due to direct inactivation of the bacterial cells by the UV irradiation. In fact, for the MW-treated and HT-treated $TiO_2$ catalysts, the inactivation rates were higher using the sandwich arrangement then photocatalysis (260% and 1370% higher, respectively). This was thought to be due to the competitive action of inorganic ions and humic substances for hydroxyl radicals, as well as the humic acids physically screening the cells from UV and hydroxyl radical attack.

A significant lag period of approximately 60 minutes in *E. coli* inactivation was observed when using all three catalyst types in natural river water. As this was also present when using distilled water (albeit over a shorter time frame), it was mainly

attributed to bacterial recovery. However, inorganic ions and the isotonic nature of the river water may have extended the lag period.

A decrease in colony size (from 1.5 mm to 0.3 mm) was noted during photocatalytic experiments. These so-called SCV's are thought to occur during sublethal $^{\bullet}OH$ and $O_2^{\bullet-}$ attack. SCV's have been linked to persistent, recurrent and antibiotic-resistant infections and their presence after photocatalytic treatment is worrisome regarding potential health risks involved with this water treatment method.

## 3.7 References


(1) Ollis, O. F.; Al-Ekabi, H. *Photocatalytic Purification and Treatment of Water and Air*; Elsevier-Science: Lausanne, 1993.

(2) Liang, J.; Feng, Y.; Liang, G.; Ji, Z.; Wang, J.; Yan, X.; Jin, Z. *J. Mater. Sci. Lett.* **2003**, *22*, 1503-1506.

(3) Tseng, I. H.; Wu, J. C. S.; Chou, H.-Y. *J. Catal.* **2004**, *221*, 432-440.

(4) Murakami, T. N.; Kijitori, Y.; Kawashima, N.; Miyasaka, T. *J. Photochem. Photobiol., A* **2004**, *164*, 187-191.

(5) Jung, C.-K.; Bae, I. S.; Song, Y. H.; Boo, J. H. *Surf. Coat. Technol.* **2005**, *200*, 1320-1324.

(6) Usami, A.; Ozaki, H. *J. Phys. Chem. B* **2005**, *109*, 2591-2596.

(7) Hore, S.; Palomares, E.; Smit, H.; Bakker, N. J.; Comte, P.; Liska, P.; Thampi, K. R.; Kroon, J. M.; Hinsch, A.; Durrant, J. R. *J. Mater. Chem.* **2005**, *15*, 412-418.

(8) Bavykin, D. V.; Parmon, V. N.; Lapkin, A. A.; Walsh, F. C. *J. Mater. Chem.* **2004**, *14*, 3370-3377.

(9) Hoang, T. K. N.; Deriemaeker, L.; La, V. B.; Finsy, R. *Langmuir* **2004**, *20*, 8966-8969.

(10) Bensebaa, F.; Patrito, N.; Le Page, Y.; L'Ecuyer, P.; Wang, D. *J. Mater. Chem.* **2004**, *14*, 3378-3384.

(11) Ren, T.-Z.; Yuan, Z.-Y.; Su, B.-L. *Langmuir* **2004**, *20*, 1531-1534.

(12) Wilson, G. J.; Matijasevich, A. S.; Mitchell, D. R. G.; Schulz, J. C.; Will, G. D. *Langmuir* **2006**, *22*, 2016-2027.

(13) Patra, C. R.; Gedanken, A. *New J. Chem.* **2004**, *28*, 1060-1065.

(14) Herrmann, J.-M. *Catal. Today* **1999**, *53*, 115-129.

(15) Byrne, J. A.; Eggins, B. R. *J. Electroanal. Chem.* **1998**, *457*, 61-72.

(16) Mills, A.; Le Hunte, S. *J. Photochem. Photobiol., A* **1997**, *108*, 1-35.

(17) Alfano, O. M.; Bahnemann, D.; Cassano, A. E.; Dillert, R.; Goslich, R. *Catal. Today* **2000**, *58*, 199-230.

(18) Matthews, R. W. *Sol. Energy* **1987**, *38*, 405-13.

(19) Matthews, R. W. *J. Phys. Chem.* **1987**, *91*, 3328-33.

(20) Aguado, J.; van Grieken, R.; Lopez-Munoz, M. J.; Marugan, J. *Catal. Today* **2002**, *75*, 95-102.

(21) Fernandez, A.; Lassaletta, G.; Jimenez, V. M.; Justo, A.; Gonzalez-Elipe, A. R.; Herrmann, J.-M.; Tahiri, H.; Ait-Ichou, Y. *Appl. Catal., B* **1995**, *7*, 49-63.

(22) Ding, Z. PhD, The University of Queensland, 2000.

(23) Pozzo, R. L.; Baltanas, M. A.; Cassano, A. E. *Catal. Today* **1997**, *39*, 219-231.

(24) Minabe, T.; Tryk, D. A.; Sawunyama, P.; Kikuchi, Y.; Hashimoto, K.; Fujishima, A. *J. Photochem. Photobiol., A* **2000**, *137*, 53-62.

(25) Rachel, A.; Subrahmanyam, M.; Boule, P. *Appl. Catal., B* **2002**, *37*, 301-308.

(26) Mills, A.; Morris, S. *J. Photochem. Photobiol., A* **1993**, *71*, 285-289.

(27) Dijkstra, M. F. J.; Michorius, A.; Buwalda, H.; Panneman, H. J.; Winkelman, J. G. M.; Beenackers, A. A. C. M. *Catal. Today* **2001**, *66*, 487-494.

(28) Herrmann, J.-M.; Tahiri, H.; Ait-Ichou, Y.; Lassaletta, G.; Gonzalez-Elipe, A. R.; Fernandez, A. *Appl. Catal., B* **1997**, *13*, 219-228.

(29) Horikoshi, S.; Watanabe, N.; Onishi, H.; Hidaka, H.; Serpone, N. *Appl. Catal., B* **2002**, *37*, 117-129.

(30) Byrne, J. A.; Eggins, B. R.; Brown, N. M. D.; McKinney, B.; Rouse, M. *Appl. Catal., B* **1998**, *17*, 25-36.

(31) Horikoshi, S.; Satou, Y.; Hidaka, H.; Serpone, N. *J. Photochem. Photobiol., A* **2001**, *146*, 109-119.

(32) Guillard, C.; Beaugiraud, B.; Dutriez, C.; Herrmann, J.-M.; Jaffrezic, H.; Jaffrezic-Renault, N.; Lacroix, M. *Appl. Catal., B* **2002**, *39*, 331-342.

(33) Ray, A. K.; Beenackers, A. A. C. M. *Catal. Today* **1998**, *40*, 73-83.

(34) Matsunaga, T.; Tomada, R.; Nakajima, T.; Wake, H. *FEMS Microbiol. Lett.* **1985**, *29*, 211-214.

(35) Amezaga-Madrid, P.; Silveyra-Morales, R.; Cordoba-Fierro, L.; Nevarz-Moorillon, G. V.; Miki-Yoshida, M.; Orrantia-Borunda, E.; Solis, F. J. *J. Photochem. Photobiol., B* **2003**, *70*, 45-50.

(36) Blake, D. M.; Maness, P.-C.; Huang, Z.; Wolfrum, E. J.; Huang, J.; Jacoby, W. A. *Sep. Purif. Meth.* **1999**, *28*, 1-50.

(37) Tao, H.; Wei, W.; Zhang, S. *J. Photochem. Photobiol., B* **2004**, *161*, 193-199.

(38) Maness, P.-C.; Smolinski, S.; Blake, D. M.; Huang, Z.; Wolfrum, E. J.; Jacoby, W. A. *Appl. Environ. Microbiol.* **1999**, *65*, 4094-4098.

(39) Huang, Z.; Maness, P.-C.; Blake, D. M.; Wolfrum, E. J.; Smolinski, S. L.; Jacoby, W. A. *J. Photochem. Photobiol., A* **2000**, *130*, 163-170.

(40) Watts, R. J.; Kong, S.; Orr, M. P.; Miller, G. C.; Henry, B. E. *Water Res.* **1995**, *29*, 95-100.

(41) Arana, J.; Herrera Melian, J. A.; Dona Rodriguez, J. M.; Gonzalez Diaz, O.; Viera, A.; Perez Pena, J.; Marrero Sosa, P. M.; Espino Jimenez, V. *Catal. Today* **2002**, *76*, 279-289.

(42) Ireland, J.; Klostermann, P.; Rice, E.; Clark, R. *Appl. Environ. Microbiol.* **1993**, *59*, 1668-1670.

(43) Dunlop, P. S. M.; Byrne, J. A.; Manga, N.; Eggins, B. R. *J. Photochem. Photobiol., A* **2002**, *148*, 355-363.

(44) O'Regan, B.; Moser, J.; Anderson, M.; Graetzel, M. *J. Phys. Chem.* **1990**, *94*, 8720-6.

(45) Barbe, C. J.; Arendse, F.; Comte, P.; Jirousek, M.; Lenzmann, F.; Shklover, V.; Gratzel, M. *J. Am. Ceram. Soc.* **1997**, *80*, 3157-3171.

(46) Wilson, G. J.; Will, G. D.; Frost, R. L.; Montgomery, S. A. *J. Mater. Chem.* **2002**, *12*, 1787-1791.

(47) McMurray, T. A. PhD, University of Ulster, 2004.

(48) McMurray, T. A.; Byrne, J. A.; Dunlop, P. S. M.; Winkelman, J. G. M.; Eggins, B. R.; McAdams, E. T. *Appl. Catal., A* **2004**, *262*, 105-110.

(49) *Bergey's Manual of Systematic Bacteriology*; Krieg, N.; Holt, J., Eds.; Williams and Wilkins: Baltimore, MD, 1984; 1.

(50) Bilmes, S. A.; Mandelbaum, P.; Alvarez, F.; Victoria, N. M. *J. Phys. Chem. B* **2000**, *104*, 9851-9858.

(51) Boschloo, G.; Fitzmaurice, D. *J. Phys. Chem. B* **1999**, *103*, 2228-2231.

(52) Atashbar, M. Z.; Sun, H. T.; Gong, B.; Wlodarski, W.; Lamb, R. *Thin Solid Films* **1998**, *326*, 238-244.

(53) Zanoni, R.; Righini, G.; Montenero, A.; Gnappi, G.; Montesperelli, G.; Traversa, E.; Gusmano, G. *Surf. Interface Anal.* **1994**, *22*, 376-9.

(54) Moulder, J. F.; Stickle, W. F.; Sool, P. E.; Bomben, K. D. *Handbook of X-ray Photoelectron Spectroscopy*; Perkin-Elmer: Eden Prairie, 1992.

(55) Yu, J.; Yu, J. C.; Ho, W.; Jiang, Z. *New J. Chem.* **2002**, *26*, 607-613.

(56) Kun, R.; Szekeres, M.; Dekany, I. *Appl. Catal., B* **2006**, *68*, 49-58.

(57) Presley, R. W. In *Sci. Technol. Alliance, Mater. Conf.* 1995, p 211-16.

(58) Egerton, T. A.; Tooley, I. R. *J. Phys. Chem. B* **2004**, *108*, 5066-5072.

(59) Nargiello, M.; Herz, T. *Trace. Met. Environ.* **1993**, *3*, 801-7.

(60) Gregg, S.; Sing, K. *Adsorption, Surface Area and Porosity*; 2 ed.; Academic Press: New York, 1982.

(61) Sing, K. S. W.; Everett, D. H.; Haul, R. A. W.; Moscou, L.; Pierotti, R. A.; Rouquerol, J.; Siemieniewska, T. *Pure Appl. Chem.* **1985**, *57*, 603-19.

(62) Agrios, A. G.; Gray, K. A. *Environ. Catal.* **2005**, 369-390.

(63) McMurray, T. A.; Byrne, J. A.; Dunlop, P. S. M.; McAdams, E. T. *J. Appl. Electrochem.* **2005**, *35*, 723-731.

(64) Brusa, M. A.; Grela, M. A. *J. Phys. Chem. B* **2005**, *109*, 1914-1918.

(65) Blazkova, A.; Csolleova, I.; Brezova, V. *J. Photochem. Photobiol., A* **1998**, *113*, 251-256.

(66) Stafford, U.; Gray, K. A.; Kamat, P. V. *J. Catal.* **1997**, *167*, 25-32.

(67) Noguchi, H.; Ohtani, B.; Uosaki, K. *Chem. Lett.* **2005**, *34*, 694-695.

(68) Bickley, R. I.; Gonzalez-Carreno, T.; Lees, J. S.; Palmisano, L.; Tilley, R. J. D. *J. Solid State Chem.* **1991**, *92*, 178-90.

(69) Yu, J. C.; Zhang, L.; Yu, J. *New J. Chem.* **2002**, *26*, 416-420.

(70) Hurum, D. C.; Agrios, A. G.; Gray, K. A.; Rajh, T.; Thurnauer, M. C. *J. Phys. Chem. B* **2003**, *107*, 4545-4549.

(71) Augugliaro, V.; Loddo, V.; Marci, G.; Palmisano, L.; Lopez-Munoz, M. J. *J. Catal.* **1997**, *166*, 272-283.

(72) Piscopo, A.; Robert, D.; Weber, J. V. *J. Photochem. Photobiol., A* **2001**, *139*, 253-256.

(73) Ibarz Grau, C. "Unpublished Results," University of Zaragoza, 2005.

(74) Bangun, J.; Adesina, A. A. *Appl. Catal., A* **1998**, *175*, 221-235.

(75) Dunlop, P. S. M. D. Phil., University of Ulster, 2001.

(76) Jaussaud, C.; Paisse, O.; Faure, R. *J. Photochem. Photobiol., A* **2000**, *130*, 157-162.

(77) Trillas, M.; Peral, J.; Domenech, X. *Appl. Catal., B* **1995**, *5*, 377-87.

(78) Gimenez, J.; Aguado, M. A.; Cervera-March, S. *J. Mol. Catal. A: Chem.* **1996**, *105*, 67-77.

(79) Vidal, A.; Herrero, J.; Romero, M.; Sanchez, B.; Sanchez, M. *J. Photochem. Photobiol., A* **1994**, *79*, 213-19.

(80) Madigan, M. T.; Martinko, J. M.; Parker, J. *Brock Biology of Microorganisms*; 9th ed.; Prentice-Hall, Inc.: New Jersey, 2000.

(81) Claessens, J.; Van Lith, Y.; Laverman, A. M.; Van Cappellen, P. *Geochim. Cosmochim. Acta* **2006**, *70*, 267-276.

(82) Abdullah, M.; Low, G. K. C.; Matthews, R. W. *J. Phys. Chem.* **1990**, *94*, 6820-5.

(83) Belhacova, L.; Krysa, J.; Geryk, J.; Jirkovsky, J. *J. Chem. Technol. Biotechnol.* **1999**, *74*, 149-154.

(84) Eggins, B. R.; Palmer, F. L.; Byrne, J. A. *Water Res.* **1997**, *31*, 1223-1226.

(85) Ogawa, S.; Tanigawa, M.; Fujioka, M.; Hanasaki, Y. *Jpn J. Toxicol. Environ. Health* **1995**, *41*, P7.

(86) Shah, S. K.; McBean, E. A.; Anderson, W. A. *Can. J. Civ. Eng.* **1996**, *23*, 373-380.

(87) Dillert, R.; Siemon, U.; Bahnemann, D. *Chem. Eng. Technol.* **1998**, *21*, 356-358.

(88) Melian, J. A. H.; Rodriguez, J. M. D.; Suarez, A. V.; Rendon, E. T.; Do Campo, C. V.; Arana, J.; Pena, J. P. *Chemosphere* **2000**, *41*, 323-327.

(89) Lu, Y.-g.; Ma, J.-j. *Beijing Gongshang Daxue Xuebao, Ziran Kexueban* **2005**, *23*, 4-7.

(90) Rincon, A. G.; Pulgarin, C.; Adler, N.; Peringer, P. *J. Photochem. Photobiol., A* **2001**, *139*, 233-241.

(91) Koizumi, Y.; Yamada, R.; Nishioka, M.; Matsumura, Y.; Tsuchido, T.; Taya, M. *J. Chem. Technol. Biotechnol.* **2002**, *77*, 671-677.

(92) Lee, S.-A.; Choo, K.-H.; Lee, C.-H.; Lee, H.-I.; Hyeon, T.; Choi, W.; Kwon, H.-H. *Ind. Eng. Chem. Res.* **2001**, *40*, 1712-1719.

(93) Sunada, K.; Watanabe, T.; Hashimoto, K. *J. Photochem. Photobiol., A* **2003**, *156*, 227-233.

(94) McNamara, P. J.; Proctor, R. A. *Inter. J. Antimicrob. Agents* **2000**, *14*, 117-122.

(95) Proctor, R. A.; Balwit, J. M.; Vesga, O. *Infect. Agents Dis.* **1994**, *3*, 302-12.

(96) Proctor, R. A.; van Langevelde, P.; Kristjansson, M.; Maslow, J. N.; Arbeit, R. D. "Persistent and relapsing infections associated with small-colony variants of Staphylococcus aureus," Department of Medicine, University of Wisconsin-Madison Medical School 53706, 1995.

(97) Robertson, J. M. C.; Robertson, P. K. J.; Lawton, L. A. *J. Photochem. Photobiol., A* **2005**, *175*, 51-56.

(98) von Eiff, C.; Heilmann, C.; Proctor, R. A.; Woltz, C.; Peters, G.; Gotz, F. *J. Bacteriol.* **1997**, *179*, 4706-4712.

(99) Schiemann, D. A. *FEMS Microbiol. Lett.* **1995**, *130*, 45-9.

# Chapter 4

## *IN SITU* FTIR STUDIES OF IMMOBILISED-$TiO_2$ PHOTOCATALYSIS AND ELECTROCHEMICALLY-ASSISTED PHOTOCATALYSIS

**Note to Reader**: The work described in this chapter was carried out by the candidate under the supervision of Dr Geoffrey Will and A. Prof. Louise Hafner. All colloidal dispersions utilised by the candidate were prepared by Aaron Matijasevich. *In situ* FTIR spectroscopic studies were performed by the candidate at the University of Newcastle upon Tyne (UK), within the School of Chemical Engineering and Advanced Materials, under the supervision of Prof. P.A. Christensen.

## 4.1 Introduction

The first *in situ* FTIR spectroscopic study was reported by Pons and co-workers in 1981.[1] Since then, it has become a well-recognised analytical tool in studying electrochemical mechanisms and has been used to study a range of systems including the reduction of halogenated phenols,[2] temperature effects on the electro-oxidation of organic molecules,[3,4] and photodegradation of paints.[5]

Modern FTIR spectrometers are capable of high signal-to-noise ratios with further improvements gained through the use of co-adding and averaging spectra. Although the sensitivity of modern FTIR spectroscopy is adequate for *in situ* applications, solvent absorption must be minimised. An excellent review by Christensen and Hamnett[6] covers how this can be accomplished using transmission, internal reflection and external reflectance techniques; however the most common approach is external reflectance. This method minimises solvent absorption by trapping a thin layer of electrolyte (1 – 50 μm) between the IR transparent window and the reflective working electrode. Although this minimises solvent absorption, water absorption is still strong and as such, absorptions due to solution and adsorbed species are relatively weak. In order to reveal these, a 'difference protocol' is usually employed. Spectra are represented as:[6]

$$\frac{\Delta R}{R} = \frac{(S_s - S_r)}{S_r} \quad versus \quad \tilde{\upsilon} \qquad \textbf{4.1}$$

or:

$$Absorbance = -\log_{10}\left(\frac{S_s}{S_r}\right) \quad versus \quad \tilde{\upsilon} \qquad \textbf{4.2}$$

$$= -(\log_{10} S_s - \log_{10} S_r) \quad versus \quad \tilde{\upsilon}$$

where, $\tilde{\upsilon}$ is wavenumber ($cm^{-1}$). During electrochemical studies,[6] the reference spectrum, $S_r$, is collected at the reference potential, $E_r$, usually chosen to be in the electro-inactive region. The potential is then stepped to successively higher or lower values, $E_s$, and spectra, $S_s$, are collected at each step, or the potential is changed in a single increment and the spectra, $S_s$, collected as a function of time. Both equations 4.1 and 4.2 result in difference spectra which only contain absorptions that change with potential and/or time. In the case of the protocol in equation 4.2, which was

employed in the FTIR experiments reported in this chapter, features pointing up, positive absorbance, are due to species gained, while features pointing down, negative absorbance, are due to species lost. While the signal-to-noise ratio for spectra is proportional to the square root of the scans taken, a disadvantage of taking a large number of scans for each spectrum is the stability of the system over the period of measurements. Christensen and co-workers have noted that fluctuations in the source temperature and a change in the concentration of $CO_2$ and $H_2O$ vapour in the sample compartment, can adversely affect spectra collected.[7]

### 4.1.1 *In situ* FTIR and $TiO_2$

*In situ* FTIR spectroscopy is a powerful technique in identifying surface processes on semiconductors as classical (eg. *Ivt*) electrochemical techniques can not be satisfactorily used to unambiguously establish mechanistic pathways.[8] In 1983, Bockris and co-workers reported the first study of a photoexcited electrode, however, it was not until 1994 that Grätzel and co-workers[9] and Hug and Sulzberger[10] used the technique to study solvent break-down mechanisms at irradiated $TiO_2$ electrodes. Since then extensive research in the field has been undertaken.[5,8,11-13] Although the basic photocatalytic reactions of $TiO_2$ are well known and the evidence of hydroxyl radicals as the primary oxidant is extensive, understanding of the chemistry at the $TiO_2$ surface and the surface states within photocatalytic systems remains speculative.[13] Surface structure plays a role in this process and it has been shown that rutile is much less photoactive despite the larger (200 meV larger)[14] bandgap compared to anatase. The enhanced photoactivity of anatase has been attributed to greater $O_2$ surface adsorption and the greater reduction rate of $O_2$ by electrons in the conduction band. The type and extent of surface hydroxylation also plays a significant role.

*In situ* FTIR has been used to examine $TiO_2$ electrodes prepared via the oxidation of Ti metal substrates,[8,11] as well as mesoporous films, such as Degussa P25,[12] and single $TiO_2$ crystals.[13] These works have shown that photo-induced evolution of oxygen from water and the oxidation of model organics can be followed. In particular, detailed behaviour of the surface-bound oxygen and carbon dioxide can be investigated.[8]

The appearance of unusual baseline features has been observed by many researchers. An optical phonon band near 1580 $cm^{-1}$ under UV irradiation has been identified, which was not observed in the dark, and was associated with the accumulation of surface-mobile holes at the complex, porous film-electrolyte interface.[11] The capacity of such holes were thought to enhance the absorption cross-section of rutile at the surface of the $TiO_2$/ectrolyte interface. Szczepankiewicz et al. have also shown that band-gap irradiation produced a broad baseline feature with increasing absorption to longer wavelength,[15-17] while the opposite effect (increasing to shorter wavelength) has been demonstrated in several studies.[12,18] This line of research is controversial and under continued investigation.

### 4.1.2 Micro-organisms and N-acetyl-*D*-glucosamine (NAG)

Many investigations into the mechanisms responsible for the bactericidal effect during photocatalysis have been performed with substantial evidence that the cell membrane is the site of primary attack.[19-21]

Oxidative attack on bacterial cells causes lipid peroxidation leading to loss of integrity of the cell membrane.[20] Once this occurs cell respiration ceases. This, combined with subsequent oxidative attack of intracellular components,[22,23] ultimately leads to cell death. Despite compelling evidence of these mechanisms, and the cell wall destruction mechanism proposed by Sunada et al.,[19] little research regarding the photocatalytic effect on the peptidoglycan layer has been performed. This layer protects the cell from environmental factors and in the case of gram-positive bacteria, it is the first structure encountered by external factors.[24] As such, to fully understand the mechanisms of bacterial disinfection, it is vitally important to understand the effects of photocatalysis on all cellular components, especially those within the cell wall as it is the primary site of attack.

### 4.1.3 Choice of model pollutants

Model pollutants for a standard test system should be a recognised organic pollutant which is water soluble, inexpensive, easily analysed, non-volatile, photochemically

inactive and completely photomineralised using $TiO_2$ as the semiconductor photocatalyst. The electrochemical oxidation of oxalate $(COO)_2^{2-}$ on a pyrolytic graphite electrode has been reported to occur via an irreversible $2e^-$ process to yield $CO_2$ as the sole product (equation 4.3).[25] Hence, the photocatalytic oxidation of oxalate should not be complicated by the production of intermediate species, nor should oxygen be necessary for mineralisation.

$$^{-}OOC - COO^{-} \xrightarrow{-2e^{-}} 2CO_2 \qquad \textbf{4.3}$$

Oxalic acid is an intermediate product from the photocatalytic degradation of larger organic compounds, it does not undergo photolysis in the 300 – 400 nm region and has been previously used in other photocatalytic studies.[26,27] This compound, when in aqueous solution, displays a relatively simple FTIR spectrum with two peaks observed at 1310 and 1565 $cm^{-1}$ due to the anti-symmetric and symmetric C=O stretching vibrations, respectively.[28]

To investigate the effect of photocatalysis on a component of the bacterial cell wall, the carbohydrate, NAG was chosen as a model compound. All bacterial species possess a layer of peptidoglycan consisting of repeating units of NAG and NAM, within their cell wall (see Figure 4.1).[29] Due to the build-up of the carbohydrate components, it provides added protection from external factors.

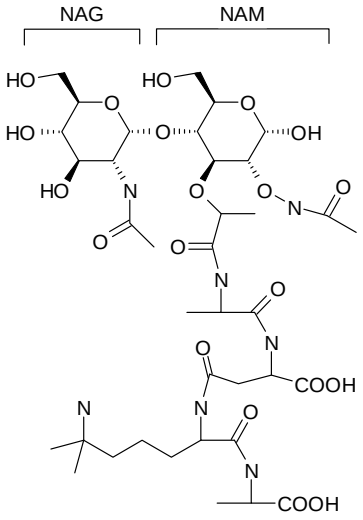


**Figure 4.1 Chemical structure of N-acetyl-D-glucosamine (NAG) and N-acetyl-muramic acid (NAM)**

Similar studies into the oxidation of other carbohydrates have been performed, also using *in situ* FTIR spectroscopy. The investigations to date have mainly focused on the degradation of glucose; however some investigations into other sugars, such as D-sorbitol[30-32] and fructose[33] have been performed. *In situ* FTIR spectra of glucose and D-sorbitol during electro-oxidation showed a strong positive absorbance band at 1780 $cm^{-1}$ which was assigned to the ν(C=O) stretch of a saturated γ-lactone (five-membered ring) and a weaker gain at 1740 $cm^{-1}$ due to the carbonyl stretch in a six-membered ring.[30,34] There was also the presence of a band at 1731 $cm^{-1}$ due to adsorbed δ-lactone.[32] It must be noted that no evidence to date has been found of any *in situ* FTIR investigation into the *photocatalytic* degradation of carbohydrates. In addition, knowledge of the mechanisms of carbohydrate degradation within the literature is limited. This is even more apparent with regards to the degradation of NAG, as no evidence of this could be found.

## 4.2 Aims and Objectives

The aim of this section of work was to use *in situ* FTIR spectroscopy to compare the photocatalytic and electrochemically-assisted photocatalytic (EAP) efficiency of immobilised $TiO_2$ electrodes using a model organic compound and a component present in the bacterial cell wall.

Objectives:

1. To determine a technique suitable for immobilisation of powders onto electrodes for *in situ* FTIR spectroscopic investigations.
2. To characterise the $TiO_2$-coated electrode using standard electrochemical techniques.
3. To investigate the photocatalytic degradation of $Na_2(OOC)_2$ using *in situ* FTIR spectroscopy.
4. To investigate the EAP degradation of $Na_2(OOC)_2$ using *in situ* FTIR spectroscopy.
4. To investigate photocatalytic and EAP degradation on a bacterial cell wall component (NAG) using different types of $TiO_2$ colloids.
5. To compare photocatalytic and EAP degradation kinetics and mechanisms of the $TiO_2$ catalyst types.

## 4.3 Experimental

### 4.3.1 Substrate preparation

The substrate used was Ti metal (99.6 % purity, Goodfellow). The 25 mm diameter metal rod was cut to the required size and shape. Before coating, the substrate's face was roughly polished with fine-grade sandpaper until a smooth surface was obtained. The substrate was rinsed with deionised water and air-dried, followed by fine polishing using 0.3 μm alumina (BDH). Once a mirror-like sheen was produced, the substrate was cleaned by ultrasonic treatment in 18 MΩ cm Milli-Q water for 30 minutes. The washing procedure was then repeated. After drying, the substrate was accurately weighed.

### 4.3.2 Stabilised $TiO_2$ colloidal preparation

Degussa P25 $TiO_2$ powder (TITANDIOXID P25, D-60287, PI-52342) was purchased from Degussa AG (Frankfurt). Degussa P25 consists of 25:75 rutile:anatase crystal form, with a purity of 99.9 %.

Stable colloidal $TiO_2$ solutions were prepared via the hydrolysis of titanium (IV) isopropoxide following a procedure adapted from O'Regan et al.[35] and is described in detail in Chapter 3, Section 3.4.7.

HT- and MW-treated $TiO_2$ colloids were prepared following procedures also described in Chapter 3, Section 3.4.7. Briefly, convective HT-treated $TiO_2$ colloids were prepared by placing a portion of the previously prepared stable colloidal $TiO_2$ solution into a Pyrex glass-lined, stainless steel parr bomb and treating in a convection oven at 145 °C for 15 hours. MW-treated $TiO_2$ colloids were prepared by a method developed by Wilson et al[36] by placing a portion of the previously prepared stable colloidal $TiO_2$ solution into a Teflon-lined digestion vessel and treating in a microwave oven at 145 °C for 1 hour. Both the convective hydrothermal and microwave treated colloidal suspensions were then dehydrated at 80 °C for 3 hours.

### 4.3.3 Coating of substrates with $TiO_2$

30 mg of $TiO_2$ colloid was suspended in 5.0 $cm^3$ of 18 MΩ cm Milli-Q water by ultrasonic treatment for 10 minutes. The substrate face was coated with the colloid suspension using an eye-dropper and dried at 80 °C for 30 minutes and accurately weighed after cooling to room temperature.

Thermal $TiO_2$ electrodes were prepared following a procedure developed by Christensen et al.[37] Briefly, the polished Ti electrode was placed into a preheated furnace (700 °C) in air to induce oxidation of the Ti electrode surface. After heating for 10 minutes the electrode was immediately removed from the furnace and allowed to cool to room temperature.

### 4.3.4 Electrochemical measurements

An Autolab potentiostat (PGSTAT30, Windsor Scientific Ltd.) with PC control and GPES v 4.8 software was used for electrochemical measurements.

### 4.3.5 pH measurements

pH was measured using a pH electrode (Gelpas BDH) linked to a digital pH meter (Philips 9404).

### 4.3.6 *In situ* external reflectance FTIR reactor design

The *in situ* FTIR cell (see Figure 4.2) was developed by Christensen and co-workers[8] and was of a thin layer design. The cell required careful design and manufacture, particularly the solution seals.

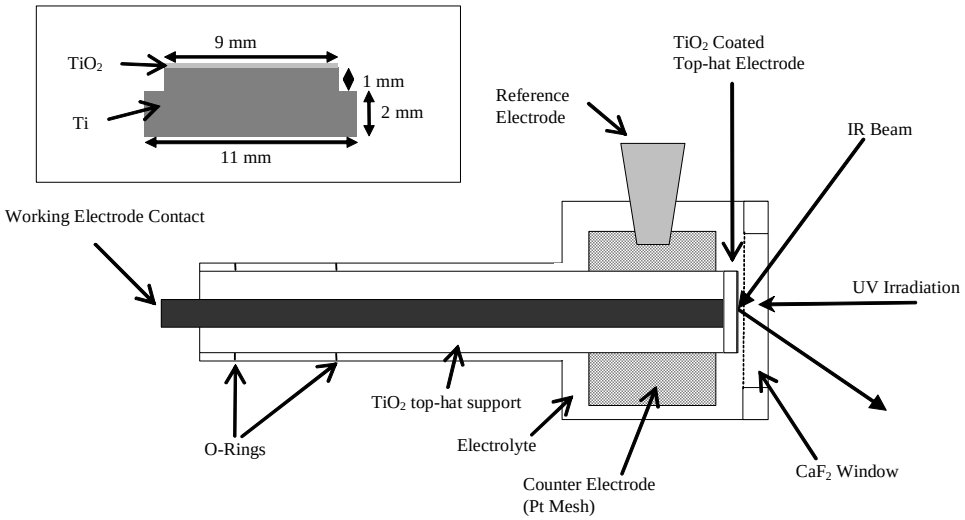


**Figure 4.2 Schematic representation of cross-sectional view of *in situ* FTIR photocatalytic sample cell arrangement. Inset: schematic representation of Ti 'top-hat' electrode with dimensions.**

The $TiO_2$ catalyst was immobilised onto a polished Ti 'top-hat' (Figure 4.2 inset). The top-hat was secured onto the PTFE top-hat supporting rod using a PTFE screw-top with hollowed centre which exposed the $TiO_2$-coated face. The supporting rod was inserted into an external glass sample housing creating a seal at the base of the glass housing via an O-ring. The $CaF_2$ window was secured in place using an outer PTFE screw-top. The sample cell housing arrangement is shown in Figure 4.3. The distance of the $TiO_2$-coated top-hat from the $CaF_2$ window was able to be increased and decreased using a screw mechanism attached to the butt of the supporting rod shown in Figure 4.3. During experiments the top-hat was positioned so that only a thin layer of electrolyte was trapped between the surface and the $CaF_2$ window.

The electrolyte solution was aqueous 0.1 mol $dm^{-3}$ $Na_2SO_4$, was stored in a reservoir and was introduced into the reactor cell using a PTFE screw-tap. Waste electrolyte was removed using the waste outlet allowing the reactor to be refilled without dismantling. Electrolyte solution was replenished after each experiment by withdrawing the $TiO_2$ coated top-hat from the $CaF_2$ window and allowing fresh electrolyte to flow from the reservoir, displacing the used electrolyte to waste.

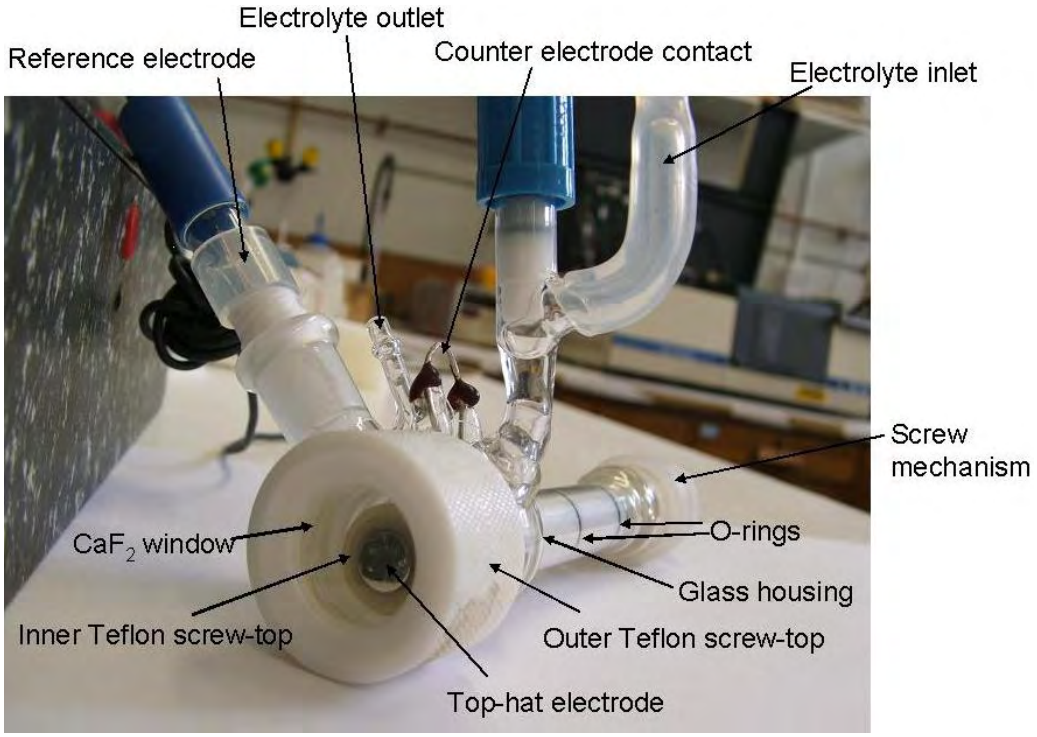


**Figure 4.3 Photograph of *in situ* FTIR photocatalytic sample cell**

**Table 4.1 Specifications of *in situ* FTIR reactor**

| Dimensions of *in situ* FTIR Sample Cell | |
|---|---|
| Diameter of top-hat electrode face (mm) | 9.0 |
| Diameter of $CaF_2$ window (mm) | 25.0 |
| Thickness of $CaF_2$ window (mm) | 3.0 |
| Internal diameter of glass housing (at irradiated face) (mm) | 25.0 |
| External diameter of glass housing (at base) (mm) | 15.0 |
| Length (from irradiated face to inner O-ring (mm) | 55.0 |
| Reactor volume ($cm^3$) | 16.0 |

Figure 4.4 shows the sample cell arrangement during experiments. The reactor cell was horizontally mounted on a custom-made holder which also held a series of mirrors arranged to position the beam of IR irradiation onto the sample face and then direct the subsequent IR beam into the FTIR detector.

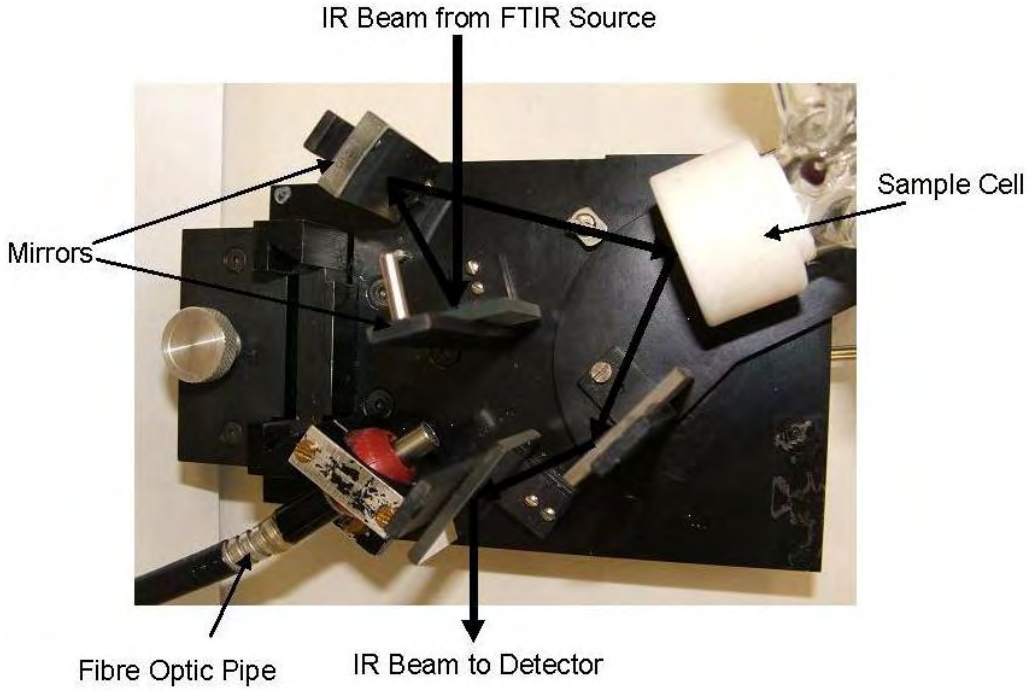


**Figure 4.4 Photograph of *in situ* FTIR reactor cell holder showing mirror arrangement for IR irradiation focusing and UV light pipe mounting.**

The UV lamp was a 150 W high pressure Xe lamp (6253, Oriel, UK) with a broad band output over 300 – 800 nm, equipped with an AM 0 filter and a 100 mm water filter to reduce sample heating effects. UV irradiation was directed onto the sample face at a ~ 45 ° angle to the IR irradiation via a 1 m flexible liquid light guide (Oriel, UK) (see Figure 4.4). Constant light intensity was ensured by switching on the lamp at least 1 hour prior to experiment commencement. The intensity of light from the light pipe was routinely monitored[38] by a Radiometer and found to be constant over time.

### 4.3.7 Electrochemically-assisted photocatalysis (EAP)

To investigate EAP, the reactor was modified to act as a three-electrode, one compartment electrochemical cell (see Figure 4.2 and Figure 4.3). 1 cm x 2 cm Pt gauze was situated within the reactor cell as the counter electrode. The reference was a Ag/AgCl electrode (Sentek). The working electrode included the $TiO_2$ coated Ti top-hat which was connected to a steel rod spanning the length of the top-hat

electrode support. An Autolab potentiostat with PC control was used to control potential and monitor current during experiments.

### 4.3.8 Determination of photocatalytic and EAP efficiency of $TiO_2$-coated substrates

The electrodes were examined for photocatalytic and EAP degradation of $Na_2(OOC)_2$ and NAG in the one compartment *in situ* FTIR photocatalytic cell. An aliquot of 16 $cm^3$ of aqueous solution containing 0.1 mol $dm^{-3}$ $Na_2SO_4$, or 0.1 mol $dm^{-3}$ $Na_2SO_4$ and 0.2 mol $dm^{-3}$ of model pollutant was added to the photoelectrochemical cell. The cell was placed into the FTIR sample compartment and sparged with $N_2$, in the dark, for at least 1 hour. A background spectrum was obtained immediately before the experiment commenced. Further spectra were taken at predetermined time intervals (every 3 minutes for time-dependent EAP and photocatalytic experiments; every 2 minutes for potential-dependent EAP experiments).

Infrared spectra were obtained using a Bio-Rad FTS-60-A FTIR spectrometer equipped with a liquid $N_2$-cooled MCT detector. 100 co-added scans were collected in the spectral range 4000 – 1000 $cm^{-1}$ at a resolution of 4 $cm^{-1}$ requiring approximately 30 seconds. Computer software used for spectral collection was Bio-Rad WinIR Pro (Bio-Rad Digilab). Positive peaks indicate an increase in absorption at that wavenumber, whereas negative peaks indicate a decrease in absorption. Data manipulation, when required, was performed using Origin 6.0 computer software package.

#### 4.3.8.1 Photocatalytic experiments

Photocatalytic experiments were performed using the same cell setup as above, however, these were performed without an applied potential. Initially a spectrum was collected in the dark, after which the sample cell was irradiated and sample spectra were collected every 3 minutes for a total of 27 minutes. The irradiation was then removed and spectra were collected every 3 minutes for a further 27 minutes.

### 4.3.8.2 EAP experiments: collected as a function of potential

EAP experiments were performed as a function of potential using the above *in situ* FTIR spectrochemical cell. These experiments were performed to determine the effect of slow increase in positive applied potential by stepping the potential in 200 mV increments every 2 minutes, commencing at -0.2 V vs. Ag/AgCl for the mesoporous $TiO_2$ films. The initial potential for the Thermal $TiO_2$ electrode was -0.8 V vs. Ag/AgCl, the reason for which will be explained later. Sample FTIR spectra were obtained at each potential step. The cell was UV irradiated immediately after the first sample spectrum was collected. Upon reaching 1.2 V vs. Ag/AgCl, the potential was lowered in one step to the starting potential, after which sample spectra were obtained over time to determine the effect of removal of the positive applied potential on the system.

### 4.3.8.3 EAP experiments: collected as a function of time

EAP experiments performed as a function of time were performed using the above *in situ* FTIR spectrochemical cell. These experiments were executed to determine the effect of a rapid increase in positive applied potential and commenced at the initial potentials used in the EAP collected as a function of potential experiments. Again, the cell was UV irradiated immediately after the first FTIR sample spectrum was collected. Two further sample spectra were collected at this starting potential, after which time the applied potential was immediately raised to 1.2 V vs. Ag/AgCl and held there for 27 minutes. During this time FTIR spectra were obtained at 3 minute intervals. The potential was then lowered to the starting potential in one step and further FTIR spectra collected at 3 minute intervals for a further 27 minutes.

Current-voltage responses were obtained on the $TiO_2$ electrodes mounted in the spectroelectrochemical cell before each *in situ* FTIR experiment to check the cell was correctly set-up and to maximise the photocurrent by adjusting the light pipe.

All experiments were performed in duplicate.

### 4.3.9 Spectral presentation

Spectra are represented as:[6]

$$Absorbance = -\log_{10}(\frac{S_s}{S_r}) \quad versus \quad \tilde{\upsilon} \qquad \textbf{4.2}$$
$$= -(\log_{10} S_s - \log_{10} S_r) \quad versus \quad \tilde{\upsilon}$$

where, $\tilde{\upsilon}$ is wavenumber ($cm^{-1}$). During electrochemical studies,[6] the reference spectrum, $S_r$, was collected at the reference potential, $E_r$, chosen to be in the electro-inactive region. The potential was then stepped to successively higher or lower values, $E_s$, and spectra, $S_s$, collected at each step, or the potential was changed in a single increment and the spectra, $S_s$, collected as a function of time. Equation 4.2 results in difference spectra which only contain absorptions that change with potential and/or time. In these spectra features pointing up, + Abs, are due to species gained, while features pointing down, - Abs, are due to species lost at $E_s$ relative to $E_r$. For clarity, in all figures of FTIR spectra, every second spectrum collected is displayed.

In addition to a full explanation of experimental parameters for FTIR spectral collection, included within each figure label for *in situ* FTIR spectra is a short label for quick reference purposes:

**$TiO_2$ type:** T (Thermal); P25 (Degussa P25); MW (MW-treated); or HT (HT-treated)

**Pollutant type:** $Na_2SO_4$; $Na_2(OOC)_2$; or NAG

**Experiment type:** PC (photocatalysis); P-EAP (potential-dependent EAP); or T-EAP (time-dependent EAP)

**UV illumination:** Light (UV illuminated); or dark

For example: MW, $Na_2(OOC)_2$, P-EAP, Light.

Due to the inherent difficulty in observing many spectra on one graph, plots of spectral absorbances of vibrational bands of interest were also compiled and displayed throughout this chapter. It was necessary to perform background corrections for differing solution film thickness within the FTIR sampling window

for each experiment performed. These were performed using the single beam background spectrum (Figure 4.5) collected at the commencement of each experiment.

The absorbance at 1640 $cm^{-1}$ corresponding to water absorption was calculated:

$$-\log_{10}\left(\frac{I_o}{I}\right) = A_{1640} \qquad \textbf{4.4}$$

The absorbance at the vibrational frequency of interest was then ratioed against this value ($A_x$ / $A_{1640}$) to remove solution layer thickness effects.

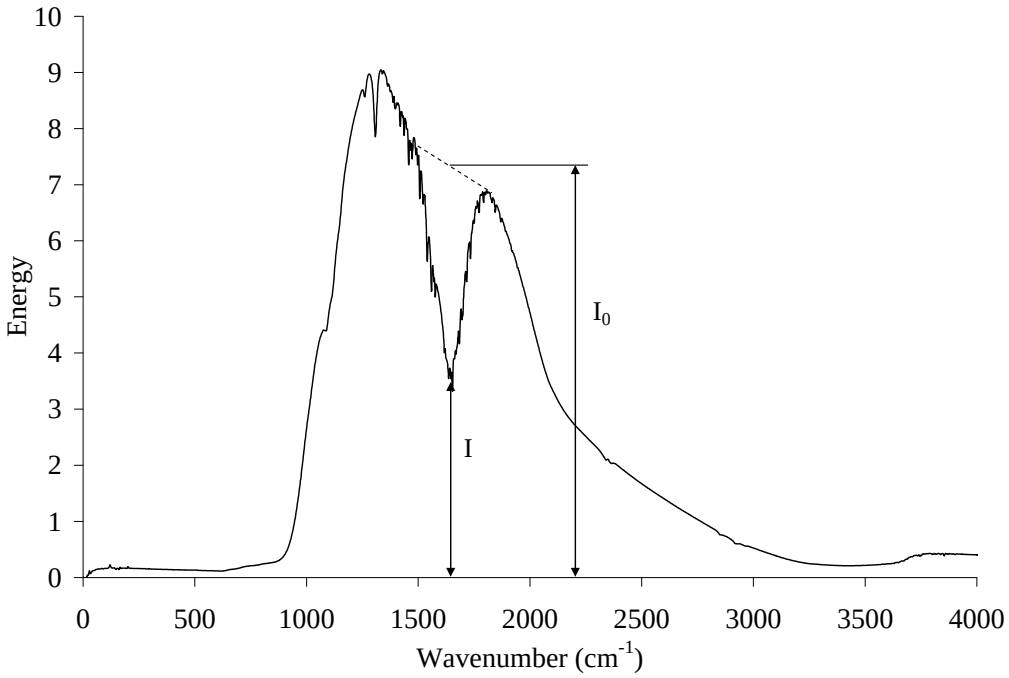


**Figure 4.5 Sample background spectrum collected during *in situ* FTIR experiments**

## 4.4 Results and Discussion

### 4.4.1 Electrochemical characterisation

#### 4.4.1.1 Current-voltage response

Cyclic voltammetry (CV) measurements were carried out on the $TiO_2$ electrodes using 0.1 mol $dm^{-3}$ $Na_2SO_4$ (pH 6.1) as the supporting electrolyte and 0.2 mol $dm^{-3}$ $Na_2(OOC)_2$ as the model pollutant (final pH 6.7), as shown in Figure 4.6a and b. Upon addition of 0.2 mol $dm^{-3}$ $Na_2(OOC)_2$ to the electrolyte, a considerable increase in photocurrent magnitude was observed for all mesoporous $TiO_2$ catalysts i.e. Degussa P25, MW- and HT-treated $TiO_2$, consistent with literature.[39]

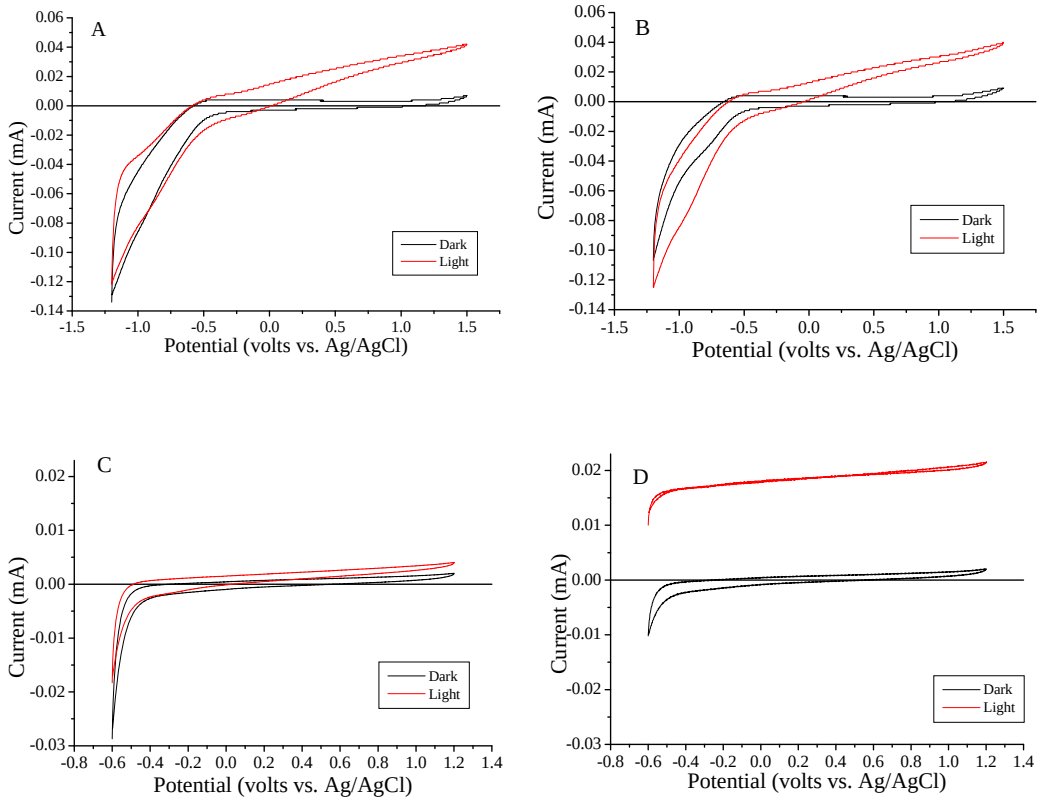


**Figure 4.6a Cyclic Voltammograms collected in the dark and under UV irradiation of: (A) thermal, 0.1 mol $dm^{-3}$ $Na_2SO_4$: (B) thermal, 0.1 mol $dm^{-3}$ $Na_2SO_4$/0.2 mol $dm^{-3}$ $Na_2(OOC)_2$; (C) Degussa P25, 0.1 mol $dm^{-3}$ $Na_2SO_4$; (D) Degussa P25, 0.1 mol $dm^{-3}$ $Na_2SO_4$/0.2 mol $dm^{-3}$ $Na_2(OOC)_2$. Scan rate 100 mV $s^{-1}$.**

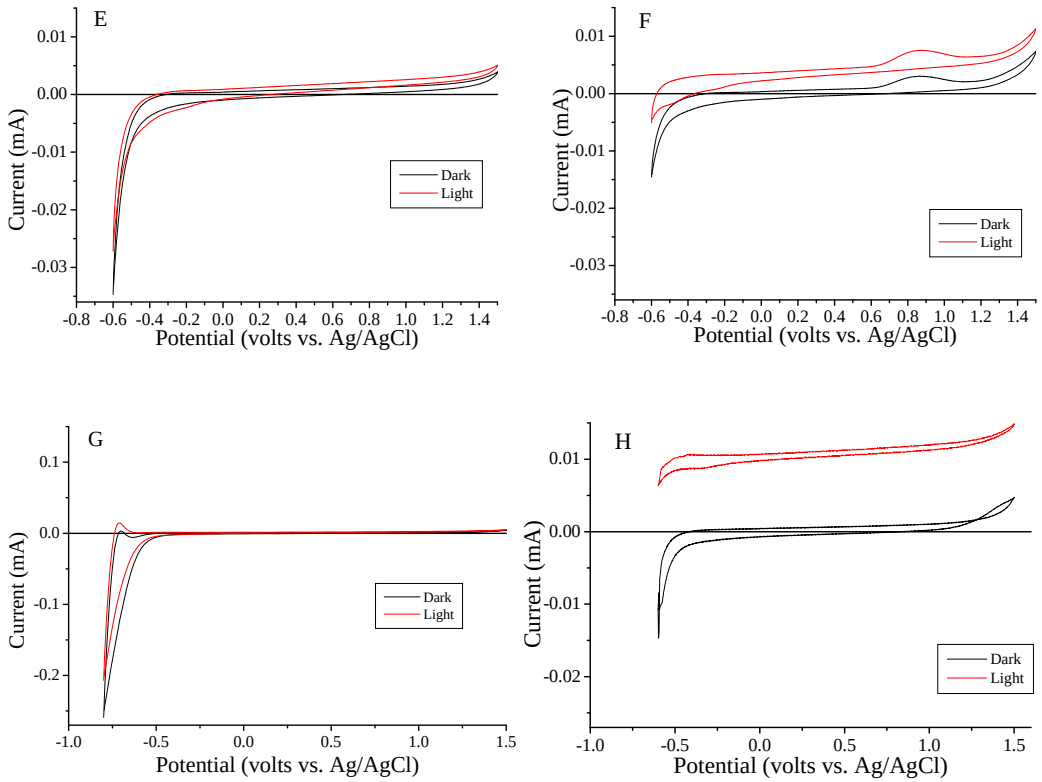


**Figure 4.6b Cyclic Voltammograms collected in the dark and under UV irradiation of: (E) MW-treated $TiO_2$, 0.1 mol $dm^{-3}$ $Na_2SO_4$: (F) MW-treated $TiO_2$, 0.1 mol $dm^{-3}$ $Na_2SO_4$/0.2 mol $dm^{-3}$ $Na_2(OOC)_2$; (G) HT-treated $TiO_2$, 0.1 mol $dm^{-3}$ $Na_2SO_4$; (H) HT-treated $TiO_2$, 0.1 mol $dm^{-3}$ $Na_2SO_4$/0.2 mol $dm^{-3}$ $Na_2(OOC)_2$. Scan rate 100 mV $s^{-1}$.**

A photocurrent is the difference between the current observed upon irradiation with UV light and that observed in the dark, and measures the rate of charge crossing the semiconductor/electrolyte interface and therefore determines the rate of $OH^{\bullet}$ generation at the interface.[40] Classical semiconductor theory predicts that the measured photocurrent varies as:[41]

$$j_p = qI_0[1-e^{-(\alpha W)/(1+\alpha L)}] \qquad \textbf{4.5}$$

where $j_p$ is the photocurrent density, $q$ is the charge on an electron, $I_0$ the photon flux, α the absorption coefficient, $L$ the minority carrier length and $W$ is the thickness of the depletion layer.

*W* increases with the square root of the applied overpotential according to:[41]

$$W = (2_{\varepsilon\varepsilon_0}\left|V - V_f\right| / qN_d)^{1/2} \qquad \textbf{4.6}$$

where $\varepsilon$ is the relative permittivity in the direction normal to the surface, $\varepsilon_0$ the relative permittivity of free space, $V$ the potential at the conduction band edge, $V_f$ the flat band potential and $N_d$ the donor density.

All electrode types showed a photocurrent, however the thermal $TiO_2$ photocurrent response was significantly different to the mesoporous $TiO_2$ electrodes i.e. Degussa P25, MW- and HT-treated $TiO_2$. The photocurrent seen for the thermal film was in general agreement with classical semiconductor theory, in that the photocurrent response is dependant on (applied potential)$^{1/2}$ (see Figure 4.7); however, the current-voltage response of the mesoporous $TiO_2$ films did not follow classical semiconductor theory as the photocurrent appeared independent of applied potential.

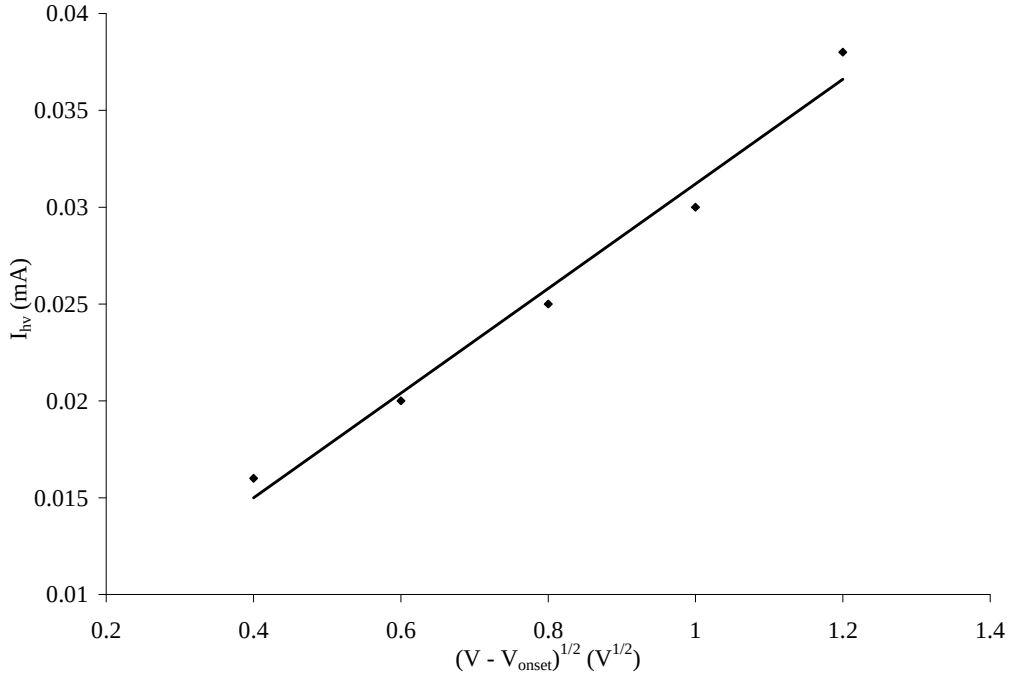


**Figure 4.7 Plot of photocurrent density as a function of square root of applied potential on the Thermal film $TiO_2$ electrode**

Vinodgopal and co-workers[42] have displayed I-V characteristics of irradiated Degussa P25 films which are consistent with those seen in the present study for the

Degussa-P25, MW- and HT-treated $TiO_2$ films. They also expounded the differences in electrochemical mechanisms between polycrystalline (Thermal $TiO_2$) materials and mesoporous semiconductor films. In polycrystalline materials, charge separation is facilitated by the space charge layer at the electrode/electrolyte interface. The potential gradient of this region promotes the flow of electrons and holes in opposite directions. However, photocurrent generation in mesoporous semiconductor films operates under a different mechanism. Here, the individual particles are too small ($D_p$ approximately 30 nm) to form a space charge layer at the electrolyte interface. Even under heavy doping, when some band-bending may occur, charge recombination is still the dominant process in small particles. The fact that an increase in degradation was seen on the application of a potential to the mesoporous $TiO_2$ electrodes was thought to be dominated by the differing rates of electron and hole diffusion at the solution interface.[43] The increased degradation is also controlled by the potential gradient within the film which drives the electrons and holes in different directions. This energy gradient is very similar to the band bending observed in conventional photoelectrochemical cells.[42]

The electrode reactions responsible for the generation of photoanodic current are:[42]

at $TiO_2$ photoanode: $TiO_2 + h\upsilon \rightarrow e_{cb}^- + h_{vb}^+$ **4.7**

$h_{vb}^+ + OH^-_{surf}$ *or* $(OH^-) \rightarrow OH^\bullet$ **4.8**

or $h_{vb}^+ + OH^- \rightarrow {}^1\!/_4 O_2 + {}^1\!/_2 H_2O$ **4.9**

at dark Pt cathode: $e_{cb}^- + O_2 \rightarrow O_2^-$ **4.10**

Although $O_2$ evolution (equation 4.9) is a major process on rutile surfaces,[44] no $O_2$ formation was observed during these experiments, even when using the Degussa P25 $TiO_2$ electrode, which contained approximately 25% rutile. The mesoporous films used were predominately anatase (approximately 75 – 80%) and, as hypothesised by Vindgopal and co-workers,[42] were more likely to have a high over-voltage for $O_2$ generation. Thus, equation 4.8 dominated the anodic process. $O_2$ is known to be a good electron scavenger and further research performed by Vindgopal and co-workers have shown that under the influence of an anodic potential, it can readily

accept photogenerated electrons reducing molecular oxygen to $O_2^{\cdot-}$ or $HO_2^{\cdot}$ and possibly other reactive species such as $H_2O_2$.[45]

Figure 4.8 presents the potential dependence of the photocurrent obtained using the Degussa P25 $TiO_2$ electrode in electrolyte solution with and without $Na_2(OOC)_2$ under UV illumination. The photocurrent responses shown here are representative of those seen using MW- and HT-treated $TiO_2$ (see Appendix Figure A.1A and A.1B). In both cases photocurrent-potential dependence was characteristic for n-type semiconductor electrodes: after initial growth, the photocurrent increases with electrode potential, tending towards some limiting value.

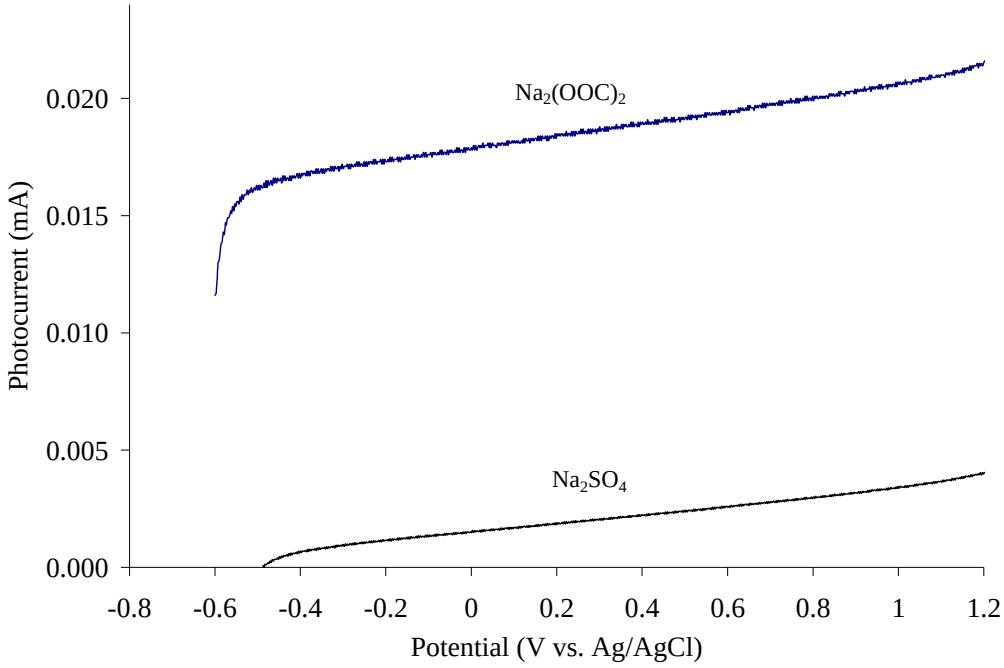


**Figure 4.8 Potential dependence of photocurrent obtained for the Degussa P25 $TiO_2$ electrode within supporting electrolyte only ($Na_2SO4$); and with the addition of $Na_2(OOC)_2$. Potential scan rate was 100 mV/s.**

In addition, the photocurrent values when using $Na_2(OOC)_2$ are larger than those in the background solution over the whole potential range. There was an observed shift in onset potential to more negative values (Degussa-P25: -0.14 V vs. Ag/AgCl; MW-treated $TiO_2$: -0.23 V vs. Ag/AgCl; and HT-treated $TiO_2$: -0.19 V vs. Ag/AgCl) which is typical of the behaviour of anatase to organic compounds.[39] The Thermal $TiO_2$ electrode displayed an onset potential of approximately -0.55 V vs. Ag/AgCl;

the reason for which the initial applied potential used during *in situ* FTIR experiments with the Thermal $TiO_2$ electrode was -0.8 V vs. Ag/AgCl. This was to ensure that FTIR experiments were commenced at a potential lower than the onset potential.

The increase in the saturation photocurrent observed with $Na_2(OOC)_2$ at high band-bending (applied potential) was related to the phenomenon of photocurrent doubling.[46,47] This occurs where the rate of surface recombination is negligible and all the photoexcited holes that reach the semiconductor electrode surface are transferred to the species in solution. This leads to the photogeneration of intermediates that undergo further oxidation, with injection of electrons into the CB of the semiconductor electrode. Upon the addition of $Na_2(OOC)_2$, the measured photocurrent increased substantially using the Degussa P25 and MW-treated $TiO_2$ electrodes, which showed a 5-fold and 2.3-fold increase respectively. The HT-treated $TiO_2$ showed a slightly smaller increase (1.7-fold), while the measured photocurrent for the Thermal $TiO_2$ electrode was identical with or without $Na_2(OOC)_2$.

**Table 4.2 Photocurrent responses at 1.2 V vs. Ag/AgCl for thermal and mesoporous $TiO_2$ films using 0.1 mol $dm^{-3}$ $Na_2SO_4$ as supporting electrolyte with 0.2 mol $dm^{-3}$ $Na_2(OOC)_2$.**

| Photocurrent response at 1.2 V vs. Ag/AgCl (μA) | Thermal (10 min @ 700 °C) | Degussa P25 | MW-treated $TiO_2$ | HT-treated $TiO_2$ |
|---|---|---|---|---|
| 0.1 mol $dm^{-3}$ $Na_2SO_4$/ 0.2 mol $dm^{-3}$ $Na_2(OOC)_2$ | 0.03 | 0.2 | 0.007 | 0.01 |
| 0.1 mol $dm^{-3}$ $Na_2SO_4$ | 0.03 | 0.004 | 0.003 | 0.006 |

The phenomenon of photocurrent doubling is particularly evident at high potential and appears here when using the mesoporous $TiO_2$ electrodes with the supporting electrolyte. There is however, no evidence of photocurrent doubling at low band-bending, as surface electron-hole recombination is thought to be the governing effect at low band-bending, which strongly affects the efficiency of the overall photoprocess near the flat-band potential.[48] This situation was changed upon the addition of an organic species to the solution. This results in suppression of the

recombination process on the $TiO_2$ photocatalyst surface and, even at low band-bending, more of the photoexcited holes that reached the semiconductor electrode surface participated in the oxidation of species in the solution, thus giving rise to an increase in efficiency of the overall photoprocess. In particular, suppression of surface recombination can produce the shift in photocurrent onset potential seen when mesoporous semiconductors are in the presence of an organic species, as seen with $Na_2(OOC)_2$ (see Figure 4.8).

While the MW-treated $TiO_2$ produced potential-dependent photocurrents characteristic of $TiO_2$ semiconductor electrodes, an anomaly was seen at high applied voltages in the form of an oxidative peak at +0.85 V vs. Ag/AgCl. Such anomaly did not occur when using the other electrode types or when using a sugar as the organic species present, so it likely that the observed peak was due to the $Na_2(OOC)_2$ strongly adsorbing onto the MW-treated $TiO_2$ electrode surface, resulting in its direct oxidation.

### 4.4.2 *In situ* FTIR of photocatalysis of $TiO_2$ electrodes with $Na_2SO_4$

Representative *in situ* FTIR spectra obtained using the $TiO_2$ electrodes in the presence of 0.1 mol $dm^{-3}$ $Na_2SO_4$ (pH 6.1) in the dark are shown in Figure 4.9 (see Appendix Figures A.2A, A.2B and A.3A for spectra obtained using mesoporous electrodes under identical conditions). The spectra were largely featureless; the negative bands near 1640 and 3800 $cm^{-1}$ were due to water vapour and the negative features near 2350 and 2390 $cm^{-1}$ to $CO_2$, both indicating a slight purge problem.

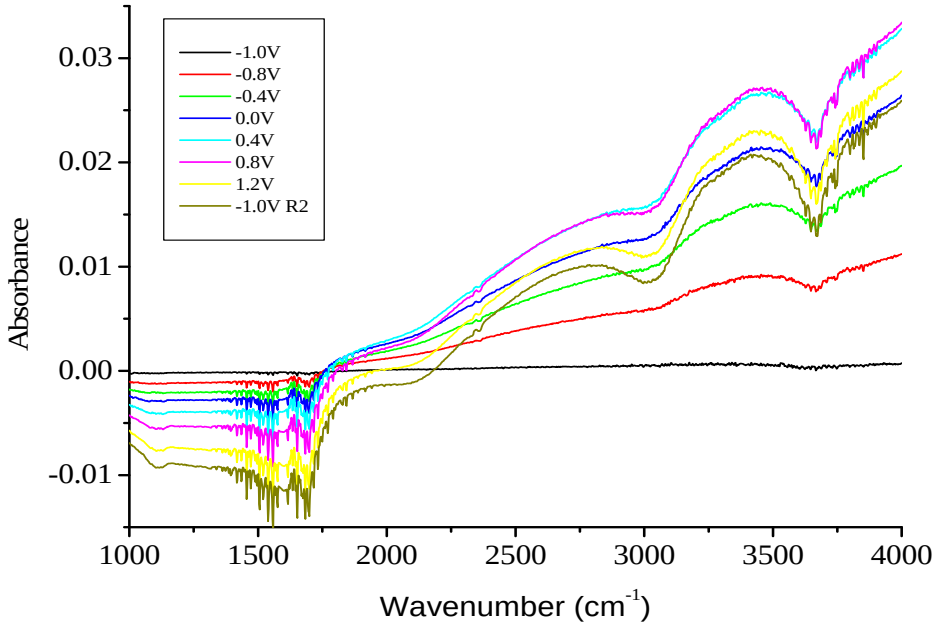


**Figure 4.9 Thermal, $Na_2SO_4$, P-EAP, dark: *In situ* FTIR absorbance spectra obtained using Thermal $TiO_2$ electrodes immersed in 0.1 mol $dm^{-3}$ $Na_2SO_4$, in the dark. Spectra were collected at the indicated potentials. 'R' denotes spectra obtained after the applied potential was returned to the initial potential.**

There did, however, appear to be a broad featureless absorption from approximately 1500 $cm^{-1}$ out into the near-IR which was observed with the other films and which did not collapse on stepping back to -0.2 V vs. Ag/AgCl, and hence appeared to be due to instrumental drift. Figure 4.10 showed analogous *in situ* FTIR spectra collected as a function of potential from an irradiated MW-treated $TiO_2$ electrode. The observed effects were characteristic for those obtained with an irradiated HT-treated $TiO_2$ electrode (see Appendix Figure A.3B).

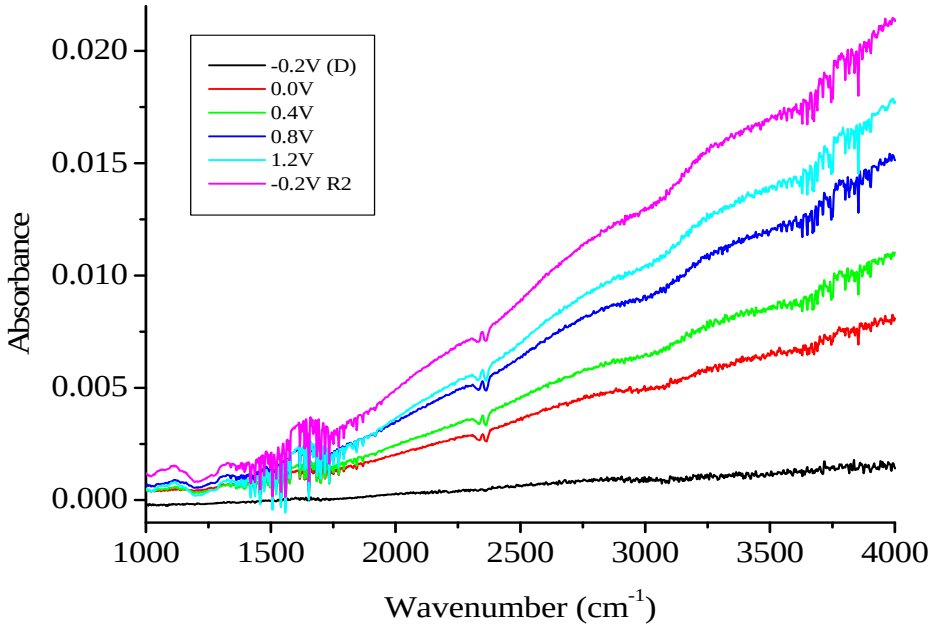


**Figure 4.10 MW, $Na_2SO_4$, P-EAP, light: *In situ* FTIR absorbance spectra obtained using MW-treated $TiO_2$ electrodes immersed in 0.1 mol $dm^{-3}$ $Na_2SO_4$, under irradiation with UV light. UV irradiation was commenced immediately after collection of first spectrum (-0.2 V (D)). Spectra were collected at the indicated potentials. 'R' denotes spectra obtained after the applied potential was returned to the initial potential.**

Figure 4.11 shows spectra analogous to those in Figure 4.10 except using a Degussa P25 $TiO_2$ anode. Again, there appeared to be the gain of a broad absorption extending out to the near-IR, albeit weaker than that observed in Figure 4.10 and commencing at a higher frequency, approximately 2200 $cm^{-1}$. Superimposed on this absorption are positive bands near 1065 and 1130 $cm^{-1}$ which may be attributed to the gain of $SO_4^{2-}$. The pH of the thin electrolyte layer decreased during oxidative processes[49] therefore $SO_4^{2-}$ is converted to $HSO_4^-$ (evidenced by the broad shoulder at 1200 $cm^{-1}$ superimposed on the $SO_4^{2-}$ bands). $SO_4^{2-}$ was drawn into the thin layer as the anode was made more positive, hence the overall increase of $SO_4^{2-}$ seen in the spectra. Another feature observed was a band at 2350 $cm^{-1}$ which may be unambiguously attributed to the production of $CO_{2\,(aq)}$. This was a result of oxidation of residual hydrocarbons (negative peaks at 2850 and 2915 $cm^{-1}$) within the Degussa P25 $TiO_2$. Evidence for this hypothesis came when the experiment was repeated. Upon repetition, no $CO_{2\,(aq)}$ production was observed, with the FTIR spectra similar to those seen using the other irradiated $TiO_2$ electrodes (see Figure 4.10).

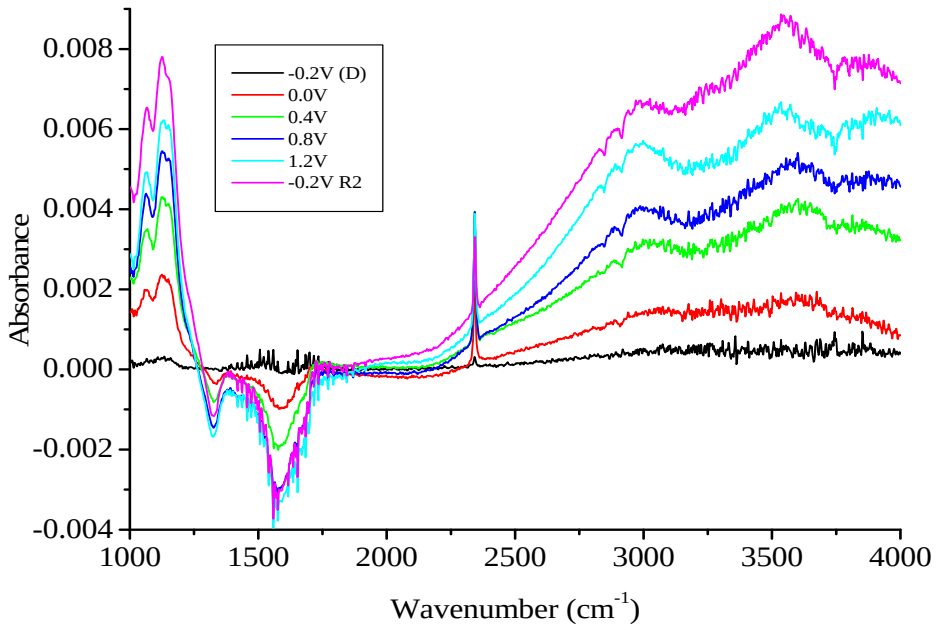


**Figure 4.11 P25, $Na_2SO_4$, P-EAP, light: *In situ* FTIR absorbance spectra obtained using P25 $TiO_2$ electrodes immersed in 0.1 mol $dm^{-3}$ $Na_2SO_4$, under irradiation with UV light. UV irradiation was commenced immediately after collection of first spectrum (-0.2 V (D)). Spectra were collected at the indicated potentials. 'R' denotes spectra obtained after the applied potential was returned to the initial potential.**

Further examination of the spectra shown in Figure 4.11 revealed negative features near 1325 and 1585 $cm^{-1}$ which were attributed to adsorbed $CO_3^{2-}$ and $HCO_3^-$, respectively.[50,51] Figure 4.12 shows a plot of $CO_{2\,(aq)}$ absorbance gain, as well as the decreased absorbance of $CO_3^{2-}$ and $HCO_3^-$ from spectra displayed in Figure 4.11. Between 0 – 10 minutes (0.6 V vs. Ag/AgCl), a gradual increase in $CO_{2\,(aq)}$ absorbance was seen. It was possible that the diminish $CO_3^{2-}$ and $HCO_3^-$ absorbance may be due to its reduction to water and $CO_{2\,(aq)}$, thus increasing the net $CO_{2(aq)}$ absorbance:

$$CO_3^{2-} + H^+ \rightarrow HCO_3^- \qquad \textbf{4.11}$$

$$HCO_3^-{}_{(ads)} + H^+ \rightarrow H_2O + CO_2 \qquad \textbf{4.12}$$

$$HCO_3^-{}_{(soln)} + H^+ \rightarrow H_2O + CO_2 \qquad \textbf{4.13}$$

This could be the case, because the loss of $CO_3^{2-}$ and $HCO_3^-$ absorbance continued to increase, even after the $CO_{2\ (aq)}$ maximum was observed. So, during the experiment, it appeared that the $CO_{2\ (aq)}$ production was due to the combination of the oxidation of residual organic species and the conversion of $CO_3^{2-}$ and $HCO_3^-$ . After 10 minutes, the rate of $CO_{2\ (aq)}$ diffusion from the thin layer was greater than the rate of production, corresponding to a net loss in absorbance.

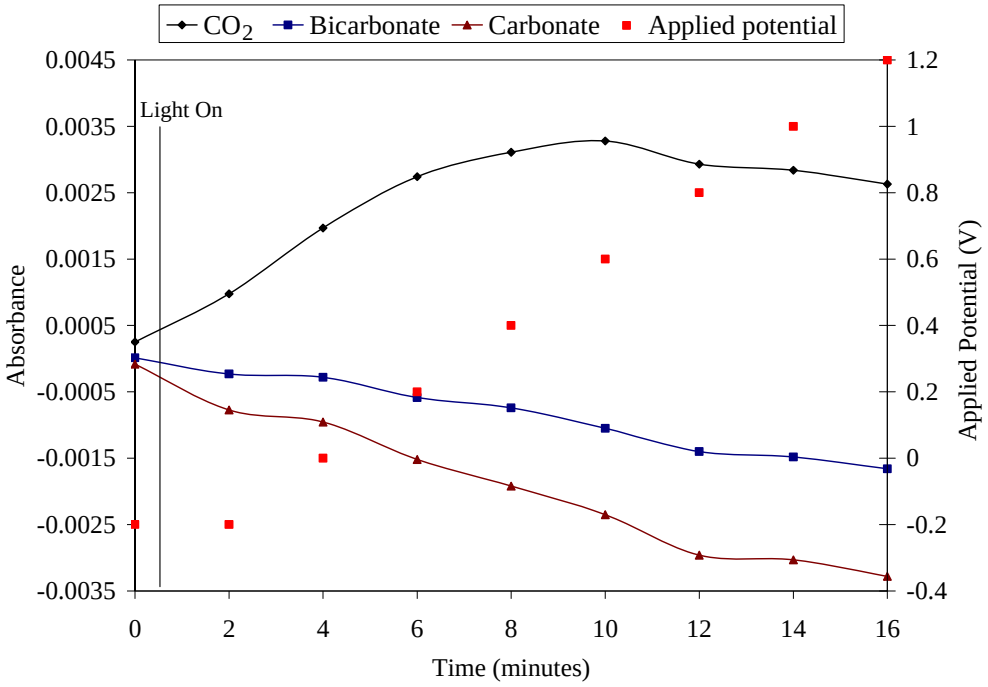


**Figure 4.12 Plot of $CO_{2\ (aq)}$ (2350 $cm^{-1}$) gain and bicarbonate (1325 $cm^{-1}$) and carbonate (1585 $cm^{-1}$) loss with respect to applied potential over time for Degussa P25 $TiO_2$ electrode immersed in 0.1 mol $dm^{-3}$ $Na_2SO_4$. Initial value was obtained at -0.2 V vs. Ag/AgCl in the dark, after which cell was irradiated with UV light. Applied potential was increased in 200 mV step up to a maximum at 1.2 V vs. Ag/AgCl (16 minutes). Absorbance values were taken from *in situ* FTIR spectra shown in Figure 4.11.**

*In situ* FTIR experiments were also performed where the applied potential was shifted from the starting negative potential of -0.2 V to 1.2 V vs. Ag/AgCl in one step and held there for a period of time, after which the potential was again lowered to the starting potential and the FTIR signal monitored. These spectra were similar to those shown in Figure 4.10, and were largely featureless despite the presence of a slight purge problem evidenced by bands near 1640 and 3800 $cm^{-1}$ due to water

vapour and the features near 2350 and 2390 $cm^{-1}$ to gaseous $CO_2$. There also appeared to be a broad featureless absorption from approximately 1500 $cm^{-1}$ out into the near-IR, which was observed with the other films.

To further investigate the broad featureless absorption, plots of the absorbance at 2500 $cm^{-1}$ were compiled. This wavenumber was chosen because no overlapping vibrational bands were present in this region. Figure 4.13 and Figure 4.14 show plots of the change in baseline absorbance at 2500 $cm^{-1}$ with respect to applied potential, where the applied potential increased in 200 mV steps every 2 minutes, for irradiated $TiO_2$ electrodes immersed in 0.1 mol $dm^{-3}$ $Na_2SO_4$.

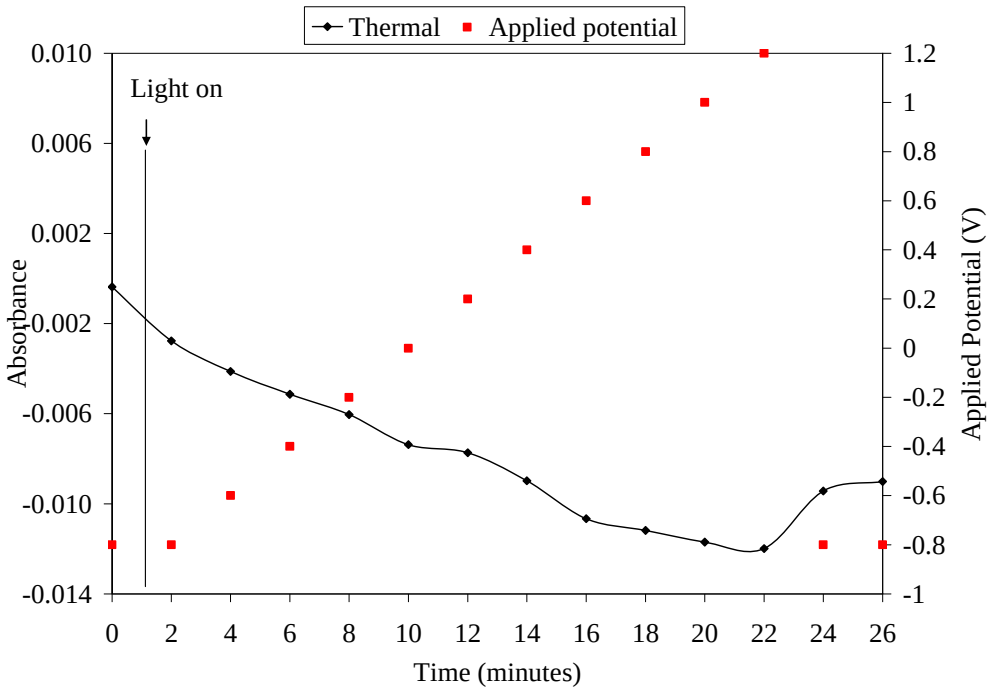


**Figure 4.13 Plot of 2500 $cm^{-1}$ absorbance for irradiated Thermal $TiO_2$ electrode immersed in 0.1 mol $dm^{-3}$ $Na_2SO_4$. Applied potential (■). Initial value was obtained at -0.8 V vs. Ag/AgCl in the dark, after which cell was irradiated with UV light. Applied potential was increased in 200 mV step up to a maximum at 1.2 V vs. Ag/AgCl (16 minutes).**

Two things were evident from these plots. Firstly, the direction of drift was not uniform: in this case, Thermal and HT-treated $TiO_2$ electrodes displayed negative movement, while the Degussa P25 and MW-treated $TiO_2$ electrodes showed positive absorbance. Secondly, if the drift was due to electronic interferences, then the

direction should change with respect to a reversal of the polarity of the applied potential. This was only evident in the Thermal $TiO_2$ electrode, which showed a sudden positive change after the applied potential was reversed to the initial potential of -0.8 V vs. Ag/AgCl at 22 minutes. The three other $TiO_2$ electrode types showed no such reversal.

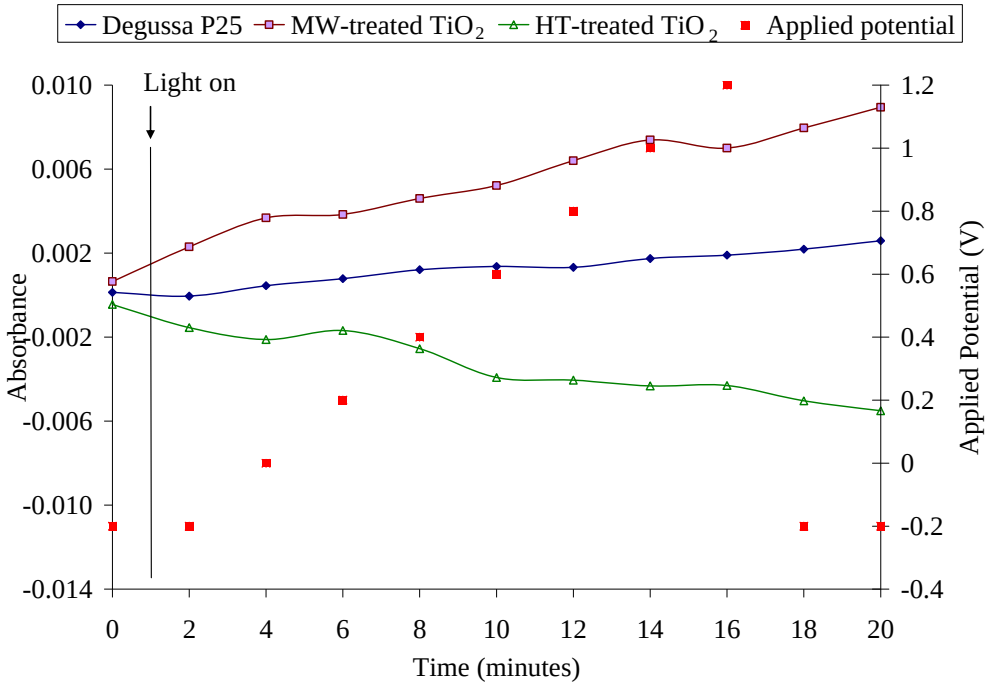


**Figure 4.14 Plot of 2500 $cm^{-1}$ absorbance for irradiated Degussa P25, MW- and HT-treated $TiO_2$ electrodes immersed in 0.1 mol $dm^{-3}$ $Na_2SO_4$ as the supporting electrolyte. Initial potential was -0.2 V vs. Ag/AgCl and stepped up to 1.2 V vs. Ag/AgCl in 200 mV increments every 2 minutes. Final 2 samples were collected at initial potential for each electrode type.**

Further evidence of the broad featureless absorption was provided by examining Figure 4.15 which shows plots of the 2500 $cm^{-1}$ absorbance obtained during time-dependent EAP experiments for the four irradiated $TiO_2$ electrodes immersed in 0.1 mol $dm^{-3}$ $Na_2SO_4$ as the supporting electrolyte. Clearly, there was a trend in the baseline movement of the MW-treated $TiO_2$ electrode; however, the inflection point of the trend did not correspond to a change in applied potential which suggested that the broad featureless absorption seen was due to instrumental drift. In the Thermal $TiO_2$ and to a lesser degree, Degussa P25 $TiO_2$ electrodes, a slight change in absorbance was noted after changing the applied potential from positive to negative

polarity. The change; however was not significant enough at this stage to determine if the broad featureless absorption seen in the spectra were due to electronic effects.

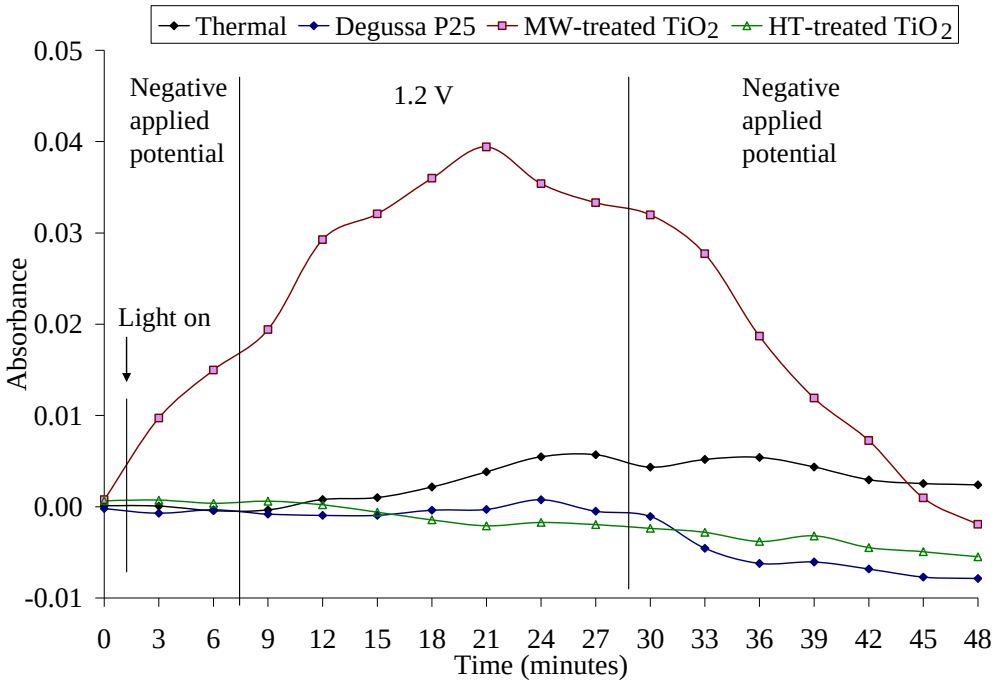


**Figure 4.15 Plot of the absorbance at 2500 $cm^{-1}$ for irradiated $TiO_2$ electrodes in 0.1 mol $dm^{-3}$ $Na_2SO_4$. Negative applied potential for Thermal $TiO_2$ electrode was -0.8 V and for Degussa P25, MW- and HT-treated $TiO_2$ electrodes was -0.2 V vs. Ag/AgCl, whilst the positive applied potential was 1.2 V vs. Ag/AgCl for all the $TiO_2$ electrode types.**

In summary, whilst the $TiO_2$ electrodes were submersed within the supporting electrolyte, no oxidation occurred in the dark or in the presence of light, except for when the Degussa P25 $TiO_2$ electrode was used for the first time which was attributed to the removal of residual hydrocarbons present from its manufacture. A broad featureless absorption was seen throughout all spectra obtained which was attributed to instrumental drift.

For additional *in situ* FTIR spectra of $TiO_2$ electrodes in $Na_2SO_4$ see Appendix Figures A.4A and B, A5.A and B, and A6.A.

### 4.4.3 *In situ* FTIR of photocatalysis of $TiO_2$ electrodes with oxalate

Figure 4.16 displays *in situ* FTIR spectra obtained using the un-irradiated Degussa P25 $TiO_2$ electrode in 0.1 mol $dm^{-3}$ $Na_2SO_4$/0.2 mol $dm^{-3}$ $Na_2(OOC)_2$ (pH 6.7). These spectra were similar to those obtained using un-irradiated $TiO_2$ electrodes in the supporting electrolyte only (see Appendix Figures A.6B, and A.7A and B), as they were largely featureless; the negative bands near 1640 and 3800 $cm^{-1}$ were due to water vapour. The broad featureless absorption commencing at 1600 $cm^{-1}$ and extending into the near-IR region was also evident; however, this did not collapse on stepping to -0.2 V vs. Ag/AgCl, and hence appeared to be due to instrumental drift.

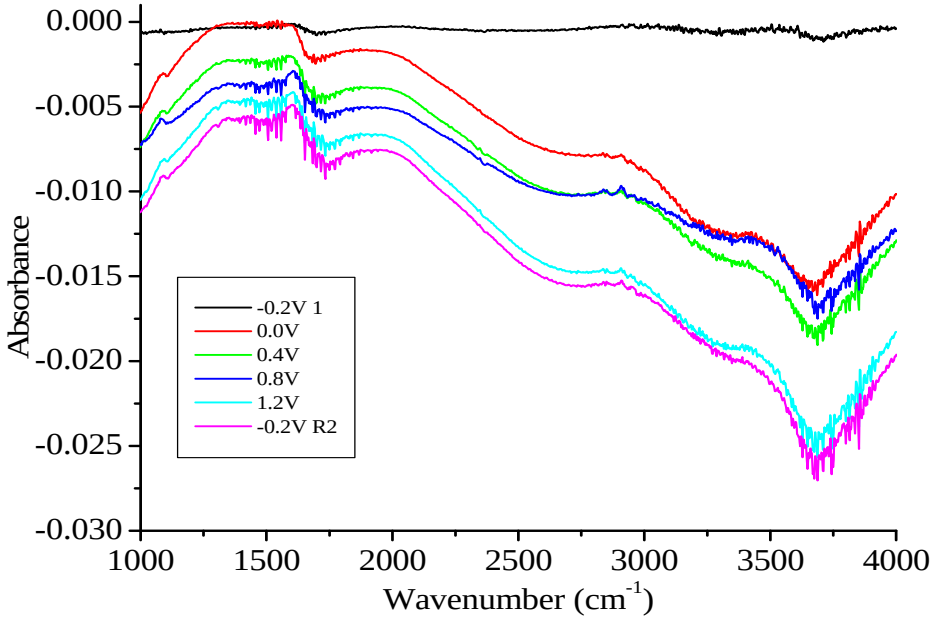


**Figure 4.16 P25, $Na_2(OOC)_2$, P-EAP, dark: *In situ* FTIR absorbance spectra obtained using a Degussa P25 $TiO_2$ electrode immersed in 0.1 mol $dm^{-3}$ $Na_2SO_4$/0.2 mol $dm^{-3}$ $Na_2(OOC)_2$, in the dark. Spectra were collected every 2 minutes at the indicated applied potentials. 'R' denotes spectra obtained after the applied potential was returned to the initial potential.**

Figure 4.17 displays *in situ* FTIR spectra obtained of the $Na_2(OOC)_2$ solution during photocatalytic experiments (with UV light) using the Thermal $TiO_2$ electrode. No potential was applied during these experiments, and as such are only monitoring the photocatalysis of $Na_2(OOC)_2$. These spectra are similar to those shown in Figure 4.16 in that they are largely featureless; small bands near 1640 and 3800 $cm^{-1}$ due to water vapour are present, and a broad featureless absorption extending from

approximately 1900 $cm^{-1}$ into the near-IR dominated the spectra. With close examination, a small band at 2350 $cm^{-1}$ appeared during UV irradiation and diminished once the irradiation was removed. This band was assigned to $CO_{2\ (aq)}$, produced from the photocatalytic oxidation of the organic species (oxalate) present in solution.

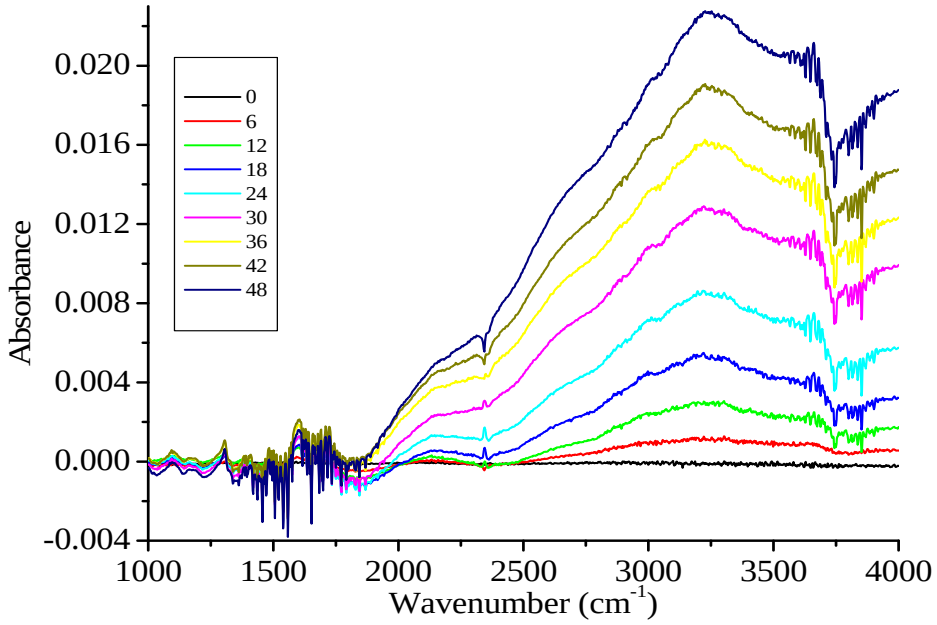


**Figure 4.17 T, $Na_2(OOC)_2$, PC: *In situ* FTIR absorbance spectra obtained during photocatalytic experiments using a Thermal $TiO_2$ electrode in 0.1 mol $dm^{-3}$ $Na_2SO_4$/0.2 mol $dm^{-3}$ $Na_2(OOC)_2$. Spectra were collected every 3 minutes, as indicated. UV irradiation was applied after 6 minutes and removed after 27 minutes.**

Figure 4.18 shows spectra from similar experiments analogous to those displayed in Figure 4.17, except using a MW-treated $TiO_2$ electrode. Close examination revealed that the spectra obtained up to 6 minutes were relatively featureless. However, once irradiation was applied, rapid changes occurred. The dominant feature throughout the spectra was the appearance of a wave-like absorption extending from 1800 – 3400 $cm^{-1}$ with highs at 1870 and 2600 $cm^{-1}$ and troughs at 2130 and 3020 $cm^{-1}$. Superimposed on this absorption was a $CO_{2\ (aq)}$ absorption band (2350 $cm^{-1}$) due to the photo-oxidation of $Na_2(OOC)_2$. This will be further discussed in a later section. The characteristic vibrational bands of $Na_2(OOC)_2$ in aqueous solution occur as a sharp medium band at 1310 $cm^{-1}$ and a broader, stronger band at 1565 $cm^{-1}$ due to

anti-symmetric and symmetric stretching vibrations, respectively.[28] Losses in spectral absorbance occurred at both of these frequencies, which showed that $CO_{2\,(aq)}$ production was directly related to the oxidation of $Na_2(OOC)_2$. It must be noted that when using the MW-treated $TiO_2$ electrode the shape and strength of the symmetric oxalate vibration was altered from that found when oxalate is in aqueous solution. This, combined with the presence of a negative band at 1700 $cm^{-1}$ led to the belief that partial adsorption of the oxalate to the $TiO_2$ electrode surface had occurred. This will be discussed in more detail later.

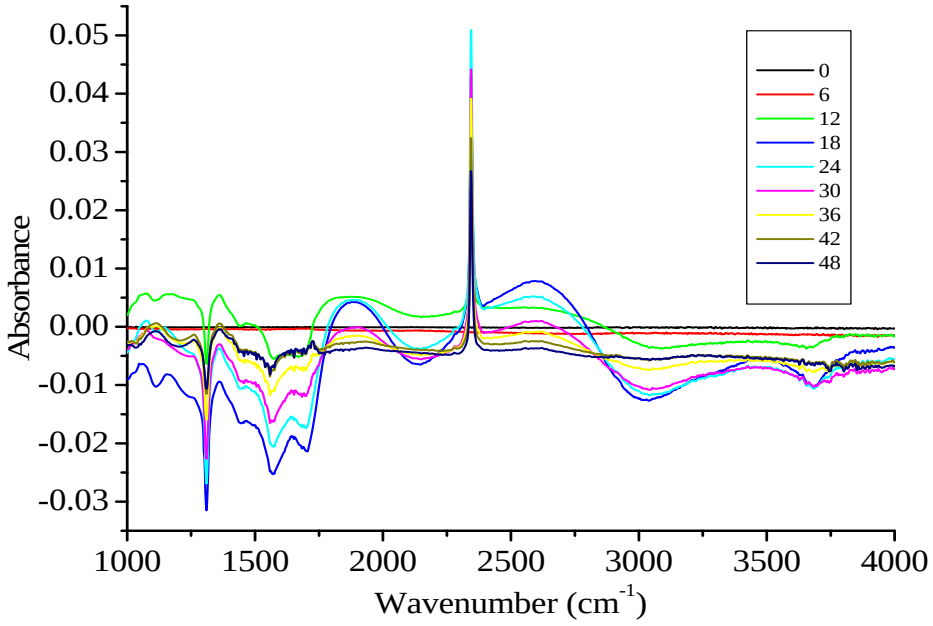


**Figure 4.18 MW, $Na_2(OOC)_2$, PC: *In situ* FTIR absorbance spectra obtained during photocatalytic experiments using a MW-treated $TiO_2$ electrode in 0.1 mol $dm^{-3}$ $Na_2SO_4$/0.2 mol $dm^{-3}$ $Na_2(OOC)_2$. Spectra were collected every 3 minutes, as indicated. UV irradiation was applied after 6 minutes and removed after 27 minutes.**

Figure 4.19 shows *in situ* FTIR spectra obtained using the HT-treated $TiO_2$ electrode. $Na_2(OOC)_2$ negative and $CO_{2\,(aq)}$ positive bands were apparent. However, when compared to Figure 4.18, it was obvious that the broad absorption throughout the spectra was now the dominant feature and extended farther into the mid-IR than that seen using the MW-treated $TiO_2$ electrode. The Degussa P25 $TiO_2$ electrode displayed effects similar to, although less intense than, the HT-treated $TiO_2$ electrode (see Appendix Figure A.8A for spectra).

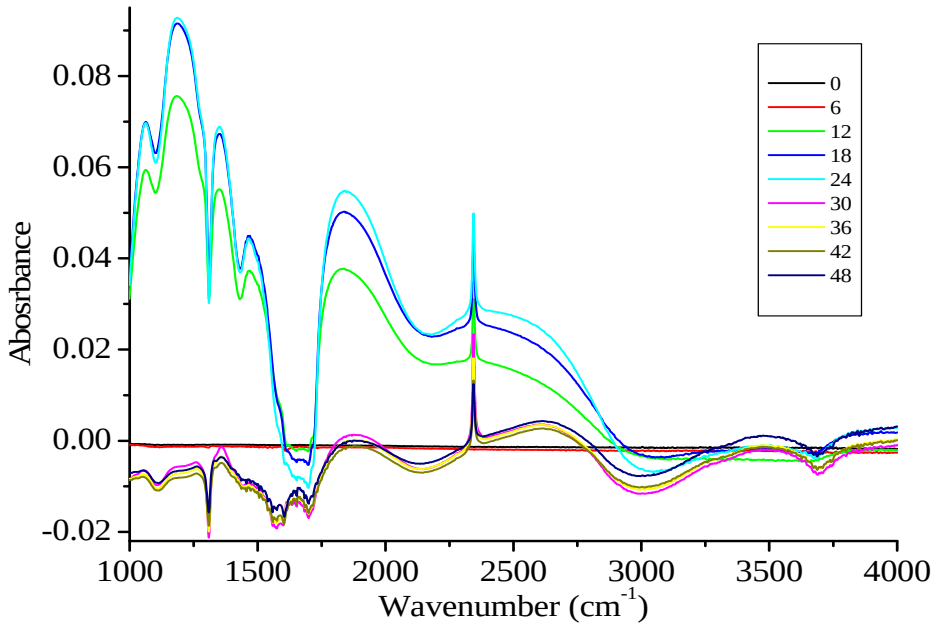


**Figure 4.19 HT, $Na_2(OOC)_2$, PC: *In situ* FTIR absorbance spectra obtained during photocatalytic experiments using a HT-treated $TiO_2$ electrode immersed in 0.1 mol $dm^{-3}$ $Na_2SO_4$/0.2 mol $dm^{-3}$ $Na_2(OOC)_2$. Spectra were collected every 3 minutes, as indicated. UV irradiation was applied after 6 minutes and removed after 27 minutes.**

In order to simply compare the photodegradation rates observed, one vibrational band was chosen and the change in absorbance plotted throughout the *in situ* FTIR experiments. Due to the overlap of water and sulphate vibrations in the oxalate region, oxalate absorbance bands were unsuitable. As the production of $CO_{2\ (aq)}$ has been shown to directly arise from the photo-oxidation of $Na_2(OOC)_2$, and the lack of other vibrational features in the $CO_{2\ (aq)}$ region of the FTIR spectrum, comparisons between photodegradation rates would be performed using the change in $CO_{2\ (aq)}$ absorbance. Figure 4.20 shows plots of $CO_{2\ (aq)}$ absorbance with respect to time for the four electrode types. (Error bars not shown for clarity. Average standard error was: Thermal, 0.032; P25, 0.095; MW, 0.061; and HT, 0.0034.) The film types, in decreasing order of the maximum absorbance of $CO_{2\ (aq)}$ were P25 < MW < HT < Thermal. The mesoporous films showed photo-degradation of $Na_2(OOC)_2$ with UV irradiation, however the Thermal $TiO_2$ electrode with UV irradiation only displayed very weak $Na_2(OOC)_2$ degradation.

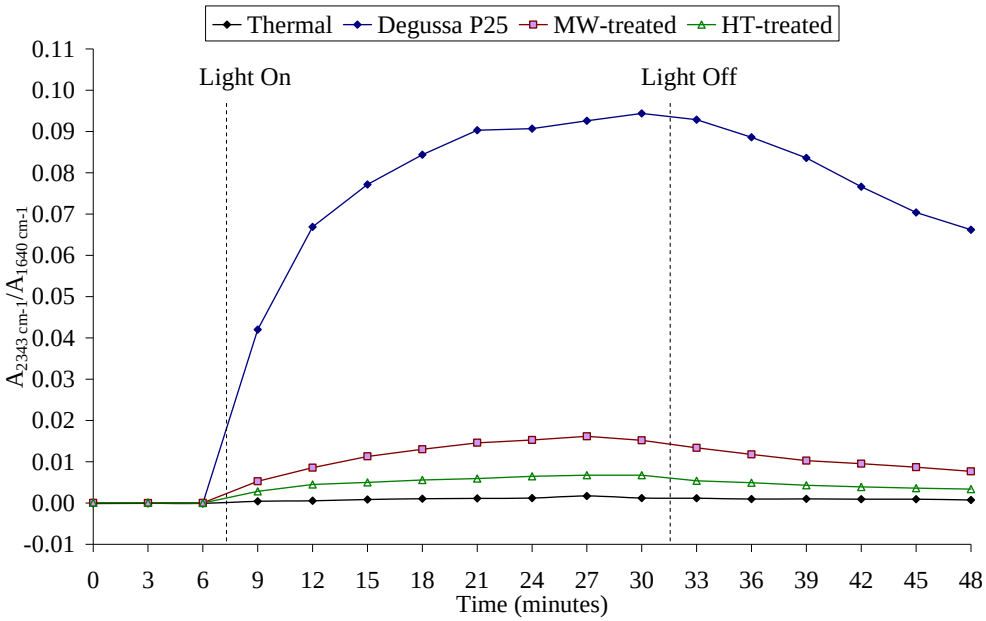


**Figure 4.20 Plots of average $CO_{2\ (aq)}$ absorbances produced during photocatalytic experiments with Thermal, Degussa P25, and MW- and HT-treated $TiO_2$ electrodes immersed in 0.1 mol $dm^{-3}$ $Na_2SO_4$/0.2 mol $dm^{-3}$ $Na_2(OOC)_2$, with and without UV irradiation. Spectral absorbance was background corrected and normalised for differing $TiO_2$ film thickness against background water intensity values obtained at the start of each experiment.**

Within the mesoporous electrodes, it was evident that $CO_{2\ (aq)}$ loss continued to occur after the removal of irradiation. It was possible that the loss in $CO_{2\ (aq)}$ was due to the production of carbonate and bicarbonate:

$$H_2O + CO_2 \rightarrow HCO_3^{-}{}_{(soln)} + H^+ \qquad \textbf{4.14}$$

$$H_2O + CO_2 \rightarrow HCO_3^{-}{}_{(ads)} + H^+ \qquad \textbf{4.15}$$

$$HCO_3^- \rightarrow CO_3^{2-} + H^+ \qquad \textbf{4.16}$$

However, this did not occur as there was no gain in absorbance at 1325 or 1585 $cm^{-1}$ due to $CO_3^{2-}$ or $HCO_3^-$, respectively, in any of the mesoporous $TiO_2$ spectra.

Another possible cause for the $CO_{2\ (aq)}$ absorbance loss after the removal of the UV irradiation, was differing overall diffusion rates due to the dissimilarity of $TiO_2$ surface areas. Degussa P25 has the lowest surface area of the three (50 $m^2\ g^{-1}$), while

the MW- and HT-treated $TiO_2$ possess much greater surface areas (235 and 371 $m^2$ $g^{-1}$, respectively). (See Chapter 3.5.1.3 for surface area determination.) Thus, within the Degussa P25 *in situ* FTIR cell, $CO_{2\ (aq)}$ molecules must travel a shorter distance to move out of the thin layer, which accounted for the greater diffusion from the thin electrolyte layer.

### 4.4.4 *In situ* FTIR with EAP of $TiO_2$ electrodes with oxalate

Figure 4.21 shows *in situ* FTIR spectra collected as a function of potential from an irradiated Thermal $TiO_2$ electrode in 0.1 mol $dm^{-3}$ $Na_2SO_4$/0.2 mol $dm^{-3}$ $Na_2(OOC)_2$. The initial potential was -0.8V vs. Ag/AgCl, and the potential increased in 200 mV steps every 2 minutes, with spectra collected at each step.

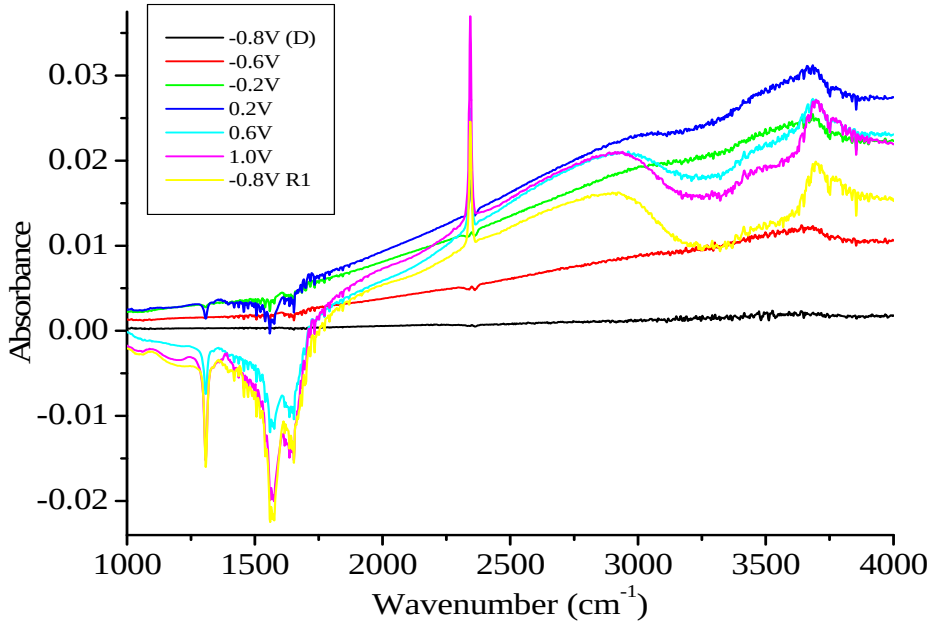


**Figure 4.21 T, $Na_2(OOC)_2$, P-EAP, Light: *In situ* FTIR absorbance spectra obtained using a Thermal $TiO_2$ electrode immersed in 0.1 mol $dm^{-3}$ $Na_2SO_4$/0.2 mol $dm^{-3}$ $Na_2(OOC)_2$, UV irradiated after initial spectrum (-0.8V (D)) was collected in the dark. Spectra were collected every 2 minutes at the indicated applied potentials. Potential steps were 200 mV. 'R' denotes spectra obtained after the applied potential was returned to the initial potential.**

Despite UV irradiation at the commencement of the experiment, no significant change was seen until 0.0 V vs. Ag/AgCl was reached. Spectra from the mesoporous

$TiO_2$ films however, showed dramatic changes in the spectra immediately upon UV irradiation (representative spectra are shown in Figure 4.22).

Most notable, was a strong positive band at 2343 $cm^{-1}$ assigned to $CO_{2\,(aq)}$, produced from the photocatalytic oxidation of the organic species present in solution. Negative bands at 1310 and 1560 $cm^{-1}$ due to $Na_2(OOC)_2$ were seen in all spectra collected after illumination and in the case of the Thermal $TiO_2$ electrode, after both illumination and the onset potential (0.0 V vs. Ag/AgCl) was reached.

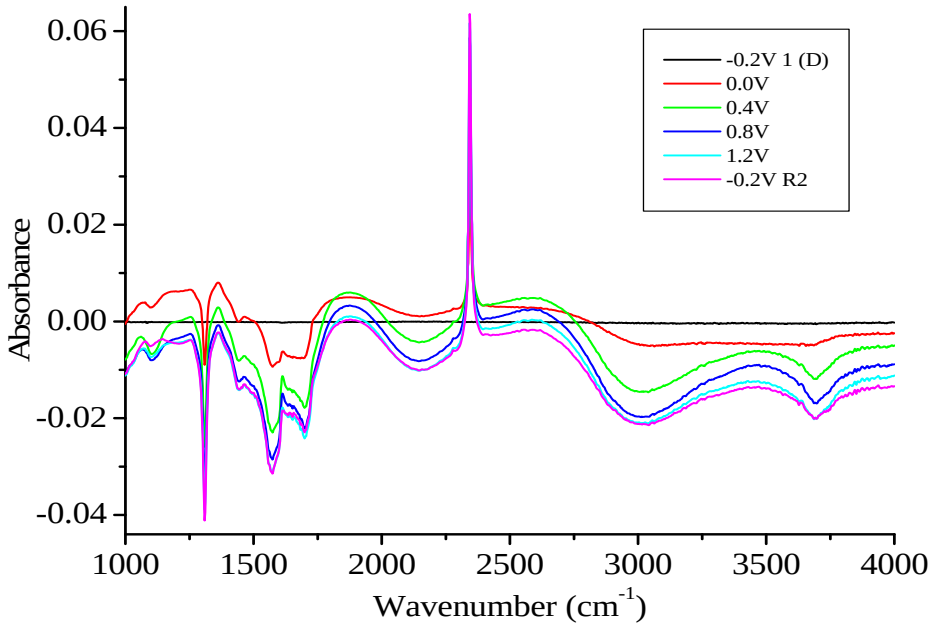


**Figure 4.22 HT, $Na_2(OOC)_2$, P-EAP, Light *In situ* FTIR absorbance spectra obtained during potential-dependent EAP using HT-treated $TiO_2$ electrodes immersed in 0.1 mol $dm^{-3}$ $Na_2SO_4$/0.2 mol $dm^{-3}$ $Na_2(OOC)_2$, under irradiation with UV light after initial spectrum (-0.2V 1 (D)) was collected in the dark. Spectra were collected at the indicated potentials. 'R' denotes spectra obtained after the applied potential was returned to the initial potential.**

The presence of dissolved $CO_{2\,(aq)}$ rather than the expected carbonate has been explained by Christensen and co-workers.[13] Here the authors used a similar spectroelectrochemical cell and collected CV's of single crystal $TiO_2$ samples. When the electrode was pressed against the cell window and illuminated, the observed photocurrent was lower than those seen when the electrode was pulled back from the cell window. A change in the shape of the CV was also observed. The shift and shape alteration was due to substantial electrolyte resistance and a shift in pH of the

thin layer of electrolyte trapped between the electrode and window. This was caused by hole capture reactions of the type:

$$2H_2O + 4h^+ \rightarrow 4H^+ + O_2 \qquad \textbf{4.17}$$

The pH shifts by 59 mV per pH unit.[52] This was evident in the present investigation using the Thermal $TiO_2$ films. CV's with the electrode pulled back from the cell window showed the photocurrent onset potential at ca. - 0.5 V vs. Ag/AgCl (see Figure 4.6), while during *in situ* FTIR experiments (Figure 4.21), where the electrode was pressed against the cell window, no photo-oxidation was seen until 0.0 V vs. Ag/AgCl was reached. This corresponds to a pH drop of approximately 8.5 units. Hence, as the potential was scanned positive, protons were generated and the position of the flat band potential moved more positive. A pH shift of this scale would result in $CO_{2\,(aq)}$, not carbonate, as was observed by FTIR.

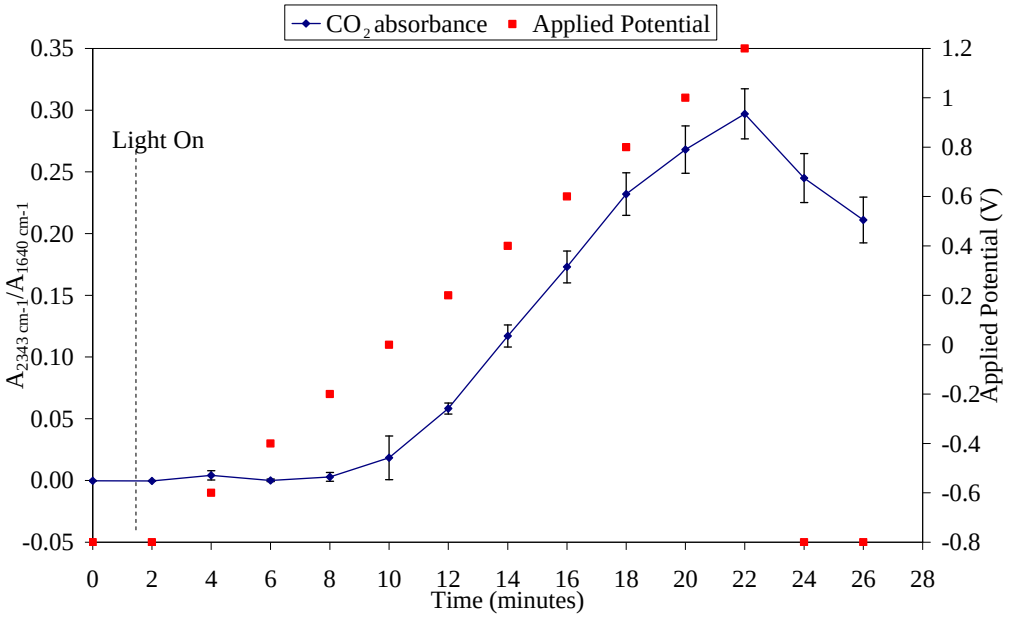


**Figure 4.23 Plots of average $CO_{2\,(aq)}$ absorbances produced during potential-dependent EAP with Thermal $TiO_2$ electrodes immersed in 0.1 mol $dm^{-3}$ $Na_2SO_4$/0.2 mol $dm^{-3}$ $Na_2(OOC)_2$, under irradiation with UV light. Spectral absorbance was background corrected and normalised for differing solution thickness against background water intensity values obtained at the start of each experiment. (■) Applied potential at each step.**

Plots of average $CO_{2\ (aq)}$ absorbances are shown in Figure 4.23 and Figure 4.24. The film types, in decreasing order of $CO_{2\ (aq)}$ maximum absorbance were P25 < Thermal < HT < MW, however there was minimal difference between the maximum intensity of the Thermal, HT- and MW-treated films. As previously observed, the Thermal film displayed increased $CO_{2\ (aq)}$ production dependent on the applied potential during photo-oxidation. This was vastly different to the Degussa P25, MW- and HT-treated $TiO_2$ films, where $CO_{2\ (aq)}$ production commenced immediately upon irradiation and increased to a steady state. Once the positive applied bias was removed, $CO_{2\ (aq)}$ absorbance remained constant, leading to the conclusion that these three $TiO_2$ types continue to photo-oxidise $Na_2(OOC)_2$ during light driven conditions.

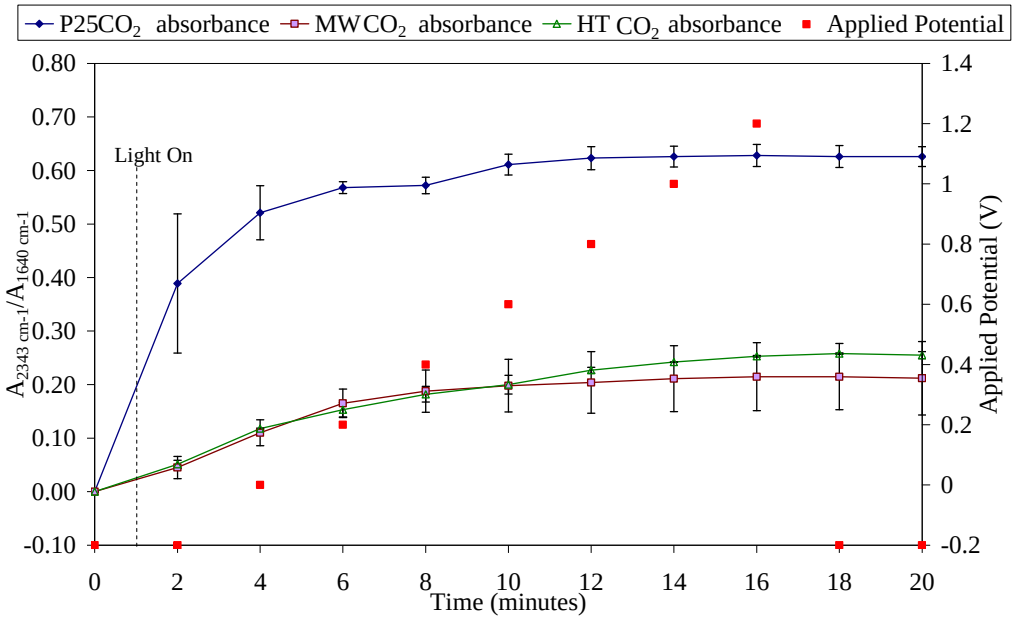


**Figure 4.24 Plots of average $CO_{2\ (aq)}$ absorbances produced during potential-dependent EAP with Degussa P25, MW- and HT-treated $TiO_2$ electrodes immersed in 0.1 mol $dm^{-3}$ $Na_2SO_4$/0.2 mol $dm^{-3}$ $Na_2(OOC)_2$, under irradiation with UV light. Spectral absorbance was background corrected and normalised for differing solution thickness against background water intensity values obtained at the start of each experiment. (■) Applied potential at each step.**

The FTIR spectra, collected during experiments with $Na_2(OOC)_2$, in the region between 1000 and 1800 $cm^{-1}$, displayed several differences when compared to those spectra collected using the electrolyte only. Once the onset potential was reached, the Thermal $TiO_2$ electrode displayed strong negative bands of oxalate at 1310 $cm^{-1}$ and

1570 $cm^{-1}$. The spectra also showed a negative water band at 1640 $cm^{-1}$. As there was no corresponding loss of electrolyte species (1100 $cm^{-1}$) it can be concluded that the water loss was not due to electrolyte diffusing out of the trapped thin layer. Also, due to the absence of a 2100 $cm^{-1}$ combination water band, it was thought that the observed water loss was not due to bulk water or its photo-oxidation within the thin layer.

When examining the mesoporous $TiO_2$ electrodes, the spectra were similar to the Thermal $TiO_2$, in that there was a relatively large negative peak at 1310 $cm^{-1}$, however, there were significant differences from 1550 – 1800 $cm^{-1}$. Whilst the HT- and MW-treated $TiO_2$ electrodes exhibited a negative absorbance band at 1570 $cm^{-1}$, similar to the Thermal $TiO_2$ electrode, the size and shape with respect to the symmetric stretching vibration had altered dramatically, with no loss of relative intensity or sharpness of the 1310 $cm^{-1}$ band. The differences in the anti-symmetric stretching vibration were even greater when examining the Degussa P25 $TiO_2$ electrode. There was also a new negative band at higher frequency (~ 1700 $cm^{-1}$) found in all the mesoporous $TiO_2$ electrodes. Table 5.1 summarises the frequency of oxalate peaks observed during potential-dependent EAP experiments.

**Table 4.3 Frequency assignments of oxalate bands produced during *in situ* FTIR EAP potential-dependent experiments**

| Film Type | Frequency ($cm^{-1}$) | Assignment |
|---|---|---|
| Thermal | 1560 | $(COO^-)_2\ \upsilon_s$ |
| | 1310 | $(COO^-)_2\ \upsilon_{as}$ |
| P25 | 1730 | |
| | 1560 | $(COO^-)_2\ \upsilon_s$ |
| | 1310 | $(COO^-)_2\ \upsilon_{as}$ |
| MW | 1700 | |
| | 1565 | $(COO^-)_2\ \upsilon_s$ |
| | 1310 | $(COO^-)_2\ \upsilon_{as}$ |
| HT | 1700 | |
| | 1570 | $(COO^-)_2\ \upsilon_s$ |
| | 1310 | $(COO^-)_2\ \upsilon_{as}$ |

Within aqueous solution, the relative intensities of oxalate bands are such that the band at 1310 $cm^{-1}$ is significantly weaker than the band at 1570 $cm^{-1}$. This was seen during potential-dependent EAP experiments using the thermal $TiO_2$ film (Figure 4.21). The mesoporous $TiO_2$ films all showed a sharp 1310 $cm^{-1}$ peak as seen for aqueous oxalate, but the band at 1570 $cm^{-1}$ was broad and significantly less intense than the corresponding 1310 $cm^{-1}$ band.

Hug and Sulzberger[10] have shown adsorption of oxalate onto the surface of Degussa P25 produces both band broadening and band movement within the IR spectrum. The anit-symmetric stretching C=O vibration appears at a lower wavenumber, whilst the symmetric vibration appears at a higher wavenumber. Furthermore, investigations have shown that when oxalate was complexed to various metals, the band at 1570 $cm^{-1}$ was no longer apparent and additional bands were seen at higher frequency.[28] Interestingly, when complexed to metals, the band at 1310 $cm^{-1}$ remained relatively unchanged, both in relative intensity and shape.

Table 4.4 shows the ratio of the 1570 $cm^{-1}$ symmetric vibrational band to the 1310 $cm^{-1}$ anti-symmetric vibrational band at 1.2 V vs. Ag/AgCl for the four electrode types.

**Table 4.4 Ratio of oxalate vibrational bands found using $TiO_2$ electrodes during photoelectrochemical oxidation. Absorbance values were baseline-corrected and corrected for solution thickness effects.**

| | Thermal | Degussa P25 | MW-treated $TiO_2$ | HT-treated $TiO_2$ |
|---|---|---|---|---|
| $A_{1570\ cm^{-1}}$ / $A_{1310\ cm^{-1}}$ | 1.5 | 0.35 | 0.79 | 0.84 |

The Thermal electrode showed the highest ratio and the Degussa P25 electrode the lowest. From this, and the fact that in all the mesoporous $TiO_2$ types used, the band at 1310 $cm^{-1}$ remained sharp throughout the photo-degradation experiments, the reduction in intensity at 1570 $cm^{-1}$ was due to the adsorption of oxalate onto the Ti atoms at the surface of the mesoporous $TiO_2$ electrodes.

### 4.4.5 *In situ* FTIR of EAP of $TiO_2$ electrodes with oxalate: investigated as a function of time

Representative *in situ* FTIR spectra obtained during time-dependent EAP experiments using the Thermal $TiO_2$ electrode in the presence of 0.1 mol $dm^{-3}$ $Na_2SO_4$/0.2 mol $dm^{-3}$ $Na_2(OOC)_2$ (pH 6.7) are shown in Figure 4.25. These spectra were similar to those obtained during potential-dependent EAP experiments, which were typical for this type of $TiO_2$ electrode.[11] No photo-oxidation of $Na_2(OOC)_2$ was witnessed, despite the application of UV illumination, until a positive potential (1.2 V vs. Ag/AgCl) was applied. However, in addition to the oxalate loss features (1310 and 1570 $cm^{-1}$) previously discussed during potential-dependent EAP experiments, weak positive bands were also seen in the region 1680 to 1725 $cm^{-1}$.

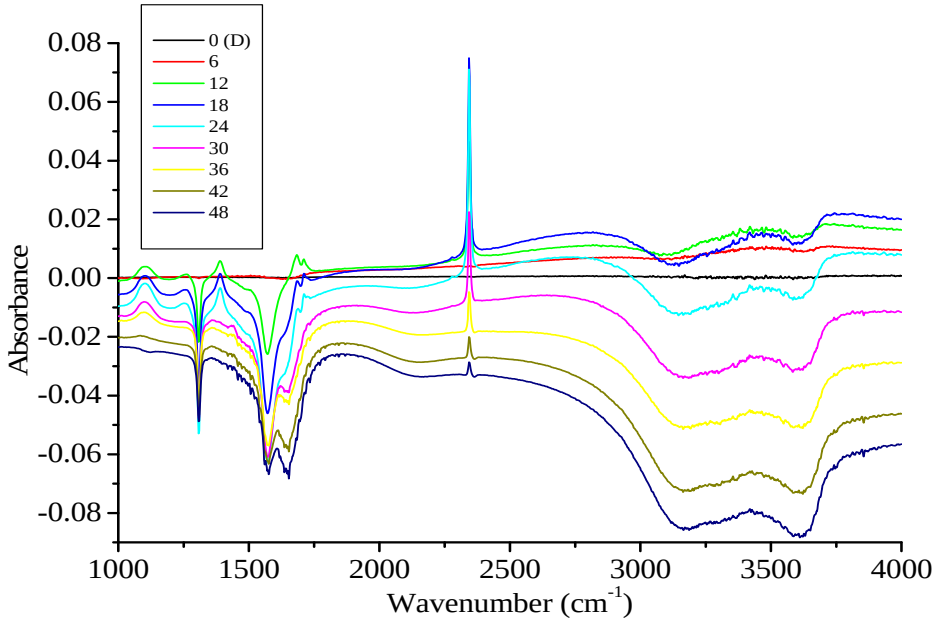


**Figure 4.25 T, $Na_2(OOC)_2$, T-EAP: *In situ* FTIR absorbance spectra obtained during photocatalysis using Thermal $TiO_2$ electrodes immersed in 0.1 mol $dm^{-3}$ $Na_2SO_4$/0.2 mol $dm^{-3}$ $Na_2(OOC)_2$, under irradiation with UV light (light switched on after initial spectrum was collected). Initial spectrum was collected in the dark (0 (D)). Spectra were collected at the indicated time intervals (minutes). Initial applied potential -0.8 V vs. Ag/AgCl; applied potential shifted to 1.2 V vs. Ag/AgCl in a single step after 6 minutes and held until 27 minutes. After 27 minutes potential was lowered to initial potential and held for the remainder of the experiment.**

Further inspection of the spectra, showed two broad positive bands which sharpened to form three bands centred at 1685, 1710 and 1725 $cm^{-1}$ whilst the positive applied potential remained present. Hug and Sulzberger have demonstrated the appearance of the oxalate bands is dependent on pH.[10] They showed that as the pH was lowered the 1570 $cm^{-1}$ band split into two weaker, broader bands which shift to higher wavenumber. Broadening of the anti-symmetric stretching vibration also occurred, and this band moved to approximately 1230 $cm^{-1}$. In the present study, a weak band centred at this wavenumber was also evident whenever the bands at 1685 and 1725 $cm^{-1}$ were present. It is known that the pH of the thin layer dramatically changes during the application of positive applied potentials, and has been demonstrated to shift to pH 2 under similar experimental conditions.[49] It was therefore thought that these bands arise from protonated oxalate, due to the increased $H^+$ content in the thin layer as a result of the lowered pH. Further evidence of this can be found by the disappearance of these bands from spectra collected immediately after the positive potential was removed, and for the remainder of the collection time. The protonation of oxalate and its effect on vibrational bands will be discussed in further detail after examining the *in situ* FTIR spectra obtained using the mesoporous $TiO_2$ electrodes.

Figure 4.26 displays spectra analogous to those shown in Figure 4.25, except using a HT-treated $TiO_2$ electrode. Spectral features seen using this electrode type were similar to the MW-treated $TiO_2$ electrode (see Appendix Figure A.8B). All of these spectra display characteristics similar to those previously discussed in section 4.4.5 when investigating the photo-electrochemical response with respect to applied potential (See Figure 4.22).

$CO_{2\,(aq)}$ was produced upon UV irradiation from the photo-oxidation of $Na_2(OOC)_2$, displaying no dependence on applied potential for photocatalysis. Immediately upon UV irradiation, the FTIR spectra obtained for both the HT- and MW-treated $TiO_2$ electrodes displayed a sharp $Na_2(OOC)_2$ anti-symmetric (C=O) stretching negative band at 1310 $cm^{-1}$, as well as a weak broad negative band at 1220 $cm^{-1}$. The presence of these bands indicated that while $Na_2(OOC)_2$ was photo-oxidised, it was also being converted to the protonated form within the thin layer. The oxalate negative band at 1570 $cm^{-1}$ was found in both the MW- and HT-treated $TiO_2$ spectra, and was much

less intense than the 1310 $cm^{-1}$ band. Additional bands at 1705 $cm^{-1}$ (negative) and 1725 $cm^{-1}$ (positive) were also evident.

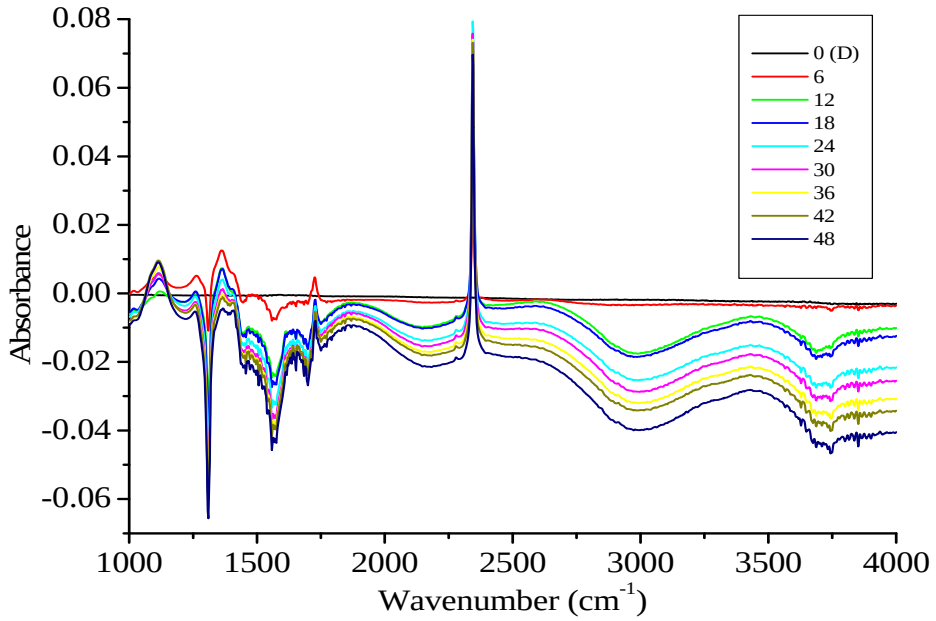


**Figure 4.26 HT, $Na_2(OOC)_2$, T-EAP: *In situ* FTIR absorbance spectra obtained using HT-treated $TiO_2$ electrodes immersed in 0.1 mol $dm^{-3}$ $Na_2SO_4$/0.2 mol $dm^{-3}$ $Na_2(OOC)_2$, under irradiation with UV light. Light was applied after initial spectrum was collected in the dark (0 (D)). Spectra were collected at the indicated time intervals (minutes). Initial applied potential -0.2 V vs. Ag/AgCl; applied potential shifted to 1.2 V vs. Ag/AgCl in a single step after 6 minutes and held until 27 minutes. After 27 minutes potential was lowered to initial potential and held for the remainder of the experiment.**

Spectra obtained using the Degussa P25 $TiO_2$ electrode displayed very weak negative bands in the 1500 – 1580 $cm^{-1}$ region, which were extremely broad (Figure 4.27). These spectra also displayed a moderate negative band between 1660 and 1800 $cm^{-1}$ due to oxalate protonation which was initially centred at 1715 $cm^{-1}$, however after UV irradiation for less than 6 minutes, had changed shape so that the maximum intensity was found at 1730 $cm^{-1}$, and the peak at 1715 $cm^{-1}$ was almost totally obscured.

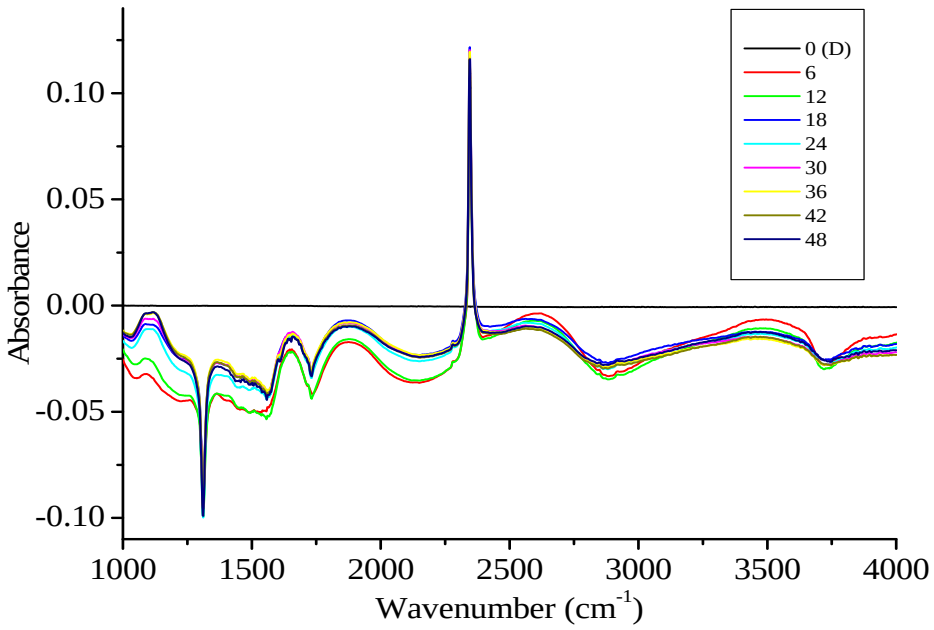


**Figure 4.27 P25, $Na_2(OOC)_2$, T-EAP: *In situ* FTIR absorbance spectra obtained using Degussa P25 $TiO_2$ electrodes immersed in 0.1 mol $dm^{-3}$ $Na_2SO_4$/0.2 mol $dm^{-3}$ $Na_2(OOC)_2$, under irradiation with UV light. Light was applied after initial spectrum was collected in the dark (0 (D)). Spectra were collected at the indicated time intervals (minutes). Initial applied potential -0.2 V vs. Ag/AgCl; applied potential shifted to 1.2 V vs. Ag/AgCl in a single step after 6 minutes and held until 27 minutes. After 27 minutes potential was lowered to initial potential and held for the remainder of the experiment.**

The proposed mechanism for each electrode type will now be discussed. It is well known that protonation of aqueous $(COO^-)_2$ can occur; forming either a singly or doubly protonated species, depending on the pH:

$$(COO^-)_2 + H^+ \rightarrow HOOCOO^- \qquad \textbf{4.18}$$

$$(COO^-)_2 + 2H^+ \rightarrow (COOH)_2 \qquad \textbf{4.19}$$

The pKa of $HOOCOO^-$ and $(COOH)_2$ are 3.84 and 1.52, respectively. Hug and Sulzberger produced FTIR spectra of each of these compounds with respect to the $(COO^-)_2$.[10] The vibrational bands within these spectra were as follows. The $(COO^-)_2$ produces a sharp strong absorption at 1310 $cm^{-1}$ and a slightly stronger, but broader

absorption at 1570 $cm^{-1}$. $HOOCOO^-$ displays a weak band at 1230 $cm^{-1}$ due to the combination of the symmetric (C=O) stretch and bending of the O-C=O bonds; a medium band at 1620 $cm^{-1}$ which was unassigned, and a weaker band at 1725 $cm^{-1}$ assigned to anti-symmetric (C=O) stretching vibrations. $(COOH)_2$ displayed bands at the same frequency as $HOOCOO^-$, however, the intensity of the 1230 $cm^{-1}$ was stronger, and the band at 1710 $cm^{-1}$ was stronger than 1680 $cm^{-1}$. The possible dimerisation of oxalic acid and association with $H_2O$ in aqueous solution complicated the vibrational assignments.

The adsorption of oxalate onto $TiO_2$ has also been examined. It was determined that deprotonated oxalate can form specific inner-sphere co-ordination complexes of oxalate with surface $Ti^{4+}$ sites.[10] Figure 4.28 shows the proposed structures of these complexes. Due to the coupling of the two C=O groups in Figure 4.28A and B, the C=O stretching vibration was split into two lines at 1680 and 1710 $cm^{-1}$.

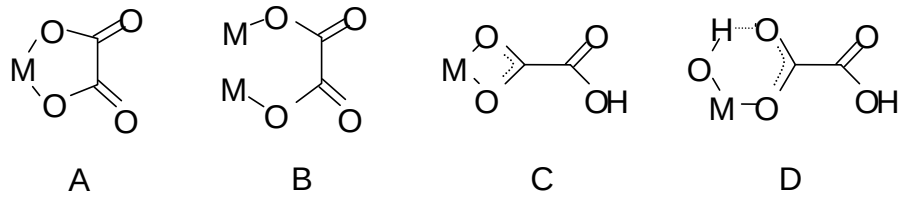


**Figure 4.28 Proposed structures of inner-sphere oxalate complexes on titanium surface sites.[10]**

Once protonated the two possible inner-sphere complexes are shown in Figure 4.28 C and D, with the latter being more stable as formation of a five-membered ring is energetically preferable over formation of a four-membered ring. With both of these complexes, the two vibrations for C=O are absent, with spectra no longer displaying a band at 1680 $cm^{-1}$.

In the present study, it was hypothesised that when using the Thermal $TiO_2$ electrode minimal co-ordination complexes of oxalate with surface $Ti^{4+}$ sites occurred and the majority of the oxalate was initially present in the deprotonated aqueous form. Upon application of the positive potential, a large loss of this species occurred, due to the simultaneous photo-oxidation into $CO_{2\,(aq)}$ and the protonation of the excess oxalate to $HOOCOO^-$ and $(COOH)_2$ due to the lowered pH.

When using the MW- and HT-treated $TiO_2$ electrodes, initially the $Na_2(OOC)_2$ was present in its deprotonated aqueous form. Upon UV irradiation, a pH swing in the thin electrolyte layer occurred, which protonated the oxalate to $HOOCOO^-$, resulting in the large loss of aqueous oxalate vibrational bands. The protonation produced a weak positive absorbance band at 1725 $cm^{-1}$ due to the anti-symmetric stretch of the C=O vibration. However, due to the lowered intensity of the aqueous oxalate symmetric stretching vibration relative to the aqueous anti-symmetric stretching vibration, and the presence of additional negative bands at approximately 1705 $cm^{-1}$, co-ordination complexes of oxalate with surface $Ti^{4+}$ sites were present. The loss of vibrational intensity at 1705 $cm^{-1}$ with time was due to the photo-oxidation of the adsorbed oxalate to $CO_{2\ (aq)}$. When using the Degussa P25 $TiO_2$ electrode, due to the diminished loss of vibrational absorbance at 1570 $cm^{-1}$, it was thought that initially the majority of oxalate present had formed co-ordination complexes with surface $Ti^{4+}$ sites. It is believed that the absence of the strong 1680 $cm^{-1}$ band of deprotonated oxalate adsorbed onto $TiO_2$ was to obscurity by strong water absorption in this region.

Plots of $CO_{2\ (aq)}$ production during time-dependent EAP experiments are shown in Figure 4.29 (Thermal $TiO_2$) and Figure 4.30 (Degussa P25, MW- and HT-treated $TiO_2$). The film types, in decreasing order of the maximum absorbance of $CO_{2\ (aq)}$ were P25 < Thermal < HT < MW, however the difference between the maximum $CO_{2\ (aq)}$ absorbances between the Thermal, HT- and MW-treated $TiO_2$ films was minimal.

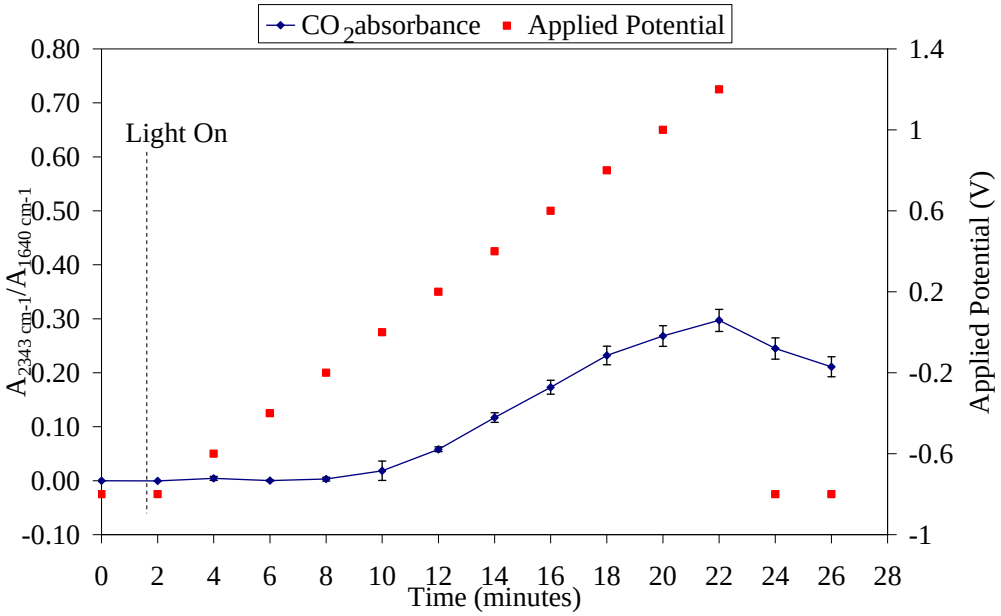


**Figure 4.29 Plots of average $CO_{2\ (aq)}$ absorbances produced during time-dependent EAP experiments with the Thermal $TiO_2$ electrode immersed in 0.1 mol $dm^{-3}$ $Na_2SO_4$/0.2 mol $dm^{-3}$ $Na_2(OOC)_2$, under irradiation with UV light. Spectral absorbance was background corrected and normalised for differing $TiO_2$ film thickness against background water intensity values. (■) Applied potential during sampling.**

Inspection of Figure 4.29 revealed that upon stepping of the potential to negative values, a sharp reduction in $CO_{2\ (aq)}$ absorbance occurred. As stated earlier, the Thermal $TiO_2$ does not show photocatalytic oxidation without a positive applied potential and UV irradiation. Therefore, as the oxidation of $Na_2(OOC)_2$ ceases, no more $CO_{2\ (aq)}$ will be produced, and the $CO_{2\ (aq)}$ present will diffuse out of the thin layer. On the other hand, $CO_{2\ (aq)}$ production began immediately upon UV irradiation, demonstrating that these electrode types do not require a positive applied potential to produce photocatalytic effects (Figure 4.30).

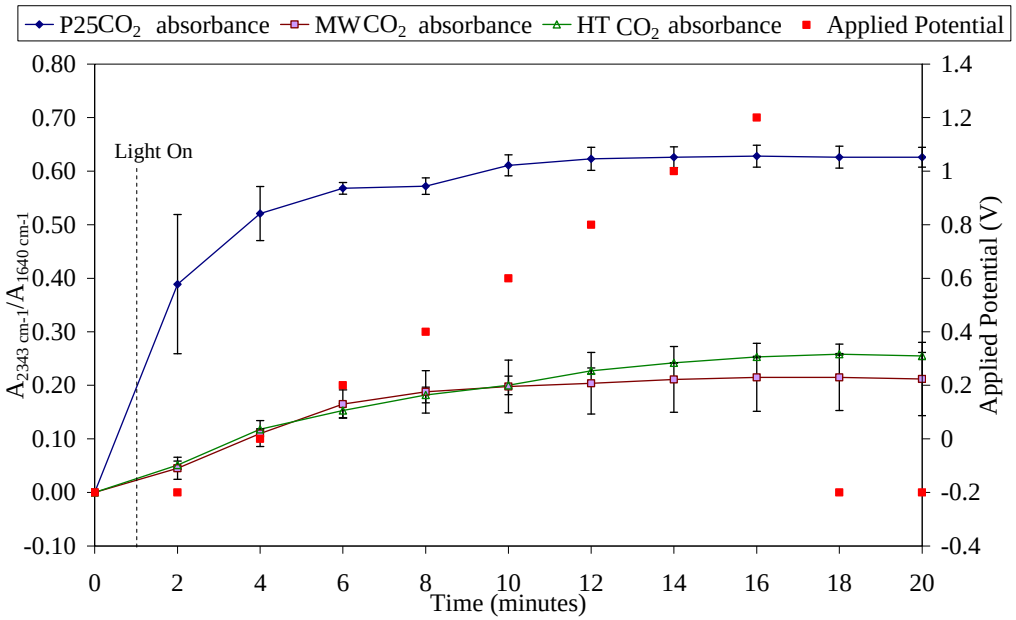


**Figure 4.30 Plots of average $CO_{2\ (aq)}$ absorbances produced during time-dependent EAP experiments with Degussa P25, MW- and HT-treated $TiO_2$ electrodes immersed in 0.1 mol $dm^{-3}$ $Na_2SO_4$/0.2 mol $dm^{-3}$ $Na_2(OOC)_2$, under irradiation with UV light. Spectral absorbance was background corrected and normalised for differing $TiO_2$ film thickness against background water intensity values obtained at the start of each experiment. (■) Applied potential during sampling.**

In addition, the production of $CO_{2\ (aq)}$ remained constant after removal of the positive applied potential for all of the mesoporous $TiO_2$ electrodes, demonstrating that the production of $CO_{2\ (aq)}$ occurred at a similar rate to diffusion of $CO_{2\ (aq)}$ from the thin layer.

### 4.4.6 *In situ* FTIR of Photocatalysis of NAG with $TiO_2$ electrodes

#### 4.4.6.1 Current-voltage response

Figure 4.31 displays CV measurements carried out on the $TiO_2$ electrodes using 0.1 mol $dm^{-3}$ $Na_2SO_4$ (pH 6.1) as the supporting electrolyte and 0.2 mol $dm^{-3}$ NAG as the compound to be oxidised (final pH 6.2).

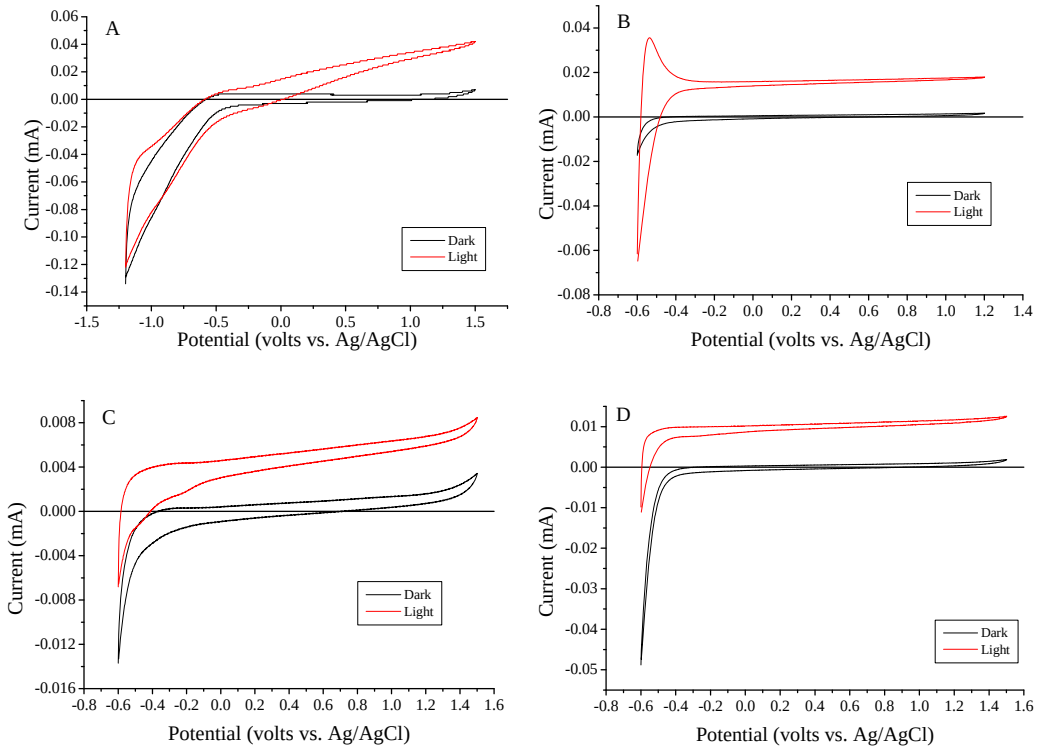


**Figure 4.31 Cyclic Voltammograms of (A) Thermal; (B) Degussa P25; (C) MW-treated; and (D) HT-treated $TiO_2$ electrodes immersed in 0.1 mol $dm^{-3}$ $Na_2SO_4$/0.2 mol $dm^{-3}$ NAG in the dark and under UV irradiation (labelled 'light'). Scan rate 100 mV $s^{-1}$.**

As discussed in section 4.4.1.1, upon the addition of an electron acceptor, in this case NAG, and in the presence of UV irradiation, the mesoporous $TiO_2$ films show enhanced photocurrents. However, as seen when using $Na_2(OOC)_2$, only the Thermal $TiO_2$ film showed photocurrents dependent on applied potential. The photocurrent onset potential using the Thermal $TiO_2$ electrode was found to be -0.5 V vs. Ag/AgCl. The mesoporous films all showed photocurrents independent of potential. Table 4.5 shows photocurrent responses for all film types tested using NAG. The CV

of the Degussa P25 electrode showed an oxidative peak at approximately -0.6 V vs. Ag/AgCl, possibly due to pH shifts which have moved the entire voltammogram to more positive values, and hence the reformation of NAG can be witnessed.

**Table 4.5 Photocurrent observed at 1.2 V vs. Ag/AgCl for Thermal and mesoporous $TiO_2$ films using 0.1 mol $dm^{-3}$ $Na_2SO_4$ as supporting electrolyte with 0.2 mol $dm^{-3}$ NAG.**

| Photocurrent response at 1.2 V vs. Ag/AgCl (μA) | Thermal (10 min @ 700 °C) | Degussa P25 | MW-treated $TiO_2$ | HT-treated $TiO_2$ |
|---|---|---|---|---|
| 0.1 mol $dm^{-3}$ $Na_2SO_4$ / 0.2 mol $dm^{-3}$ NAG | 9.25 | 10.59 | 4.25 | 10.83 |
| 0.1 mol $dm^{-3}$ $Na_2SO_4$ | 0.03 | 0.004 | 0.003 | 0.006 |

### 4.4.7 Photocatalytic degradation of NAG probed by *in situ* FTIR spectroscopy

There is conflicting evidence within the literature regarding the break-down of the bacterial cell wall during disinfection using photocatalytic means. To gain greater insight into the process, the effects of $TiO_2$ photocatalysis on a model cell wall component, NAG, were studied using *in situ* FTIR spectroscopy. Experiments of this nature were performed using an identical cell arrangement and experimental protocol to those experiments using $Na_2(OOC)_2$.

Figure 4.32 shows *in situ* FTIR spectra collected as a function of time from an irradiated Thermal $TiO_2$ electrode. The spectra were largely featureless; the positive band near 1650 $cm^{-1}$ was due to drawing of water into the thin layer. There was also a large featureless loss of absorption extending from 1800 $cm^{-1}$ into the near IR due to instrumental drift. Overlaid on this absorption was a very weak positive band at 2340 $cm^{-1}$, unambiguously assigned to $CO_{2\,(aq)}$.

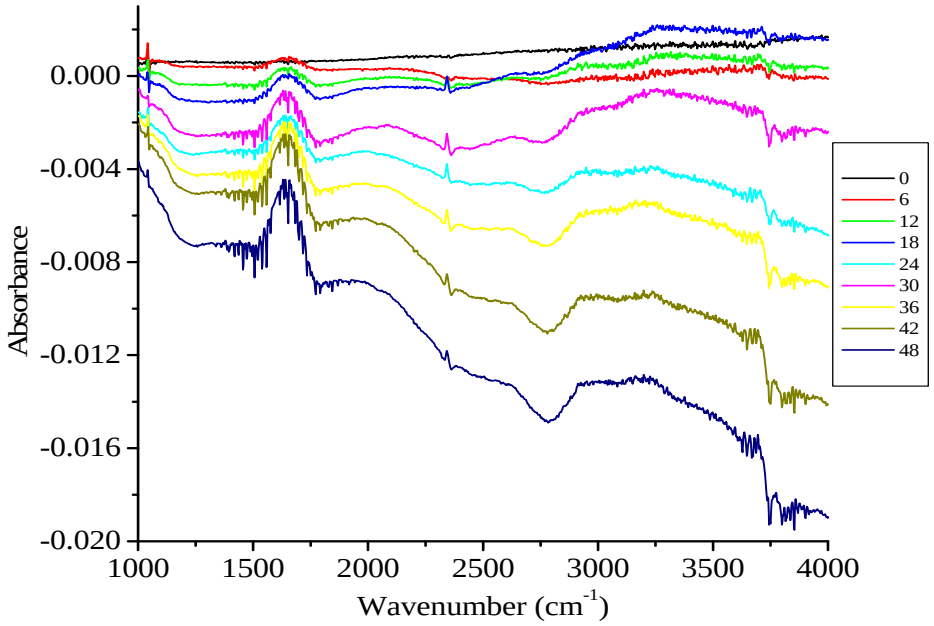


**Figure 4.32 T, NAG, PC: *In situ* FTIR absorbance spectra obtained during photocatalytic experiments using a Thermal $TiO_2$ electrode immersed in 0.1 mol $dm^{-3}$ $Na_2SO_4$/0.2 mol $dm^{-3}$ NAG. Spectra were collected every 3 minutes, as indicated. UV irradiation was applied after 6 minutes and removed after 27 minutes.**

Figure 4.33 displays *in situ* FTIR spectra analogous to those shown in Figure 4.32, except using a Degussa P25 $TiO_2$ electrode. These spectra were vastly different to those collected using the Thermal $TiO_2$ electrode. There was a large positive band from 1000 to 2000 $cm^{-1}$ with a negative peak at 1650 $cm^{-1}$. The latter, attributed to water, may be due to minimal absorbance in that region from a thick electrolyte film causing the complete absorption of incident IR radiation in this region. However, from examination of the single beam reference spectrum collected at the commencement of the experiments, there was sufficient energy within this region to discount this theory as the cause of the spectral effects seen. The increase in baseline from 1000 to 3000 $cm^{-1}$ was also seen when using the HT-treated $TiO_2$ electrodes (Appendix Figure A.9B), and to a lesser extent with the MW-treated $TiO_2$ electrodes (Appendix Figure A.9A). The possible causes of this effect will be discussed in further detail in a later section.

Also overlaid on this broad baseline change was a less intense absorption trough centred at 2154 $cm^{-1}$ due to a combination water band of vibrational and librational modes.[53]

Any features relating to the possible break-down of the NAG within the cell, and any intermediate break-down products from photocatalytic action on the compound were obscured by the intense baseline changes seen throughout the spectra collected using the mesoporous $TiO_2$ electrodes.

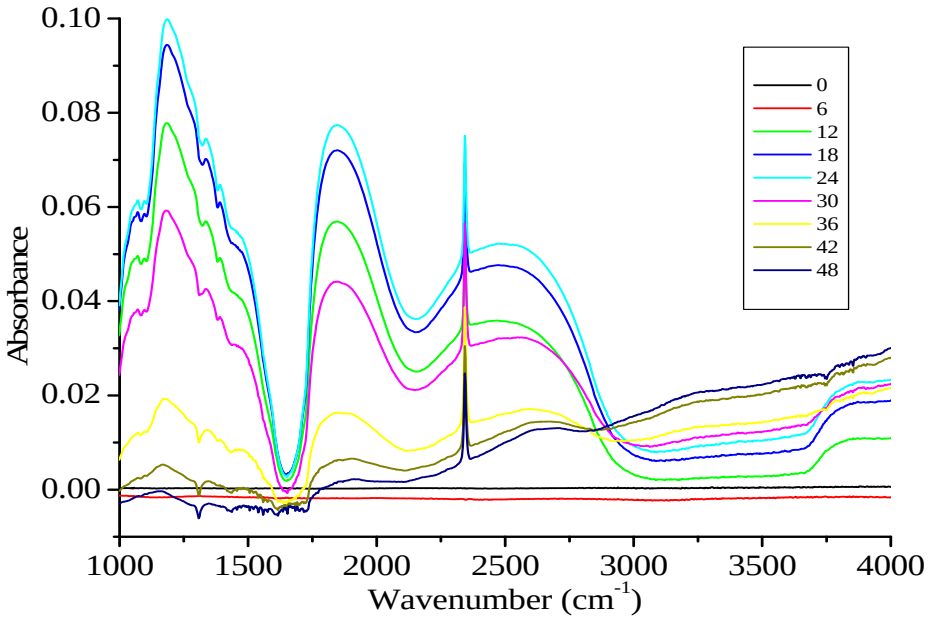


**Figure 4.33 P25, NAG, PC: *In situ* FTIR absorbance spectra obtained during photocatalytic experiments using a Degussa P25 $TiO_2$ electrode immersed in 0.1 mol $dm^{-3}$ $Na_2SO_4$/0.2 mol $dm^{-3}$ NAG. Spectra were collected every 3 minutes, as indicated. UV irradiation was applied after 6 minutes and removed after 27 minutes.**

In addition to the above features, when using the mesoporous $TiO_2$ electrodes, a sharp positive absorbance band at 2340 $cm^{-1}$ unambiguously $CO_{2\ (aq)}$ was apparent upon UV irradiation. Plots of the $CO_{2\ (aq)}$ absorbance during the photocatalytic experiments are shown in Figure 4.34.

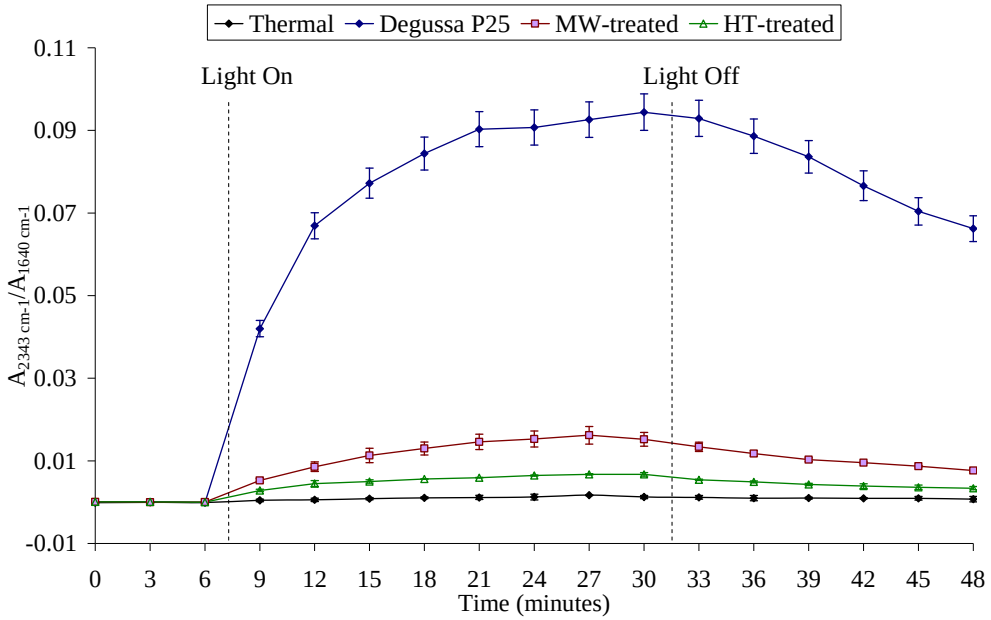


**Figure 4.34 Plots of average $CO_{2\ (aq)}$ absorbances produced during photocatalysis experiments with Thermal, Degussa P25, and MW- and HT-treated $TiO_2$ electrodes immersed in 0.1 mol $dm^{-3}$ $Na_2SO_4$/0.2 mol $dm^{-3}$ NAG, with and without UV irradiation. Spectral absorbance was background corrected and normalised for differing $TiO_2$ film thickness against background water intensity values obtained at the start of each experiment.**

All electrode types showed no $CO_{2\ (aq)}$ absorbance until UV irradiation commenced. Once irradiation occurred, the MW- and HT-treated $TiO_2$ electrodes produced only small amount of $CO_{2\ (aq)}$ due to the photocatalytic break-down of NAG; however Degussa P25 displayed an initial rapid increase in the rate of $CO_{2\ (aq)}$ production, which began to plateaux after approximately 24 minutes had elapsed. The Thermal $TiO_2$ electrode, however, displayed no $CO_{2\ (aq)}$ production in the presence of UV light. Once UV irradiation was removed, all three mesoporous electrode types showed decreasing concentrations of $CO_{2\ (aq)}$ within the thin electrolyte layer due to diffusion into the surrounding solution.

### 4.4.8 *In situ* FTIR of EAP of $TiO_2$ electrodes with NAG

Figure 4.35 shows *in situ* FTIR spectra collected as a function of potential from an un-irradiated Thermal $TiO_2$ electrode. These spectra are representative of those spectra collected from the mesoporous $TiO_2$ electrodes under identical conditions. These spectra are similar to those collected using un-irradiated $TiO_2$ electrodes

immersed in $Na_2(OOC)_2$; and were largely featureless, with a small amount of water entering into the thin electrolyte layer during the experiment, and a broad featureless loss of absorbance which extended into the near-IR due to instrumental drift.

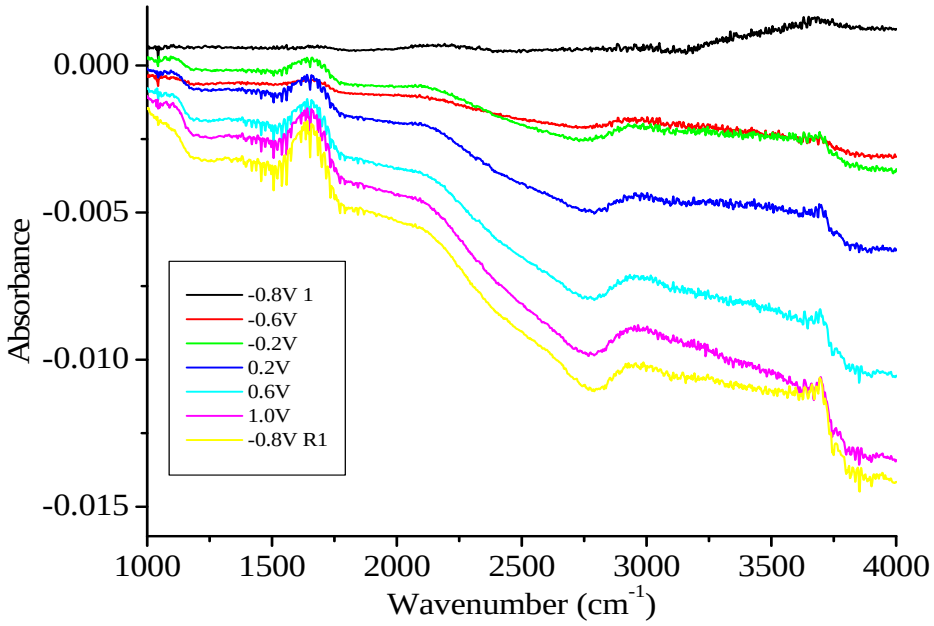


**Figure 4.35 T, NAG, P-EAP, Dark: *In situ* FTIR absorbance spectra obtained using a Thermal $TiO_2$ electrode immersed in 0.1 mol $dm^{-3}$ $Na_2SO_4$/0.2 mol $dm^{-3}$ NAG, in the dark. Spectra were collected every 2 minutes at the indicated applied potentials. Potential steps were 200 mV. 'R' denotes spectra obtained after the applied potential was returned to the initial potential.**

Figure 4.36 shows the *in situ* FTIR spectra collected as a function of potential from an irradiated Thermal $TiO_2$ electrode. In contrast to those spectra collected using the same electrode under UV irradiation only, and those in the dark as a function of potential, these spectra displayed several features.

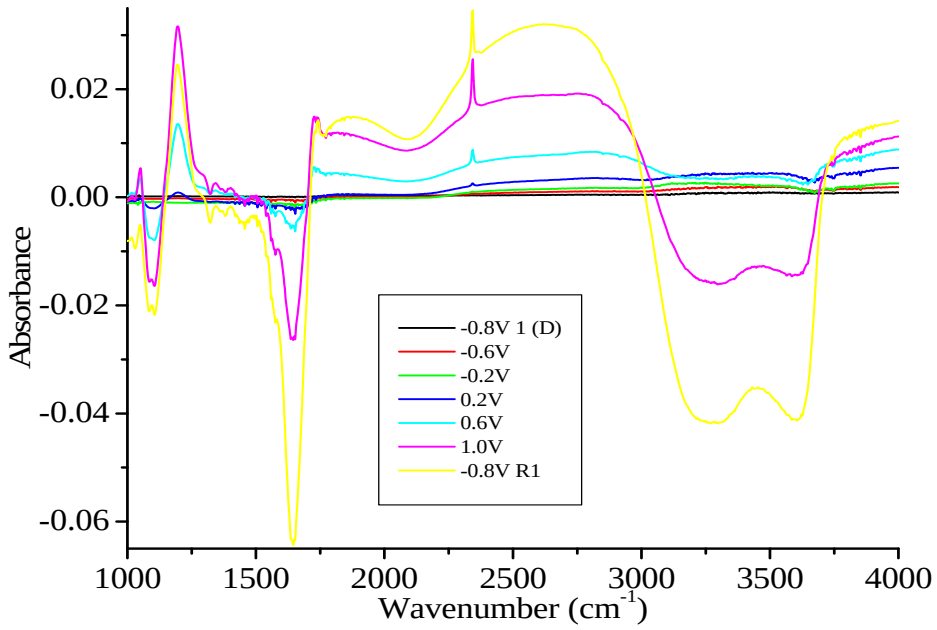


**Figure 4.36 T, NAG, P-EAP, Light: *In situ* FTIR absorbance spectra obtained during potential-dependent EAP using Thermal $TiO_2$ electrodes immersed in 0.1 mol dm$^{-3}$ $Na_2SO_4$/0.2 mol dm$^{-3}$ NAG, under irradiation with UV light (light applied after -0.8V 1 (D)). Spectra were collected at the indicated potentials. 'R' denotes spectra obtained after the applied potential was returned to the initial potential.**

Negative water bands at 1645, 2100 and 3275 cm$^{-1}$ dominated the spectra. The predominant processes contributing to this were the aforementioned rapid pH drop in the thin layer caused by the oxidation of water at the $TiO_2$:[8]

$$2H_2O + 4h_s^+ \rightarrow 4H^+ + O_{2(g)} + 4e^- \qquad \textbf{4.20}$$

where $h_s^+$ refers to a photogenerated hole at the electrode surface. It is believed that the first step is:

$$h_s^+ + OH_{ads}^- \rightarrow {}^{\bullet}OH_{ads/sol} \qquad \textbf{4.21}$$

which appears to be an extremely fast process. Evidence to support the overall increase in positive charge within the electrolyte thin layer was provided by the observation of the bulk gain feature of sulfate near 1196 cm$^{-1}$ from the protonation of bisulfate:[49]

$$SO_4^{2-} + H^+ \rightarrow HSO_4^- \qquad \textbf{4.22}$$

The loss of water from the thin layer was however, attributed to the expulsion of bulk water[8] from the thin layer due to the formation of small $O_2$ bubbles that have nucleated and grown on the $TiO_2$ surface. Such bubbles may remain attached to the $TiO_2$ surface or become detached, in which case they will migrate out of the thin layer. An additional negative band at 3600 $cm^{-1}$ was evident, also assigned to water. Similar IR responses have been noted when using irradiated rutile $TiO_2$ in the presence of ethylene glycol,[13] where an additional water loss band at 3600 $cm^{-1}$ was present. The higher position of this band compared to bulk water, was attributed to the 'increased ionic strength of the thin layer associated with electrochemical processes at the $TiO_2$ surface'.[13]

When examining Figure 4.36, it was apparent that $CO_{2\ (aq)}$ was produced; however, the band intensity was minimal. It was possible that the lack of $CO_{2\ (aq)}$ was due to its reduction to $HCO_3^-$ or $CO_3^{2-}$. However, negative and not positive bands arising from both of these species were witnessed (1576 and 1322 $cm^{-1}$) due to the pH swing to lower value within the thin layer. Plots of the $CO_{2\ (aq)}$ production with respect to bicarbonate loss highlight this (Figure 4.37) as there appeared to be conversion of bicarbonate to $CO_{2\ (aq)}$ due to the lowered pH within the thin layer, which occurred after 10 minutes. This time corresponded to the photocurrent onset potential of 0.2 V vs. Ag/AgCl. This however, did not account for the rapid production of $CO_{2\ (aq)}$ up to 22 minutes or from 0.2 – 1.2 V vs. Ag/AgCl. Therefore, this demonstrated that the Thermal $TiO_2$ electrode can photo-oxidise NAG; however, the small quantity of $CO_{2\ (aq)}$ produced also showed that this electrode could either be fairly inactive with respect to the photo-oxidation of NAG, or that NAG could be degraded through a multi-step mechanism with $CO_{2\ (aq)}$ as a final product.

Further evidence for the EAP of NAG by the Thermal $TiO_2$ electrode was found within the FTIR spectra. A series of weak negative bands were attributed to NAG species. Table 4.6 shows the positions and vibrational assignments for each of these bands. The amide I and II vibrations, which are dominate in amino-saccharides, including NAG, were obscured by water vibrations and therefore could not be identified within the spectra.

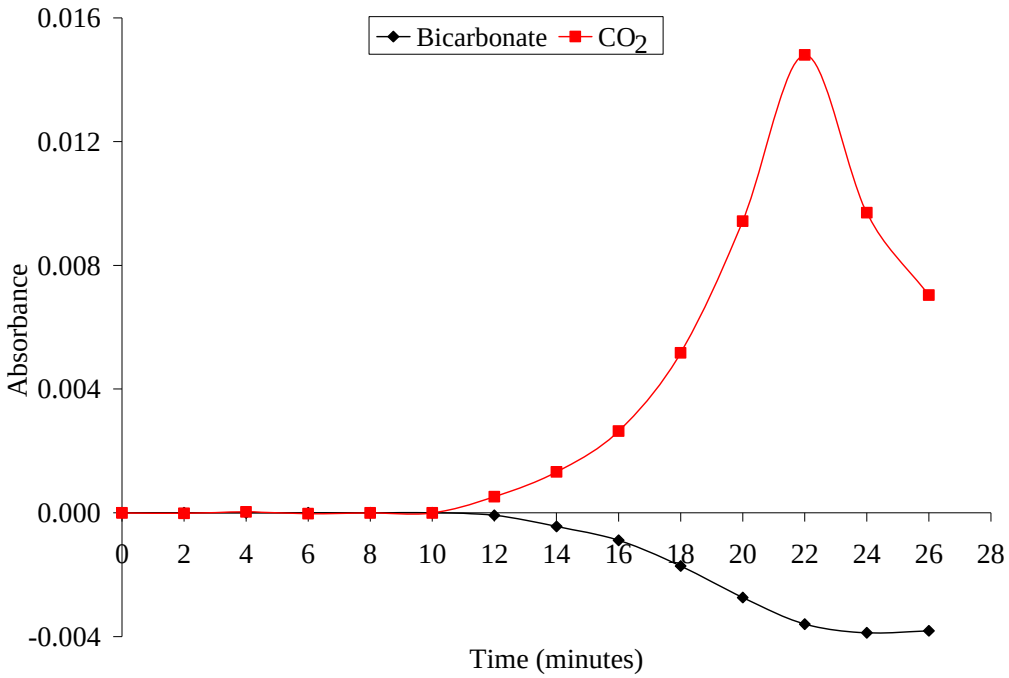


**Figure 4.37 Plot of absorbance of the bicarbonate (1322 $cm^{-1}$) and $CO_{2\ (aq)}$ (2343 $cm^{-1}$) bands from spectra shown in Figure 4.36**

**Table 4.6 NAG degradation bands seen when using the Thermal $TiO_2$ electrode**

| Band position ($cm^{-1}$) | Vibrational assignment | Reference |
|---|---|---|
| 1455 | $CH_2$ | 54 |
| 1435 | δ(C-H), δ(O-H) | 54 |
| 1419 | $\delta(C_6\text{-}H_2)$, δ(O-H) | 54 |
| 1381 | $\delta(CH_3)$ | 55 |
| 1363 | $\delta(C_6\text{-}H_2)$ | 30 |
| 1084 | $\nu(C_1\text{-}H)$, δ(C-O-H) | 54 |
| 1030 | δ(C-O-H) | 54 |
| 1011 | $CH_3$ | 54 |

Consistent with the production of $CO_{2\ (aq)}$, a positive band at 1726 $cm^{-1}$ and two overlapping positive bands at 1740 $cm^{-1}$ were also observed (Figure 4.36). Figure 4.38 displays plots of these bands with respect to applied potential and elapsed time. These features were evident from 0.4 to 1.2 V vs. Ag/AgCl and once the negative bias was re-applied the intensity of these bands decreased, as did $CO_{2\ (aq)}$ absorbance,

which indicated products diffusing out of the thin layer. The slower rate of diffusion of the 1726 and 1740 $cm^{-1}$ bands, compared to the $CO_{2\ (aq)}$, may indicate that the unknown product was strongly adsorbed to the $TiO_2$ or that the product was physically larger than the $CO_{2\ (aq)}$ molecules, thus slowing diffusion. Two weak negative bands at 2850 and 2920 $cm^{-1}$ were also apparent once the photocurrent onset potential (0.2 V vs. Ag/AgCl) was reached. These bands were assigned to ν(C-H) and ν(C-$H_2$) stretching vibrations, respectively.[56]

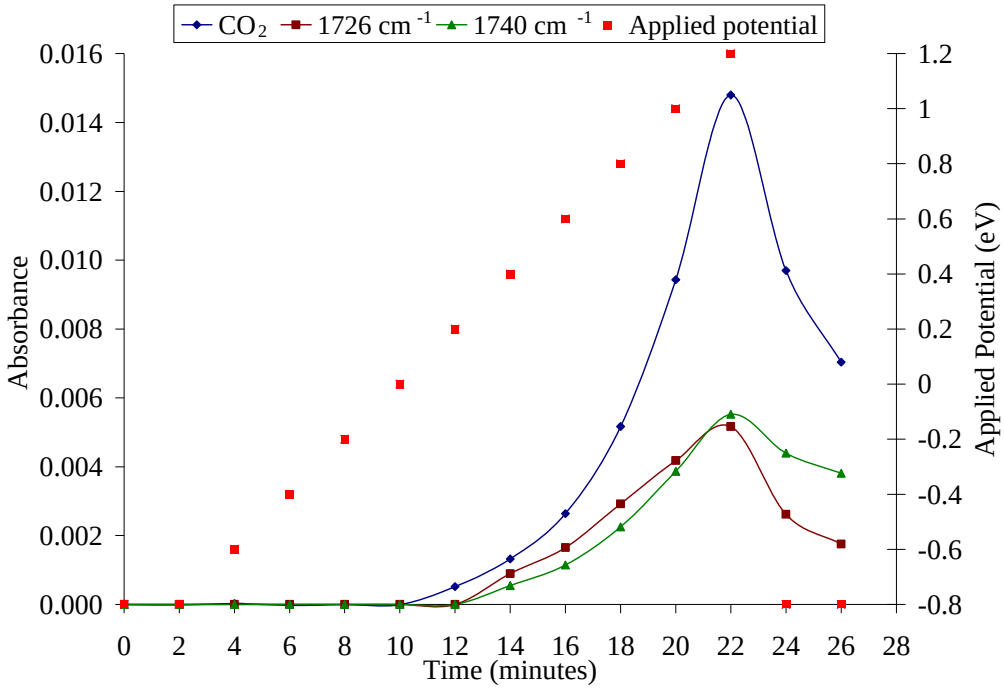


**Figure 4.38 Plots of baseline corrected absorbance of $CO_{2\ (aq)}$ (2343 $cm^{-1}$) with respect to positive bands located at 1726 and 1740 $cm^{-1}$. Absorbances used were from spectra obtained using the Thermal $TiO_2$ electrode shown in Figure 4.36. Applied potential at each sample point indicated (■).**

Figure 4.39 shows spectra analogous to those in Figure 4.36, except using the Degussa P25 $TiO_2$ electrode. Upon close examination, despite the presence of a strong negative band centred at 1640 $cm^{-1}$ after UV irradiation, there were no accompanying water bands around 2100 or 3275 $cm^{-1}$, thus there was no evidence of the photo-oxidation of water or the loss of water from thin layer by $O_2$ production.

Superimposed on the broad featureless baseline change from 1000 $cm^{-1}$ extending into the near-IR, was a very strong positive band around 1170 $cm^{-1}$ and a slightly weaker band around 1053 $cm^{-1}$. Due to the strong baseline absorbance increase in this region, analysis of this region was far from simple. These bands were not thought to arise from sulfate/bisulphate, as their frequencies were not the same as seen in previous experiments under similar conditions. Because the baseline is ill-defined, it appeared that these positive bands may actually be the trough of two overlapping negative bands around 1100 $cm^{-1}$.

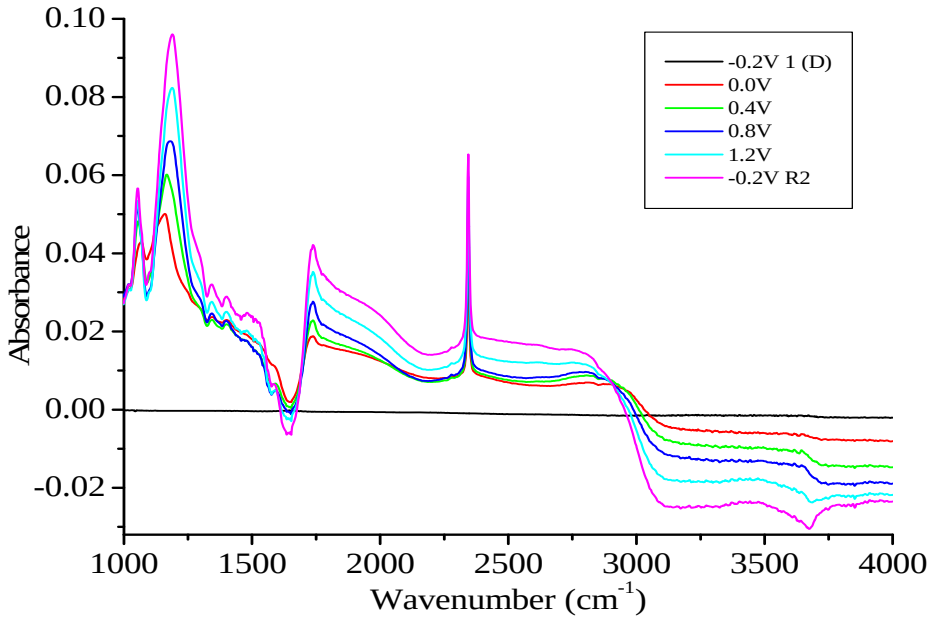


**Figure 4.39 P25, NAG, P-EAP, Light: *In situ* FTIR absorbance spectra obtained during potential-dependent EAP using Degussa P25 $TiO_2$ electrodes immersed in 0.1 mol $dm^{-3}$ $Na_2SO_4$/0.2 mol $dm^{-3}$ NAG, under irradiation with UV light. Light was applied after initial spectrum was collected in the dark (-0.2V 1 (D)). Spectra were collected at the indicated potentials. 'R' denotes spectra obtained after the applied potential was returned to the initial potential.**

No vibrational assignments for the negative bands can be made at this stage due to the dramatic shift in baseline throughout the experiment. However, it is well known that bands within this region arise from a combination of C-O, C-C, C-O-H and C-O-C vibrations[56] which are strong within carbohydrates in general, and NAG in particular. Conclusive structural assignments were extremely difficult to perform

using this region and in this case, due to the change in baseline absorbance within this region, such assignments would be imprudent.

The region from 1280 – 1800 $cm^{-1}$ showed minimal baseline changes during irradiation, thus spectral features within this region were more easily interpreted. A series of negative bands were evident from irradiation and occurred at 1325, 1384, 1458, 1576 and 1650 $cm^{-1}$. 1325 and 1576 $cm^{-1}$ were assigned to bicarbonate and carbonate, respectively. The other three bands were assigned to NAG, arising from a loss of $CH_3$ and amide groups. Two bands at 1726 and 1739 $cm^{-1}$ were formed upon irradiation, with the latter producing a stronger absorbance than the former over time. These bands occur within the carbonyl stretching region and are thought to be formed due to an increase in double bond character of the C=O bond possibly resulting from $CH_3$ cleavage.[57] The presence of two vibrational bands could indicate that the product was initially adsorbed to the $TiO_2$ surface producing a band at 1726 $cm^{-1}$ which then moved into the bulk solution causing the shift in wavenumber to a higher frequency at 1739 $cm^{-1}$.[30]

Figure 4.40 displays *in situ* FTIR spectra obtained using the MW-treated $TiO_2$ electrode immersed in 0.1 mol $dm^{-3}$ $Na_2SO_4$/0.2 mol $dm^{-3}$ NAG under irradiation, with respect to applied potential. (See Appendix Figure A.10A for *in situ* FTIR spectra collected using the HT-treated $TiO_2$ electrode under indentical conditions.) These spectra displayed only weak baseline changes and as a result were much clearer and more easily interpreted than the Degussa P25. In particular the two positive bands were present which added weight to the argument that these are real gain bands in Degussa P25.

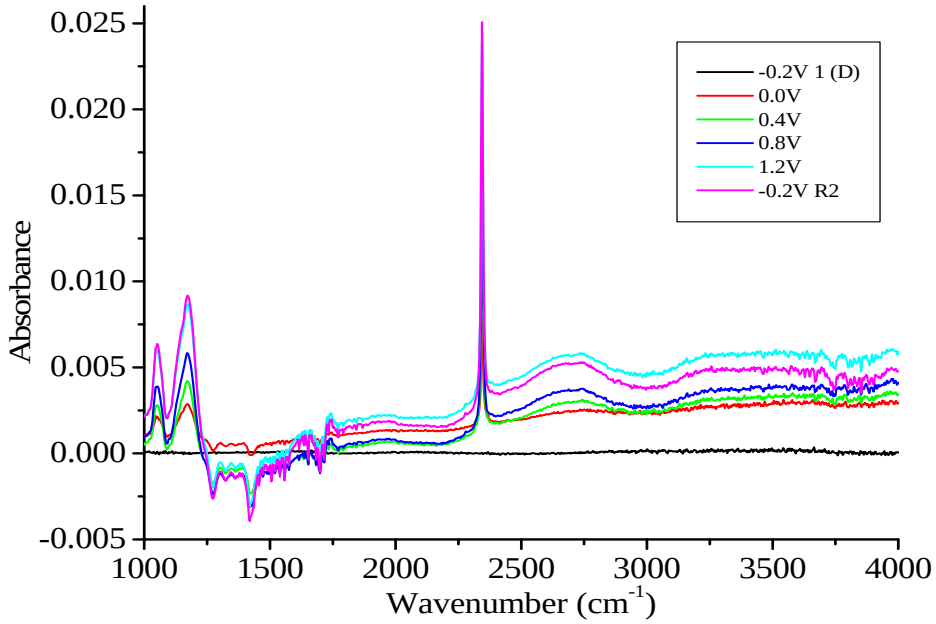


**Figure 4.40 MW, NAG, P-EAP, Light: *In situ* FTIR absorbance spectra obtained during potential-dependent EAP using MW-treated $TiO_2$ electrodes immersed in 0.1 mol $dm^{-3}$ $Na_2SO_4$/0.2 mol $dm^{-3}$ NAG, under irradiation with UV light. Light was applied after initial spectrum was collected in the dark (-0.2V 1 (D)). Spectra were collected at the indicated potentials. 'R' denotes spectra obtained after the applied potential was returned to the initial potential.**

Figure 4.40 also shows negative bands attributed to NAG degradation; the vibrational positions and assignments of which are shown in Table 4.7. It was apparent that the $CH_3$ group was removed when using this electrode type, as was found when using the Thermal $TiO_2$ electrode. There was also evidence of the loss of $C_6$-$H_2$ vibrations and ring attack in the $C_1$ position. NAG in aqueous solution shows no significant vibrational bands at 1388 or 1362 $cm^{-1}$. The negative bands seen during the *in situ* FTIR study may be due to the loss of photo-oxidation products produced during the break-down of NAG and led to the hypothesis that the break-down mechanism occurred as a multi-step process. Glucose produces a characteristic band[30] at 1363 $cm^{-1}$ and it was therefore thought that one of the break-down products of NAG could be close in structure to that of glucose. The reduction of intensity of this band may indicate that this break-down product was further oxidised to $CO_{2\,(aq)}$.

**Table 4.7 NAG degradation bands seen when using the MW-treated $TiO_2$ electrode**

| Band position ($cm^{-1}$) | Vibrational assignment | Reference |
|---|---|---|
| 1436 | δ(C-H), δ(O-H) | 54 |
| 1418, 1434 | δ(C-H), δ(O-H) | 54 |
| 1385 | δ($CH_3$) | 55 |
| 1372 | δ(C-H), δ(O-H) | 54 |
| 1362 | δ($C_6$-$H_2$) | 30 |
| 1272 | $C_6$-OH, $C_1$-OH | 54 |

When using the MW-treated $TiO_2$ electrode, three positive bands at 1726, 1737 and 1743 $cm^{-1}$ were apparent. Plots of the change in intensity of these bands with respect to time/applied potential showed that initially all three bands increased at the same rate, but after 4 minutes or once 0.0 V vs. Ag/AgCl was reached, the rate the 1726 $cm^{-1}$ production decreased, while the two other bands continued to increase at the same rate (Figure 4.41). This was consistent with results obtained using the other electrode types including the Thermal $TiO_2$ electrode. It was theorised that the band at 1726 $cm^{-1}$ arose from an absorbed carboxyl product and as the possible sites for adsorption were saturated, the rate of production of adsorbed species would slow.

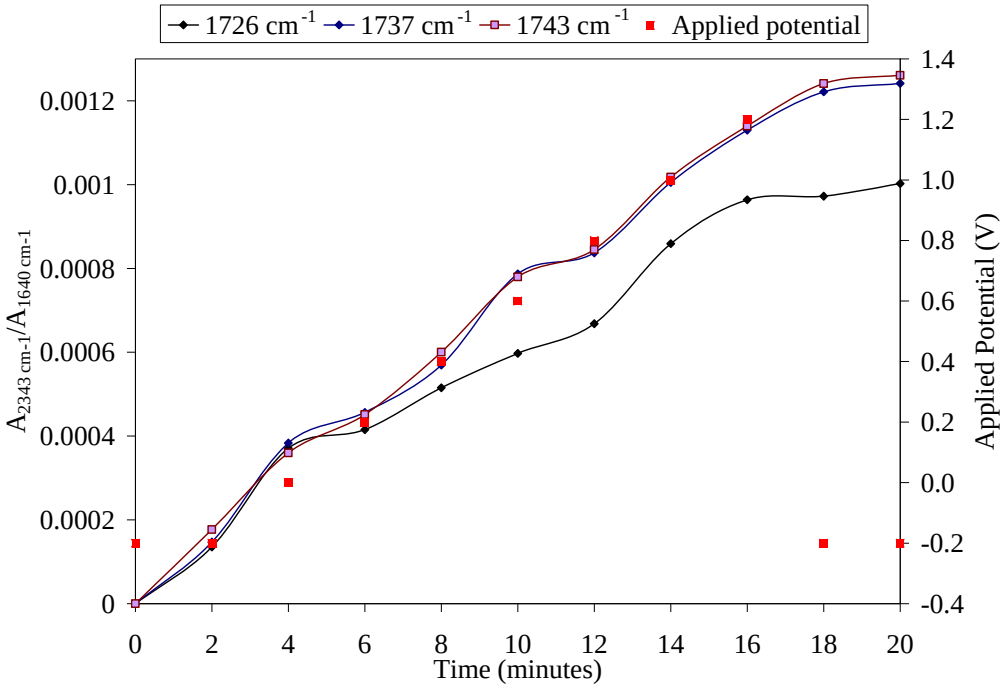


**Figure 4.41 Plots of 1726, 1737 and 1743 $cm^{-1}$ absorbances produced during potential-dependent EAP with MW-treated $TiO_2$ electrodes immersed in 0.1 mol $dm^{-3}$ $Na_2SO_4$/0.2 mol $dm^{-3}$ NAG, under irradiation with UV light. Spectral absorbance was background corrected and normalised for differing $TiO_2$ film thickness against background water intensity values obtained at the start of each experiment. (■) Applied potential during sampling.**

Plots of the $CO_{2\ (aq)}$ absorbance during potential-dependent EAP experiments are shown in Figure 4.42 and Figure 4.43. As discussed previously, Thermal films are dependent on a positive applied potential for degradation to occur. In contrast, as was seen when using $Na_2(OOC)_2$, the mesoporous films all showed photodegradation immediately after UV illumination which continued to increase throughout the experiment.

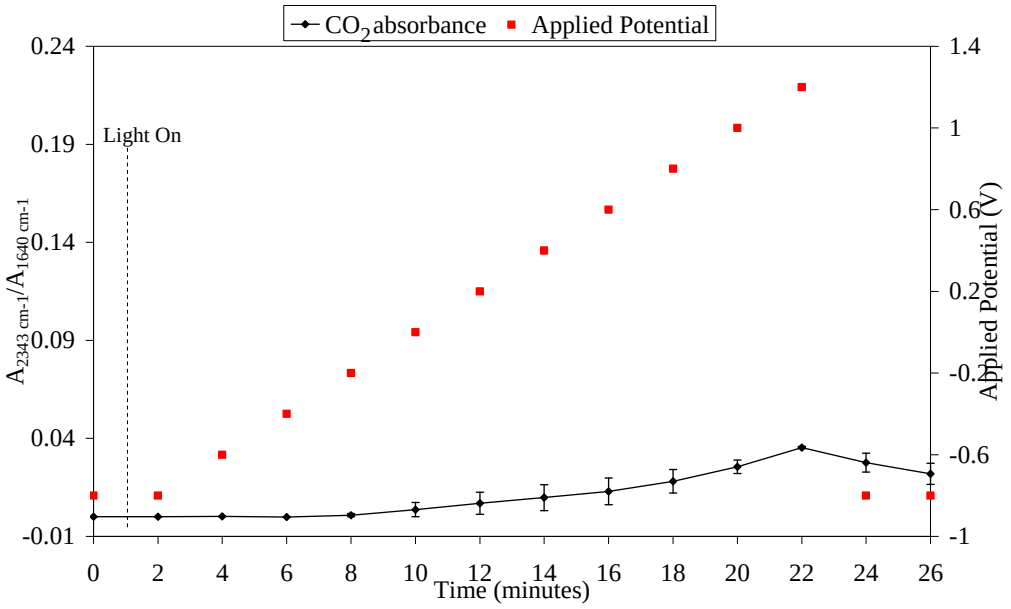


**Figure 4.42 Plots of average $CO_{2\ (aq)}$ absorbances produced during potential-dependent EAP with Thermal $TiO_2$ electrodes immersed in 0.1 mol $dm^{-3}$ $Na_2SO_4$/0.2 mol $dm^{-3}$ NAG, under irradiation with UV light. Spectral absorbance was background corrected and normalised for differing $TiO_2$ film thickness against background water intensity values obtained at the start of each experiment. (■) Applied potential during sampling.**

When comparing the mesoporous $TiO_2$, Degussa P25 $TiO_2$ displayed rapid onset of $CO_{2\ (aq)}$ immediately after UV illumination which continued to increase until 12 minutes had elapsed, when a plateaux was reached. Upon removal of the positive potential, after 16 minutes, only a slight reduction in $CO_{2\ (aq)}$ absorbance was seen, due to an equilibrium being reached between the rate of $CO_{2\ (aq)}$ production and diffusion from the thin layer. The MW- and HT-treated $TiO_2$ electrodes showed onset of $CO_{2\ (aq)}$ production after UV illumination which continued to increase throughout the experiment. Even after the positive bias was removed, the rate of $CO_{2\ (aq)}$ production remained constant, and showed no decline in the overall absorbance over the time-frame of the investigation.

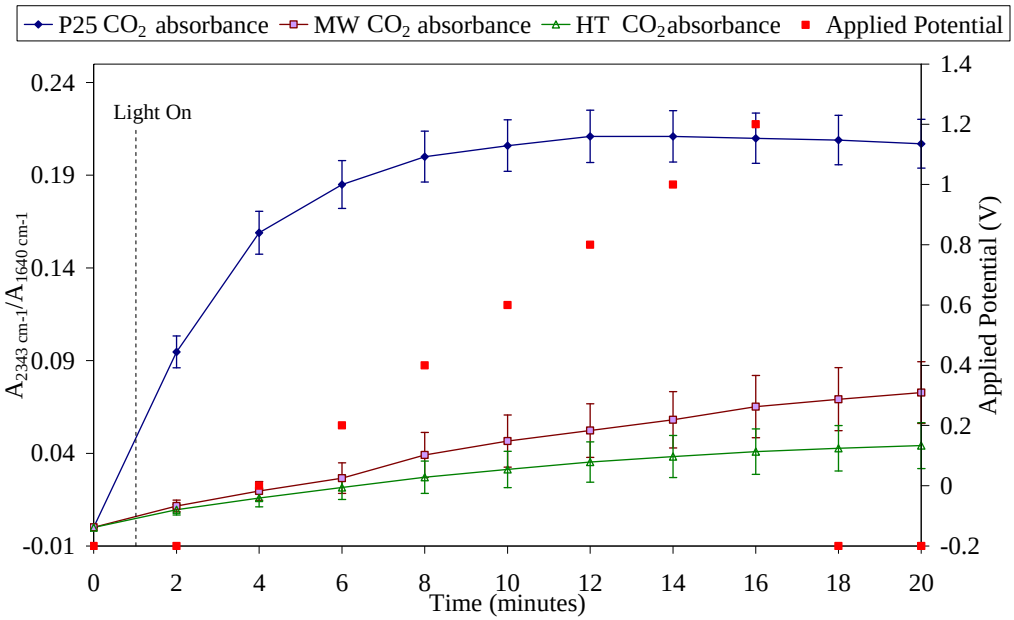


**Figure 4.43 Plots of average $CO_{2\ (aq)}$ absorbances produced during potential-dependent EAP experiments with Degussa P25, MW- and HT-treated $TiO_2$ electrodes immersed in 0.1 mol $dm^{-3}$ $Na_2SO_4$/0.2 mol $dm^{-3}$ NAG, under irradiation with UV light. Spectral absorbance was background corrected and normalised for differing $TiO_2$ film thickness against background water intensity values obtained at the start of each experiment. (■) Applied potential during sampling.**

Upon comparing these results, the film types in decreasing order of maximum absorbance of $CO_{2\ (aq)}$ were P25 < MW < HT < Thermal. It was possible that the increased $CO_{2\ (aq)}$ production seen when using the Degussa P25 film may be due to surface area effects, which will be discussed in more detail in a later section.

### 4.4.9 *In situ* FTIR of EAP of $TiO_2$ electrodes with NAG: investigated as a function of time

Figure 4.44 displays *in situ* FTIR spectra obtained using the Thermal $TiO_2$ electrode investigated under applied potential as a function of time. These spectra were very similar to those obtained using the same electrode during potential-dependent experiments (Figure 4.36). The predominant features arose from the photo-oxidation of bulk water which caused an increase in $O_2$ content within the thin layer. This in

turn drove bulk water out of the thin layer. Further evidence of this was found by the conversion of bisulphate to sulfate due to the rapid drop in pH within the thin layer.

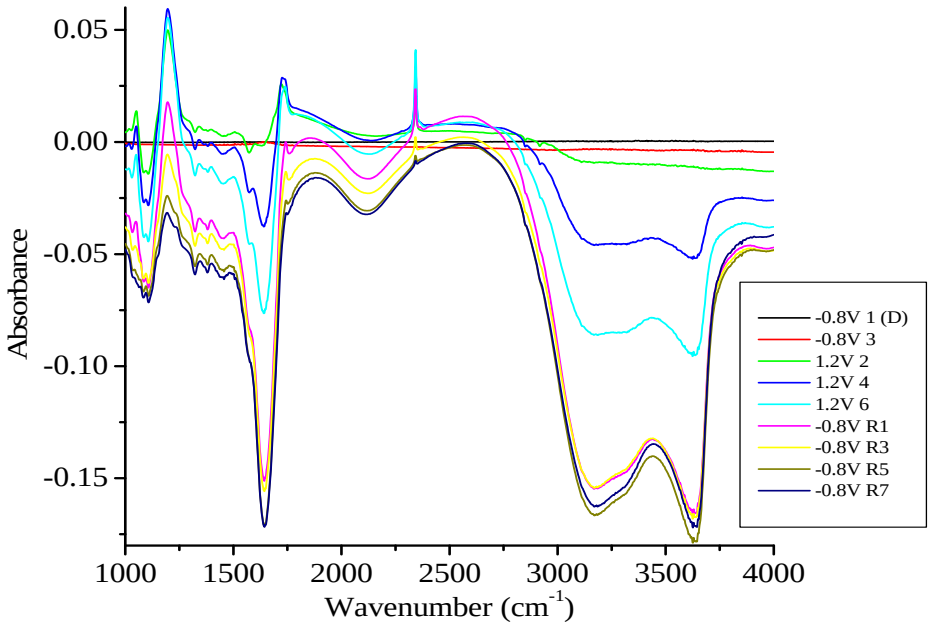


**Figure 4.44 T, NAG, T-EAP: *In situ* FTIR absorbance spectra obtained using Thermal $TiO_2$ electrodes immersed in 0.1 mol $dm^{-3}$ $Na_2SO_4$/0.2 mol $dm^{-3}$ NAG, under irradiation with UV light (light switched on after initial spectrum was collected (-0.8 V 1 (D)). Spectra were collected at the indicated time intervals (minutes). Initial applied potential -0.8 V vs. Ag/AgCl; applied potential shifted to 1.2 V vs. Ag/AgCl in a single step after 6 minutes and held until 27 minutes. After 27 minutes potential was lowered to initial potential and held for the remainder of the experiment.**

Peaks characteristic of NAG degradation were observed after both irradiation and 1.2 V vs. Ag/AgCl was applied. These peaks occurred at the same wavenumbers as seen during the Thermal $TiO_2$ electrode experiments performed as a function of potential and have been previously provided in Table 4.6.

This experiment showed the first occurrence of $CO_{2\,(aq)}$ bubble formation, as evident by an additional peak at 2365 $cm^{-1}$; however from comparison of the relative intensities of these bands, it was evident that the majority of the $CO_{2\,(aq)}$ remained in solution. Apart from the usual $CO_{2\,(aq)}$ production, there were positive bands at 1720 and 1741 $cm^{-1}$. Plots of the absorbance of these peaks show that they were not

produced until UV irradiation and a positive potential was applied (Figure 4.45). Once this occurred an initial rapid increase in the band at 1720 $cm^{-1}$ ensued, until a maximum was reached at 12 minutes, after which a steady decline occurred until the positive bias was removed, at which time the band was no longer apparent. Comparatively, the 1741 $cm^{-1}$ band showed an initial rapid increase up to 12 minutes, after which it increased steadily until the positive bias was removed, where it declined in intensity until the conclusion of the experiment.

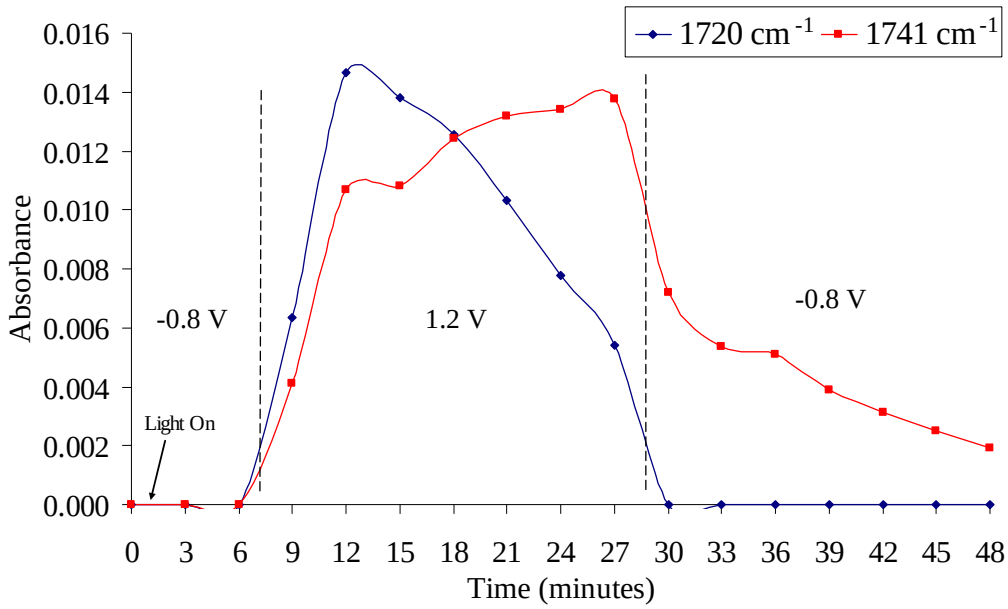


**Figure 4.45 Plot of absorbance of 1720 and 1741 $cm^{-1}$ bands collected from Thermal $TiO_2$ electrode immersed in 0.1 mol $dm^{-3}$ $Na_2SO_4$/0.2 mol $dm^{-3}$ NAG, under irradiation with UV light, with respect to time. Initial applied potential was -0.8 V vs. Ag/AgCl; after 6 minutes was 1.2 V vs. Ag/AgCl and reduced to -0.8 V vs. Ag/AgCl after 27 minutes irradiation.**

From this, it appeared that the photo-electrochemical degradation of NAG at the $TiO_2$ electrode surface occurred via a multi-step process, yielding intermediates and $CO_{2\ (aq)}$. Also apparent at 1.2V vs. Ag/AgCl was small negative bands due to the $\nu$(C-H) and $\nu$(C-$H_2$) stretching vibrations, seen at 2850 and 2920 $cm^{-1}$.

Spectra collected as a function of time using the Degussa P25 $TiO_2$ electrode displayed characteristics similar to those obtained when using the Thermal $TiO_2$ electrode (see Appendix Figure A.10B). The dominant features were the photo-

oxidation of water evidenced by loss of bulk water, bisulphate to sulfate conversion, the NAG photo-oxidation to $CO_{2\,(aq)}$ and an intermediate product at 1741 $cm^{-1}$.

The spectra collected as a function of time using the MW-treated $TiO_2$ electrode (Figure 4.46) were vastly different to those collected using the Degussa P25 and Thermal $TiO_2$ electrodes. Minimal baseline changes occurred, which resulted in clearer, more easily interpreted spectra. No water photo-oxidation was witnessed, which further enabled vibrational band assignments.

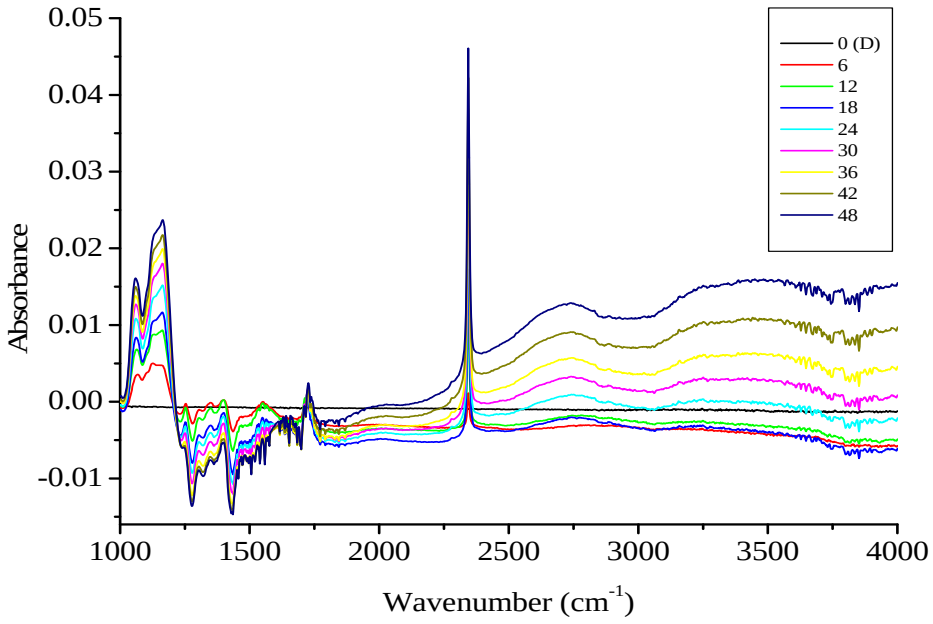


**Figure 4.46 MW, NAG, T-EAP: *In situ* FTIR absorbance spectra obtained using MW-treated $TiO_2$ electrodes immersed in 0.1 mol $dm^{-3}$ $Na_2SO_4$/0.2 mol $dm^{-3}$ NAG, under irradiation with UV light. Initial spectrum was collected in the dark (0 (D)). Spectra were collected at the indicated time intervals (minutes). Initial applied potential -0.2 V vs. Ag/AgCl; applied potential shifted to 1.2 V vs. Ag/AgCl in a single step after 6 minutes and held until 27 minutes. After 27 minutes potential was lowered to initial potential and held for the remainder of the experiment.**

When examining the lower wavenumber region, 1000 – 1200 $cm^{-1}$, strong positive bands at 1060, 1100, 1125 and 1161 $cm^{-1}$ dominated. Assignments were complex due to vibrational combinations; however, when examining these bands as a group, the dominate feature was an increase in the bending vibrations of C-O-H groups within the electrolyte layer. This could be due to complete decomposition of the

carbohydrate molecule; however this did not appear to occur here as no free OH vibrations were observed (3500 – 3650 $cm^{-1}$). Therefore it was more likely that the increase in absorbance in this region merely denoted a change in structure of the carbohydrate molecule resulting from its partial decomposition.

When examining the region from 1200 – 1600 $cm^{-1}$, it was apparent that a loss in absorbance of almost all the vibrational bands arising from NAG occurred. A summary of these can be found in Table 4.8. In all previous examples, especially in the $Na_2(OOC)_2$ model experiments, $CO_3^{2-}$ and $HCO_3^-$ *always* appeared together and never one or the other. As no peak was present at 1585 $cm^{-1}$ here, the band at 1321 $cm^{-1}$ was assigned to the $CH_3$ vibration within NAG[54] rather than $CO_3^{2-}$. From these bands it was thought that during the photo-oxidation of the NAG molecule, the $CH_2$, $CH_3$ and OH groups were removed. No loss of amide character was apparent; however, strong water vibrations within this region can obscure these spectral features.

**Table 4.8 NAG degradation bands seen when using the MW-treated $TiO_2$ electrode from Figure 4.46**

| Band position ($cm^{-1}$) | Vibrational assignment | Reference |
|---|---|---|
| 1471 | $CH_2$ scissoring | 55 |
| 1436 | δ(C-H), δ(O-H) | 54 |
| 1372 | δ(C-H), δ(O-H) | 54 |
| 1362 | $\delta(C_6\text{-}H_2)$ | 30 |
| 1321 | $CH_3$ | 54 |
| 1277 | $C_6$-OH, $C_1$-OH | 54 |
| 1237 | $CH_2$ | 54 |
| 1161 (+) | δ(C-H), δ(C-O-H) | 54,55 |
| 1125 (+) | ν(C-O-C) | 55 |
| 1060 (+) | $\delta(C_1\text{-}H_2)$, δ(C-O-H) | 54 |

Spectra collected using a HT-treated $TiO_2$ electrode (Figure 4.47) were similar to those obtained when using the MW-treated $TiO_2$ electrode, as they displayed no

water oxidation. Strong $CO_{2\ (aq)}$ production upon UV irradiation occurred which was superimposed on a broad baseline change in the region from 1900 – 3000 $cm^{-1}$. The production of $CO_{2\ (aq)}$ was accompanied by a set of degradation bands assigned to NAG, which are tabulated for reference purposes (Table 4.9). Some water vapour was detected within the *in situ* FTIR cell, possibly due to a slight seal problem, producing several negative bands between 1450 and 1900 $cm^{-1}$ (and 3500 – 4000 $cm^{-1}$). Once these bands were discounted, there was strong negative band at 1680 $cm^{-1}$ assigned to the amide I vibration. Other spectral assignments showed degradation of $CH_3$ and OH groups.

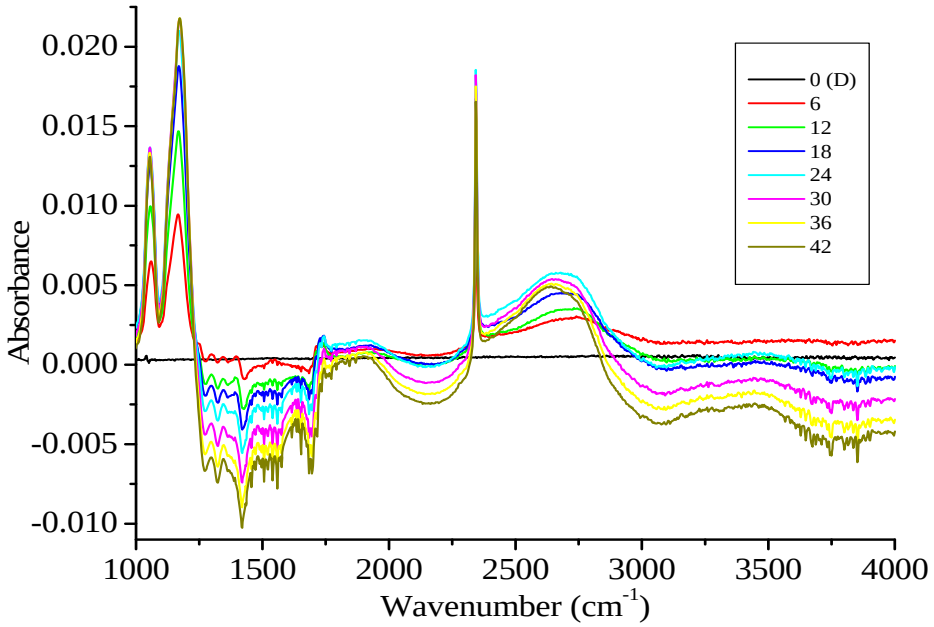


**Figure 4.47 HT, NAG, T-EAP: *In situ* FTIR absorbance spectra obtained using HT-treated $TiO_2$ electrodes immersed in 0.1 mol $dm^{-3}$ $Na_2SO_4$/0.2 mol $dm^{-3}$ NAG, under irradiation with UV light (light switched on after initial spectrum was collected). Spectra were collected at the indicated time intervals (minutes). Initial applied potential -0.2 V vs. Ag/AgCl; applied potential shifted to 1.2 V vs. Ag/AgCl in a single step after 6 minutes and held until 27 minutes. After 27 minutes potential was lowered to initial potential and held for the remainder of the experiment.**

In addition to these negative bands, positive bands were seen around 1167 and 1060 $cm^{-1}$. Interestingly, the maxima of latter band shifted from 1060 $cm^{-1}$ at the start of the experiment, to 1056 $cm^{-1}$ by the experiment end. As stated previously, it was thought that these bands arose from the partial decomposition of NAG resulting in a

change in carbohydrate character. Also, three small positive bands around 1730 $cm^{-1}$ were witnessed. However, as the experiment progressed, the increasing negative of absorbance around the amide I region swamped the small absorbance gains seen near 1730 $cm^{-1}$. The positions of these bands (1712, 1727 and 1742 $cm^{-1}$) were similar to those seen with the other $TiO_2$ electrodes.

**Table 4.9 NAG degradation bands seen when using the MW-treated $TiO_2$ electrode from Figure 4.47**

| Band position ($cm^{-1}$) | Vibrational assignment | Reference |
|---|---|---|
| 1680 | amide I | 57 |
| 1437 | δ(C-H), δ(O-H) | 54 |
| 1375 | δ(C-H), δ(O-H) | 54 |
| 1361 | $\delta(C_6\text{-}H_2)$ | 30 |
| 1323 | $CH_3$ | 54 |
| 1270 | $C_6$-OH, $C_1$-OH | 54 |
| 1167 (+) | δ(C-H), δ(C-O-H) | 54,55 |
| 1060 → 1056 (+) | $\delta(C_1\text{-}H_2)$, δ(C-O-H) | 54 |

Plots of the $CO_{2\ (aq)}$ absorbance during the time-dependent EAP experiments are shown in Figure 4.49. The film types, in decreasing order of the maximum absorbance of $CO_2$ were P25 < MW < HT < Thermal.

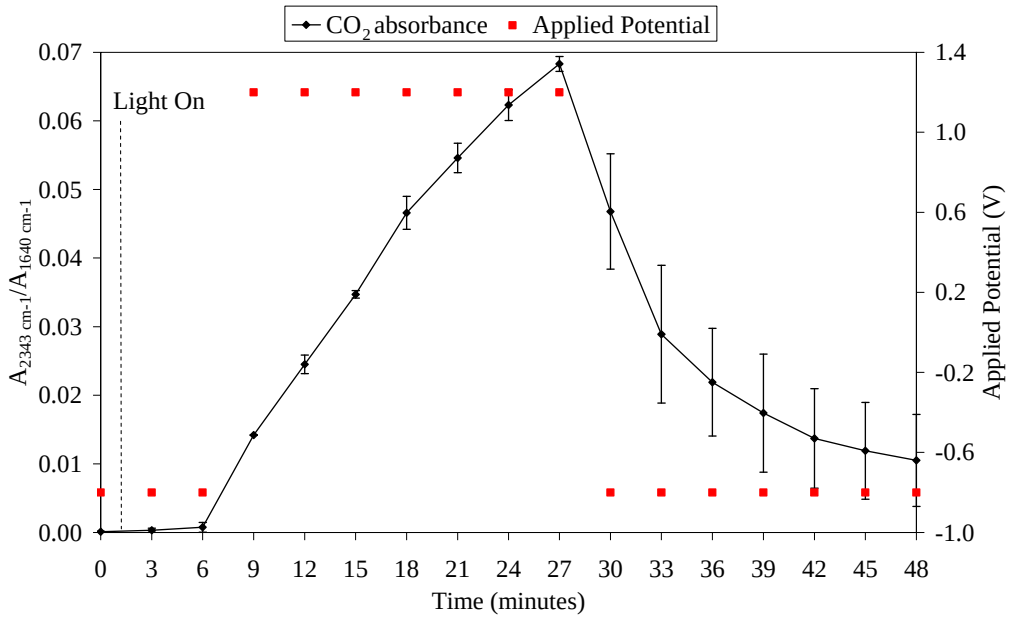


**Figure 4.48 Plots of average $CO_{2\ (aq)}$ absorbances produced during time-dependent EAP experiments with Thermal $TiO_2$ electrodes immersed in 0.1 mol $dm^{-3}$ $Na_2SO_4$/0.2 mol $dm^{-3}$ NAG, under irradiation with UV light. Spectral absorbance was background corrected and normalised for differing $TiO_2$ film thickness against background water intensity values obtained at the start of each experiment. (■) Applied potential during sampling.**

The Thermal $TiO_2$ electrode again showed potential-dependent photocatalytic degradation, whilst the mesoporous $TiO_2$ electrodes all showed potential independence. The Degussa P25 and HT-treated $TiO_2$ electrode showed a rapid rise in $CO_{2\ (aq)}$ production before reaching a steady state after 27 minutes, which was unaffected by the drop in applied potential after this time. The MW-treated $TiO_2$ electrode, however, displayed low $CO_{2\ (aq)}$ production upon UV illumination which increased throughout the experiment, despite the removal of the positive bias after 27 minutes. This could be due to slower than usual diffusion of $CO_{2\ (aq)}$ out of the thin layer resulting in a net gain in $CO_{2\ (aq)}$ absorbance with time.

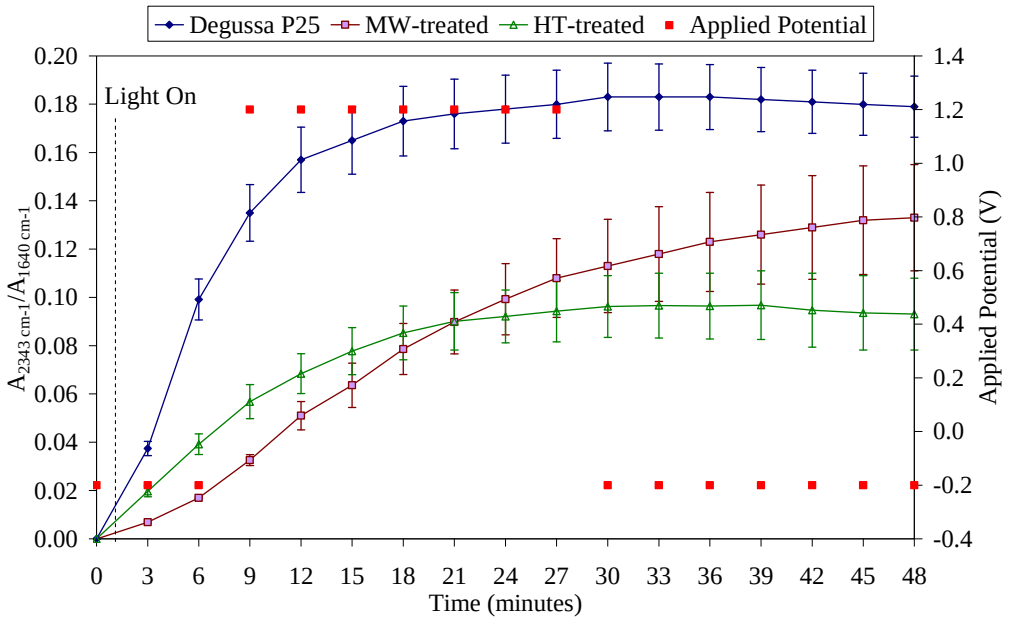


**Figure 4.49 Plots of average $CO_{2\ (aq)}$ absorbances produced during time-dependent EAP experiments with Degussa P25, MW- and HT-treated $TiO_2$ electrodes immersed in 0.1 mol $dm^{-3}$ $Na_2SO_4$/0.2 mol $dm^{-3}$ NAG, under irradiation with UV light. Spectral absorbance was background corrected and normalised for differing $TiO_2$ film thickness against background water intensity values obtained at the start of each experiment. (■) Applied potential during sampling.**

## 4.4.10 Proposed intermediates of NAG degradation

As stated above three positive bands were observed during the NAG experiments. These bands were positioned around 1720, 1730 and 1742 $cm^{-1}$. The 1720 $cm^{-1}$ could be assigned to a carbonyl stretching vibration, most likely due to an acid.[58] This acid could be produced from attack of the carbonyl functionality of the amide group of the NAG by hydroxyl radicals, producing an acetic acid derivative and water (Equation 4.23).

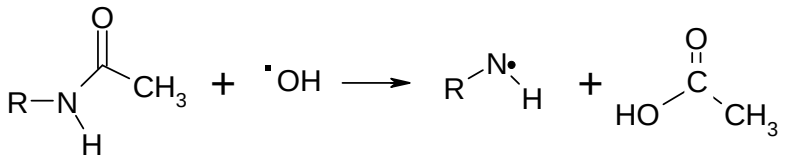


**4.23**

Possible hydroxyl radical attack on the $C_1$-OH position of the cyclic hemi-acetal could lead to ring opening resulting in the formation of a stable aldehyde (Equation

4.24).[59] Aldehydes of this nature produce a characteristic carbonyl stretching vibration at 1730 $cm^{-1}$.[58] Although this theory is unlikely, as the cyclic hemi-acetals are in equilibrium with their ring opened form and therefore do not require a hydroxyl radical for the intermediate aldehyde. Also, the band at 1730 $cm^{-1}$ was only seen using the MW-treated $TiO_2$ electrode.

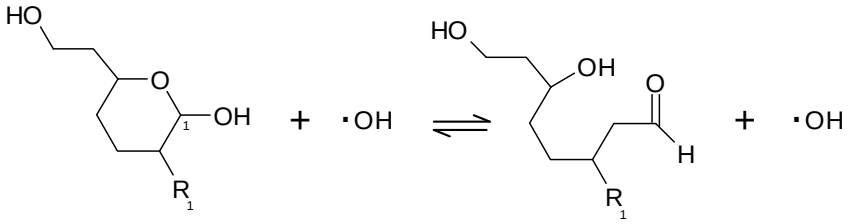


**4.24**

Similar carbohydrate degradation studies have shown that adsorbed glucose produces a lactone intermediate which possesses characteristic carbonyl vibrations.[30,60] These studies have shown that the glucose must be adsorbed to the metal surface to ensure the initial molecule skeleton remains intact. Two types of lactone can be formed: δ-lactone; and γ-lactone (Equations 4.25 and 4.26).[30]

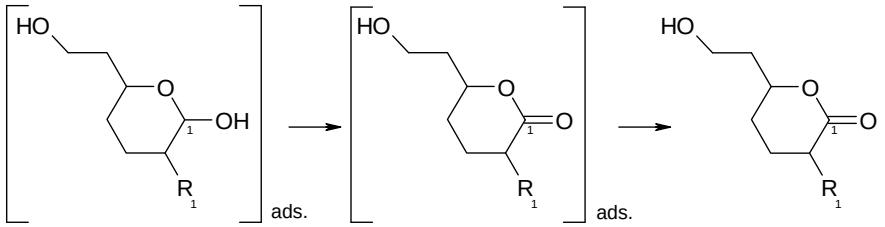


**4.25**

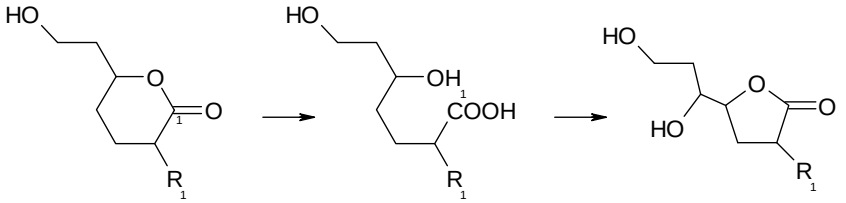


**4.26**

D-glucono-δ-lactone D-gluconic acid D-glucono-γ-lactone

These species produce characteristic carbonyl vibrational bands at 1740 and 1780 $cm^{-1}$, respectively.[61] In the present study a band at 1740 $cm^{-1}$ was formed, however there was an absence of a band at 1780 $cm^{-1}$ leading to the hypothesis that a δ-lactone derivative could have been formed. An additional carbonyl stretching vibration at 1730 $cm^{-1}$ has been tentatively assigned to the lactone in an adsorbed state by Proenca and co-workers.[30] Therefore the 1730 $cm^{-1}$ found in the NAG

spectra of the MW-treated $TiO_2$ could also be attributed to an adsorbed lactone species.

### 4.4.11 Photocatalysis compared to EAP

Figure 4.50 displays the baseline- and electrolyte layer thickness-corrected maximum $CO_{2\ (aq)}$ absorbances at 27 minutes obtained during the photocatalysis and EAP experiments for each of the $TiO_2$ electrodes immersed in $Na_2(OOC)_2$ and NAG. The maximum $CO_{2\ (aq)}$ absorbances seen for each of the organic species tested were very different, with a greater conversion of $Na_2(OOC)_2$ to $CO_{2\ (aq)}$ than NAG. Compared to the NAG molecule, the $Na_2(OOC)_2$ proved to be easier to catalyse due to its chemical simplicity.

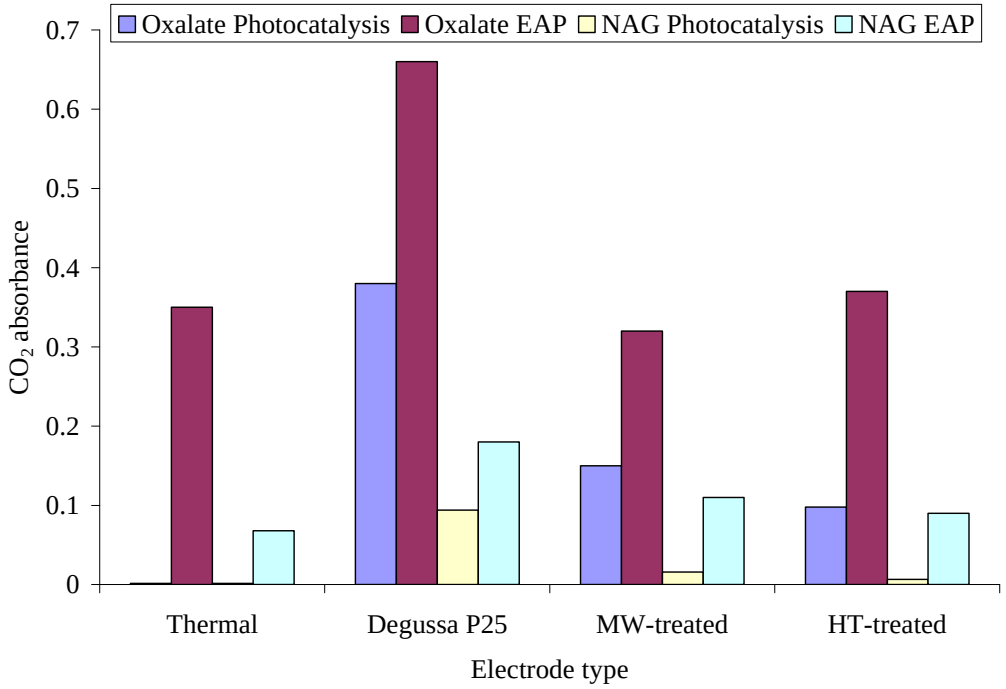


**Figure 4.50 Maximum $CO_2$ absorbances found after 27 minutes during time-dependent photocatalysis and EAP experiments for each $TiO_2$ electrode type.**

For both organic species tested Degussa P25 performed the best during both the photocatalysis and EAP experiments. When taking specific surface area of the $TiO_2$

catalysts into account, as discussed in Chapter 3 section 3.5.1.3, this only serves to increase the efficiency of the Degussa P25 $TiO_2$ compared to the other $TiO_2$ types.

When comparing the increase in efficiency with electrochemical assistance, the Thermal $TiO_2$ showed the most dramatic increase for both organic species tested (207 and 40.2 fold increase for $Na_2(OOC)_2$ and NAG, respectively) (Table 4.10).

**Table 4.10 Comparison of the increase in $CO_{2\ (aq)}$ absorbance after 27 minutes during time-dependent experiments for each $TiO_2$ electrode**

| Organic species | Thermal | Degussa P25 | MW-treated | HT-treated |
|---|---|---|---|---|
| $Na_2(OOC)_2$ | 207 | 1.75 | 2.08 | 3.74 |
| NAG | 40.2 | 1.91 | 6.67 | 14 |

This was expected due to this electrode's reliance on applied potential for photocatalytic activity. When comparing the mesoporous $TiO_2$ types, the HT-treated $TiO_2$ electrode, followed by the MW-treated $TiO_2$ electrode, showed the greatest improvement in photocatalytic rate with electrochemical assistance, which was true for both organic species examined. Despite this, the Degussa P25 $TiO_2$ was the best performer overall for both the $Na_2(OOC)_2$ and NAG, again proving its superior performance due to its mixed phase composition.[62]

### 4.4.12 Changes in FTIR baseline upon UV illumination

During some of the experiments large baseline movement was observed upon UV illumination. This was especially prevalent when performing the photocatalysis only experiments i.e. those without electrochemical enhancement, when using the mesoporous $TiO_2$ electrodes. Similar effects have been observed by other authors when performing *in situ* FTIR investigations.[12,13,18,63-66]

Shaw and co-workers[13] observed an apparent decrease in baseline over the entire spectral range upon UV illumination when using rutile $TiO_2$ electrodes. Whilst the origin of this effect was not clear, it did not appear to be an experimental artefact arising from stray reflected UV irradiation from the light pipe incident on the MCT

detector. The effect was relatively large and was therefore thought to be of electronic origin. The authors tentatively assigned the effect to the emptying of very-deep lying states near the $TiO_2$ surface; these states lying just above or within the valence band edge. In the present study the baseline increased, so this theory can be discounted.

Christensen and co-workers have witnessed an increase in baseline absorbance when using gold and platinum electrodes.[66] These changes were reminiscent of the single-beam characteristic of the spectrometer and were thought to be dependent on the thin layer thickness. Whilst the detailed changes seen when using the gold and platinum electrodes were different the basic phenomenon was the same, indicating the metal itself played a role in the reflectivity effect. It was found that a solution layer of several μm in thickness was required for the effect to manifest.

The spectral effects described by Christensen and co-workers[66] were remarkably similar to those seen in the present study, as they appeared similar to the single beam spectra. No baseline changes of this nature were witnessed when using the Thermal $TiO_2$ electrodes which could be due to the nature of the electrode, allowing a very thin electrolyte layer to be formed. The mesoporous electrodes could produce thicker electrolyte layers due to the increased thickness of the $TiO_2$ deposit and the inherent roughness of the layer. To test this theory the pathlength for each of the $TiO_2$ electrodes was calculated using the background spectrum obtained from each experiment and an extinction co-efficient of 900 ± 100 mol $dm^{-3}$ $cm^{-1}$ for the 1310 $cm^{-1}$ oxalate band.[67] Table 4.11 displays the collated results.

**Table 4.11 Pathlength calculations for the $TiO_2$ electrodes**

| | Thermal | Degussa P25 | MW-treated | HT-treated |
|---|---|---|---|---|
| Pathlength (μm) | 3.63 | 4.05 | 9.76 | 4.21 |
| ± (μm) | 0.68 | 0.68 | 1.95 | 1.31 |

Whilst the Thermal $TiO_2$ electrode did produce a thin electrolyte layer, the electrolyte layer from the Degussa P25 $TiO_2$ and HT-treated $TiO_2$ electrodes were very similar. If the effects arose solely from the electrolyte layer thickness, one would expect the Degussa P25 and HT-treated $TiO_2$ mesoporous electrodes to

produce lower changes than the MW-treated $TiO_2$ electrode; however the opposite was observed. Also, these effects would be independent of applied potential and would be witnessed in all experiments including those under potential control. The effect was markedly reduced when the $TiO_2$ electrodes were under an applied potential, thus discrediting this theory as cause of the observed phenomenon.

Yaniger and Vidrine[65] and Neugebauer and co-workers[63] have both reported a broad IR absorption stretching from the mid-IR to the near-IR when investigating polymer film growth by *in situ* FTIR-ATR. It was concluded that this absorption was derived from electronic absorption by free charge carriers present in the conducting state of the polymers. Christensen and co-workers[64] have also witnessed a broad electronic absorption band when performing similar polymer growth studies and attributed this to bipolaronic excitation as the main mobile charge carrier. The effects described do correlate with those seen in this investigation.

However, it was Yamamkata et al.[18] who used time-resolved IR spectroscopy to study the kinetics of photogenerated electrons in a Degussa P25 $TiO_2$ film, who best described the effects seen in the present study. The authors observed an increasing baseline absorption from 3000 to 900 $cm^{-1}$ which was attributed to photogenerated electrons trapped in shallow mid-gap states within picoseconds of irradiation. Two possible origins for the absorption due to electrons trapped on co-ordinatively unsaturated Ti atoms were put forward, which were further extrapolated by Warren and McQuillian (Figure 4.51).[12]

The absorption was a result: of intra-band transitions of electrons within the CB; and direct optical transition from the trap state to the CB. While both mechanisms would give very similar broad IR absorptions, the latter mechanism would be characterised by an absorption cut-off associated with the energy gap between the trap state and the CB. This would lie below the present 1000 $cm^{-1}$ experimental limit, but has been confirmed to occur at 880 $cm^{-1}$.[12]

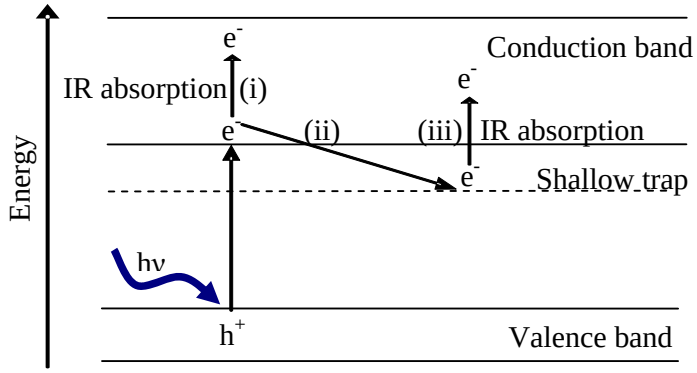


**Figure 4.51 Schematic representation of the processes involving the optical promotion of electrons into the CB: (i) by intraband excitation; (ii) electrons trapped in shallow traps; and (iii) excitation of shallowly trapped electrons into the CB.**

The application of a potential to the *in situ* FTIR system abated the baseline changes. This was consistent with EAP theory, that upon the application of an electrical bias, electrons are removed to the back contact and on to the counter electrode. This would reduce the time spent within the $TiO_2$ CB, thus minimising intra-band transitions.

## *4.5 Conclusions*

Thermal $TiO_2$ coated electrodes were manufactured and Degussa P25, MW- and HT-treated $TiO_2$ powders were immobilised onto 'top-hat' electrodes. These electrodes were examined for photocatalytic and EAP degradation of $Na_2(OOC)_2$ and the carbohydrate, N-acetyl-*D*-glucosamine, found in bacterial cell walls with $Na_2SO_4$ as the supporting electrolyte.

Current-voltage measurements performed using both $Na_2(OOC)_2$ and NAG showed that the Thermal $TiO_2$ electrodes produce photocurrents dependent on applied potential, whereas all three mesoporous $TiO_2$ immobilised colloids showed independent photocurrents.

*In situ* FTIR spectra obtained using all $TiO_2$ electrode types except the Degussa P25 $TiO_2$ electrode in the presence of the electrolyte only, with the cell both illuminated and in the dark, when first used, showed negligible spectral changes. The Degussa

P25 $TiO_2$ electrode displayed the photo-oxidation of hydrocarbon species present from the Degussa P25 manufacture, when first used, but subsequent experiments did not show this. Upon the addition of an organic species, changes in the spectra upon UV illumination were substantial and striking.

All $TiO_2$ electrode types examined possessed the ability to degrade $Na_2(OOC)_2$, producing a characteristic negative band at 1310 $cm^{-1}$ assigned to oxalate. A corresponding gain at 2343 $cm^{-1}$ was unambiguously assigned to $CO_2$ produced from the photo-oxidation of $Na_2(OOC)_2$. The Thermal $TiO_2$ electrode, and to a lesser extent, the Degussa P25 $TiO_2$ electrode also displayed characteristic negative vibrational bands attributed to the photo-oxidation of bulk water. The FTIR spectra obtained using the Thermal $TiO_2$ electrode displayed vibrational bands due to $Na_2(OOC)_2$ in solution. For the mesoporous $TiO_2$ electrodes, whilst bulk $Na_2(OOC)_2$ losses were observed, additional adsorbed oxalate bands were identified within the *in situ* FTIR spectra. The Thermal $TiO_2$ displayed continued potential dependence, whereby oxalate degradation was only displayed in FTIR spectra collected in the presence of UV illumination and a positive applied potential. The mesoporous $TiO_2$ electrodes all displayed $Na_2(OOC)_2$ degradation under UV illumination. The degradation rate, measured by the production of $CO_{2\ (aq)}$, increased with a positive applied potential for all the examined $TiO_2$ electrode types.

The degradation NAG was examined for the first time using the same $TiO_2$ electrodes. Degradation bands assigned to characteristic saccharide peaks were identified from *in situ* FTIR spectra obtained from all four examined $TiO_2$ electrode types. These were accompanied by the production of $CO_{2\ (aq)}$ within the electrolyte layer confirming the degradation of NAG within the cell. Additional positive bands around the 1710 – 1740 $cm^{-1}$ region were observed and attributed to intermediate products produced during NAG photo-degradation. These bands were tentatively assigned to acetic acid and δ-lactone, both in solution and in its adsorbed state. The application of a positive potential increased the production of $CO_{2\ (aq)}$ due to the increased rate of NAG photo-degradation.

During the FTIR photocatalytic investigations, all the spectra obtained from the mesoporous $TiO_2$ electrodes displayed baseline changes upon UV illumination. The

origin of such changes are controversial, but were attributed to intra-band electron transitions within the $TiO_2$ CB and shallow mid-gap trap states. The application of a potential abated such changes, further confirming this theory.

For both $Na_2(OOC)_2$ and NAG photodegradation, the Degussa P25 $TiO_2$ catalyst was the best performer, both during the photocatalysis and EAP investigations. This confirmed results displayed and examined in Chapter 3.

## 4.6 References


(1) Davidson, T.; Pons, B. S.; Bewick, A.; Schmidt, P. P. *J. Electroanal. Chem.* **1981**, *401*, 215.

(2) Chetty, R.; Christensen, P. A.; Golding, B. T. *Chem. Commun.* **2003**, 984-985.

(3) Lin, W. F.; Christensen, P. A.; Hamnett, A. *Phys. Chem. Chem. Phys.* **2001**, *3*, 3312-3319.

(4) Lin, W. F.; Christensen, P. A. *Faraday Discuss.* **2002**, *121*, 267-284.

(5) Christensen, P. A.; Dilks, A.; Egerton, T. A.; Temperley, J. *J. Mater. Sci.* **2000**, *35*, 5353-5358.

(6) Christensen, P.; Hamnett, A. *Electrochim. Acta* **2000**, *45*, 2443-2459.

(7) Munk, J.; Christensen, P. A.; Hamnett, A.; Skou, E. *J. Electroanal. Chem.* **1996**, *401*, 215-222.

(8) Christensen, P. A.; Eameaim, J.; Hamnett, A. *Phys. Chem. Chem. Phys.* **1999**, *1*, 5315-5321.

(9) Kavan, L.; Krtil, P.; Gratzel, M. *J. Electroanal. Chem.* **1994**, *373*, 123-131.

(10) Hug, S. J.; Sulzberger, B. *Langmuir* **1994**, *10*, 3587-97.

(11) Christensen, P. A.; Eameaim, J.; Hamnett, A.; Lin, W. F. *Chem. Phys. Lett.* **2001**, *344*, 488-494.

(12) Warren, D. S.; McQuillan, A. J. *J. Phys. Chem. B* **2004**, *108*, 19373-19379.

(13) Shaw, K.; Christensen, P.; Hamnett, A. *Electrochim. Acta* **1996**, *41*, 719-728.

(14) Gerischer, H.; Heller, A. *J. Phys. Chem.* **1991**, *95*, 5261-7.

(15) Szczepankiewicz, S. H.; Colussi, A. J.; Hoffmann, M. R. *J. Phys. Chem. B* **2000**, *104*, 9842-9850.

(16) Szczepankiewicz, S. H.; Moss, J. A.; Hoffmann, M. R. *J. Phys. Chem. B* **2002**, *106*, 2922-2927.

(17) Szczepankiewicz, S. H.; Moss, J. A.; Hoffmann, M. R. *J. Phys. Chem. B* **2002**, *106*, 7654-7658.

(18) Yamakata, A.; Ishibashi, T.-a.; Onishi, H. *J. Phys. Chem. B* **2001**, *105*, 7258-7262.

(19) Sunada, K.; Watanabe, T.; Hashimoto, K. *J. Photochem. Photobiol., A* **2003**, *156*, 227-233.

(20) Maness, P.-C.; Smolinski, S.; Blake, D. M.; Huang, Z.; Wolfrum, E. J.; Jacoby, W. A. *Appl. Environ. Microbiol.* **1999**, *65*, 4094-4098.

(21) Huang, Z.; Maness, P.-C.; Blake, D. M.; Wolfrum, E. J.; Smolinski, S. L.; Jacoby, W. A. *J. Photochem. Photobiol., A* **2000**, *130*, 163-170.

(22) Matsunaga, T.; Tomada, R.; Nakajima, T.; Wake, H. *FEMS Microbiol. Lett.* **1985**, *29*, 211-214.

(23) Wamer, W. G.; Yin, J. J.; Wei, R. R. *Free Radical Biol. Med.* **1997**, *23*, 851-8.

(24) Volk, W. A.; Wheeler, M. F.; Brown, J. C. *Basic microbiology*; Benjamin Cummings: Menlo Park, Calif., 1997.

(25) Dryhurst, G.; McAllister, D. L. *Anal. Chim. Acta* **1974**, *72*, 209-14.

(26) McMurray, T. A.; Byrne, J. A.; Dunlop, P. S. M.; Winkelman, J. G. M.; Eggins, B. R.; McAdams, E. T. *Appl. Catal., A* **2004**, *262*, 105-110.

(27) Byrne, J. A.; Eggins, B. R. *J. Electroanal. Chem.* **1998**, *457*, 61-72.

(28) Nakamoto, K. *Infrared and Raman Spectra of Inorganic and Coordination Compounds*; 5th ed.; John Wiley and Sons, Inc.: New York, 1997; B.

(29) Madigan, M. T.; Martinko, J. M.; Parker, J. *Brock Biology of Microorganisms*; 9 ed.; Prentice-Hall, Inc.: Upper Saddle River, New Jersey, 2000.

(30) Proenca, L.; Lopes, M. I. S.; Fonseca, I.; Hahn, F.; Lamy, C. *Electrochim. Acta* **1998**, *44*, 1423-1430.

(31) Proenca, L.; Lopes, M. I. S.; Fonseca, I.; Rodes, A.; Gomez, R.; Aldaz, A. *Electrochim. Acta* **1998**, *44*, 1163-1171.

(32) Proenca, L.; Lopes, M. I. S.; Fonseca, I.; Rodes, A.; Gomez, R.; Aldaz, A. *Electrochim. Acta* **1998**, *44*, 735-743.

(33) Veness, R. G.; Evans, C. S. *J. Chromatogr. A* **1996**, *721*, 165-72.

(34) Hsiao, M. W.; Adzic, R. R.; Yeager, E. B. *J. Electrochem. Soc.* **1996**, *143*, 759-767.

(35) O'Regan, B.; Moser, J.; Anderson, M.; Graetzel, M. *J. Phys. Chem.* **1990**, *94*, 8720-6.

(36) Wilson, G. J.; Will, G. D.; Frost, R. L.; Montgomery, S. A. *J. Mater. Chem.* **2002**, *12*, 1787-1791.

(37) Christensen, P. A.; Eameaim, J.; Hamnett, A. *In situ FTIR studies of the photo-electrochemical behaviour of thermal $TiO_2$ films as a function of temperature* **1999**, *1*, 5315-5321.

(38) Ferdenaz, S. "Unpublished results," University of Newcastle upon Tyne, 2005.

(39) Wahl, A.; Ulmann, M.; Carroy, A.; Jermann, B.; Dolata, M.; Kedzierzawski, P.; Chatelain, C.; Monnier, A.; Augustynski, J. *J. Electroanal. Chem.* **1995**, *396*, 41-51.

(40) Harper, J. C.; Christensen, P. A.; Egerton, T. A.; Curtis, T. P.; Gunlazuardi, J. *J. Appl. Electrochem.* **2001**, *31*, 623-628.

(41) Hamnett, A. *Compr. Chem. Kinet.* **1987**, *27*, 61-246.

(42) Vinodgopal, K.; Hotchandani, S.; Kamat, P. V. *J. Phys. Chem.* **1993**, *97*, 9040-4.

(43) Lee, M. S.; Cheon, I. C.; Kim, Y. I. *Bull. Korean Chem. Soc.* **2003**, *24*, 1155-1162.

(44) Fujishima, A.; Honda, K. *Nature* **1972**, *238*, 37.

(45) Vinodgopal, K.; Stafford, U.; Gray, K. A.; Kamat, P. V. *J. Phys. Chem.* **1994**, *98*, 6797-803.

(46) Solarska, R.; Rutkowska, I.; Morand, R.; Augustynski, J. *Electrochim. Acta* **2006**, *51*, 2230-2236.

(47) Morrison, S. R.; Freund, T. *J. Chem. Phys.* **1967**, *47*, 1543-52.

(48) Semenikhin, O. A.; Kazarinov, V. E.; Jiang, L.; Hashimoto, K.; Fujishima, A. *Langmuir* **1999**, *15*, 3731-3737.

(49) Mundy, G. R.; Potter, R. J.; Christensen, P. A.; Hamnett, A. *J. Electroanal. Chem.* **1990**, *279*, 257-272.

(50) Berna, A.; Rodes, A.; Feliu, J. M.; Illas, F.; Gil, A.; Clotet, A.; Ricart, J. M. *J. Phys. Chem. B* **2004**, *108*, 17928-17939.

(51) Little, L. H. *Infrared Spectra of Adsorbed Species*; Academic Press: London, 1966.

(52) Finklea, H. O. *Semiconductor Electrodes*; Elsevier: New York, 1988.

(53) Sidorova, A. I.; Zhukovskii, A. P. *Optika i Spektroskopiya* **1969**, *26*, 1055-7.

(54) Twardowski, J.; Anzenbacher, P. *Raman and IR spectroscopy in biology and biochemistry*; Ellis Horwood: New Yok, 1994.

(55) Parker, F. S. *Applications of Infrared, Raman, and Resonance Raman Spectroscopy in Biochemistry*, 1983.

(56) Ede, S. M.; Hafner, L. M.; Fredericks, P. M. *Appl. Spectrosc.* **2004**, *58*, 317-322.

(57) Williams, D. F.; Flemming, I. *Spectroscopic methods in inorganic chemistry*; 5th ed.; McGraw-Hill Publishing Company: New York, 1995.

(58) Smith, B. *Infrared spectral interpretation: a systematic approach*; CRC Press LLC: New York, 1999.

(59) Clayden, J.; Greeves, N.; Warren, S.; Wothers, P. *Organic Chemistry*; Oxford University Press: Oxford, 2001.

(60) Beden, B.; Largeaud, F.; Kokoh, K. B.; Lamy, C. *Electrochim. Acta* **1996**, *41*, 701-9.

(61) Colthup, N. B.; Daly, L. H.; Wiberley, S. E. *Introduction to Infrared and Raman Spectroscopy*; 3rd ed.; Academic Press: Boston, 1990.

(62) Hurum, D. C.; Agrios, A. G.; Gray, K. A.; Rajh, T.; Thurnauer, M. C. *J. Phys. Chem. B* **2003**, *107*, 4545-4549.

(63) Neugebauer, H.; Nauer, G.; Neckel, A.; Tourillon, G.; Garnier, F.; Lang, P. *J. Phys. Chem.* **1984**, *88*, 652-4.

(64) Christensen, P. A.; Hamnett, A.; Hillman, A. R. *J. Electroanal. Chem. Interfac. Electrochem.* **1988**, *242*, 47-62.

(65) Yaniger, S. I.; Vidrine, D. W. *Appl. Spectrosc.* **1986**, *40*, 174-80.

(66) Christensen, P. A.; Hamnett, A.; Trevellick, P. R. *J. Electroanal. Chem. Interfac. Electrochem.* **1988**, *242*, 23-45.

(67) Christensen, P. A.; Higgins, S. J. *J. Electroanal. Chem.* **1995**, *387*, 127-132.

# CHAPTER 5

# CONCLUSIONS AND FUTURE WORK

## 5.1 Conclusions

The use of IR lasers for water treatment purposes was investigated. Illumination of vegetative cells of *E. cloacae* suspended in sterile distilled water with a $CO_2$ laser produced 99.99 % inactivation after 270 seconds of exposure. When comparing the inactivation rates of the $CO_2$ laser with that of UV irradiation, similar rates were observed. However, when investigating the inactivation of the more resistant *B. subtilis* endospores in water, illumination by UV irradiation produced similar inactivation after 120 seconds, but an increase in viable concentration occurred after the IR treatment.

Additional investigation of the cellular alterations during IR laser treatment were performed using FTIR-ATR spectroscopy, which showed increases in carbohydrate content within the *E. cloacae* cells. To further examine this, the IR treatment process was applied to a selection of simple carbohydrates; however FTIR and Raman spectroscopy failed to show definitive alterations of the carbohydrates due to treatment.

The *E. cloacae* inactivation during IR irradiation was thought to be due to an overall temperature increase of the water solution throughout the treatment process. The inability to inactivate the more resistant *B. subtilis* endospores clearly established that this method was not suitable for water disinfection purposes.

Preliminary investigations into the photocatalytic ability of MW-treated $TiO_2$ colloids, compared to Degussa P25 and HT-treated $TiO_2$, showed its capacity to inactivate *E. cloacae* in a slurry suspension. This led to a more in-depth study of the MW-treated $TiO_2$ photocatalytic activity.

Degussa P25, the MW- and HT-treated $TiO_2$ colloids were successfully immobilised onto borosilicate glass substrates and *E. coli* inactivation studies were performed within a stirred-tank reactor. These results were performed in parallel with photocatalytic degradation studies of oxalic acid, to further investigate the colloidal performance. All catalysts were shown to degrade oxalic acid and inactivate *E. coli* cells within distilled water. The application of UVB (compared with UVA)

irradiation was also investigated using oxalic acid, which highlighted Degussa P25's higher performance due to its mixed-phase composition. Surprisingly, the pure anatase colloids, MW- and HT-treated $TiO_2$, displayed no improved photocatalytic rate when the UV wavelength was shortened.

Due to the promising *E. coli* inactivation rates obtained in the stirred-tank reactor using distilled water, a more 'real-world' investigation was performed using natural river water. It was discovered that in order to observe inactivation during a 5 hours treatment period using UVA irradiation, the pH had to be lowered and the bacterial cell loading must be no greater than approximately $1 \times 10^3$ CFU $cm^{-3}$. Development of a sandwich arrangement within the stirred-tank reactor enabled a realistic estimation of the direct effect of UVA during photocatalytic experiments using the MW- and HT-treated $TiO_2$ colloids.

The Degussa P25, MW- and HT-treated $TiO_2$ colloids were also examined using via current-voltage measurements and *in situ* FTIR spectroscopy, and compared with a thermally-prepared $TiO_2$ catalyst. These catalysts were immobilised onto a titanium electrode whereby photocatalytic and EAP degradation were examined. Spectral changes which occurred during photocatalytic degradation of sodium oxalate and the bacterial cell wall component, NAG, were observed and the rates of degradation were followed using the $CO_2$ vibrational band.

Loss of oxalate was studied by two characteristic symmetric and anti-symmetric (C=O) stretching vibrations; however, this was complicated when using the mesoporous $TiO_2$ electrodes by adsorption of the molecule onto the catalyst's surface. NAG degradation was observed via the loss of absorbance bands characteristic of this molecule. In addition, gain bands other than $CO_2$ were identified, which were attributed to intermediate break-down products, tentatively assigned to acetic acid and δ-lactone.

In conjunction with $CO_2$ production and the loss of the model degradants, the oxidation of water was observed, most often when using the Thermal $TiO_2$ electrode. Large baseline changes occurred when performing photocatalytic experiments under UV illumination, the extent of which was abated when the system was under a

positive electrical bias. This was attributed to intra-band electron transitions within the $TiO_2$ CB and shallow mid-gap trap states.

For all the catalysts types examined, the application of a positive bias increased the rate of degradation, for both oxalate and NAG. Degussa P25 produced the highest degradation rates for both degradants studied.

## 5.2 Future work

Overall, this study further demonstrated the ability of $TiO_2$ catalysts for potential use within the water treatment industry as an alternative to conventional treatment practices. However further work, particularly using natural water sources, must be completed before this occurs on a wide-scale.

Whilst a suite of micro-organisms have been inactivated using photocatalysis within literature, the two major organisms of public health, *Giardia* and *Cryptosporidium* cysts, have not been examined to date. This has been due to difficulties encountered with the culture and detection of these micro-organisms, and these problems must be overcome before photocatalysis is accepted as a viable alternative water treatment. In addition, more researcher awareness of SCV's must occur and further investigation into their possible health risks must be performed to ensure the public health safety of photocatalysis.

Whilst the MW-treated $TiO_2$ possessed a very high surface area out of those studied, Degussa P25 remains the best available catalyst. Further post-synthesis modification of $TiO_2$ colloids to improve their catalytic ability could be performed. Following from this work, the production of a high surface area, mixed-phase catalyst should be attempted.

Further use of *in situ* FTIR spectroscopy for photocatalytic rate determination should occur as this technique is rapid, sensitive and provides detailed information regarding degradant break-down products and catalyst surfaces to further enhance the understanding of $TiO_2$ catalysts within water treatment systems.

# APPENDIX

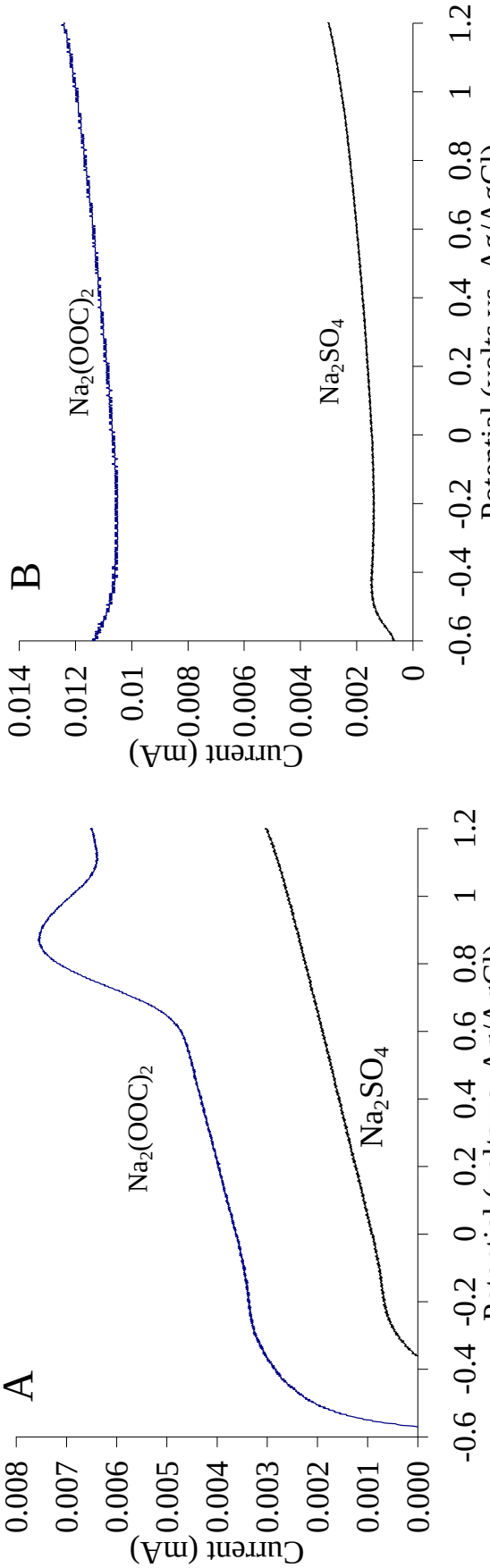


**Figure A.1A Potential dependence of photocurrent obtained for the MW-treated $TiO_2$ electrode with supporting electrolyte ($Na_2SO_4$); and with the addition of $Na_2(OOC)_2$. Potential scan rate was 100 mV/s.**

**Figure A.1B Potential dependence of photocurrent obtained for the HT-treated $TiO_2$ electrode with supporting electrolyte ($Na_2SO_4$); and with the addition of $Na_2(OOC)_2$. Potential scan rate was 100 mV/s.**

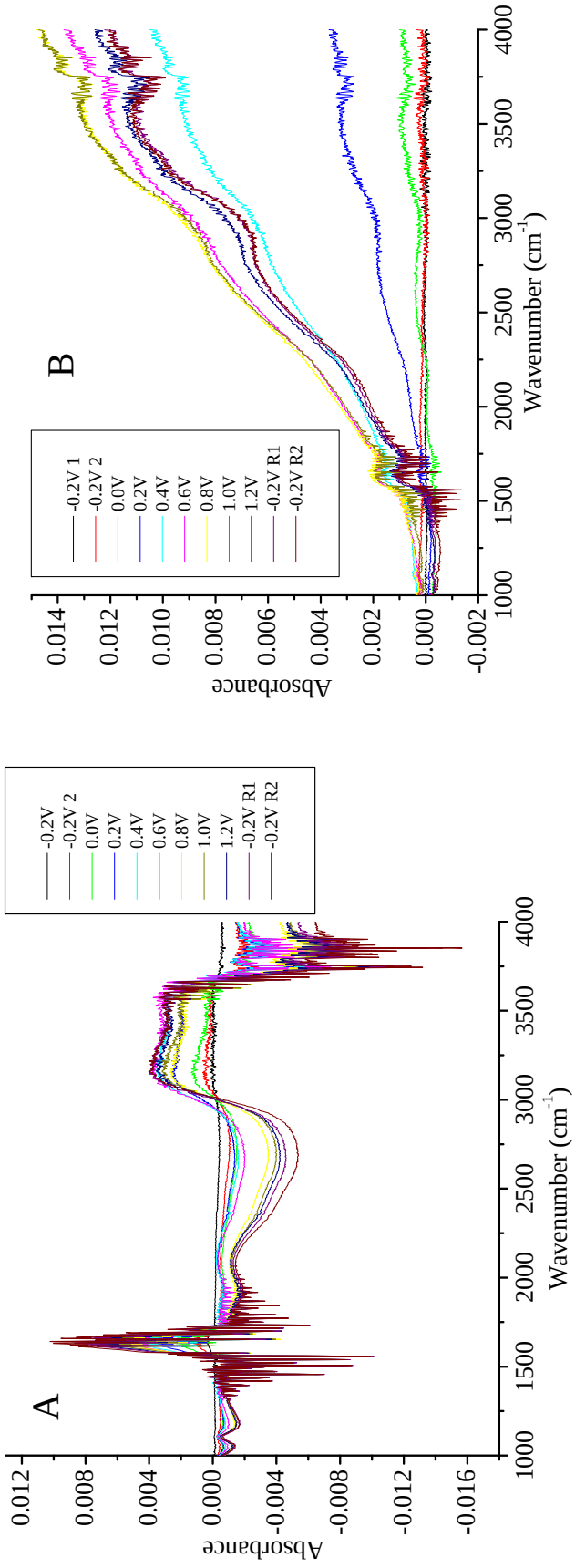


**Figure A.2A P25, $Na_2SO_4$, P-EAP, Dark: *In situ* FTIR absorbance spectra obtained using a Degussa P25 $TiO_2$ electrode immersed in 0.1 mol $dm^{-3}$ $Na_2SO_4$, in the dark. Spectra were collected at the indicated potentials. 'R' denotes spectra obtained after the applied potential was returned to the initial potential.**

**Figure A.2B MW, $Na_2SO_4$, P-EAP, Dark: *In situ* FTIR absorbance spectra obtained using a MW-treated $TiO_2$ electrode immersed in 0.1 mol $dm^{-3}$ $Na_2SO_4$, in the dark. Spectra were collected at the indicated potentials. 'R' denotes spectra obtained after the applied potential was returned to the initial potential.**

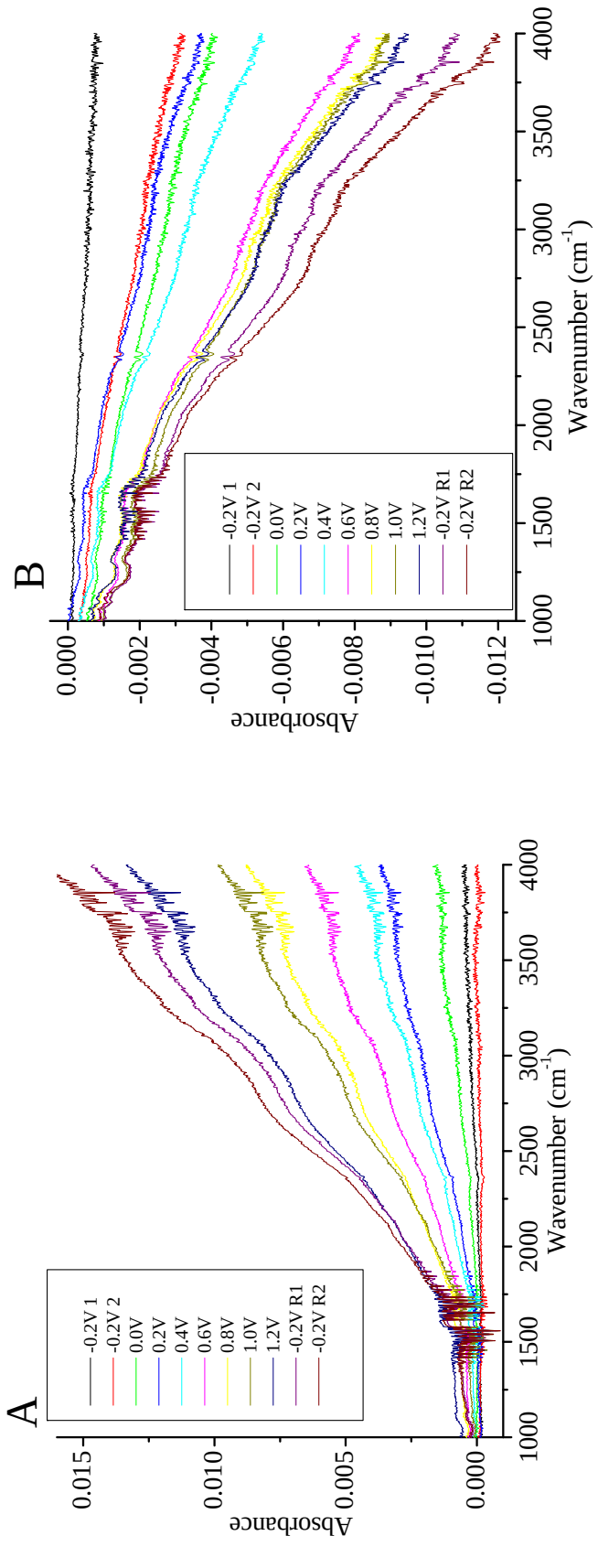


**Figure A.3A HT, $Na_2SO_4$, P-EAP, Dark: *In situ* FTIR absorbance spectra obtained using a HT-treated $TiO_2$ electrode immersed in 0.1 mol $dm^{-3}$ $Na_2SO_4$, in the dark. Spectra were collected at the indicated potentials. 'R' denotes spectra obtained after the applied potential was returned to the initial potential.**

**Figure A.3B HT, $Na_2SO_4$, P-EAP, Light: *In situ* FTIR absorbance spectra obtained using a HT-treated $TiO_2$ electrode immersed in 0.1 mol $dm^{-3}$ $Na_2SO_4$ under UV illumination (UV illumination was commenced after -0.2 V 1). Spectra were collected at the indicated potentials. 'R' denotes spectra obtained after the applied potential was returned to the initial potential.**

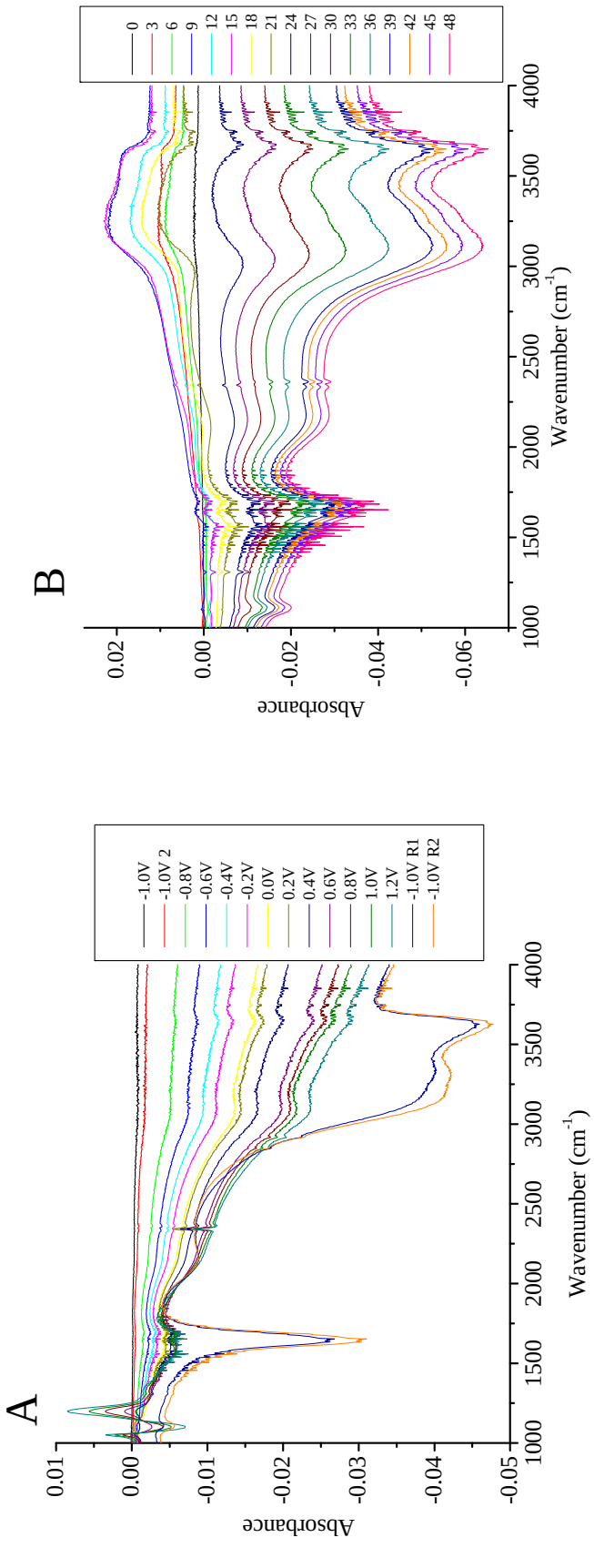


**Figure A.4A T, $Na_2SO_4$, P-EAP, Light: *In situ* FTIR absorbance spectra obtained using a Thermal $TiO_2$ electrode immersed in 0.1 mol $dm^{-3}$ $Na_2SO_4$ under UV illumination during potential dependent EAP experiments. UV illumination was applied after the initial spectrum was collected. Spectra were collected at 2 minutes intervals, at the indicated potentials. 'R' denotes spectra obtained after the applied potential was returned to the initial potential.**

**Figure A.4B T, $Na_2SO_4$, T-EAP: *In situ* FTIR absorbance spectra obtained using a Thermal $TiO_2$ electrode immersed in 0.1 mol $dm^{-3}$ $Na_2SO_4$ under UV illumination during time dependent EAP experiments. UV illumination was applied after the initial spectrum was collected. Spectra were collected at the indicated times (minutes). Applied potential was -0.8 V vs. Ag/AgCl, potential was shifted to 1.2 V vs. Ag/AgCl in a single step after 6 minutes and held until 27 minutes.**

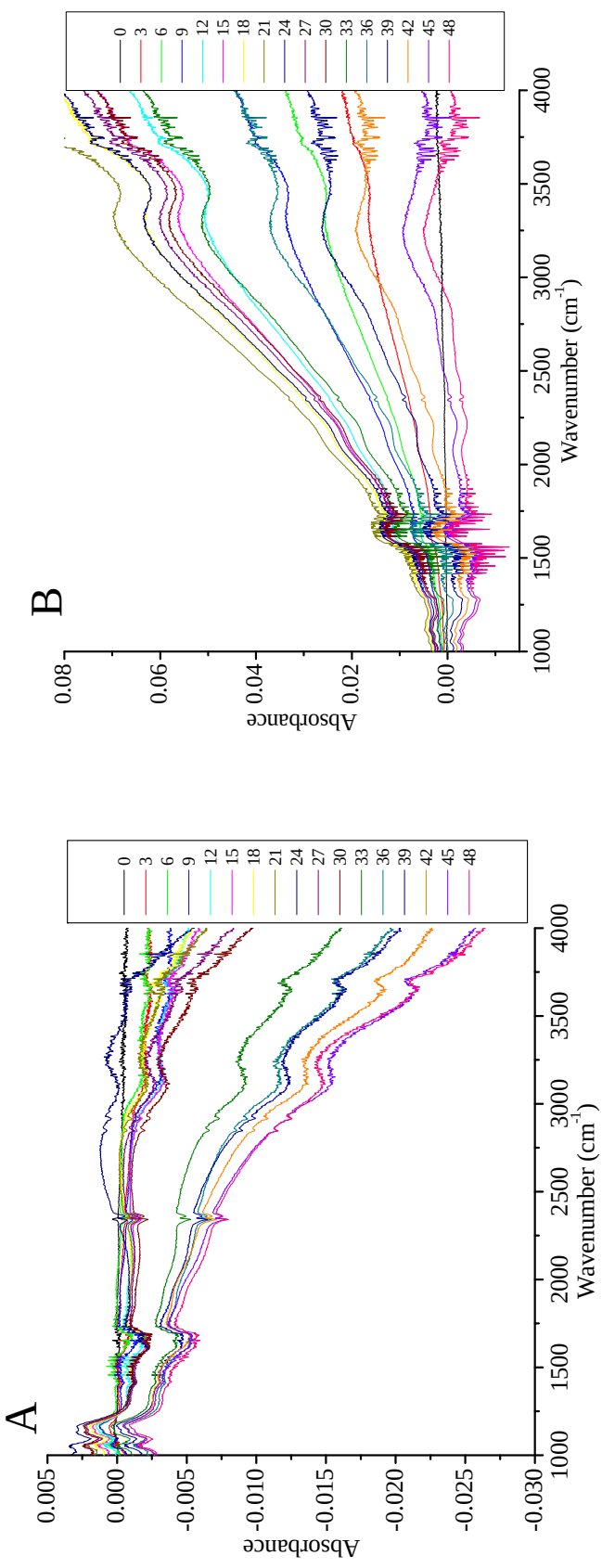


**Figure A.5A T, $Na_2SO_4$, P-EAP, Light: *In situ* FTIR absorbance spectra obtained using a Thermal $TiO_2$ electrode immersed in 0.1 mol $dm^{-3}$ $Na_2SO_4$ under UV illumination during potential dependent EAP experiments. UV illumination was applied after the initial spectrum was collected. Spectra were collected at 2 minutes intervals, at the indicated potentials. 'R' denotes spectra obtained after the applied potential was returned to the initial potential.**

**Figure A.5B T, $Na_2SO_4$, T-EAP: *In situ* FTIR absorbance spectra obtained using a Thermal $TiO_2$ electrode immersed in 0.1 mol $dm^{-3}$ $Na_2SO_4$ under UV illumination during time dependent EAP experiments. UV illumination was applied after the initial spectrum was collected. Spectra were collected at the indicated times (minutes). Applied potential was -0.8 V vs. Ag/AgCl, potential was shifted to 1.2 V vs. Ag/AgCl in a single step after 6 minutes and held until 27 minutes.**

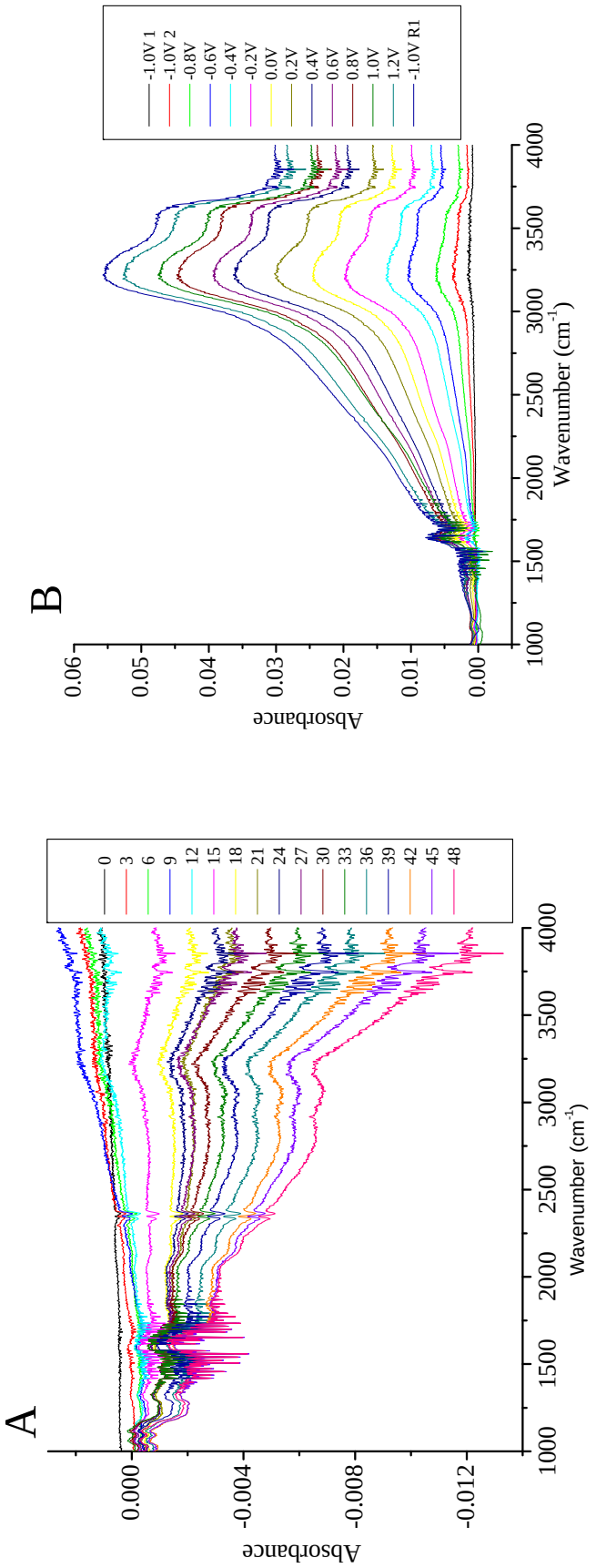


**Figure A.6A HT, $Na_2SO_4$, T-EAP: *In situ* FTIR absorbance spectra obtained using a HT-treated $TiO_2$ electrode immersed in 0.1 mol $dm^{-3}$ $Na_2SO_4$ under UV illumination. UV illumination was applied after the initial spectrum was collected. Spectra were collected at the indicated times (minutes). Applied potential was -0.8 V vs. Ag/AgCl, potential was shifted to 1.2 V vs. Ag/AgCl in a single step after 6 minutes and held until 27 minutes.**

**Figure A.6B T, $Na_2(OOC)_2$, P-EAP, Dark: *In situ* FTIR absorbance spectra obtained using a Thermal $TiO_2$ electrode immersed in 0.1 mol $dm^{-3}$ $Na_2SO_4$/0.2 mol $dm^{-3}$ $Na_2(OOC)_2$, in the dark. Spectra were collected at 2 minutes intervals, at the indicated potentials. 'R' denotes spectra obtained after the applied potential was returned to the initial potential.**

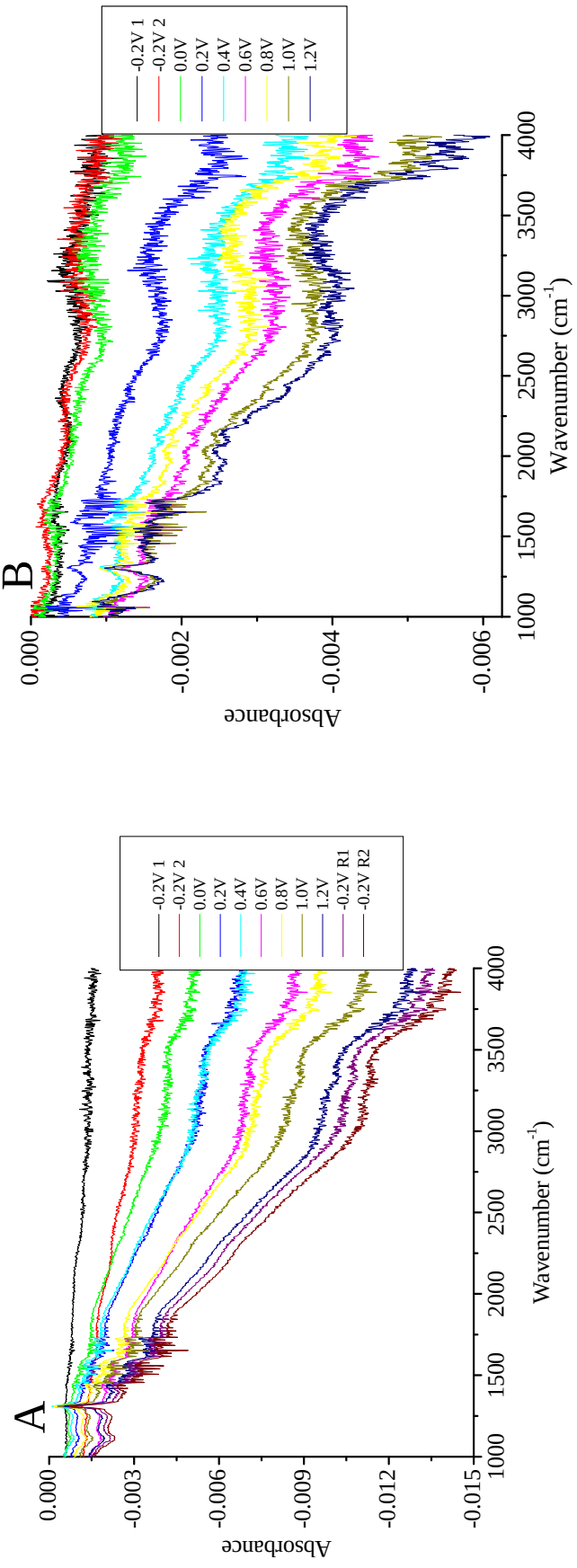


**Figure A.7A MW, $Na_2(OOC)_2$, P-EAP, Dark: *In situ* FTIR absorbance spectra obtained using a MW-treated $TiO_2$ electrode immersed in 0.1 mol $dm^{-3}$ $Na_2SO_4$/0.2 mol $dm^{-3}$ $Na_2(OOC)_2$, in the dark. Spectra were collected at 2 minutes intervals, at the indicated potentials. 'R' denotes spectra obtained after the applied potential was returned to the initial potential.**

**Figure A.7B HT, $Na_2(OOC)_2$, P-EAP, Dark: *In situ* FTIR absorbance spectra obtained using a HT-treated $TiO_2$ electrode immersed in 0.1 mol $dm^{-3}$ $Na_2SO_4$/0.2 mol $dm^{-3}$ $Na_2(OOC)_2$, in the dark. Spectra were collected at 2 minutes intervals, at the indicated potentials. 'R' denotes spectra obtained after the applied potential was returned to the initial potential.**
**was lowered to initial potential and held for the remainder of the experiment.**

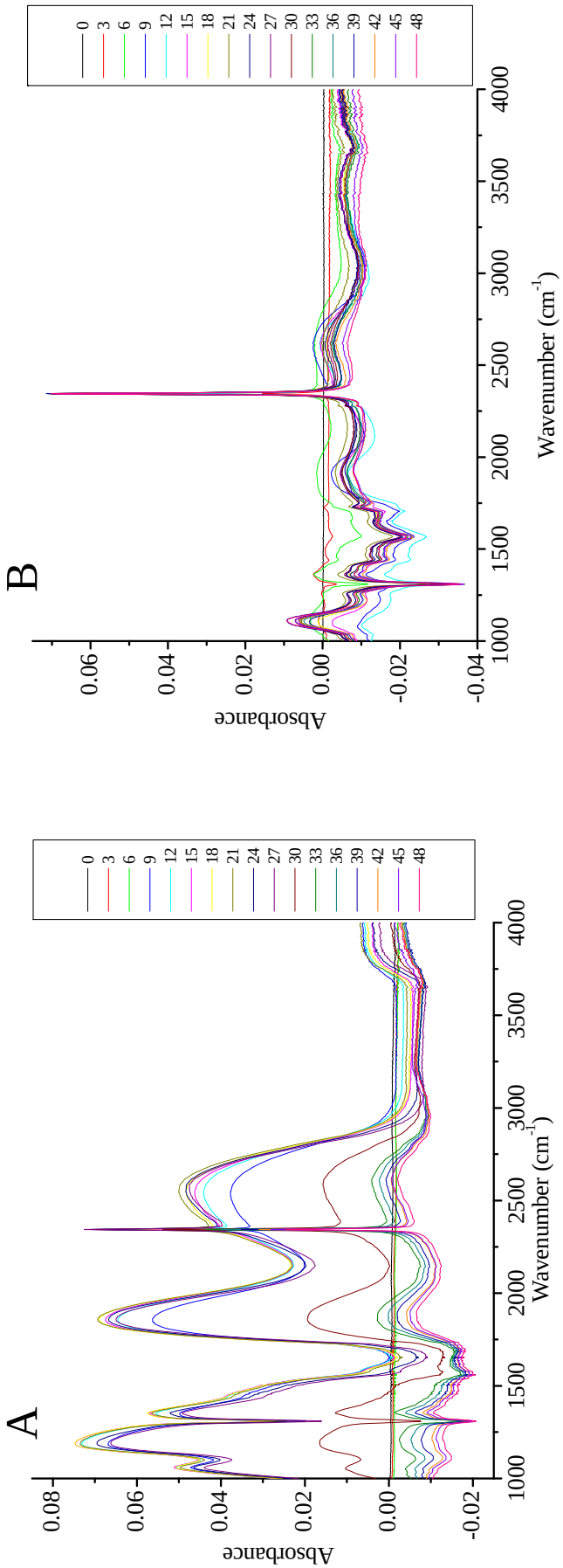


**Figure A.8A P25, $Na_2(OOC)_2$, PC: *In situ* FTIR absorbance spectra obtained during photocatalytic experiments using a Degussa P25 $TiO_2$ electrode immersed in 0.1 mol $dm^{-3}$ $Na_2SO_4$/0.2 mol $dm^{-3}$ $Na_2(OOC)_2$. Spectra were collected every 3 minutes, as indicated. UV irradiation was applied after 6 minutes and removed after 27 minutes.**

**Figure A.8B MW, $Na_2(OOC)_2$, T-EAP: *In situ* FTIR absorbance spectra obtained using MW-treated $TiO_2$ electrodes immersed in 0.1 mol $dm^{-3}$ $Na_2SO_4$/0.2 mol $dm^{-3}$ $Na_2(OOC)_2$, under irradiation with UV light. Light was applied after initial spectrum was collected in the dark (0). Spectra were collected at the indicated time intervals (minutes). Initial applied potential -0.2 V vs. Ag/AgCl; applied potential shifted to 1.2 V vs. Ag/AgCl in a single step after 6 minutes and held until 27 minutes. After 27 minutes potential was lowered to initial potential and held for the remainder of the experiment.**

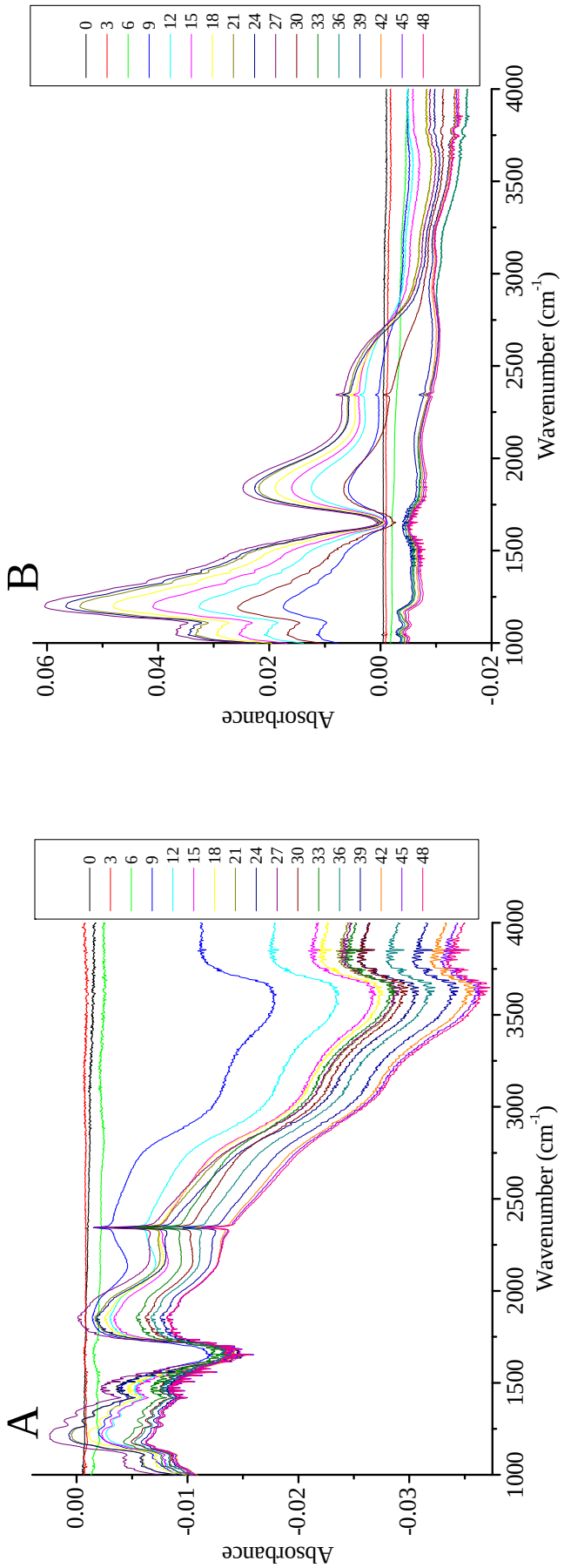


**Figure A.9A MW, NAG, PC: *In situ* FTIR absorbance spectra obtained during photocatalytic experiments using a MW-treated $TiO_2$ electrode immersed in 0.1 mol $dm^{-3}$ $Na_2SO_4$/0.2 mol $dm^{-3}$ NAG. Spectra were collected every 3 minutes, as indicated. UV irradiation was applied after 6 minutes and removed after 27 minutes.**

**Figure A.9B HT, NAG, PC: *In situ* FTIR absorbance spectra obtained during photocatalytic experiments using a HT-treated $TiO_2$ electrode immersed in 0.1 mol $dm^{-3}$ $Na_2SO_4$/0.2 mol $dm^{-3}$ NAG. Spectra were collected every 3 minutes, as indicated. UV irradiation was applied after 6 minutes and removed after 27 minutes.**

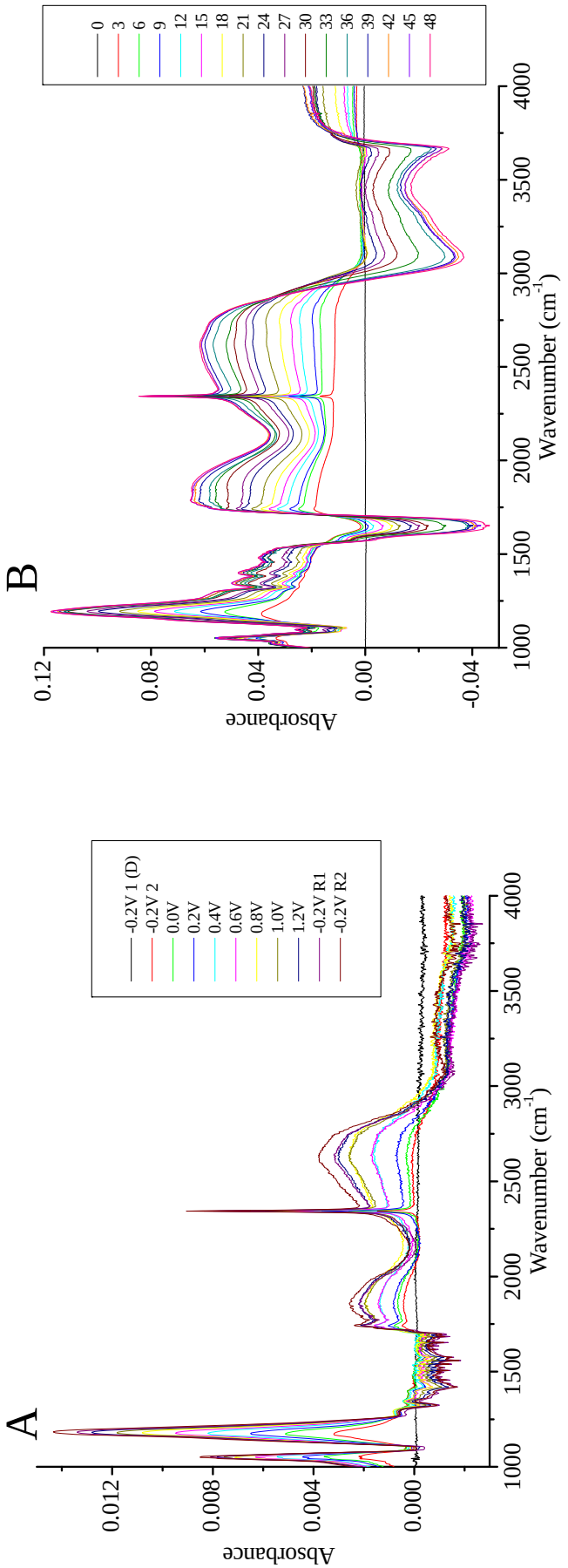


**Figure A.10A HT, NAG, P-EAP, Light: *In situ* FTIR absorbance spectra obtained during potential dependent EAP using a HT-treated $TiO_2$ electrode immersed in 0.1 mol $dm^{-3}$ $Na_2SO_4$/0.2 mol $dm^{-3}$ NAG, under irradiation with UV light (light switched on after -0.2V 1 (D)). Spectra were collected at the indicated potentials. 'R' denotes spectra obtained after the applied potential was returned to the initial potential.**

**Figure A.10B P25, NAG, T-EAP: *In situ* FTIR absorbance spectra obtained using a Degussa P25 $TiO_2$ electrode immersed in 0.1 mol $dm^{-3}$ $Na_2SO_4$/0.2 mol $dm^{-3}$ NAG, under irradiation with UV light (light switched on after initial spectrum was collected). Spectra were collected at the indicated time intervals (minutes). Initial applied potential -0.2 V vs. Ag/AgCl; applied potential shifted to 1.2 V vs. Ag/AgCl in a single step after 6 minutes and held until 27 minutes. After 27 minutes potential was lowered to initial potential and held for the remainder of the experiment.**